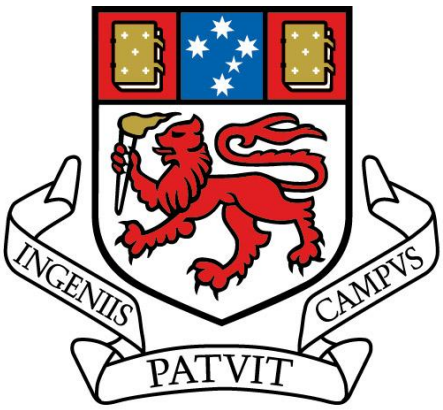

UNIVERSITY OF TASMANIA

Steric and Electronic Investigations into Samarium(II) Dinitrogen, Heteroalkyne and Heterocycle Reductions

By

Adam Norman James, B. Sc. (Hons)

A thesis submitted in fulfilment

of the requirements for the degree of

Doctor of Philosophy

School of Chemistry, University of Tasmania, October 2011

This thesis contains no material which has been accepted for the award of any other degree or diploma in any University, and contains no copy or paraphrase of material previously presented by another person, except where due reference is made in the text.

This thesis may be made available for loan and limited copying and communication in accordance with the Copyright Act 1968.

Adam James

October 2011

Acknowledgements

Sincere thanks must go to my supervisor, Dr Michael Gardiner, without whom I would have been unable to undertake this work. Dr Gardiner's understanding and, perhaps more importantly, his generosity of understanding, is remarkable. Appropriately, I feel that I have learned a great deal about a range of things too vast to truly be represented by this document alone, least of all the things I have learned about myself. Thanks, Mike.

Professors Brian Yates (a late but welcome addition as co-supervisor) and Peter Boyd (University of Auckland, NZ) have been instrumental in navigating the treacherous waters of computational chemistry. Without their generous support, and of that of Dr Nigel Brookes and Dr Ruth Amos, so much of the work presented here would be without the insight provided by the calculations they helped me to achieve. Thanks to you all for your endless patience and trouble-shooting.

My predecessors in the laboratory, Dr Jun Wang, Dr Alistair Frey and Mr Andrew Dick, must also be acknowledged for their early work upon which this work stands. Also lending support and advice in the laboratory and in general were Dr Damien Stringer, Dr Peter Molesworth, Dr Bryce Lockhart-Gillett, Dr Sam Karpiniec, Dr Roderick Jones, Mr Samuel Coe and Ms Adele Wilson.

Thanks must also go to Dr Noel Davies and Dr Thomas Rodemann for advice and support in GC-MS and elemental analysis, respectively. Finally, sincere thanks to the beamline scientists of the protein and small molecule crystallography beamline (MX1, MX2) at the Australian Synchrotron in Melbourne, Australia. Without regular access to MX1, I doubt this project would have been possible.

This thesis is dedicated to my parents, Peter and Kate, who have always believed in and supported me. I will always be grateful for everything that they have done for me. I love them both very much.

Abstract

This thesis describes the synthesis, characterisation and reactivity of a range of samarium(II) and samarium(III) complexes of a modified porphyrinogen, *trans*-*N,N'*-dimethyl-*meso*-octaethylporphyrinogen, $Et_8N_4Me_2H_2$. Various related reactivity themes include the sterically rigid porphyrinogen and the Sm^{II}/Sm^{III} redox couple.

Chapter 1 provides a broad introduction and relevant background on the properties of samarium with respect to the other lanthanoids. General aspects of the organometallic chemistry of the lanthanoid elements are discussed, including: sterically induced reduction, relevant and related chemistry of the modified porphyrinogen, and general considerations of computational techniques employed in this thesis.

Chapter 2 outlines the synthesis of a Lewis base free (unsolvated) samarium(II) porphyrinogen complex, $[\{(Et_8N_4Me_2)Sm\}_n]$, and its subsequent unprecedented reactivity with dinitrogen to provide the first example of end-on binding of dinitrogen to a lanthanoid element, $[\{(Et_8N_4Me_2)Sm\}_2(\mu\text{-}\eta^1\text{:}\eta^1\text{-}N_2)]$. The unique binding mode is rationalised by steric and electronic arguments and subsequently probed by theoretical investigations which provide a richer understanding of the degree of activation of the dinitrogen moiety. A number of other Sm^{II} complexes are also reported.

The reactions of the samarium(II) complex, $[(Et_8N_4Me_2)Sm(THF)_2]$ and simple *N*-heteroalkynes are described in Chapter 3. At room temperature, simple 2:1 and 1:1 adducts of nitriles are observed, while isonitriles and nitriles at higher

temperature are reduced by the samarium(II) complex resulting initially in C−N and C−C bond cleavage, respectively, with catalytic oligomerisation of nitriles and *t*-Butyl radical trapping chemistry observed as subsequent steps.

A systematic investigation of the interaction between substituted pyridines, benzannulated pyridines, 2,2′-bipyridine and substituted 1,10-phenanthrolines by X-ray crystallography is detailed in Chapter 4. Reaction outcomes including mono- and bis- adduct formation, single electron ligand reduction, and reductive dimerisations are reported. Computational techniques are employed to analyse unpaired electron populations and thus determine oxidation states and rationalise reactivity observations regarding ligand reduction *versus* reductive dimerisation across this series.

Concluding remarks and comments regarding further work are made in Chapter 5; all references are catalogued in Chapter 6. General experimental information is provided in Appendix A. A rigorous trigonometric definition of the molecular geometry is provided in Appendix B. The X-ray crystal structure data, by way of crystallographic information file (.CIF), is provided electronically in Appendix C. Computational output files (.OUT) are provided electronically in Appendix D.

Table of Contents

Abbreviations

8-Mequin	8-methylquinoline
Å	Angstrom
acac	acetylacetone, $[RO=C(CH_3)-C(H)=C(CH_3)-OR']^-$
acrid	acridine
atm	atmosphere (pressure)
batho	4,7-diphenyl-1,10-phenanthroline
benzo[h]	benzo[h]quinoline
benzo[f]	benzo[f]quinoline
bipy	2,2′- or 4,4′-bipyridine (specified in each case)
$(C_5H_5)^-$	cyclopentadienide anion
$(C_5Me_5)^-$	1,2,3,4,5-pentamethylcyclopentadienide anion
COT	1,3,5,7-cyclooctatetraene
Cy	cyclohexyl, $-C_6H_{11}$
DMSO	dimethylsulfoxide, Me_2SO
ex.	excess
hr(s)	hour(s)
J	Joule
Lut	2,6- or 3,5-dimethylpyridine (specified in each case)
m-	meta
Me	methyl, $-CH_3$
Me_2phen	4,7-dimethyl-1,10-phenanthroline
2-Me-6-Phpy	2-methyl-6-phenylpyridine
mol	Mole
nacnac	$[RN=C(CH_3)-C(H)=C(CH_3)-NR']$

neo	2,9-dimethyl-1,10-phenanthroline
o-	ortho
p-	para
pet.	petroleum
Ph	phenyl, C_6H_5
phen	1,10-phenanthroline
Phpy	2-phenylpyridine
pic	2-methylpyridine
py	pyridine
quin	quinoline
rt	room temperature
SIR	Sterically induced reduction
t-Bu	tertiarybutyl, $-C(CH_3)_3$
t-BuDAB	1,4-bis(tertiarybutyl)-1,4-diazabuta-1,3-diene
	$(CH_3)_3C–N=C(H)-C(H)=N-C(CH_3)_3$
terpy	2,2′;6′,2″-terpyridine
V	Volts

Chapter 1

Introduction

1.1 Group 3 Elements; the Rare Earths

Group 3 of the Periodic Table suffers from some difference of opinion regarding the elements from which it is composed[1]. The first two elements by size, scandium and yttrium, are definitively Group 3 metals, but the heavier elements (beginning with lanthanum) of Group 3 are not defined by IUPAC and thus one of several conventions dictates the format of each representation of the Periodic Table. The difficulty in classification arises due to the unique properties of the Rare Earth elements, which in turn is derived from the properties of f orbitals.

The elements scandium, yttrium, lanthanum – lutetium are the 17 elements that make up the Rare Earth elements, as defined by IUPAC. Of these, the subset of elements from lanthanum to lutetium are referred to as either the Lanthanoids (literally „like lanthanum') or the Lanthanides (usually, the –ide suffix denotes an anionic species, *cf.* chloride, however wide-spread use confers a degree of acceptability to the term). Similarly, the actinoids are the elements from actinium to lawrencium, and the position of the actinoids in the periodic table will follow the convention applied at the earlier lanthanoids. The f-block contains both the lanthanoids and actinoids.

Debate continues regarding whether lanthanum is a true Group 3 element, leaving the lanthanoids beginning with cerium and ending with lutetium, or whether lutetium is the true Group 3 element and the lanthanoids are lanthanum through ytterbium. Table 1-1 describes both the neutral and ubiquitous (across the lanthanoids) +3 oxidation states for

the Rare Earths (the chemistry of scandium is not described and will not be discussed further throughout this thesis). The merit of placing either lanthanum or lutetium in Group 3 becomes clear on inspection of the electron configuration of each; lanthanum has the expected Group 3 electronic configuration $[Xe]5d^16s^2$ with an empty f- orbital shell and lutetium has a full complement of 4f electrons ($[Xe]4f^{14}5d^16s^2$), meaning both have claim to the Group 3 position. An alternate approach to either of the aforementioned descriptions of these elements is to have no element appear in the Group 3 column; rather, to place all 15 lanthanoids from lanthanum to lutetium in a 15 element series at the bottom of the Periodic Table.

Symbol	Name	Ln^0 electron configuration	Ln^{III} electron configuration	Metallic radius (Å)	Ln^{III} radius (Å)
Y	Yttrium	$[Kr]4d^15s^2$	[Kr]	1.810	1.040
La	Lanthanum	$[Xe]5d^16s^2$	[Xe]	1.877	1.172
Ce	Cerium	$[Xe]4f^15d^16s^2$	$[Xe]4f^1$	1.825	1.150
Pr	Praseodymium	$[Xe]4f^36s^2$	$[Xe]4f^2$	1.828	1.130
Nd	Neodymium	$[Xe]4f^46s^2$	$[Xe]4f^3$	1.821	1.123
Pm	Promethium	$[Xe]4f^56s^2$	$[Xe]4f^4$	1.810	1.110
Sm	Samarium	$[Xe]4f^66s^2$	$[Xe]4f^5$	1.802	1.098
Eu	Europium	$[Xe]4f^76s^2$	$[Xe]4f^6$	2.042	1.087
Gd	Gadolinium	$[Xe]4f^75d^16s^2$	$[Xe]4f^7$	1.802	1.078
Tb	Terbium	$[Xe]4f^96s^2$	$[Xe]4f^8$	1.782	1.063
Dy	Dysprosium	$[Xe]4f^{10}6s^2$	$[Xe]4f^9$	1.773	1.052
Ho	Holmium	$[Xe]4f^{11}6s^2$	$[Xe]4f^{10}$	1.766	1.041
Er	Erbium	$[Xe]4f^{12}6s^2$	$[Xe]4f^{11}$	1.757	1.030
Tm	Thulium	$[Xe]4f^{13}6s^2$	$[Xe]4f^{12}$	1.746	1.020
Yb	Ytterbium	$[Xe]4f^{14}6s^2$	$[Xe]4f^{13}$	1.940	1.008
Lu	Lutetium	$[Xe]4f^{14}5d^16s^2$	$[Xe]4f^{14}$	1.734	1.001

Table 1-1 Electron configuration and atomic radius of yttrium and the lanthanoids.[2]

The metallic and Ln^{III} ionic radius of the lanthanoids generally decreases with increasing atomic number, as shown in Table 1-1 above. This phenomenon is a result of the diminished capacity for f- electrons to shield the nuclear charge from the electrons situated farther from the nucleus; thus the more remote electrons experience a greater effective nuclear charge and are more tightly held by the nucleus, reducing the atomic radius. As more poorly-shielding f- electrons are added with increasing atomic charge, the

diminished ability of those electrons to shield the nuclear charge becomes more pronounced, and so this reduction in ionic radius across the lanthanoids becomes more pronounced. This effect is called the Lanthanide Contraction and is experienced by all f-electron containing elements and explains, for example, the similarity in size of hafnium and zirconium.

Further contributing to the Lanthanide Contraction are the relativistic effects that contract the s- orbitals by increasing the mass of the electron. Relativistic effects are experienced by s- electrons due to the high speeds the electrons must take to avoid capture by the positive nucleus in s-orbitals (which have zero nodes). The effect becomes more pronounced as the nuclear charge increases. Figure 1-1a below shows the radial probability functions for the 4f, 5s, 5p, 5d and 6s orbitals without accounting for relativistic effects, while Figure 1-1b includes the relativistic effects to give the more accurate description. Figure 1-1b is more complex as the second outcome of including relativistic effects in the description of these orbitals is that the p, d and f orbitals are split by spin-orbit coupling, resulting in the trace for 4f-, 5p- and 5d- orbitals. Spin-orbit coupling arises when the angular momentum associated with the spin of an electron couples with the angular momentum generated by its orbital motion. Figure 1-1b demonstrates that the valence shell of the lanthanoids, the 4f shell, resides closer to the nucleus than the 5s and 5d orbitals. This feature of lanthanoid chemistry dominates the properties of the elements as only minimal ligand interaction with the f-electrons can occur.

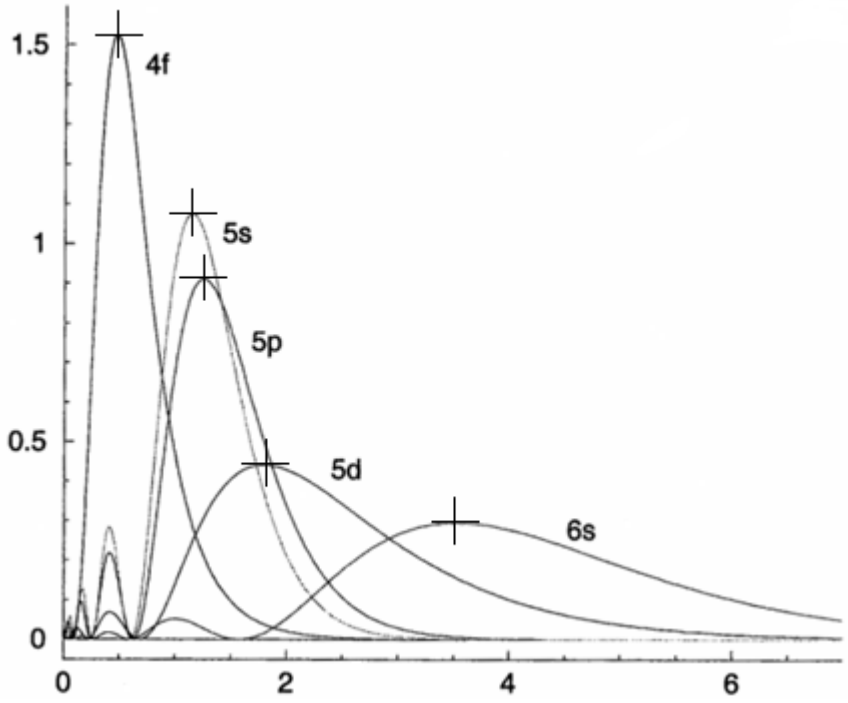

Figure 1-1a The radial probability functions for the 4f, 5s, 5p, 5d and 6s orbitals of Lu. Reproduced from Asipinall.[2] Peak maxima added for comparison with Figure 1-1b.

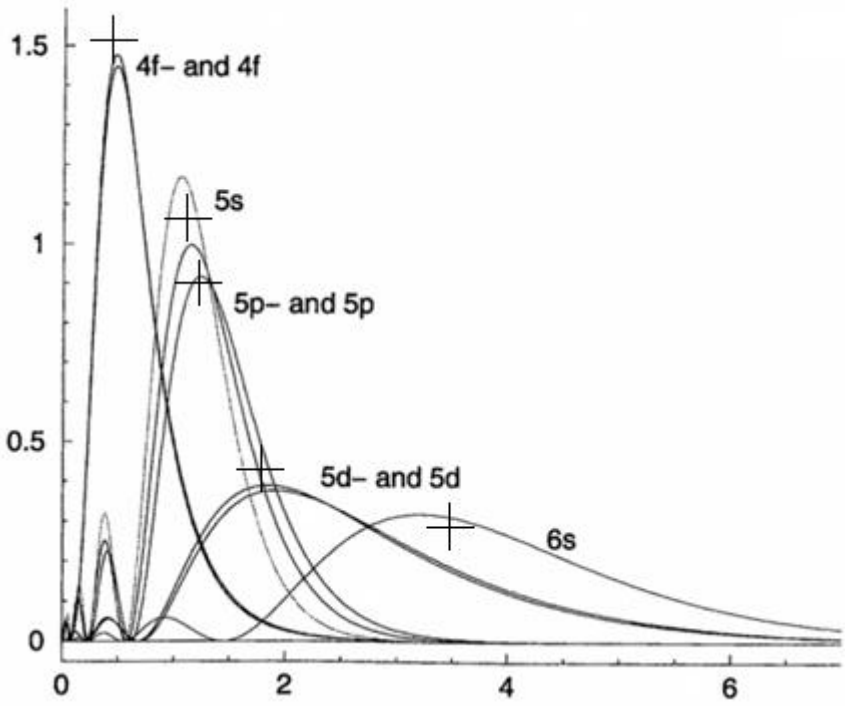

Figure 1-1b The radial probability functions for the 4f, 5s, 5p, 5d and 6s orbitals of Lu, including relativistic effects, reproduced from Aspinall.[2] Overlaid with peak maxima from Figure 1-1.

1.2 Oxidation States of the Lanthanoids

Group 3 chemistry is dominated by the +3 oxidation state since the loss of three electrons attains the previous noble gas electron configuration. Table 1-2 describes the ionisation potentials for yttrium and the lanthanoids. In all cases, the 4th ionisation potential is greater than the sum of the first three ionisation potentials, meaning that in most cases the energy return for releasing the fourth electron is less than the cost of removing it and the +4 oxidation state is largely unobtainable; thus, the highest oxidation state generally available to lanthanoids is +3 as the remaining electrons are bound too tightly to the nucleus to be reasonably accessible to further ionisation. The only lanthanoid with extensive +4 chemistry is cerium, where the loss of four electrons, including a single 4f electron, results in the preceding noble gas configuration (Table 1-1). Despite this, +4 oxidation states have been achieved in the solid state using the most electronegative ligand, fluoride, to access complexes of neodymium, dysprosium, praseodymium and terbium; the latter two elements are also observed as Ln^{IV} dioxides.

Symbol	Name	E^0 (Ln^{III}/Ln^0) (V)	1st IP (kJ mol^{-1})	2nd IP (kJ mol^{-1})	3rd IP (kJ mol^{-1})	4th IP (kJ mol^{-1})
Y	Yttrium	-2.372	616.0	1181	1980	5963
La	Lanthanum	-2.522	538.1	1067	1850	4819
Ce	Cerium	-2.483	527.4	1047	1949	3547
Pr	Praseodymium	-2.462	523.1	1018	2086	3761
Nd	Neodymium	-2.431	529.6	1035	2130	3899
Pm	Promethium	-2.423	535.9	1052	2150	3970
Sm	Samarium	-2.414	543.3	1068	2260	3990
Eu	Europium	-2.407	546.7	1085	2404	4110
Gd	Gadolinium	-2.397	592.5	1167	1990	4250
Tb	Terbium	-2.391	564.6	1112	2114	3839
Dy	Dysprosium	-2.353	571.9	1126	2200	4001
Ho	Holmium	-2.319	580.7	1139	2204	4100
Er	Erbium	-2.296	588.7	1151	2194	4115
Tm	Thulium	-2.278	596.7	1163	2285	4119
Yb	Ytterbium	-2.267	603.4	1176	2415	4220
Lu	Lutetium	-2.255	523.5	1340	2022	4360

Table 1-2 Lanthanoid(III)/Lanthanoid(0) potential and 1st – 4th ionisation potentials.[2]

Table 1-2 demonstrates the variability of the third ionisation potential across the lanthanoid series. The data is visually represented in Figure 1-2, below, and clearly shows very high values for europium and ytterbium followed immediately by very low values for gadolinium and lutetium.

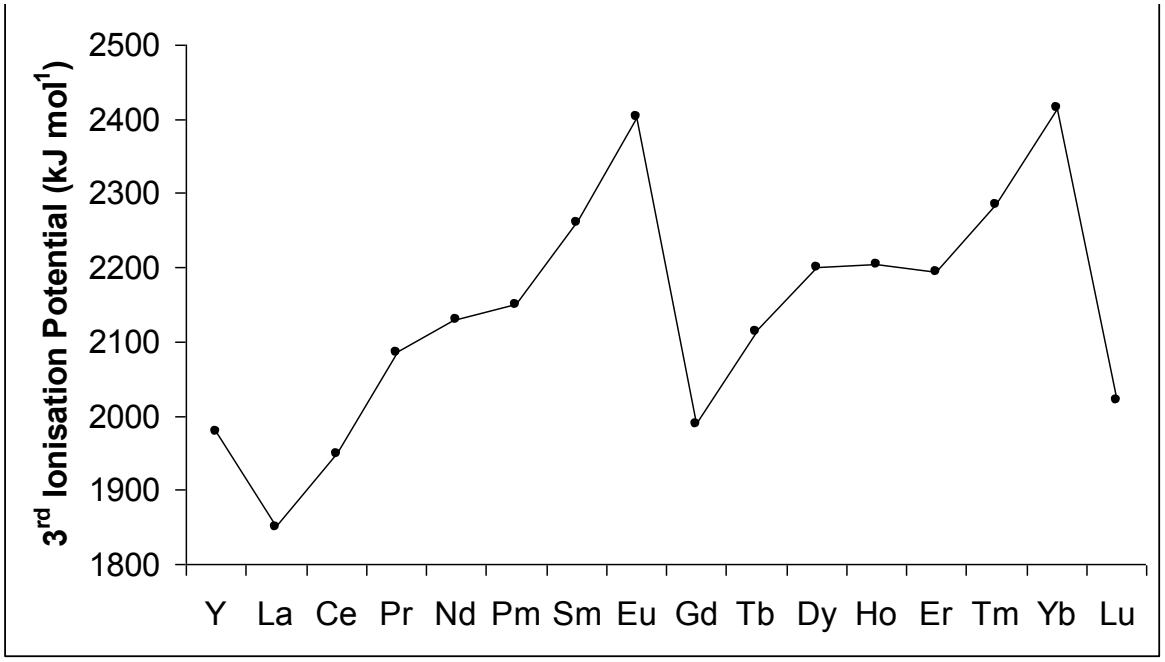

Figure 1-2 The variation in third ionisation potential across ytterbium and the lanthanoids.

The peaks in third ionisation potential across the lanthanoids in Figure 1-2 correspond to the half-filled and fully filled shells of the +2 ions Eu^{II} and Yb^{II}, while the valleys correspond to the half-filled and fully filled shells of the +3 ions Gd^{III} and Lu^{III}. The lower third ionisation potential of both gadolinium and lutetium is due to the additional stabilisation the half- and fully- filled orbitals obtained with the loss of the third electron.

The Standard Potential in acidic solution for the Eu^{II}/Eu^{III} couple is 0.35 V and for the Yb^{II}/Yb^{III} couple is 1.05 V[3], reflecting the enhanced stability of the +2 oxidation state for these species relative to the +3 state, despite the overall tendency toward the +3 state. The Standard Potential in acidic solution for the Sm^{II}/Sm^{III} couple is 1.55 V and for the

Tm^{II}/Tm^{III} couple is 2.30 V; a direct result of the third ionisation potential (Figure 1-2) of these species being „intermediate' between the stabilised +2 species that follow them and the strong preference for the +3 state in the species that precedes them. Indeed, it is the accessible yet actively reducing nature of samarium(II) that led to the investigation of samarium chemistry exclusively, as reported herein.

1.3 Samarium

Spectroscopically discovered by the Swiss chemist Jean Charles Galissard De Margnac in 1853 and first isolated in 1879 by the French chemist Paul Émile Lecoq de Boisbaudran, samarium is not present in nature in its metallic form; rather it is found in minute quantities in many minerals, primarily monazite, bastnäsite and samarskite. Samarium is extracted in relatively pure form *via* ion exchange processes, solvent extraction techniques and electrochemical deposition.

The applications of samarium are not extensive; however it has found use, along with other Rare Earths, in carbon-arc lighting for the motion picture industry. Samarium is used to dope calcium fluoride crystals for use in lasers, while samarium oxide absorbs infrared radiation and thus finds application in optical glass. Alloyed with cobalt, $SmCo_5$ has lead to the development of a permanent magnet with the highest resistance to demagnetisation of any known material. Magnetic samarium cobalt alloys are used in high-end guitar pickups and related musical instruments. The neutron absorbing capability of one isotope of samarium is exploited in nuclear control rods used in nuclear reactors. Samarium-neodymium dating is utilised in the determination of the age relationships of rocks and meteorites. Radioactive ^{153}Sm is used as an analgesic in cases of severe pain related to cancer that has spread to bone.

1.4 π- Ligand Organolanthanoid Chemistry

In 1951, Kealy and Pauson reported a new type of compound where delocalised π- electrons in an aromatic system interact with metal d- orbitals.[4] Ferrocene, (**I**), was crystallographically shown by Eiland and Pepinsky in 1952 to incorporate two cyclopentadienide anions $(C_5H_5)^-$ coordinated to the metal centre in a staggered arrangement.[5]

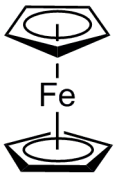

(**I**)

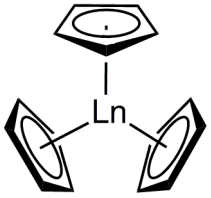

(**II**)

The structure of ferrocene, (**I**), is described as a „sandwich' complex and has paved the way for investigations of this type of chemistry across each block of the periodic table.[6, 7] Mono-, bis- and tris-cyclopentadienide complexes are known, with the bis-systems generically termed „metallocenes' (*viz*. ferrocene, ytterbocene, samarocene, *etc*.). Extension of this system to the lanthanoids lead to tris-cyclopentadienide compounds, (**II**), for Ln = Sc, Y, La, Ce, Pr, Nd, Sm, Gd, Dy, Er and Yb, some of which were preliminarily reported in 1954 and all of which were more fully reported (without crystallographic data) in 1956[8, 9]. These compounds are all similar in nature, existing as air sensitive M^{III} compounds that are only moderately soluble in pyridine and tetrahydrofuran and insoluble in non-coordinating organic solvents.

The first $[Ln^{II}(C_5H_5)_2]$ compounds were reported for Ln = Eu[10] and Yb[11] in coordinating solvents, reflecting the enhanced stability of the +2 oxidation state of these metals, as discussed in Section 1.2. $[Eu(C_5H_5)_2]$ and $[Yb(C_5H_5)_2]$ are both soluble in ammonia, which facilitated their initial synthesis. $[Sm(C_5H_5)_2]$, which is insoluble in

ammonia, was first isolated as the pyrophoric mono-THF adduct in 1969 by Watt and Gillow.[12] As with the europium monosolvate, attempts to remove the coordinating solvent resulted in decomposition.

Exploration of the ten π-electron system of dianionic cyclooctatetraendiyl, $(C_8H_8)^{2-}$, yielded in 1968 a direct analogue of ferrocene; uranocene.[13] The significant difference in atomic size between iron and uranium and the availability of 5f orbitals led to substitution of the $(C_5H_5)^-$ moiety with the larger anion, $(C_8H_8)^{2-}$, resulting in the analogous structure, (**III**).

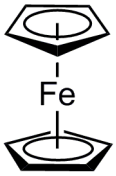

(**I**)

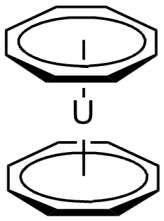

(**III**)

The structure of uranocene, (**III**), was proposed based on theoretical studies of the orbitals of uranium and $(C_8H_8)^{2-}$ prior to confirmation by X-ray crystal structure analysis.[13] Figure 1-3 shows a selection of the ligand and metal orbital sets, demonstrating the favourable orbital overlap that occurs for ferrocene, (**I**)a, and uranocene, (**III**)a.

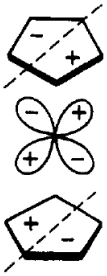

(**I**)a

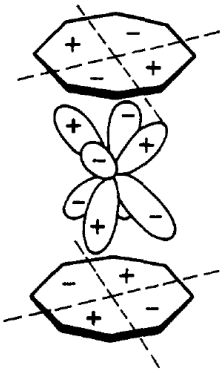

(**III**)a

Figure 1-3 Ligand e_{1g}/e_{2u} and metal $d_{xz},d_{yz}/f_{z(x^2-y^2)}$ orbital interactions of ferrocene (*left*) and uranocene (*right*).[14]

Application of the dianionic ten π-electron $(C_8H_8)^{2-}$ moiety to the Ln^{III} metals in 1973 revealed that, unlike the actinoid analogues, no significant amount of covalency occurred between the metal and the dianion, meaning that the 5f- orbitals of the actinoids interact much more in bonding than the 4f- orbitals of the lanthanoids, whose contribution is minimal.[15] The dominance of the Ln^{III} oxidation state throughout necessitated compound formulations of the type $[Ln(C_8H_8)_2K]$ or $[Ln(C_8H_8)Cl(THF)_2]$. Incorporation of the halide in this second case followed the earlier heteroleptic cyclopentadienide examples established by Maginn, Manastyrskyj and Dubeck in 1963, with their synthesis of $[Ln(C_5H_5)_2Cl]$[16] and $[Ln(C_5H_5)Cl_2]$.[17] The more stable low valent Eu^{II} and Yb^{II} ions facilitated the 1969 synthesis of the 1:1 $M(C_8H_8)$ complexes whilst maintaining the +2 oxidation state.[18]

Despite these advances, it was not until 1981 that Evans, *et al.* synthesised the first soluble samarium(II) species by introduction of the pentamethylcyclopentadienyl ligand, $(C_5Me_5)^-$, forming $[(C_5Me_5)_2Sm(THF)_2]$ *via* metal vapour synthesis.[19] Metal vapour synthesis requires uncommon and specialised equipment; however a newly developed source of Sm^{II} and Yb^{II} was identified by Girard, Namy and Kagan in 1977 *via* a simple metal oxidation reaction with diiodoethane in THF, Equation 1-1.[20, 21]

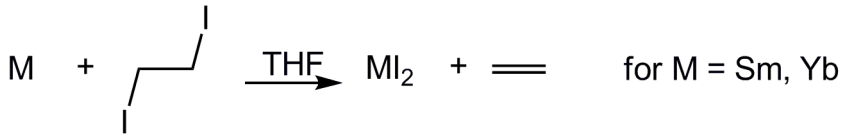

Equation 1-1

Further work by Evans *et al.* developed a convenient metathetical exchange reaction utilising the new SmI_2 reagent to access $[(C_5Me_5)_2Sm(THF)_2]$, (**IV**), *via* techniques accessible to standard laboratories, Equation 1-2.[22]

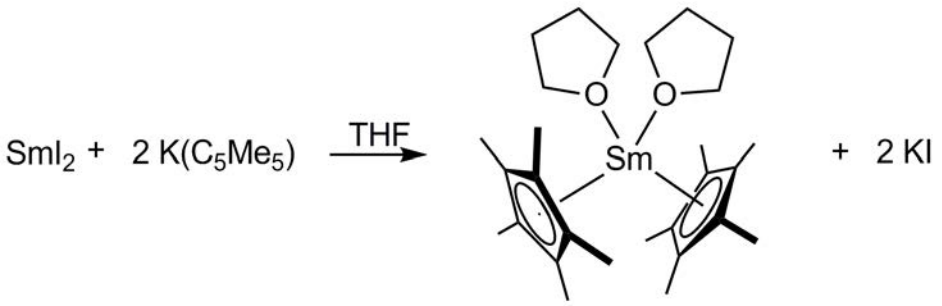

(**IV**)

Equation 1-2

Desolvation of the bis(THF) adduct, (**IV**), by sublimation *in vacuo* leads to the unsolvated species, $[(C_5Me_5)_2Sm]$, (**V**). In this way, by 1984, Evans, Hughes and Hanusa had prepared a lanthanoid complex directly comparable to ferrocene and discovered that, unlike ferrocene, it has a bent structure.[23] The intermolecular distance between the metal centre and the nearest methyl carbon of a second molecule is 3.22 Å in the solid state, significantly longer than the longest intramolecular Sm···C distance, 2.81 Å. Similarly, the shortest Sm···H intermolecular contact is 2.80 Å, *c.f.* the longest reported agostic interaction, 2.29 Å.[23] In 1986, Evans postulated that the bent structure observed in the lanthanoid sandwich complexes (following comparison with the analogous $4f^7$ Eu^{II} species) is due to the polarisation effect of one anion on the metal diminishing the electrostatic interaction between the metal and the second anion directly opposite. He surmised that adopting a bent structure may achieve better total electrostatic bonding for the two rings.[24] Schultz *et al.* reported the ytterbium analogue, decamethylytterbocene, in 2000 and provided a summary of the reported rationalisations for the observed bent geometry of lanthanocenes, reproduced *verbatim* herein:[25]

> "Several models have been advanced to rationalize this geometrical preference, including a molecular orbital model,[26, 27] an electrostatic (polarized-ion) model,[27, 28] and a model based on van der Waals attractive forces.[29, 30] To date no single explanation has been accepted. The molecular orbital model is, perhaps, unappealing, as the extent of mixing of the metal valence electrons with ligand orbitals is small for f-block metals. Indeed, it has been explicitly

stated that the molecular orbital model cannot account for the bending, as the calculated energy difference between the D_{5d} and C_{2v} structures is too small.[26] However, the 4f-electrons are more polarizable for divalent than for trivalent metals, and some polarization of metal electrons by the ligands is expected for divalent metallocenes. On the other hand, the electrostatic model treats the metal-ligand bonds as purely ionic, and this model does not allow mixing of metal and ligand electrons. Thus, the molecular orbital model overemphasizes covalent mixing, while the electrostatic model underemphasizes it. It can be seen that in those cases in which some polarization occurs, such as for divalent lanthanide metallocenes, these two models are not widely disparate.

"Bending a two-coordinate ML_2 molecule results in repulsion as the ligands approach each other at distances closer than the sum of their van der Waals radii. Such repulsion limits the bend angle. The repulsion is related to the metal radius, as a larger metal allows more bending before the ligands approach each other too closely. Generally, Me···Me distances on the order of 4.0 Å are viewed as repulsive since the van der Waals radius of a methyl group is about 2.0 Å. The closest Me··· Me inter-ring distance in the gas-phase structure of $(Me_5C_5)_2Yb$ is 4.15 Å, a distance at which the interaction may be stabilizing.[31] This is the origin of the van der Waals model.[32] In choosing among the various models, it is important to remember that the stabilization energy on bending is extremely small, probably on the order of 1 - 5 kcal/mol,[26, 27] and no experiment to date has been able to prove any of the models."

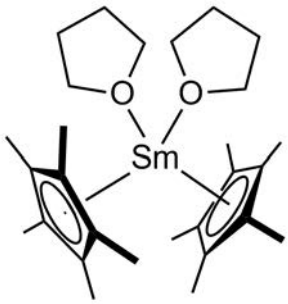

(IV)

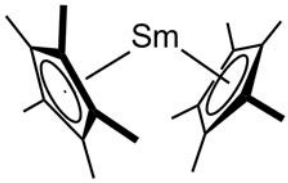

(V)

Decamethylsamarocene, (**V**), is more reactive than the bis(THF) solvated species, (**IV**), as a direct result of the decrease in electron density about the metal centre. In 1988

the first dinitrogen complex of an f- element, (**VI**) was crystallographically authenticated after several weeks of exposure of crystalline (**V**) to an atmosphere of N_2.[33] The reaction is reversible in toluene and was the first reported example of side-on bonding between two metals and dinitrogen, Figure 1-4.

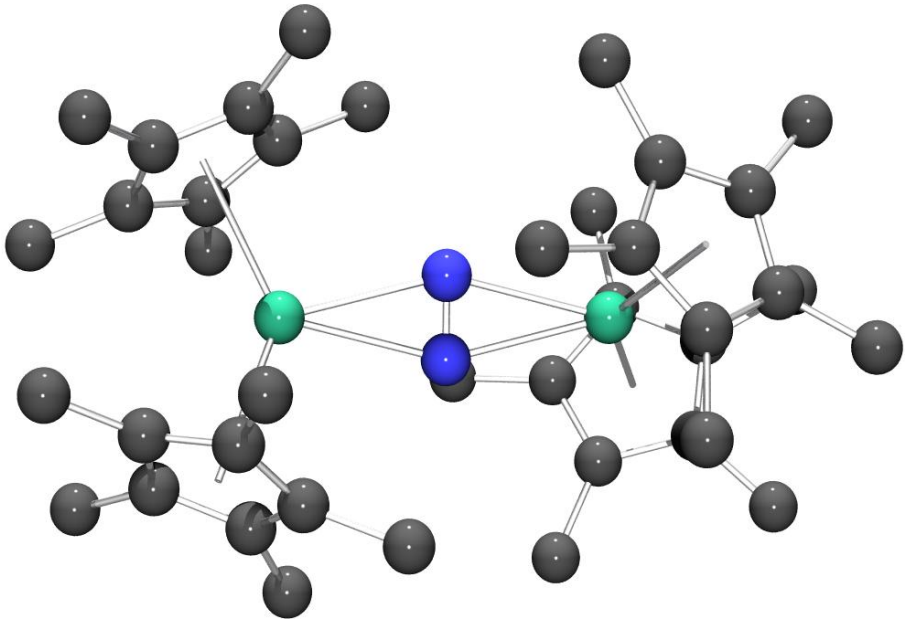

Figure 1-4 Crystal structure of the first f-element dinitrogen complex, $[\{(C_5Me_5)_2Sm\}_2(\mu\text{-}\eta^2\text{:}\eta^2\text{-}N_2)]$, (**VI**). Hydrogen atoms omitted for clarity.[33]

Reactivity of $[(C_5Me_5)_2Sm(THF)_2]$, (**IV**) and $[(C_5Me_5)_2Sm]$, (**V**), has been extensively explored by Evans *et al.* and will be discussed by direct comparison to work undertaken in the course of this candidature at a later point in this thesis.

During the course of their investigations, Evans, Gonzales and Ziller discovered the first tris(pentamethylcyclopentadienide) complex of any element, $[(C_5Me_5)_3Sm]$, (**VII**), Equation 1-3.[34] This result was unexpected since the cone angle of the $(C_5Me_5)^-$ ligand ordinarily falls between 130 - 140 ° for samarium(III) complexes, naturally precluding incorporation of three of these ligands around any spherical metal.[35] The smallest cone angle observed before $(C_5Me_5)_3Sm$ was in $(C_5Me_5)_2Sm(C_5H_5)$, which has a metallocene bend angle of 127 ° to the $(C_5Me_5)^-$ ligands.[35]

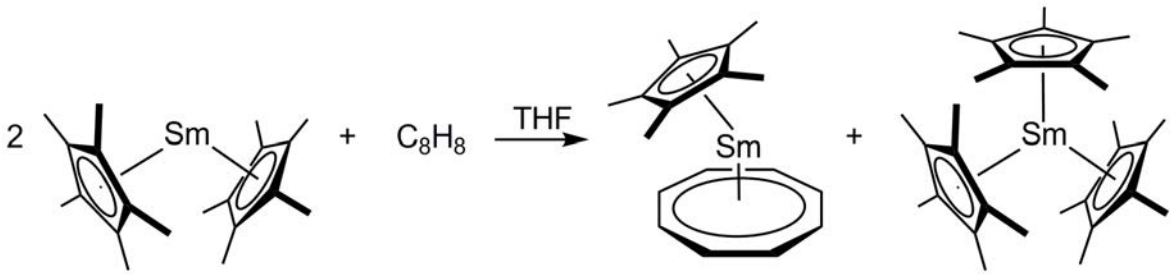

(V) **(VII)**

Equation 1-3

To accommodate the third $(C_5Me_5)^-$ moiety, the Sm−C bond lengths of (**VII**), 2.78-2.91 Å, increase compared to decamethylsamarocene, (**V**), 2.78-2.82 Å, despite the decrease in metal radius accompanying oxidisation from Sm^{II} to Sm^{III}. The increase in bond length results in a reduction in the $(C_5Me_5)^-$ cone angle, Figure 1-5. Furthermore, the methyl groups are oriented such that they minimise steric interactions by interlocking between the adjacent ligand and also splay back out of the plane of the ring by 0.17 – 0.52 Å, more than the previously observed methyl displacement in $[(C_5Me_5)_2LnL]$ complexes, for L = ligand, which range from 0.09 – 0.31 Å.[34]

In 1996, Evans *et al.* increased the steric bulk of $[(C_5Me_5)_3Sm]$, (**VII**), by substituting the tetramethylethyl- ligand, $(C_5Me_4Et)^-$, for the pentamethyl- ligand, (C_5Me_5), resulting in a similar structure.[36]

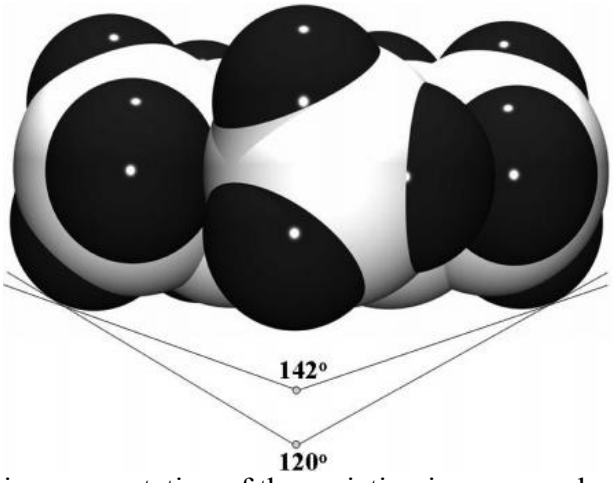

Figure 1-5 Schematic representation of the variation in cone-angle as a function of coordination distance for sterically strained pentamethylcyclopentadienide complexes.[37]

1.5 Sterically Induced Reduction

Investigation of the chemistry of the sterically crowded $[(C_5Me_5)_3Sm]$ compound, (**VII**), revealed that it has reductive reactivity similar to the unsolvated divalent samarium complex $[(C_5Me_5)_2Sm]$, (**V**). The reduction chemistry of divalent samarium complexes is a result of the Sm^{II}/Sm^{III} REDOX couple (which has a potential of 1.55 V, Section 1.3), however trivalent samarium has no higher oxidation state available and, hence, no reduction chemistry was anticipated. Despite this, reduction chemistry has been observed, with identical organosamarium derivatives featuring reduced substrates obtained from both Sm^{II} (Equation 1-4) and Sm^{III} (Equation 1-5) starting materials. The trivalent starting material also produced the coupled by-product $(C_5Me_5)_2$, indicating that the reduction was achieved *via* a $(C_5Me_5)/(C_5Me_5)^-$ redox couple.[38]

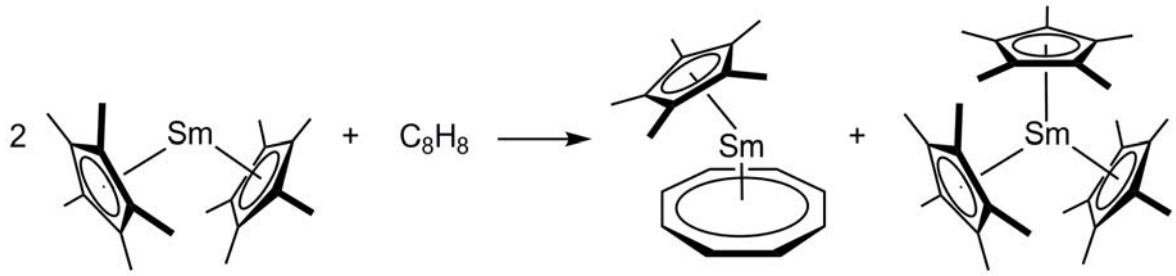

Equation 1-4

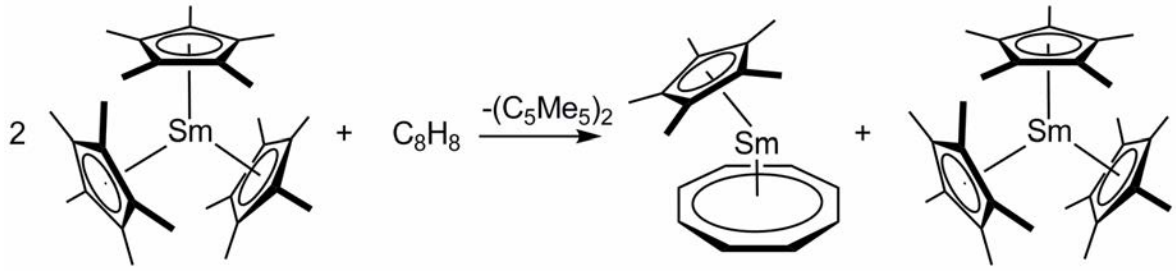

Equation 1-5

Inspection of the half-equation for each of these reactions provides rationalisation of the observed reactivity; in both cases the organosamarium products are the same, Equation 1-6 and Equation 1-7.[38]

$$[(C_5Me_5)_2Sm] \rightarrow e^- + [(C_5Me_5)_2Sm]^+$$

Equation 1-6

$$[(C_5Me_5)_3Sm] \rightarrow e^- + [(C_5Me_5)_2Sm]^+ + {}^1/_2(C_5Me_5)_2$$

Equation 1-7

Ligand based reduction is not unprecedented in lanthanoid chemistry,[39] nor, indeed, is the involvement of the $(C_5Me_5)^-$ moiety in reductions; in 1980 Tilley *et al*. prepared $[(C_5Me_5)_2Eu(THF)(Et_2O)_n]$ where $n = 0, 1$ from $EuCl_3$ and three equivalents of $[Na(C_5Me_5)]$.[40]

The unique aspect of this $(C_5Me_5)/(C_5Me_5)^-$ reduction is that it only occurs in sterically crowded complexes; thus, this type of reactivity was not observed despite many investigations into the $[(C_5Me_5)_2LnL]$ system,[41] including complexes as bulky as $[(C_5Me_5)_2Sm(C_5H_5)]$.[35] The elongation of the Sm−C bond and the splaying of the methyl groups from the aromatic ligand plane found in the sterically crowded $[(C_5Me_5)_3Sm]$ species has been rationalised to result in an electrostatic destabilisation of the complex, potentially explaining the availability of the usually stably bound $(C_5Me_5)^-$ moiety.[42] This type of reduction chemistry is clearly differentiated from previously observed metal (Equation 1-4) and ligand (Equation 1-8) based reduction chemistry, and is thus *Sterically Induced Reduction* (SIR).

$$8\ Ln(SPh)_3 + 6\ S \rightarrow Ln_8S_6(SPh)_{12}(THF)_8 + 6\ PhSSPh$$

Equation 1-8

Comparison of the relative reduction strength of $[(C_5Me_5)_2Sm]$, (**V**), and the SIR based $[(C_5Me_5)_3Sm]$, (**VII**), systems revealed that the unsolvated, divalent species is a slightly stronger reducing agent, effecting both a one (Equation 1-9)[43] and two (Equation 1-10)[44] electron reduction of azobenzene (with appropriate stoichiometry),

where the trivalent, SIR based reductant results only in a single electron reduction of azobenzene independent of stoichiometry, Equation 1-11.[38]

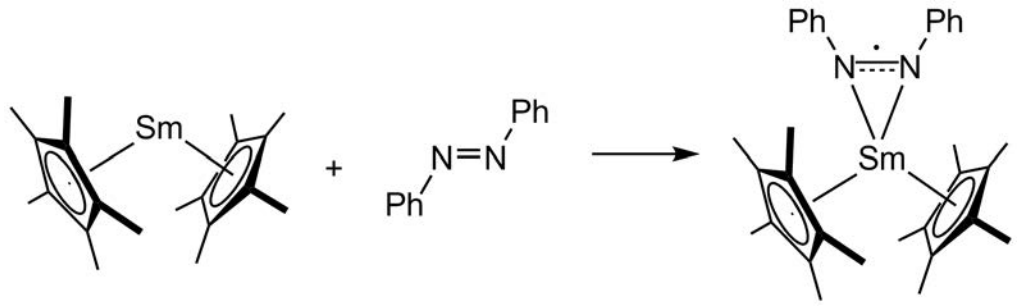

Equation 1-9

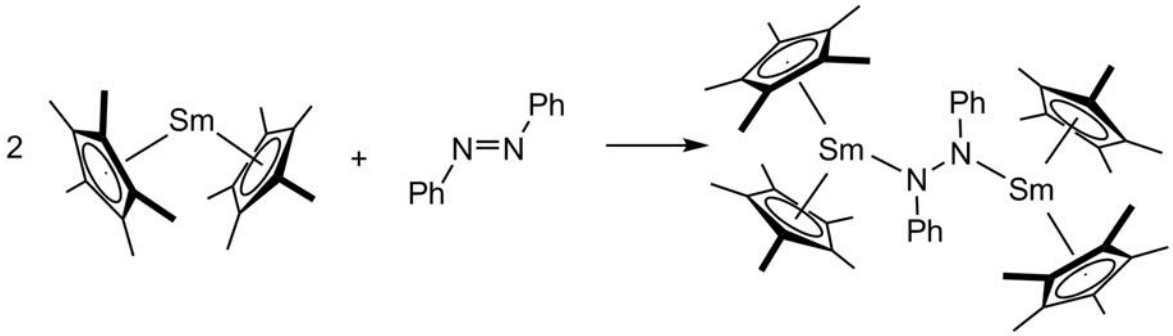

Equation 1-10

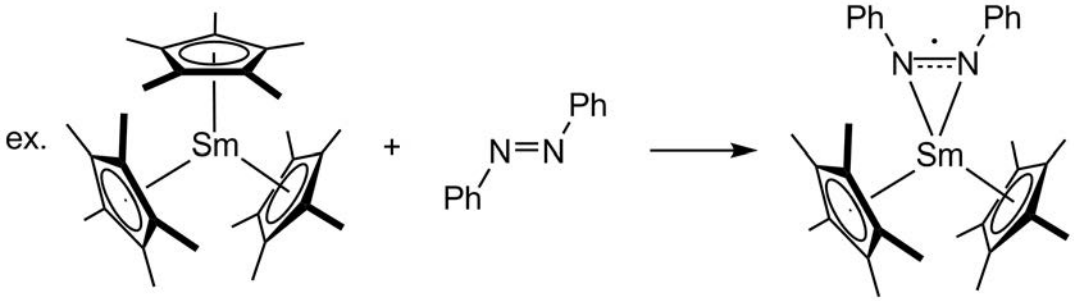

Equation 1-11

Application of SIR chemistry to other lanthanoids required identification of a general Ln^{III} route to $[(C_5Me_5)_3Ln]$, since the stability of samarium(II) is not a common feature of all of the lanthanoids (Figure 1-2), and known routes to $[(C_5Me_5)_3Sm]$, (**VII**), exploited Sm^{II} starting materials. Two new Ln^{III} routes[45, 46] to the desired species allowed the isolation of $[(C_5Me_5)_3Nd]$[46] and $[(C_5Me_5)_3La]$.[47] Subsequent investigation of their reductive chemistry revealed that $[(C_5Me_5)_3Sm]$, (**VII**) is the stronger reductant. This correlates with the higher steric crowding of the samarium(III) species, a function of the smaller radius of the metal ion (Table 1-1).[48] Multiple routes to these sterically saturated

complexes have since been reported and the reduction strength of these SIR-active complexes has been shown to correlate with the ionic radius of the metal. Thus, SIR is truly sterically based reduction, with the reduction potential dependent on the degree of steric crowding.

1.6 Porphyrinoid Complexes

Porphine, (**VIII**), is a tetrapyrrolic macrocycle with a high degree of conjugation due to the sp^2 hybridisation of the *meso*- carbon atoms, resulting in an aromatic structure. Partial saturation of porphine leads to the class of compounds known as porphyrinogens, a group of compounds found throughout nature. The particular modification that will be focussed on throughout this thesis is the result of sp^3- hybridisation of the *meso*-carbon atoms, effectively breaking the resonance of the structure to isolate it within each pyrrole unit, (**IX**).

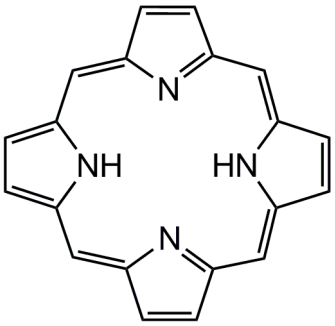

(**VIII**)

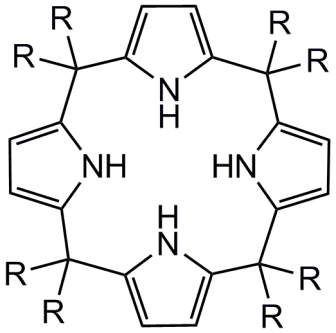

(**IX**)

The sp^3 hybridisation of the *meso*- carbon position renders greater conformational freedom of (**IX**) due to the loss of preferred planarity in the molecule. A more accurate description of the possible conformation of the porphyrinogen throughout this thesis is developed in comparison with calixarene macrocycles, which are known to adopt a variety of arrangements due to the same *meso*- sp^3 hybridisation feature, Figure 1-6.[49] For this reason, the *meso*- sp^3 porphyrinogen is sometimes referred to as "calix[4]pyrrole" in the literature; however, porphyrinogen will be used throughout this thesis.

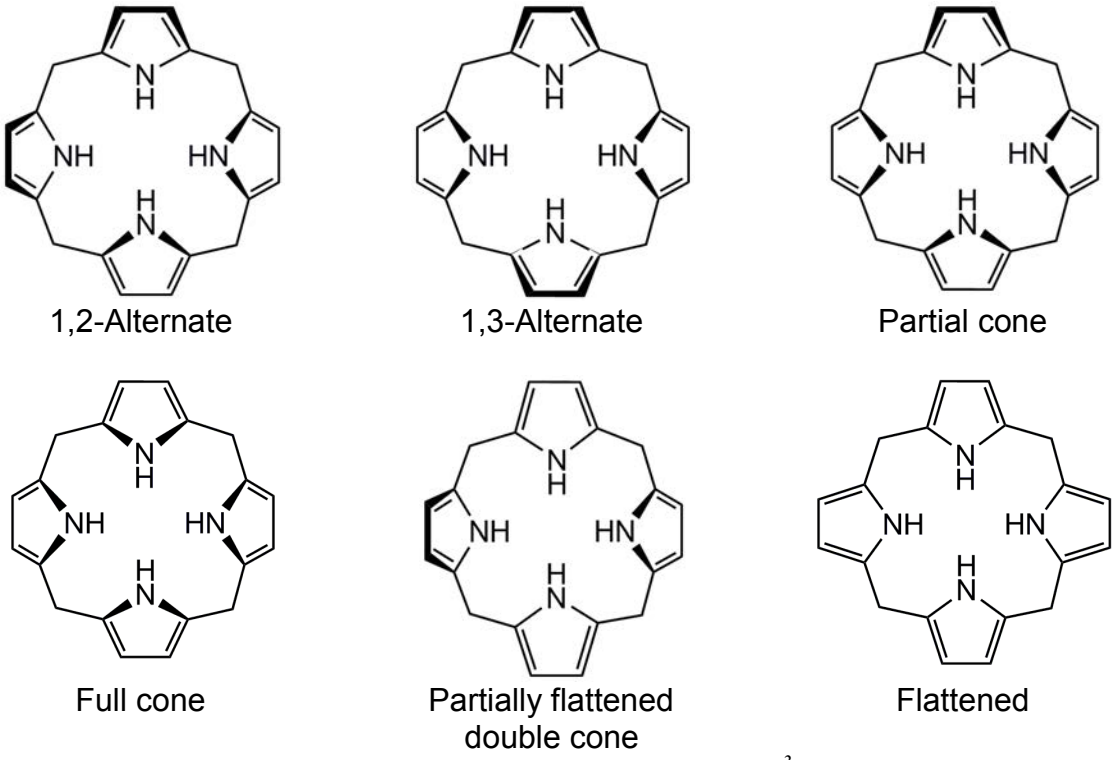

Figure 1-6: The range of conformations available to *meso*- sp^3 hybridised porphyrinogens

A convenient abbreviation for the porphyrinogens that will be discussed throughout this thesis takes the format ($R_xN_yH_z$), where R_x refers to the type (R) and number ($_x$) of *meso*- substituents, N_y accounts for the number, ($_y$), of pyrrole rings, and H_z refers to the number, ($_z$), of acidic N−H protons. Thus „$Et_8N_4H_4$' describes the parent porphyrinogen on which all synthesis undertaken in this thesis is based, *meso*-octaethylporphyrinogen, which has been crystallographically shown to generally adopt the 1,3-alternate conformation (Figure 1-6),[50] but has also been shown to adopt a full cone conformation when binding anions.[51]

Deprotonation of $[Et_8N_4H_4]$ with a suitable base gives the tetraanionic species, $[Et_8N_4]^{4-}$, which facilitates metal coordination *via* both σ- and π- binding, allowing for a full range of metal sizes and preferred binding modes. When a large metal is present, the 1,3-alternate conformation is adopted to provide two opposite anionic nitrogen centres and two opposite pyrrolide rings.[52] Solubility is promoted *via* the presence the *meso*- ethyl groups and the four pyrrole rings (*c.f.* two ($C_5Me_5^-$) rings). These properties render porphyrinogens a viable alternative to the bis($C_5Me_5^-$) ligand system in supporting lanthanoid metal centres.

The first samarium(II) porphyrinogen complex was reported in 1994 by Jubb and Gambarotta as a lithium/samarium mixed metal system that doubly reduces N_2, (**XIV**), Scheme 1-1.[53] The dependence on lithium for the reduction of dinitrogen by (**XIII**) was shown *via* the lithium-free synthesis of $[(Et_8N_4)Sm_2(Et_2O)_2]$, (**XI**), which demonstrates no coordination or reduction of dinitrogen under the same conditions, Scheme 1-1.[54] The synthesis of the mixed metal system, (**XII**), is achieved *via* reaction of $SmCl_3(THF)_3$ and the tetralithium salt of *meso*-octaethylporphyrinogen to give a fluxional species for which structural characterisation has not been achieved, but generally has the molecular formula $[(Et_8N_4)(Cl)Sm\{Li_2(THF)_3\}]$. Reduction of gold coloured (**XII**) with lithium metal gives crystallographically characterised (**XIII**), a green coloured samarium(II) species incorporating an enolate functionality *via* lithium atoms coordinating to the opposite side of the porphyrinogen, Scheme 1-1.

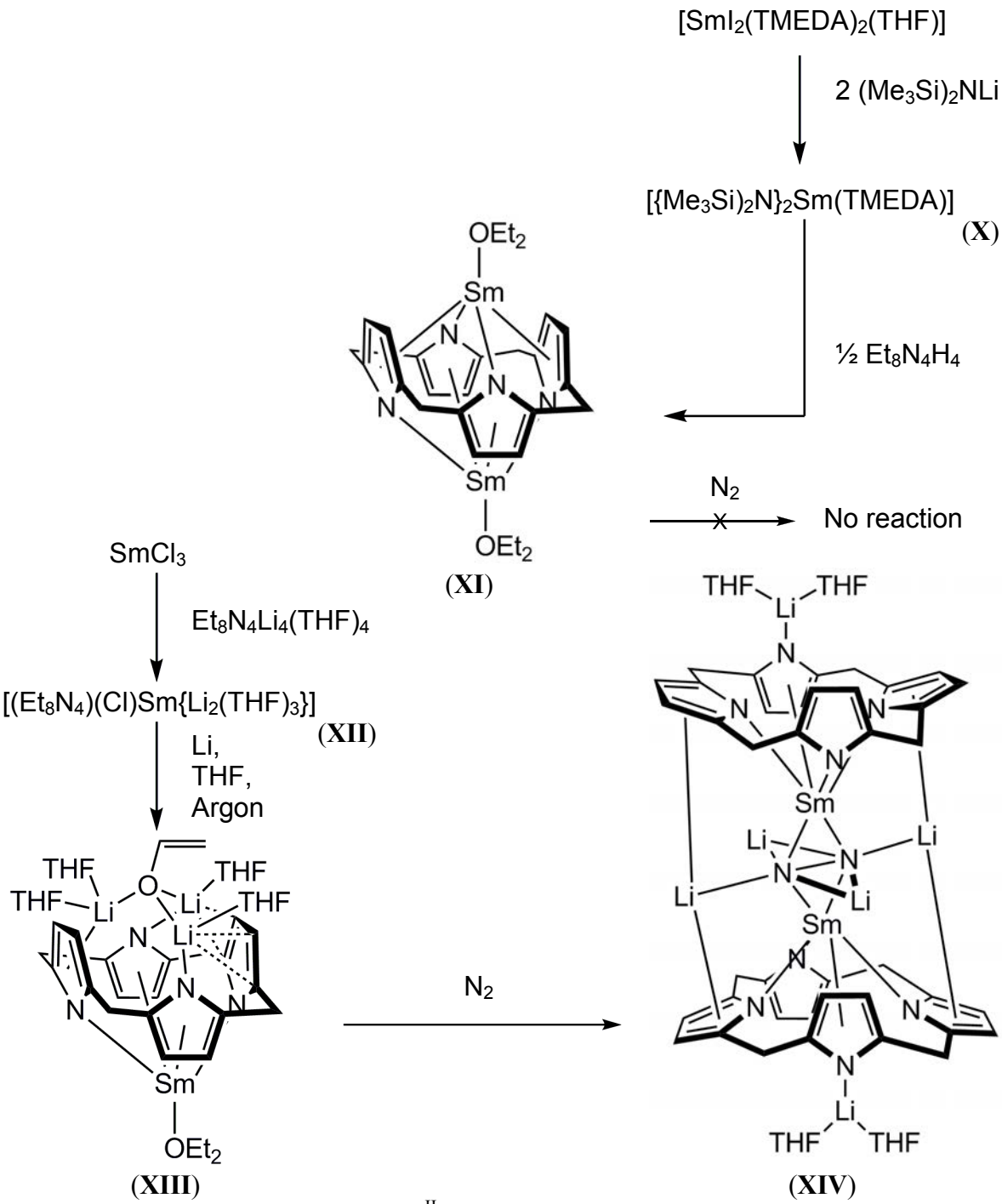

Scheme 1-1 Synthesis of the first Sm^{II} porphyrinogen complex, (**XI**), and the independent, lithium assisted, reduction of dinitrogen (**XIV**).

The conformation of the porphyrinogen in (**XI**) is 1,3-alternate (Figure 1-6), allowing two ζ- and two π- bonding environments for both metal centres. Each metal is capped by diethyl ether acting as a Lewis base *via* coordination through the electron rich oxygen atom. The Sm··· Sm distance in (**XI**) is reported as 3.316 Å and is suggested by the author to be a Sm··· Sm interaction.[54]

The enolate functionality observed in (**XIII**) is assumed to result from attack of a THF during the reaction between (**XII**) and lithium, Scheme 1-1. The flexibility of the binding mode of the porphyrinogen is clearly demonstrated in the crystallographically authenticated structure of (**XIII**), which shows one lithium coordinated *via* an η^5- interaction to a pyrrole unit while the other two are primarily ζ- bound to a pyrrolic nitrogen and stabilised *via* an η^2- interaction to either side of the same pyrrole unit. The η^5- bound lithium cation is coordinated to three oxygen atoms *via* the enolate and two THF molecules, whilst the two remaining lithium cations are each coordinated to the oxygen atom of the enolate and a molecule of THF. The samarium(II) centre resides within the macrocyclic cavity of the porphyrinogen, which maintains a 1,3-alternate conformation possessing an η^1:η^5:η^1:η^5 coordination mode. The coordination sphere of the metal is satisfied *via* Et_2O acting as a Lewis base.[55]

The conformation of the porphyrinogen in the lithium/samarium mixed metal reduced N_2 species, (**XIV**), however, is partial cone, where the Sm atoms are stabilised by one ζ- bond to an *N*-pyrrole unit and three π- interactions to the face of the remaining pyrrole units. Variation from the more common 1,3-alternate conformation presumably arises due to the steric and electronic demands of the $Li_4{-}N_2$ core, which may cause the pyrrole unit to flip. The terminal lithium cations also interact with both porphyrinogen units *via* an η^3-interaction with the back of the σ- bonded N−Sm pyrrole units. While the lithium/samarium system, (**XIV**), affords the double reduction of dinitrogen, the dependence on the presence of lithium to effect the reduction reveals a complex system. Lanthanoid metal mediated dinitrogen reductions employing external electron sources have been reported for the lanthanoid series (with the exceptions of Eu and Yb) utilising the bis(trimethylsilyl)amide supporting ligand.[56-60] To date, no reports of the application of this reduction to obtain hydrogenated derivatives of dinitrogen, N_xH_y, are known.[61]

Synthesis of a range of samarium complexes of *meso*-octaethylporphyrinogen are reported by Gambarotta *et al.*, including the bimetallic samarium(II) bis(THF) adduct analogous to the mono(ether) adduct, (**XI**), methyl- and chloro-moieties bridging solvated lithium capping cations and a mixed valence Sm^{II}/Sm^{III} species arising from stoichiometric restriction of reagents.[62] Reaction of $[(Et_8N_4)(Cl)Sm\{Li_2(THF)_3\}]$, (**XII**), with methyl- or vinyl- lithium provides the Sm-alkyl species *via* metathesis. The Sm^{III}-vinyl species is unstable over time, undergoing homolytic cleavage of ethylene to give the reduced mono(THF) adduct, $[(Et_8N_4)\{Sm(THF)\}_2]$.[63] Hydrogenation of the Sm^{III}-methyl complex provides the Sm-hydride, which is also directly accessible *via* $LiAlH_4$ reduction of (**XII**).[63] Reaction of the hydride and methyl species with acetylene is reported.[64]

Modification of the *meso*- substituent from octaethyl- substitution to the subtly different tetracyclohexyl- moiety has, interestingly, provided alternate reaction outcomes to the analogous octaethyl case.[64, 65]

In 1998, Floriani *et al.* applied *meso*-octaethylporphyrinogen to praseodymium and neodymium chemistry, effecting a sodium mediated two electron reduction of N_2.[66] The larger cation sodium was used rather than lithium to avoid incorporation of the Group 1 metal cation around the reduced N_2 moiety. Exposure of either the $[(Et_8N_4)(Na)Ln(THF)]$ (Ln = Pr, Nd) starting material or the two electron reduced N_2 species to ethylene resulted in a reduced ethylene bridged dimer.[67] Exposure of $[(Et_8N_4)(Na)Ln(THF)]$ (Ln = Pr, Nd) to acetylene resulted in coordination of a side-on reduced acetylene moiety between lanthanoid(III) porphyrinogen units.[67]

Sodium-lanthanoid(III) species of *meso*-octaethylporphyrinogen were identified in 1999 for Pr, Nd, Sm, Eu, Gd and Yb, adopting either a monomeric or dimeric structure depending on solvent choice for the reaction and recrystallisation.[68]

1.7 Modified Porphyrinogen Complexes

In 1998, Takata *et al.* reported the *N*-modification of *meso*-octaethylporphyrinogens. Addition of 18-crown-6 as a complexing agent prevents *β*-alkylation of the pyrrolide unit and allows *N*-methylation to occur.[69] The major product of the methylating reaction reported (2:1 methyl iodide:$Et_8N_4H_4$) is the *trans-N,N′*-dimethyl complex, (**XV**), which has been crystallographically shown to adopt the 1,3-alternate conformation (Figure 1-6). *Trans*-annular interactions between the N−Me substituents restricts the conformational flexibility of the porphyrinogen, effectively providing a rigid "bowl" shaped porphyrinogen with two pyrrolide nitrogens available for deprotonation and coordination at the "top" of the bowl, (**XVb**).

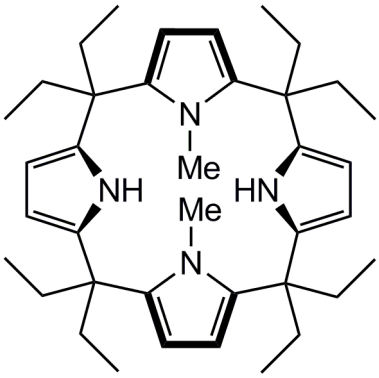

(**XV**)

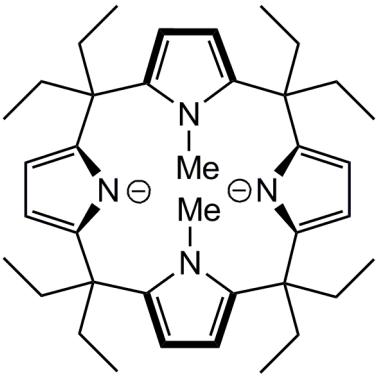

(**XVb**)

In previous work by our group, we have shown that deprotonation of the *trans-N,N′*-dimethylporphyrinogen, $Et_8N_4Me_2H_2$, (**XV**), with K_{metal} provides the dipotassium salt of the porphyrinogen where one potassium is bound inside the macrocyclic cavity and the second potassium is bound *exo*- to a pyrrolide unit, providing a polymeric structure.[70] Exploiting the reduced solubility of this polymer has been essential to purification and allows easy isolation of the potassium salt of the dimethylporphyrinogen.

Reaction of the potassium salt of the *N,N′*-dimethyl substituted porphyrinogen with SmI_2 in THF provided the first alkali-metal-free mononuclear samarium(II) porphyrinogen complex, $[(Et_8N_4Me_2)Sm(THF)_2]$, (**XVI**), *via* metathetical exchange.[71] Similarly, reaction of YbI_2 and EuI_2 with the same potassium salt yielded the mono(THF) and bis(THF) adducts, $[(Et_8N_4Me_2)Yb(THF)]$ and $[(Et_8N_4Me_2)Eu(THF)_2]$, respectively.[[71, 72]

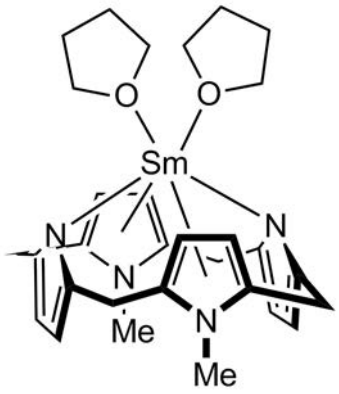

(**XVI**)

The macrocycle in $[(Et_8N_4Me_2)Sm(THF)_2]$, (**XVI**), adopts the expected 1,3-alternate conformation and the dianionic porphyrinogen coordinates the samarium(II) metal centre *via* alternating σ- and π- donation, allowing the metal to sit within the macrocyclic cavity. Binding of ancillary ligands and Lewis bases, dimerisations and small molecule activations by $[(Et_8N_4Me_2)Sm(THF)_2]$, (**XVI**), are limited by both the *meso*- alkyl substituents and the 3,4-positions of the η^5- bound *N*-methylpyrrole units of the macrocycle, resulting in a relatively narrow and short "binding groove" available for ancillary ligands. When the metal is bound within the cavity of this macrocycle, an η^1:η^5:η^1:η^5 arrangement is intrinsically favoured by the *trans*-*N,N′*-dimethyl substitution, Figure 1-7a. Figure 1-7b demonstrates the complete shielding of one side of the porphyrinogen provided by *N*-methyl modifications.

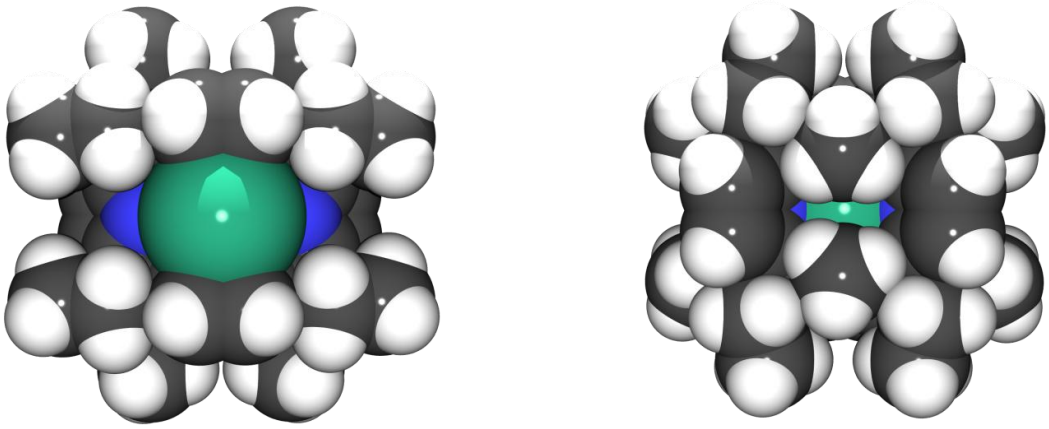

(a) (b)

Figure 1-7 Space filling representations of the binding groove, (a), and underside, (b), of $[(Et_8N_4Me_2)Sm(PhMe)]$, (**1**). Toluene omitted for clarity.

The rigid geometry of the *trans-N,N′*-substituted macrocycle results in a metallocene bend angle of 168.9 ° for $[(Et_8N_4Me_2)SmMe]$, (**XX**), *vide infra*; as governed by macrocyclic conformational restrictions and transannular interactions between the *N*-methyl substituents. The slight metallocene bend angle observed in the modified porphyrinogen represents an alternative in bulky ligand design to the much-studied peralkylated metallocenes (*c.f.* 137 ° for the Sm centre of $[\{(C_5Me_5)_2SmMe\}_3]$, which features a single Sm−Me interaction).[73] Importantly, disproportionation events in reactions of the *trans-N,N′*-dimethylporphyrinogen are inherently prevented *via* the macrocycle effect and reaction outcomes, such as presented by Equation 1-3 through Equation 1-5 and Equation 1-11, are unavailable.[74] In the case of $[(Et_8N_4Me_2)Sm(THF)_2]$, (**XVI**), two molecules of THF coordinate to the metal to satisfy the metal coordination sphere. A partial survey of the established Sm^{II}/Sm^{III} *trans-N,N′*-dimethylporphyrinogen chemistry is provided to illustrate the various reactivity features that are recurring in relation to steric influences that will be relevant to this thesis.

The samarium(III) halides [{($Et_8N_4Me_2$)SmCl}$_2$], (**XVII**), [[{($Et_8N_4Me_2$)SmBr}$_2$], (**XVIII**) and ($Et_8N_4Me_2$)SmI], (**XIX**), were prepared *via* oxidation of (**XVI**), Scheme 1-2. The iodide was found to be monomeric in the solid state, whilst the lighter halogens were shown to result in dimeric products in the solid state. In all cases the Sm^{III} centre is bound in an $\eta^1:\eta^5:\eta^1:\eta^5$ fashion to the porphyrinogen with no other coordination supported by the molecule.

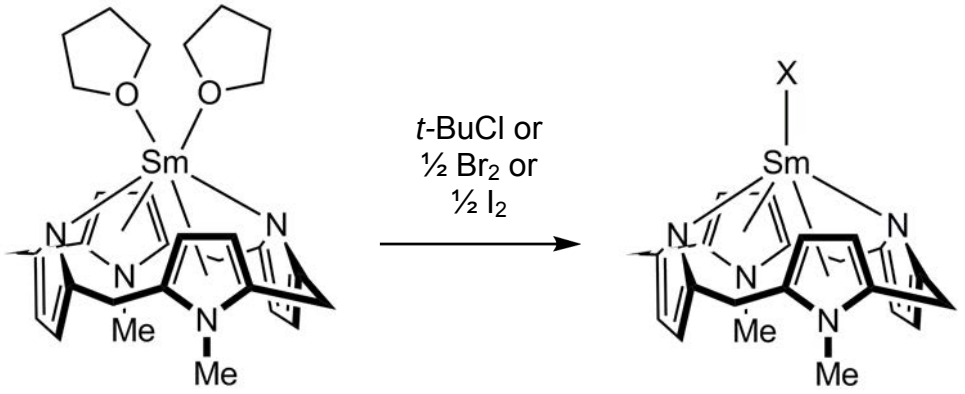

(**XVI**)

Where X = Cl, (**XVII**) – half dimer shown
= Br, (**XVIII**) – half dimer shown
= I, (**XIX**)

Scheme 1-2 Synthesis of the Sm^{III} halide complexes.

Samarium(III) alkyl species are accessible *via* metathetical exchange reactions with [{($Et_8N_4Me_2$)SmCl}$_2$], (**XVII**), Scheme 1-3. The Sm^{III}-Me complex, [($Et_8N_4Me_2$)SmMe], (**XX**), and trimethylsilylmethyl complex, [($Et_8N_4Me_2$)Sm(CH_2SiMe_3)], (**XXI**), were synthesised *via* reaction of (**XVII**) with methyllithium or (trimethylsilyl)methylsodium, respectively.[75] Each alkyl complex is monomeric with the usual $\eta^1:\eta^5:\eta^1:\eta^5$ binding to the porphyrinogen, with the methyl group being a rare terminal example; coordination of Lewis bases, alkali metals or chloride is not observed due to the steric restrictions imposed by the rigid porphyrinogen.

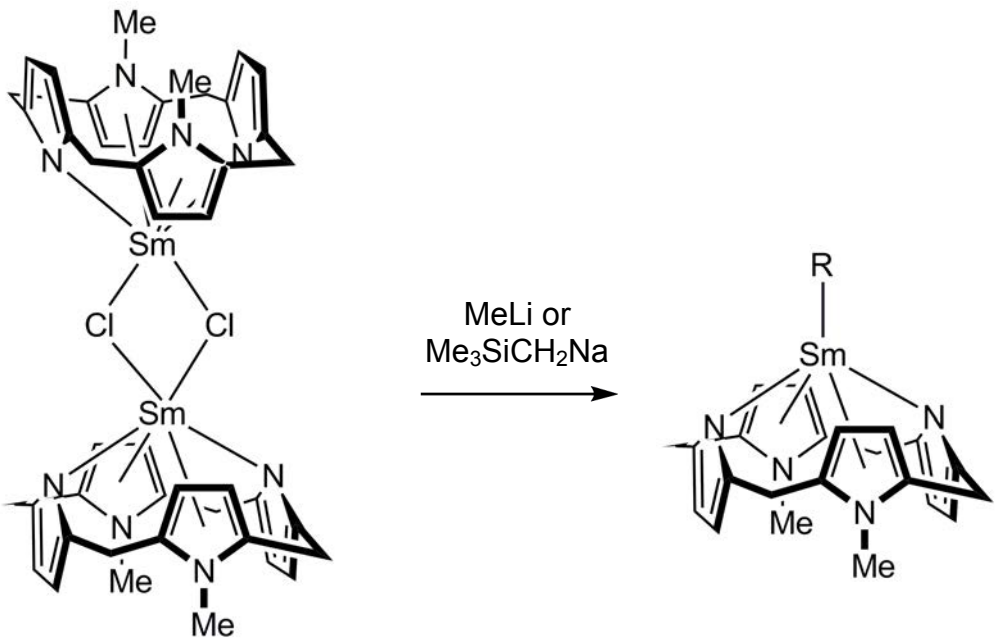

(**XVII**) Where R = Me, (**XX**)
= CH_2SiMe_3, (**XXI**)

Scheme 1-3 Synthesis of the Sm^{III} alkyl complexes.

Exposure of $[(Et_8N_4Me_2)Sm(THF)_2]$, (**XVI**), to 1,4-di-*t*-butyl-1,4-diazabuta-1,3-diene in toluene resulted in the doubly reduced diazabut-2-ene moiety bridging the two samarium(III) centres, (**XXII**), regardless of stoichiometry, Equation 1-12. Complex (**XXII**) was isolated as a poorly soluble green powder which is stable in toluene, benzene and pet. ether, but addition of THF results in conversion of the samarium(III) species back to the samarium(II) starting material, (**XVI**). Removal of THF drives the equilibrium back towards (**XXII**), which can be recrystallised from toluene.[76]

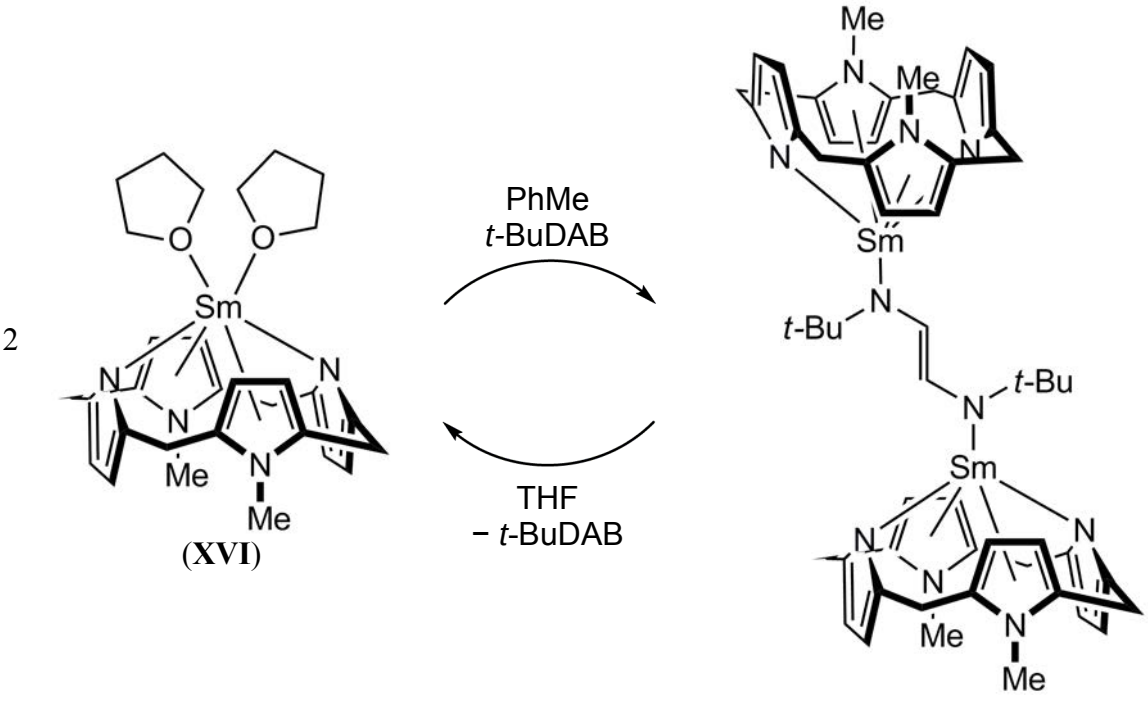

Equation 1-12

Rationalisation of the reversibility of Equation 1-12 has not been unequivocally reported, however the role of the dielectric constant of the solvents, the steric constraints of the macrocycle and/or the electronic environment of the macrocycle are all raised as potential contributing factors.[76] It is noted that close contacts between the Sm centres and the C_2H_2 portion of the reduced *t*-BuDAB moiety are present. At the time of publication, only a small number of reversible redox processes had been reported for Sm^{II}/Sm^{III} in N_2, substituted alkene and butadiene complexes of decamethylsamarocene(II),[33, 77, 78] and N_2 and C_2H_4 complexes of tetrametalated porphyrinogens.[55, 65] Additionally, a reversible Yb^{III}/Yb^{II} system based on neutral/radical anion interconversion of 1,4-*t*-butyl-1,4-diazabuta-1,3-diene, and a U^{IV}/U^{III} system based on N_2 and pyrazine reduction were noted.[79, 80]

Further exploration of the chemistry of $[(Et_8N_4Me_2)Sm(THF)_2]$, (**XVI**), by examination of its reaction chemistry with CO_2 provided the first example of an f-element

displaying reductive disproportionation reactivity, leading to a carbonate moiety bridging two samarium(III) centres, (**XXIII**), and evolution of $CO_{(g)}$, Equation 1-13.[74]

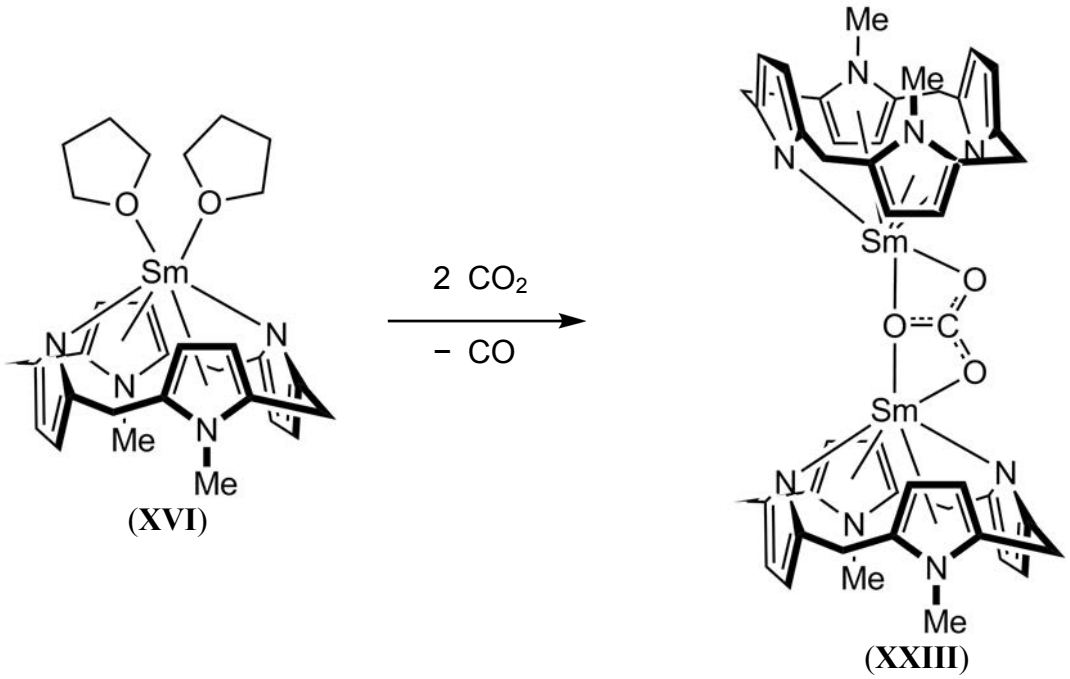

(**XVI**) (**XXIII**)

Equation 1-13

The steric limitations of $[(Et_8N_4Me_2)Sm(THF)_2]$, (**XVI**), were explored with the synthesis of two complexes featuring π- bound ancillary ligands analogous to the work previously achieved by Evans (Section 1.5-1.6).[81] Reaction of the samarium(III) chloride species, (**XVII**), with one equivalent of $[(C_5H_5)Na]$ resulted in $[(Et_8N_4Me_2)Sm(C_5H_5)]$, (**XXIV**).[81] The solid state structure of (**XXIV**) is unique; in accommodating the π-bound ancillary ligand, the macrocyclic binding mode shifts to $\eta^1{:}\eta^5{:}\eta^1{:}\boldsymbol{\eta^1}$ by splaying one *N*-methylpyrrole unit away from the metal centre, Figure 1-8. Quantitatively, the heterocycle ring of the η^1- *N*-methylpyrrole lies at an angle of 48.8(2) ° relative to the plane of the four *meso* carbon atoms, a significant distortion from the 75.7(1) ° observed in the other, η^5- bound *N*-methylpyrrole unit, Figure 1-8.[81] Consequently, transannular interactions between the *N*-methyl groups lead to significant displacement of the *N*-methyl group of the η^1- bound *N*-methylpyrrole unit from the heterocycle, with the N−C vector 27.4(2) ° from the heterocycle plane, Figure 1-8.[81]

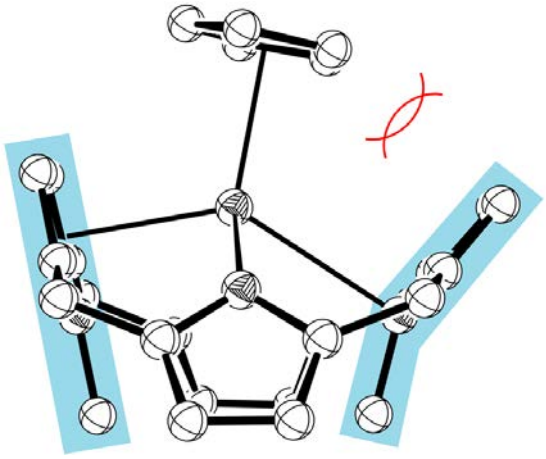

Figure 1-8 Molecular structure of $[(Et_8N_4Me_2)Sm(C_5H_5)]$, (**XXIV**), demonstrating the $\eta^1{:}\eta^5{:}\eta^1{:}\eta^1$ binding mode resulting from high steric strain imposed by η^5-bound $(C_5H_5)^-$. Thermal ellipsoids drawn at arbitrary probability; protons and *meso* ethyl groups omitted for clarity.

In contrast to the reaction of (**XVI**) with sodium cyclopentadienide, reaction of (**XVI**) with half an equivalent of cyclooctatetraene, COT, results in the two electron reduction to $(C_8H_8)^{2-}$ and formation of a bridged Sm^{III} dimer, (**XXV**), Equation 1-14. In this case, the Sm^{III} centre displays the usual $\eta^1{:}\eta^5{:}\eta^1{:}\eta^5$ binding to the macrocyclic cavity, however the steric constraints of the porphyrinogen cause the hapticity of planar $C_8H_8^{2-}$ to drop from the usual η^8- binding mode to a bridging $\eta^2{:}\eta^2$ formulation.[81]

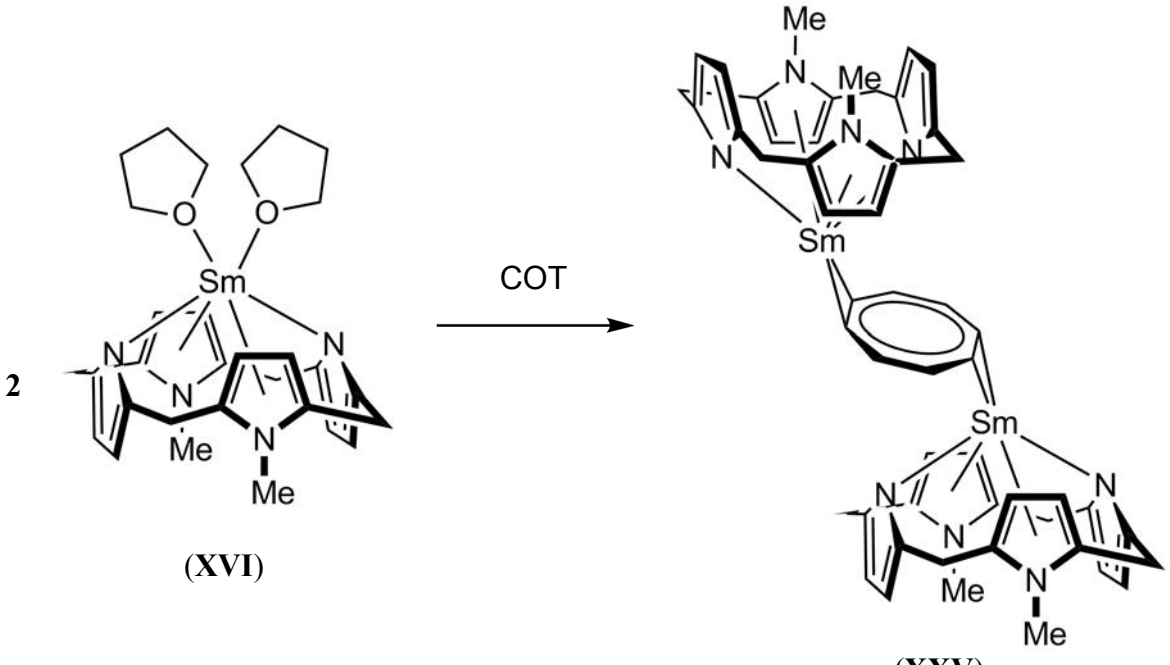

(**XVI**) (**XXV**)

Equation 1-14

1.8 Theoretical Considerations

To accurately describe a molecule using computational techniques, solutions to the Schrödinger wave equation (Equation 1-15) are derived, where H is the Hamiltonian operator, E is the energy of the particle (in this case an electron), and Ψ is the wavefunction describing the electron.

$$H\Psi = E\Psi \qquad \textbf{Equation 1-15}$$

A number of approximations must first be made for multi-electron systems in order for solutions of this equation to be determined; for example, basis functions are used to approximate molecular orbitals as linear combinations of single electron atomic orbitals. As the number of basis functions is increased (and thus, too, the complexity of the basis set), the mathematical description of the molecular orbital is improved.

Minimising the energy of the wave function with respect to the orbital coefficients in an iterative procedure until a self-consistent field (SCF) is obtained gives the optimum wavefunction for a compound at a particular geometry. The energy of the wavefunction may then be minimised with respect to Cartesian coordinates to give the optimal energy.

Density Functional Theory (DFT) is a computational method in common use which describes a compound according to its electron density, rather than its wavefunction. Using such a description defines a system that depends on only three variable properties, the *x*, *y,* and *z* spatial coordinates, rather than having the 3*N* degrees of freedom associated with the wavefunction of an electron orbital. Calculations employing appropriate basis sets have been shown to provide reliable results in relation to experimental observation.[82]

Chapter 2

Lewis Base Free Samarium(II) Species

2.1 Introduction

Coordination of Lewis basic solvents predominated early organosamarium chemistry, particularly with oxygen donor atoms due to the oxophilic nature of samarium.[83] A survey of the literature suggests that the desire for unsolvated organolanthanoid species was motivated by the presumed increase in reactivity consistent with electronic desaturation of the metal environment[84] rather than as a targeted study for reaction with small molecules. However, the applications of these more highly reactive unsolvated species was broadened once it was discovered that the absence of Lewis bases allowed for previously unobserved interactions between small, weakly donating molecules, such as dinitrogen, hitherto precluded by Lewis base coordination and the associated electronic satisfaction of the metal. It is appropriate, then, to report on the chemistry of unsolvated organolanthanoid complexes, particularly organosamarium, before discussion of any reactivity with small molecules.

2.1.1 Lewis Base Free Organolanthanoids

Evidence for the potential desolvation of organolanthanoids prior to its achievement in 1984 was not encouraging. In 1969, Watt and Gillow reported the decomposition of insoluble, pyrophoric $[(C_5H_5)_2Sm(THF)]$ with heating under vacuum.[12] By 1980, Watson had shown that these cyclopentadienyl complexes resist desolvation, reporting that

$[(C_5Me_5)_2Yb(THF)_2]$ releases only one molecule of THF upon heating *in vacuo* at 90 °C.[85]

The initial synthesis of $[(C_5Me_5)_2Sm(THF)_2]$ proceeded *via* metal vapour reaction of samarium with $(C_5Me_5)H$ and workup in THF to provide the purple solvated species; however small amounts of a green complex were observed prior to the addition of THF. It was subsequently found that high vacuum (10^{-5} torr) and elevated temperature were sufficient to obtain the green unsolvated decamethylsamarocene complex, $[(C_5Me_5)_2Sm]$, (**V**).[23] X-ray crystal structure analysis revealed that (**V**) retains the bent geometry ubiquitous amongst lanthanocenes, however desolvation has resulted in a larger metallocene bend (centroid-Sm-centroid) angle and a decrease in average Sm−C distance compared to $[(C_5Me_5)_2Sm(THF)_2]$, as discussed in Section 1.4.[23] Access to the mono(THF) solvate, $[(C_5Me_5)_2Sm(THF)]$, completed the series and, with values for both centroid-Sm-centroid angle and the average Sm−C distance intermediate between (**IV**) and (**V**), is consistent with the stepwise variation in the degree of solvation.[86]

A subsequent report detailed the synthesis of decamethyleuropocene, $[(C_5Me_5)_2Eu]$, and provided a new synthesis to obtain $[(C_5Me_5)_2Sm(THF)_2]$ in higher yield than was offered *via* metal vapour synthesis by undertaking a salt metathesis reaction between potassium pentamethylcyclopentadienide and samarium diiodide in THF, Equation 2-1.[24]

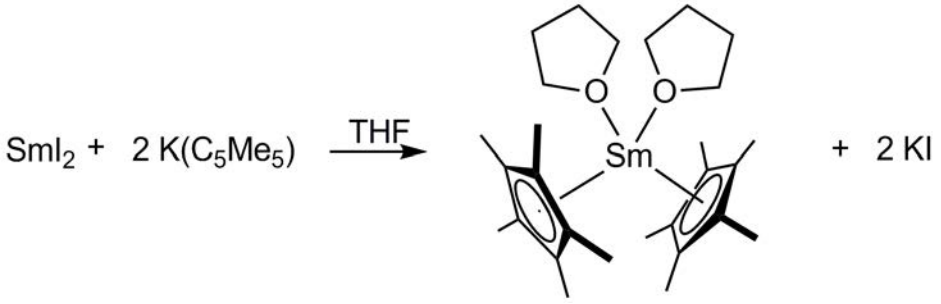

(**IV**)

Equation 2-1

Preparation of $[(C_5Me_5)_2Eu(THF)_2]$ proceeds analogously to Equation 2-1, however complete desolvation to decamethyleuropocene requires triple sublimation;[24] in contrast, sublimation of $[(C_5Me_5)_2Sm(THF)_2]$, (**IV**) provides $[(C_5Me_5)_2Sm]$, (**V**) in up to 74 % yield. Analysis of the light beige coloured residue in the sublimation vessel was consistent with formation of the previously reported oxo-bridged complex, $[\{(C_5Me_5)_2Sm\}_2(\mu\text{-}O)]$. $[\{(C_5Me_5)_2Sm\}_2(\mu\text{-}O)]$ is a common product in reactions of $[(C_5Me_5)_2Sm(THF)_2]$ with oxygen containing substrates such as NO, N_2O, pyridine *N*-oxide and 1,2-epoxybutane. [87]

In 1989, Berg *et al.* reported the synthesis of $[(C_5Me_5)_2Sm(OEt_2)(THF)]$ and subsequent desolvation to either $[(C_5Me_5)_2Sm(OEt_2)]$ or $[(C_5Me_5)_2Sm(THF)]$ depending upon reaction conditions. It was also reported that complete desolvation to $[(C_5Me_5)_2Sm]$ could be achieved *via* repeated toluene reflux of $[(C_5Me_5)_2Sm(OEt_2)]$.[88]

The difference in reactivity between $[(C_5Me_5)_2Sm(THF)_2]$, (**IV**), and $[(C_5Me_5)_2Sm]$, (**V**), is highlighted in the key reaction of each with cyclooctatetraene; the bis-solvate forms a solvated samarium complex with the reductively coupled by-product $(C_5Me_5)_2$, according to Equation 2-2.[89] In the case of the unsolvated species, the by-product is the SIR active complex $[(C_5Me_5)_3Sm]$, (**VII**) Equation 2-3.[34]

The achievement of SIR-active (Section 1.5) molecules and the extension of ligand-based reduction to other lanthanoids is reliant upon a coordinating solvent free environment for formation of the sterically crowded complex. Expansion of the field to accommodate lanthanoids without access to a stable Ln^{II} state was dependent on determining a Ln^{III} centered route.

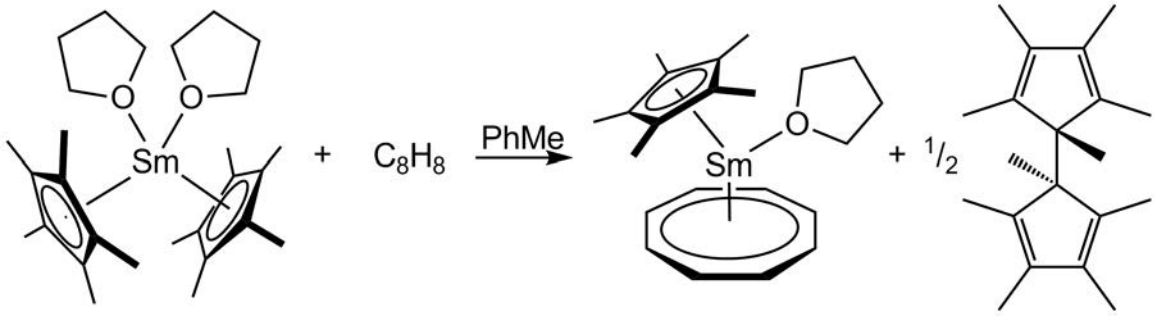

(**IV**)

Equation 2-2

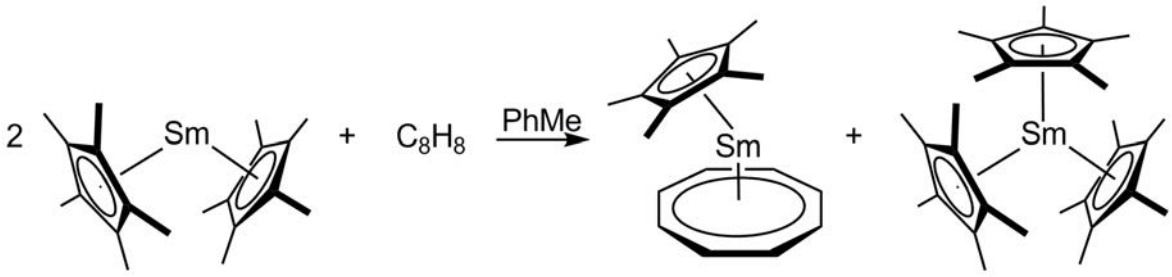

(**V**) (**VII**)

Equation 2-3

Investigation of a potential metathesis reaction to access (**VII**) demonstrated once again the differing reactivity of solvated and unsolvated samarium complexes; the presence of THF results in insertion of ring-opened THF, Equation 2-4, whilst the absence of THF provides the desired reactivity.[90] A range of routes to (**VII**) and additionally coordinated complexes have since been reported.[91]

$$[(C_5Me_5)_2Sm(THF)_2][BPh_4] + K(C_5Me_5) \rightarrow [(C_5Me_5)_2Sm\{O(CH_2)_4C_5Me_5\}] \quad \textbf{Equation 2-4}$$

$$[(C_5Me_5)_2Sm][BPh_4] + K(C_5Me_5) \rightarrow [(C_5Me_5)_3Sm] + K[BPh_4] \quad \textbf{Equation 2-5}$$

Access to $[(C_5Me_5)_2Sm][BPh_4]$ was initially achieved *via* Sm^{II} starting materials, however it was shown that $[(C_5Me_5)_2Ln][BPh_4]$ is synthetically available by the reaction of $SmCl_3$ and $K(C_5Me_5)$ in THF to give $[(C_5Me_5)_2SmCl_2K(THF)_2]$.[92] Addition of propylmagnesium chloride in toluene followed by extraction with hexanes spiked with dioxane (1 % by volume) and subsequent heating under vacuum and re-extraction in hexanes provides the coordinating solvent free species $[(C_5Me_5)_2Ln(\eta^3\text{-}CH_2CHCH_2)]$. The

allylmagnesium reaction outcome is consistent with an earlier report by Tsutsui and Ely observing that reaction between allylmagnesium bromide and the unsubstituted cyclopentadienide system, $[(C_5H_5)_2LnCl]$, results in $[(C_5H_5)_2Ln(\eta^3\text{-}CH_2CHCH_2)]$.[93] Reaction of the pentamethyl-substituted system with $Et_3NH[BPh_4]$ in benzene provides $[(C_5Me_5)_2Ln][BPh_4]$, which reacts with $[K(C_5Me_5)]$ to provide $[(C_5Me_5)_3Ln]$.[46] Formation of $[(C_5Me_5)_2Ln(\eta^3\text{-}CH_2CHCH_2)]$ also improved synthetic access to lanthanoid hydride complexes.[46] Further discussion of lanthanoid hydride complexes is beyond the scope of this introduction.

Desolvation of Lewis base solvated ytterbocenes has been investigated. Schultz *et al.* showed that the mono-ether adduct $[(C_5Me_5)_2Yb(OEt_2)]$ could be desolvated by refluxing the complex as a toluene solution.[25] The mono-THF adduct, $[(C_5Me_5)_2Yb(THF)]$, was shown to retain the coordinated THF under these conditions. Sublimation of the ether adduct was shown to be ineffective at decoordination of diethyl ether, in accordance with the previously reported outcome for sublimation of the mono-THF adduct.[40] A subsequent report by Evans, Champagne and Ziller showed that complete desolvation of $[(C_5Me_5)_2Yb(THF)_2]$ and $[(C_5Me_5)_2Sm(THF)_2]$ is possible at sufficiently low pressure (10^{-6} torr) over several days at low temperature (45-50 °C) to avoid sublimation. Even at this low pressure, elevated temperatures resulting in sublimation continue to provide the mono-THF adduct $[(C_5Me_5)_2Yb(THF)]$.[94]

Desolvation has also been achieved by increasing the bulk of the supporting ligands. Sitzmann *et al.* investigated the effect of increasing the bulk of the cyclopentadienide substitution from pentamethyl to tetraisopropyl, 1,2,4-tri(*tert*-butyl) or pentaisopropyl, resulting in formation of unsolvated Ln^{II} complexes for Sm, Eu and Yb in each case. In the most substituted, pentaisopropylcyclopentadienide, complex of europium, the C_5R_5

rings are parallel; the steric bulk has overcome the ubiquitous bent geometry seen throughout the lanthanocenes.[95]

In an independent report received five days earlier, Visseaux *et al*. also employed tetraisopropylcyclopentadienide ligands ($C_5{}^{i}Pr_4H$) in accessing unsolvated Sm^{II} species, despite undertaking the reaction in THF and recrystallising from OEt_2.[96] The metallocene bend angle is 152 °, 12 ° larger than observed in $[(C_5Me_5)_2Sm]$.[23] Addition of one equivalent of THF to a C_6D_6 solution showed no coordination to the metal by ^1H NMR spectroscopy, however the complex actively polymerises ε-caprolactone, as does $[(C_5Me_5)_2Sm]$, (**V**).[97] Visseaux *et al*. argue that the electronic demand of the metal co-contributes to solvation outcomes of these complexes in addition to the widely accepted effect of sterics, citing a previous postulation that a COT^{2-} ligand makes the cation less electrophilic than two $(C_5Me_5)^-$ ligands.[89, 96]

2.1.2 Organolanthanoid Reduction of Dinitrogen

The first report of an isolated metal-dinitrogen complex was made in 1965 by Allen and Senoff and described the reaction of aqueous hydrazine and ruthenium trichloride to form $[Ru(NH_3)_5(N_2)]^{2+}$.[98] End-on binding of N_2 to transition metals has been shown to be stabilised by back-donation of electron density from the metal into the anti-bonding π* orbital of the N_2 ligand. End-on binding of N_2 was observed exclusively until 1988, when Evans, Ulibarri and Ziller reported that slow crystallisation of a toluene solution of $[(C_5Me_5)_2Sm]$, (**V**), under a nitrogen atmosphere results in formation of a side-on dinitrogen complex, $[\{(C_5Me_5)_2Sm\}_2(\mu\text{-}\eta^2\text{:}\eta^2\text{-}N_2)]$, (**VI**).[33] Evans' complex, the first dinitrogen complex of an f-element and the first example of $(\mu\text{-}\eta^2\text{:}\eta^2\text{-}N_2)$ binding, remains hard to rationalise given the juxtaposition of the clearly Sm^{III} characteristics of ^{13}C NMR spectroscopic and solid state crystallographic data, and the limited activation of the N_2

bond. Two electron reduction of N_2 to $(N_2)^{2-}$ is reasonably anticipated to result in an N−N distance in the order of 1.25 Å, rather than the 1.088(12) Å observed in this complex (*cf.* free N_2 (1.0975 Å)).[33] DFT calculations reported by Perrin *et al.* in 2003 suggest that the observed bond length is a function of disorder in the $(N_2)^{2-}$ fragment.[99] The N_2 ligand is highly labile and released upon dissolution in toluene.[33] Shortly after $[(C_5Me_5)_2Sm]_2(\mu\ \eta^2{:}\eta^2\text{-}N_2)]$, (**VI**), was reported, Fryzuk, Haddad and Retig reported the same bridging, side-on binding geometry in a transition metal complex, $[\{[(i\text{-}Pr_2PCH_2SiMe_2)_2N]ClZr\}_2(\mu\text{-}\eta^2{:}\eta^2\text{-}N_2)]$, with the high degree of activation of N_2 reflected in the N−N distance (1.548(7) Å).[100] Since the 1988 report, a number of different binding modes for metal-dinitrogen complexes have been observed for transition metals, Table 2-1.[101]

N_2 Binding Mode	Weak Activation	Strong Activation
End-on mononuclear	M−N≡N	
End-on dinuclear	M−N≡N−M	M=N−N=M
Side-on dinuclear	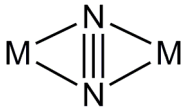	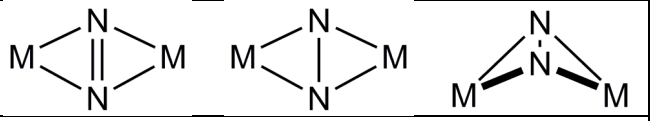
Side-on/End-on dinuclear		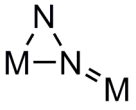

Table 2-1 General bonding modes of N_2 for mono- and dinuclear metal complexes, adapted from a review by MacLachlan and Fryzuk.[101]

End-on mononuclear,[80] mixed metal end-on dinuclear[102] and side-on dinuclear[103-105] coordination of N_2 has been observed in the actinoids, with reduction of the N_2 unit to $(N_2)^{2-}$ observed where side-on coordination occurs.[79] The limited covalency of the lanthanoids (*cf.* actinoids, Section 1.4), however, results in the ubiquitous $(\mu\text{-}\eta^2{:}\eta^2\text{-}N_2)$ binding mode observed for $Ln(N_2)$ complexes.[101]

As discussed in Section 1.6, use of the tetraanionic *meso*-octaethylporphyrinogen macrocycle allows a mixed metal Sm/Li four electron reduction of N_2 to $(N_2)^{4-}$, made possible due to the considerable geometric distortion of the macrocycle as it is allowed to adopt an $\eta^3:\eta^1:\eta^1:\eta^1$ bonding arrangement between macrocycle and samarium.[53] The cyclohexyl analogue of *meso*-octaethylporphyrinogen, *meso*-tetracyclohexylporphyrinogen, showed labile coordination of N_2 in the familiar side-on, bridging fashion, (**XXIX**). Reaction of this product with excess sodium afforded a linear polymeric divalent samarium species with a formal electron count of 30; higher than any previously reported samarium complex.[106] A second N_2 containing complex, (**XXVIII**), was achieved by concentration of a THF solution of (**XXVII**) under a nitrogen atmosphere. The resulting product, (**XXVIII**), forms as a result of samarium abstraction from a third macrocycle to bridge the equatorial plane of the coordinated N_2 moiety. The coordination environment is completed by end-on coordination of a lithium cation to each N_2 nitrogen atom, Scheme 2-1.[107] The synthesis of each of these side-on N_2 derivatives was accompanied by concomitant formation of a dinuclear oxo-bridged species as a minor impurity, analogous to Evans' observation upon sublimation of $[(C_5Me_5)_2Sm]$.[107]

Dubé *et al.* investigated the reaction of the diphenyldipyrrolylmethane dianion with samarium(II) under a dinitrogen atmosphere, resulting in a formally $(N_2)^{4-}$ moiety exhibiting $(\mu\text{-}\eta^1:\eta^1:\eta^2:\eta^2)$ binding to four units of $[\{Ph_2C(C_4H_3N)_2\}Sm^{III}]$.[108] The related supporting ligand diethyldipyrrolylmethane also showed the same irreversible coordination and four electron reduction of dinitrogen upon *trans*-amination reaction with the known Sm^{II} bis(trimethylsilyl)amide complex, $[Sm\{N(SiMe_3)_2\}_2(THF)_2]$,[109, 110] under an atmosphere of nitrogen. The reaction was also shown to proceed in DME.[111]

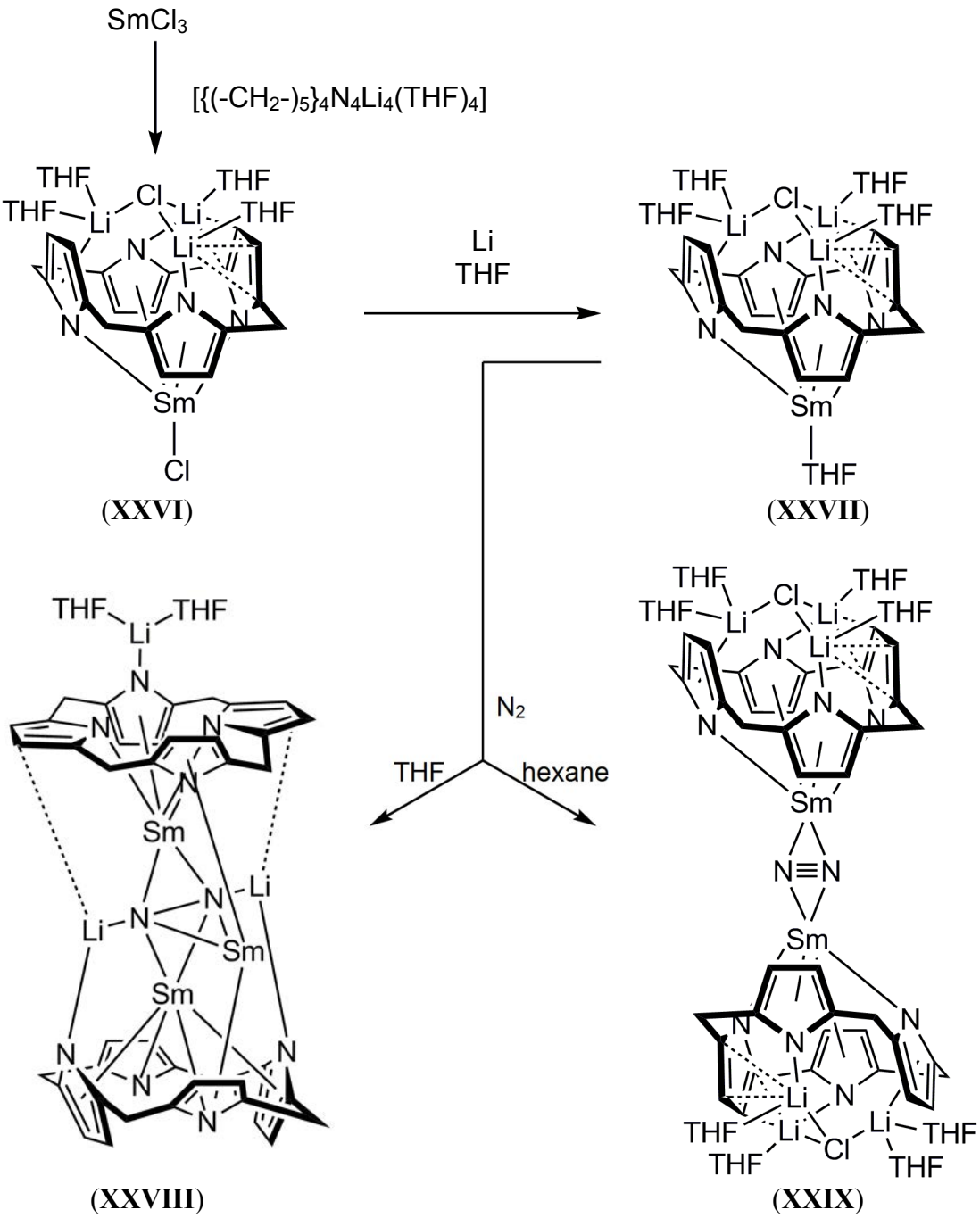

Scheme 2-1 Synthesis of samarium dinitrogen complexes supported by the *meso*-tetracyclohexylporphyrinogen ligand

Isolation of soluble divalent molecular species of Tm^{II},[112] Dy^{II},[113] and Nd^{II} [114] preceded the observation that the side-on binding of dinitrogen to lanthanoids is not a function of the steric requirements of the ancillary ligands, but a function of the lanthanoid metals themselves. This conclusion was made in 2003 upon synthesis of $[\{[(Me_3Si)_2N]_2(THF)Ln\}_2(\mu\text{-}\eta^2\text{:}\eta^2\text{-}N_2)]$, for Ln = Tm, Dy, Equation 2-6, analogous to the

previously reported Ln = Sm (although this complex that has no reported reactivity with dinitrogen),[109, 110] and [{2,6-*t*-$Bu_2C_6H_3O)_2(THF)_2Nd\}_2(\mu\text{-}\eta^2\text{:}\eta^2\text{-}N_2)$]. Each of these complexes is presumed to form a highly reactive Ln^{II} species prior to coordination and reduction of N_2 to the more stable [$\{(ligand)Ln^{III}\}_2(\mu\text{-}\eta^2\text{:}\eta^2\text{-}N_2)$] species. The coordination of the silylamide and aryloxide ligands is assumed to provide a flexible coordination environment unable to enforce a particular geometry upon the $(N_2)^{2-}$ moiety.[115] Unlike reactivity observed for [$(C_5Me_5)_2Sm$], (**V**), the presence of THF clearly does not inhibit the reduction of dinitrogen for these highly reactive species.[115]

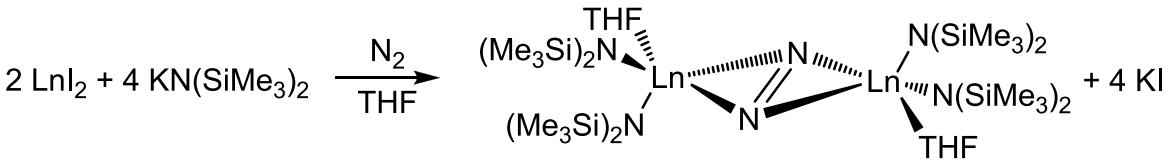

Equation 2-6

Following the successful synthesis from the Ln^{II} species, Equation 2-6, potassium reduction of the known [$Ln^{III}\{N(SiMe_3)_2\}_3$] species[116] was attempted and found to be successful in the case of Tm, Equation 2-7. The reaction was anticipated to form divalent "[$Tm\{N(SiMe_3)_2\}_2$]" which would go on to reduce N_2 according to the reactivity observed in Equation 2-6; however no intense colouration indicative of Tm^{II} was observed.

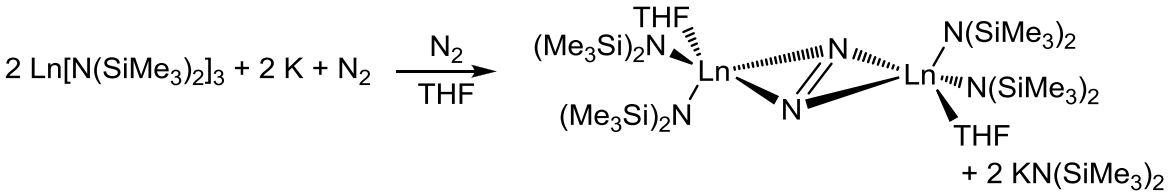

Equation 2-7

A reaction pathway apparently independent of the Ln^{II} state raised the possibility that the chemistry could be applicable to species with no feasible Ln^{II} chemistry. Indeed, it was found that the analogous side-on $(N_2)^{2-}$ complexes could be formed for Ho, Y and Lu, Equation 2-7, where divalent lanthanoid chemistry is mimicked by trivalent lanthanoids in

the reaction between $Ln[N(SiMe_3)_2]_3$ and alkali metals.[117] Extension of this chemistry to the larger lanthanoids (La, Ce, Pr) failed to provide crystalline reaction products, however ^{15}N NMR analysis indicates that the reaction proceeds and the products are simply not crystalline.[57]

Continuing the theme of alkali metal reductions, potassium reduction of samarocene(III) complexes has been reported to proceed for $[(C_5Me_5)_2Ln(\mu\text{-}Ph)_2BPh_2]$ species,[118] however the chemistry of the most obvious Sm^{III} cyclopentadienide complex, $[(C_5Me_5)_3Sm]$, is dominated by SIR chemistry, Section 1.5. Disabling SIR chemistry by reducing the steric bulk of the substituted cyclopentadienide from pentamethyl- to tetramethyl- effectively allows the potassium reduction to proceed for the cyclopentadienide system. Crystalline $(\mu\text{-}\eta^2\text{:}\eta^2\text{-}N_2)$ products utilising this synthetic route are observed across the lanthanoid series.[58, 59]

Higher order reduction, with the addition of more than two electrons per N_2 unit, as shown by Gambarotta *et al.*, *vide supra*, has also been achieved without the use of mixed metal reductions. Guillemot *et al.* report the use of calix[4]arene ligands as providing an electron-rich (*via* O-donor), pre-organising coordination environment. Four electron irreversible reduction of N_2 to $(N_2)^{4-}$ by three Sm atoms is then achieved upon reduction with sodium naphthalenide under dinitrogen, Figure 2-1. Preliminary results indicate that the reaction is applicable to other lanthanoids without ready access to Ln^{II} speciation under these conditions (*viz*. Pr).[119]

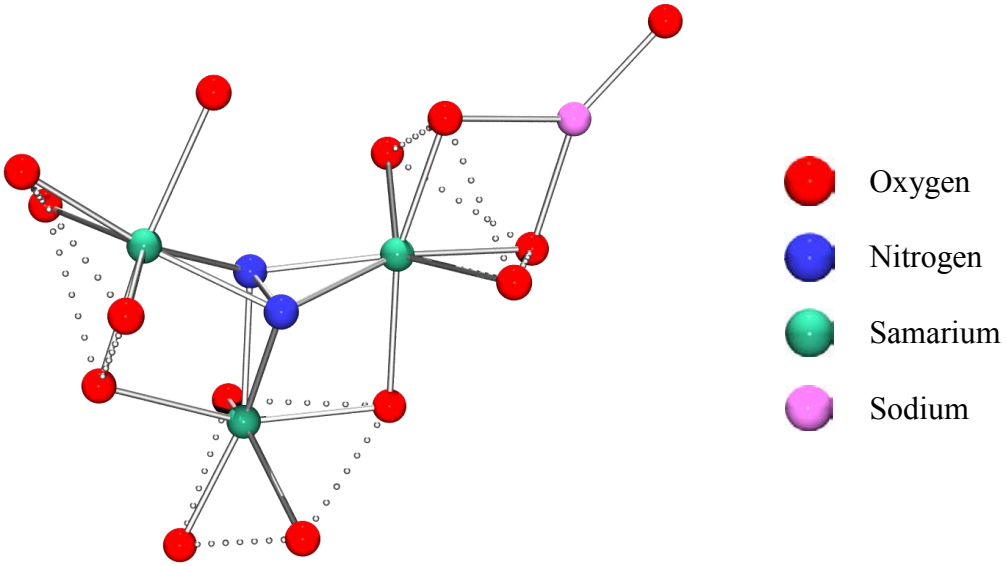

Figure 2-1 The molecular core reported by Guillemot *et. al.* showing $(N_2)^{4-}$ coordinated to three samarium centres, adapted from Guillemot.[119]

Evans *et al.* report concomitant two and three electron reduction of dinitrogen in the reaction of DyI_2 with two equivalents of KOAr (OAr = $OC_6H_3(t\text{-}Bu)_2$-2,6) at -78 °C under N_2, Scheme 2-2. Three electron reduction arises due to incorporation of potassium in either the inner coordination sphere, (**XXXII**), or via a hexa-THF solvated potassium cation, (**XXXI**).

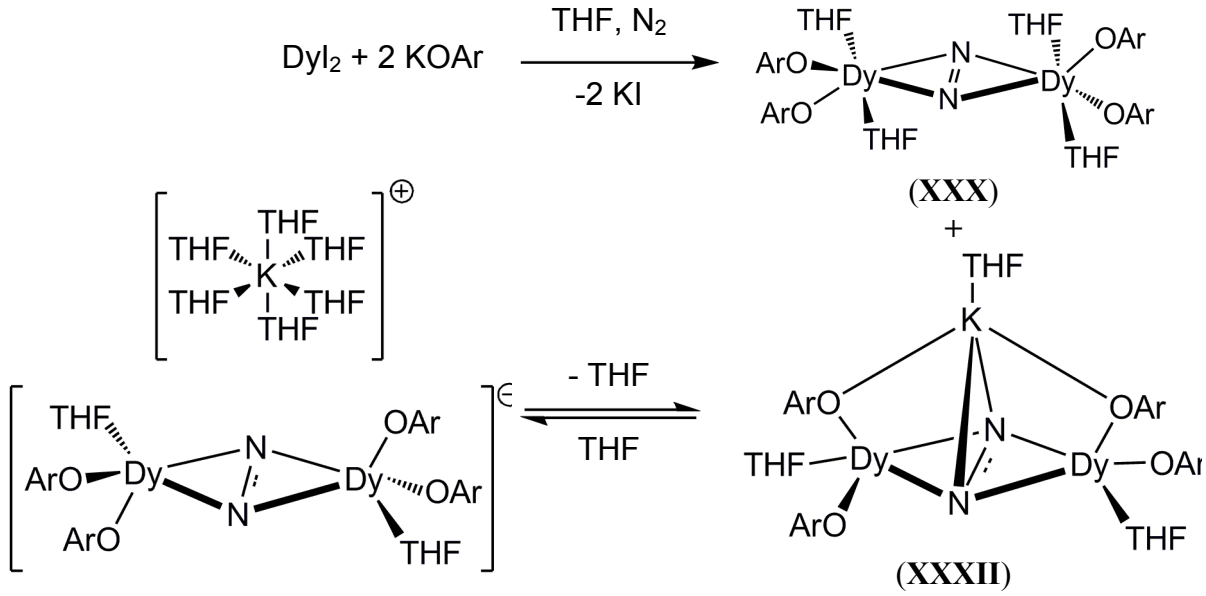

Scheme 2-2 Reaction describing the concomitant two and three electron reduction of N_2 by dysprosium.[120] OAr = OC_6H_3-2,6-$(t\text{-}Bu)_2$

The analogous yttrium complex could not be achieved with the KOAr ligand system, but was accessed using the previously reported dinitrogen complex formed between yttrium and the $N(SiMe_3)_2^-$ ligand.[117] This, too, was shown to incorporate potassium in both fashions analogous to dysprosium. EPR studies on the yttrium complexes allowed definitive assignment of $(N_2)^{3-}$. DFT was used to locate the unpaired electron in an orbital perpendicular to the metal orbitals, protected from the external environment by the other ligands.[120]

Another 2009 report by Evans investigated the effect of metal size in the reduction reactivity of $[\{(C_5Me_4H)_2Ln(THF)\}_2(\mu\text{-}\eta^2\text{:}\eta^2\text{-}N_2)]$ for the largest and smallest lanthanoids, La and Lu. It was shown that $[\{(C_5Me_4H)_2Ln(THF)\}_2(\mu\text{-}\eta^2\text{:}\eta^2\text{-}N_2)]$ species can provide the equivalent of divalent Ln^{II} reactivity and the N_2 byproduct is easily removed from any reaction product. It was shown that metal size affects reaction with some substrates and not others.[60]

2.2 Research Aim

To investigate possible routes to unsolvated samarium(II) species supported by *N*,*N*′-dimethyl-*meso*-octaethylporphyrinogen and, if found, investigate the assumed increase in reactivity by undertaking reaction of this unsolvated species with ligands that have shown no reaction with the bis(THF) solvate, $[(Et_8N_4Me_2)Sm(THF)_2]$, (**XVI**), such as naphthalene, anthracene and *cis*-stilbene.

2.3 Results and Discussion

Potential routes to unsolvated samarium(II) species are likely to require either synthetic precursors free from (or employing weakly bound) Lewis base coordinating solvents, or physical means (such as high vacuum) to remove any coordinated solvent from an isolated complex. Previous work by our group has reported an attempted synthesis of the unsolvated species by reaction of $(Et_8N_4Me_2)Li_2$ with $[(C_5Me_5)_2Sm]$ in toluene, Equation 2-8. The isolated mono(THF) solvated product, the only characterised complex obtained, accounts for only 5% yield and is presumed to arise due to incomplete desolvation of the decamethylsamarocene reagent.[72]

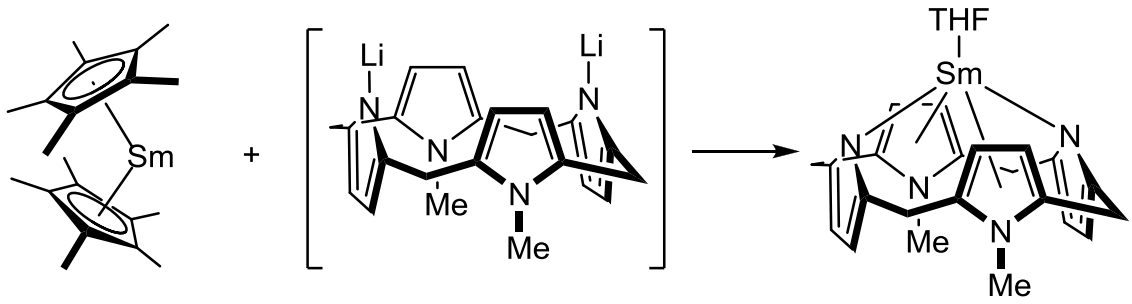

Equation 2-8

Desolvation of $[(Et_8N_4Me_2)Sm(THF)_2]$, (**XVI**), by heating under high vacuum had also been investigated by our group and deemed unsuccessful at the time based on physical and spectroscopic evidence; the results reported herein will show that this data was misinterpreted and re-examination of the procedure is warranted.

2.3.1 Lewis-base Solvent Free Complex Synthesis

Given the numerous alkali metal reduction reactions undertaken with samarium(III) species, Sections 2.1.1 and 2.1.2, the solvent free, readily isolable samarium(III) chloride species [{($Et_8N_4Me_2$)SmCl}$_2$] (**XVII**, Section 1.7) was identified as a potential candidate for access to the unsolvated Sm^{II} complex *via* potassium reduction and salt elimination reaction.[46]

[{($Et_8N_4Me_2$)SmCl}$_2$] (**XVII**, Section 1.7) was prepared *via* the method previously reported by our group in 2004.[71] A small quantity (3 mg) of the insoluble orange $Sm^{III}Cl$ complex, (**XVII**), was suspended in C_6H_6 with excess oxide-free potassium metal (5 mg). The reaction was heated at 74 °C in a sealed NMR tube under a N_2 atmosphere for 15 minutes, whereupon a clear, pale yellow solution became apparent with no visible solid material other than the potassium metal. The solution was filtered and, upon standing in the glovebox for 24 hours, large orange crystals with the same colour and morphology of the [{($Et_8N_4Me_2$)SmCl}$_2$] starting material were observed, Scheme 2-3. The reaction was repeated on the same scale under an argon atmosphere by freezing the initial suspension and evacuating the head-space of the reaction vessel. The head-space was refilled with argon and the reaction heated at 74 °C for 15 minutes, resulting in a similar clear, pale yellow solution. Upon filtering and evaporation in the glovebox, similar large orange crystals were observed and presumed to be [{($Et_8N_4Me_2$)SmCl}$_2$], Scheme 2-3.

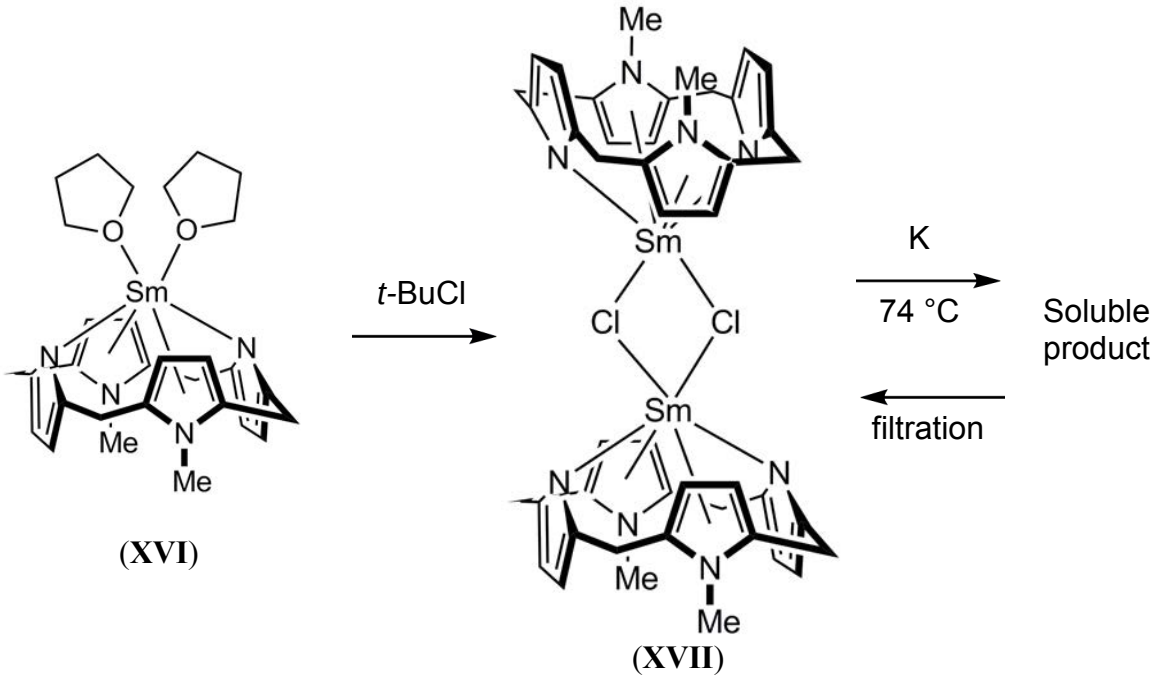

(**XVI**) (**XVII**)

Scheme 2-3 Synthesis of [{($Et_8N_4Me_2$)SmCl}$_2$], (**XVII**), and its reaction with potassium.

Although it is unclear why an excess of potassium metal should solubilise the otherwise toluene insoluble samarium chloride dimer, (**XVII**), the observation was shown to be reproducible. Irrespective of this unusual outcome, it is apparent that the desired reduction and salt elimination reaction pathway was not achieved under these conditions.

A second solvent free candidate for an analogous type of reaction was identified in the previously reported dinuclear Sm^{III} 1,4-*t*-butyl-1,4-diazabuta-1,3-diene complex, [{($Et_8N_4Me_2$)Sm}$_2$(*t*-BuDAB)], **(XXII)**, which has been shown to exhibit solvent mediated reversible Sm^{II}/Sm^{III} redox chemistry, Section 1.7.[76] The susceptibility of (**XXII**) to the desired reactivity is thus anticipated to be higher than the $Sm^{III}Cl$ complex, (**XVII**). In addition, the suitability of the RDAB ligand to alkali metal reduction and precipitation as K(*t*-BuDAB) in non-coordinating solvents offers further advantage.[121, 122] High yielding preparation of (**XXII**) is trivial upon isolation of [($Et_8N_4Me_2$)Sm(THF)$_2$], (**XVI**), and the synthesis additionally provides for the removal of THF from the system, Equation 1-12.[76]

2.3.1.1 ^{1}H NMR Spectroscopic Evidence of Lewis Base Free Sm^{II}

The reaction between [{($Et_8N_4Me_2$)Sm}$_2$(*t*-BuDAB)], **(XXII)**, and potassium was undertaken on NMR scale (~10 mg {**XXII**}, ~3 mg K) in both C_6D_6 and D_8-PhMe and under both argon and dinitrogen atmospheres. In all cases, heating was continued until a highly soluble dark red/purple solution and an orange precipitate was observed.

The high solubility of the red/purple reaction products in both toluene and benzene renders ^{1}H NMR spectroscopy a viable technique to monitor reaction progress within the limits of the paramagnetic line broadening influences of the Sm^{II} centres in the products. Conversely, due to the extreme solubility, purification of crystalline products has proven difficult. As such, the ^{1}H NMR spectra presented here are of unpurified reaction mixtures and can offer only indications of reactivity, rather than complete characterisation and spectroscopic assignment as may be achievable for the pure compounds. During final thesis editing, satisfactory elemental analysis was achieved for one species reported herein, *vide infra*. As this data only became available at the very latest stage of candidature, the associated ^{1}H NMR spectroscopic analysis of the pure complex could not be undertaken. The ^{1}H NMR spectrum of pure [($Et_8N_4Me_2$)Sm(THF)$_2$], (**XVI**), is presented for reference, Figure 2-2.

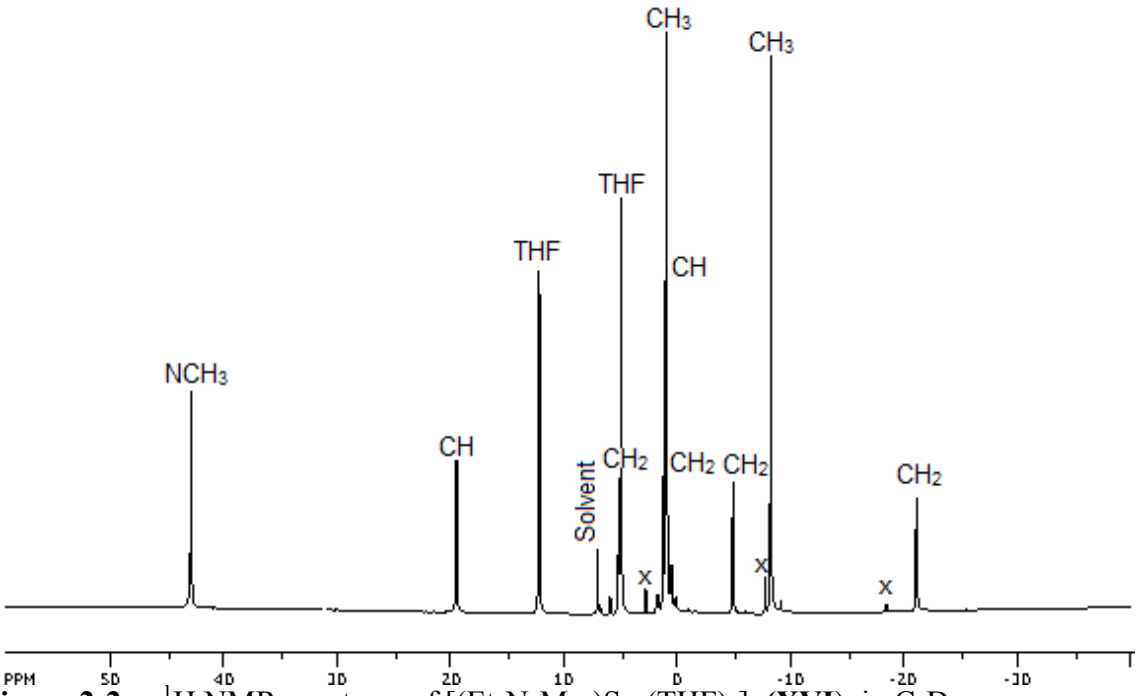

Figure 2-2 ^{1}H NMR spectrum of $[(Et_8N_4Me_2)Sm(THF)_2]$, **(XVI)** in C_6D_6.

The Sm^{II} bis(THF) adduct shows a series of reproducibly widened and shifted resonances between -21 and 43 ppm at room temperature, consistent with the paramagnetic Sm^{II} centre. As shown through prior 2D NMR spectroscopic methods, the singlet resonance at 43.2 ppm is assigned to the *N*-methyl group; at 19.7 and 1.2 ppm are the *β*-protons of the $N_{Pyrrolide}$ and N_{Methyl} rings; the two resonances at 12.4 and 5.1 are due to the coordinating THF molecules. The multiplets at -21.1, -4.8, 1.4 and 5.3 ppm are attributable to the CH_2 protons of the *meso*-ethyl groups, whilst the resonances at -8.1 and 1.1 ppm are attributable to the CH_3 protons of the *meso*-ethyl groups, Figure 2-2.

Addition of cleaned potassium metal to a D_6-benzene solution of (**XXII**) and subsequent heating at 65 °C over three days provided a red/purple solution with evidence of a precipitated orange solid. The ^{1}H NMR spectrum of the purple solution as a crude reaction mixture is presented, Figure 2-3.

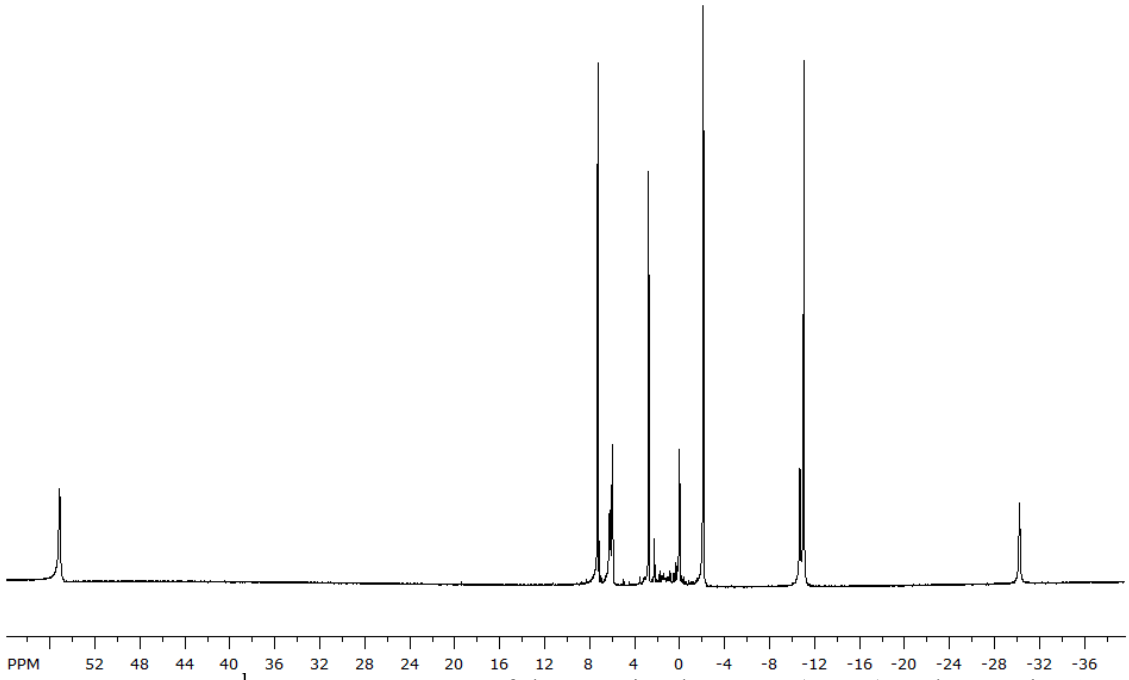

Figure 2-3 *In situ* ^{1}H NMR spectrum of the reaction between (**XXII**) and K_{metal} in C_6D_6.

When compared with the spectrum of the bis(THF) adduct, Figure 2-2, Figure 2-3 clearly shows a widening of the broadest resonances and shifting of others. The shifting of resonances away from the 0-10 ppm region of the spectrum due to paramagnetic shift influences as the degree of solvation is decreased is consistent with literature reports.[72]

The mono(THF) adduct of (**XVI**) has a partial ^{1}H NMR spectroscopic assignment reported, with resonances attributed to the *N*-methyl group at 48.20 ppm (*cf.* 43.2 ppm for {**XVI**}) and the highest field CH_2 at -25.6 ppm (*cf.* -21.1 ppm for {**XVI**}).[72] Drift of the THF and $(C_5Me_5)^-$ resonances is also observed in the two THF solvates of decamethylsamarocene, $[(C_5Me_5)_2Sm(THF)_2]$, (**IV**) and $[(C_5Me_5)_2Sm(THF)]$, although there is no correlation in the direction of the drift between the samarocenes and porphyrinogen adducts.[19, 86]

Assigning the resonances in Figure 2-3 is difficult as there appear to be fewer resonances than would be expected for a $[(Et_8N_4Me_2)Sm]$ complex. Based on integration and analogy to the bis(THF) adduct, (**XVI**), the anticipated 6 *N*-methyl (55.2 ppm), 24

meso-CH_3 (-11.2 and -2.3 ppm) and 16 *meso*-CH_2 (-30.5, -10.9, -0.1, and 5.8 ppm) protons are all observed, however only 6 (2.6 ppm, 4H, and 6.1 ppm, 2H) of the expected 8 β-protons of the $N_{Pyrrolide}$ and N_{Methyl} rings, that would make up the compliment of 54 protons for complexes of this macrocycle, are observed by integration. The remaining resonances in the spectrum are insignificant by integration and attributable to minor impurities or the residual solvent resonances.

The appearance of the ^{1}H NMR spectrum presented in Figure 2-3 may arise due to the increased influence of the paramagnetic metal centre expected for an unsolvated species compared to the bis(THF) adduct, (**XVI**). If the paramagnetic centre is more closely bound to the macrocycle in an unsolvated complex, the extent of broadening and shifting of resonances would be increased. The data is not consistent with the ^{1}H NMR spectrum anticipated for complexes bearing *t*-Butyl groups due to incorporation of the *t*-BuDAB moiety of the starting material. The presence or absence of dinitrogen in the complex cannot be confirmed without further experimental data (such as ^{15}N labelling), however the experiment is consistent with the presence of an unsolvated or Lewis basic solvent free complex, and warrants larger scale and solid state investigation.

Undertaking the analogous reaction between (**XXII**) and potassium metal in D_8-PhMe with extended heating results in a significantly more complex spectrum, with severe peak broadening observed, particularly at the extremities, Figure 2-4. No attempt has been made to assign the resonances observed, although the similarity of the spectrum to the C_6D_6 reaction (with regard to spectral width), Figure 2-3, is noted. Significantly, withdrawing some head space vapour from a vial of D_8-THF and bubbling this gas into the reaction mixture resulted in an immediate colour change. ^{1}H NMR spectrum of the resulting solution indicated a return to the known spectrum of (**XVI**), albeit with some

impurity and without the signature THF resonances due to deuteration, Figure 2-5. It is also noted that the spectrum depicted in Figure 2-4 is identical to ^{1}H NMR spectroscopic data obtained *via* reaction of decamethylsamarocene with $(Et_8N_4Me_2)Li_2$, Equation 2-8.

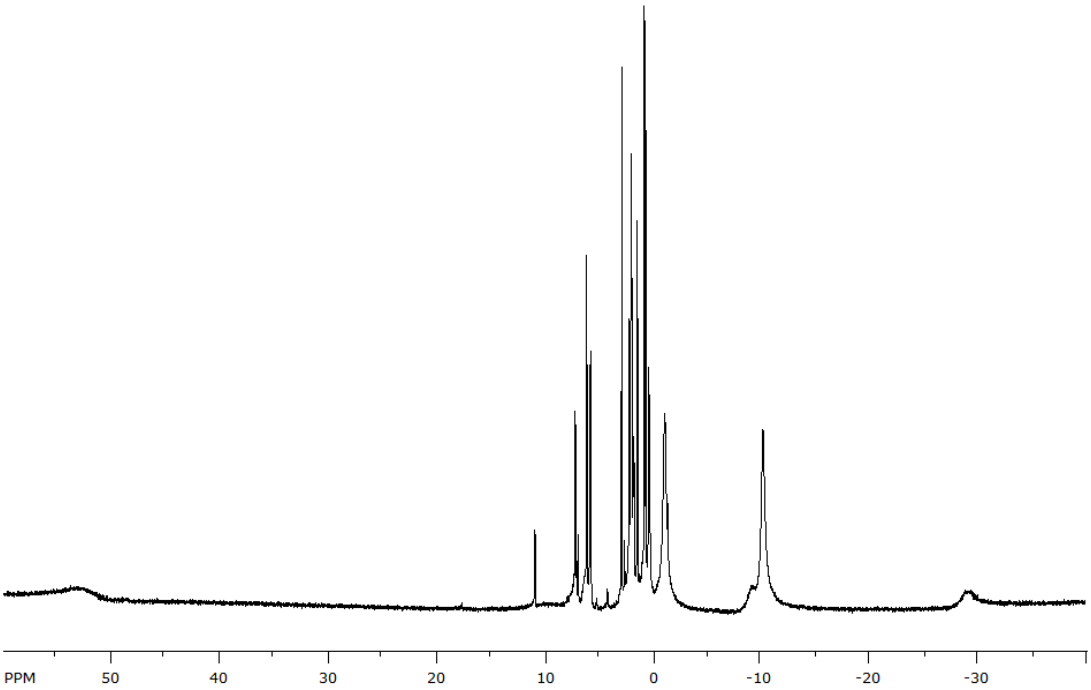

Figure 2-4 *In situ* ^{1}H NMR spectrum of the reaction between (**XXII**) and K_{metal} in D_8-PhMe.

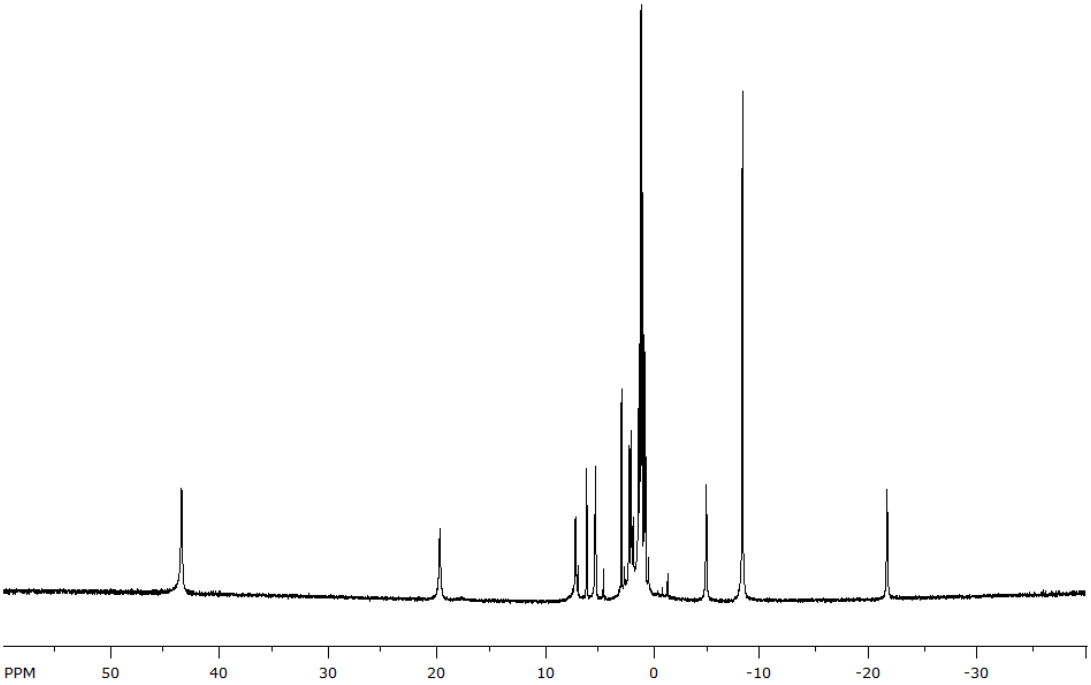

Figure 2-5 ^{1}H NMR spectrum resulting from addition of a small quantity of D_8-THF into the solution that provided the spectrum in Figure 2-4, *cf.* Figure 2-2**.**

2.3.2 Lewis Base Free Sm^{II} in the Solid State

Given the indication of the accessibility of a Lewis base free Sm^{II} species by ^1H NMR spectroscopy, further investigation into the reaction between [{$(Et_8N_4Me_2)Sm$}$_2$(*t*-BuDAB)], (**XXII**), and potassium was deemed necessary.

10 mg (**XXII**) was dissolved in 1 mL PhMe. 5 mg of carefully cleaned potassium metal was added to the solution and the dinitrogen atmosphere of the glovebox was maintained in the flask. The reaction was heated at 83 °C for six days, providing a dark purple solution over an orange precipitate (presumably arising due to [K(*t*-BuDAB)]). The solution was filtered in the glovebox and reduced *in vacuo* to one quarter of the initial volume and the head-space replaced with argon gas. Left to stand overnight, large, very dark red/purple crystals were observed in the bottom of the tube. X-ray crystal structure determination revealed a slipped η^3- toluene adduct of the Lewis base free Sm^{II} macrocycle species, [$(Et_8N_4Me_2)Sm(PhMe)$], (1), Equation 2-9.

Simultaneous undertaking of the reaction under, to best approximation, the same conditions, whilst replacing the dinitrogen atmosphere with argon prior to heating the samples resulted in similar very dark red/purple crystals. X-ray crystal structure determination revealed the same product, Equation 2-9. A detailed comparison of the X-ray crystal structure of [$(Et_8N_4Me_2)Sm(THF)_2$], (**XVI**), and [$(Et_8N_4Me_2)Sm(PhMe)$], (1), is undertaken in Section 2.3.2.1. The broadening and shifting of resonances in the ^1H NMR spectrum due to a paramagnetic metal centre, Figure 2-4, as well as the reversibility of the reaction on addition of D_8-THF, Figure 2-5, may be consistent with fluxional toluene coordination as expected for (1).

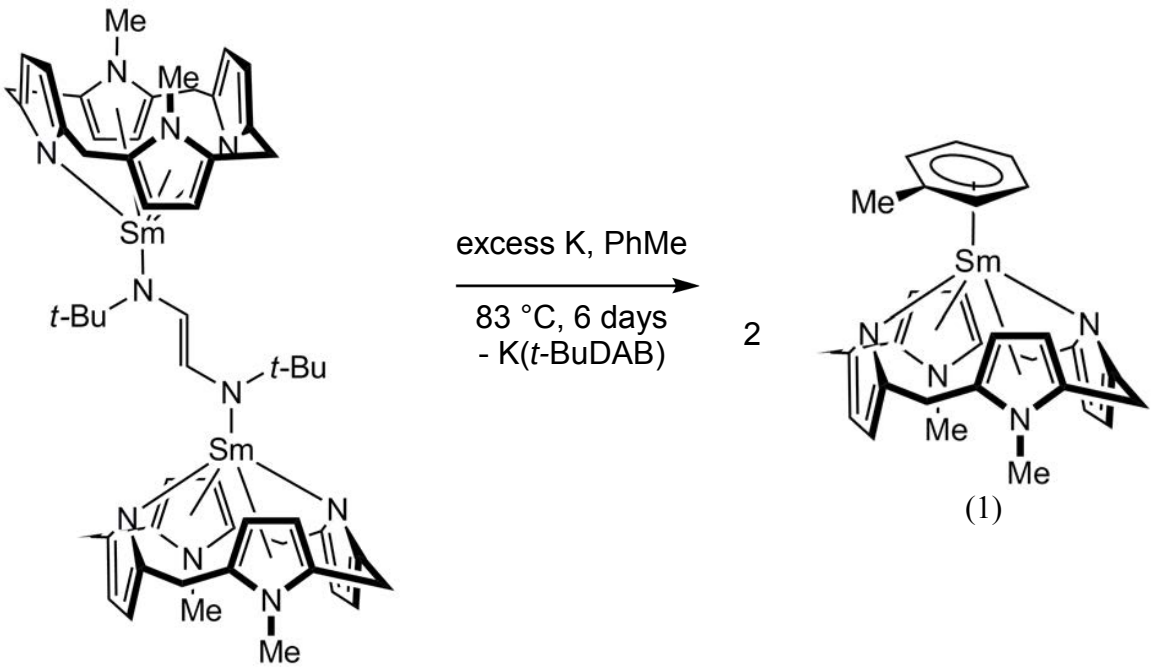

(**XXII**) (1)

Equation 2-9

When the reaction described in Equation 2-9 is undertaken at slightly higher temperature (91 °C) and allowed to proceed for an additional 24 hours, a bleaching in colour of the solution from the previously described dark red/purple to an orange/brown appearance is observed with concomitant formation of dark red/purple crystals. Two crystal morphologies were observed for the dark red/purple crystals. The crystals were insoluble, preventing NMR characterisation, and the lateness of this synthesis in the candidature timeline prevented repetition of the reaction to attempt elemental analysis. X-ray crystal structure analysis revealed that the rods and large blocks were isostructural but not isomorphous and established that the higher temperature and extended reaction time resulted in the potassium mediated metallation of toluene, forming $[\{(Et_8N_4Me_2)Sm\}_2(C_7H_7)K]$, (2), Equation 2-10.

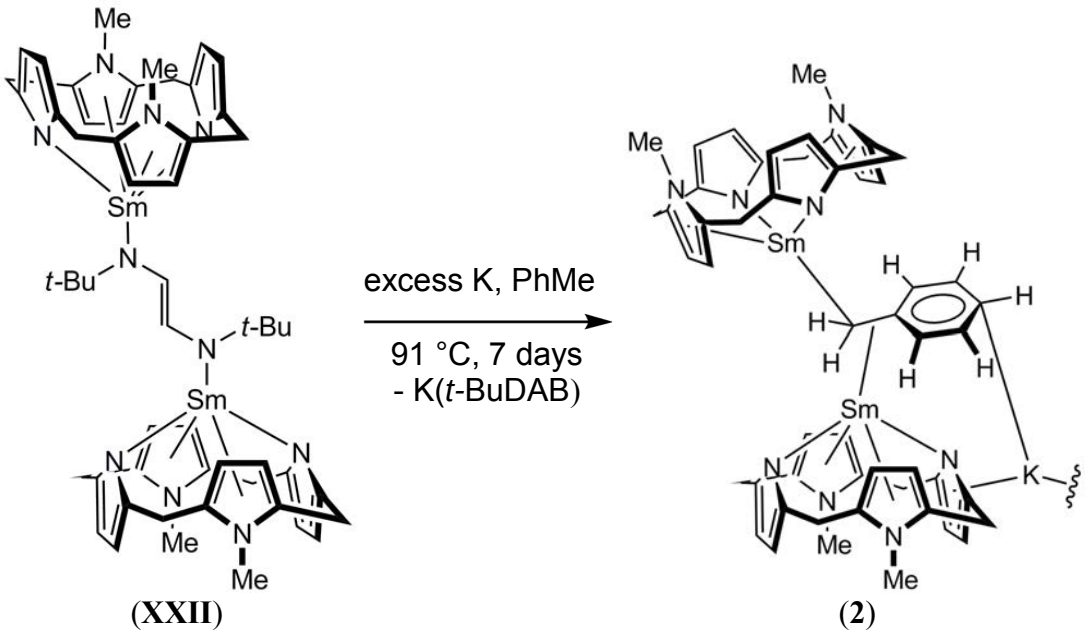

(**XXII**) (**2**)

Equation 2-10

Deprotonation and metallation of toluene has been known since the 1960s, with metallation occurring at the methyl group of toluene in the presence of *n*-BuNa,[123] *n*-BuLi-tmeda,[124] or *n*-BuK.[125] Deprotonation at the methyl group is accepted to be favoured by resonance stabilisation of the resulting carbanion, resulting in the thermodynamically favoured benzyl anion when a proton is abstracted from toluene.[126] Mixed alkali metal systems have been dubbed „superbases' due to their enhanced collaborative reactivity relative to single alkali metal systems.[127] The benzyl radical has also been formed *via* reaction of toluene with *in situ* generated $NO_3^{\bullet}$ formed by photolysis of cerium ammonium nitrate in acetonitrile.[128]

Reports of samarium benzyl complexes are limited. In 1991, Evans, Ulibarri and Ziller observed the reaction of $[(C_5Me_5)_2Sm(\mu\text{-}H)]_2$ with toluene in the presence of cyclohexene to produce a 1:1 Sm η^1-benzyl complex.[129] In 1996, Mandel and Magull reported the synthesis of a polymeric samarium benzyl complex, $[(C_5Me_5)_2Sm(CH_2C_6H_5)_2K(THF)_2]_\infty$, by reaction of $SmBr_3$ with $[K(CH_2C_6H_5)]$ and $[K(C_5Me_5)]$ in THF.[130] The complex shows the bis(THF) solvated potassium is bound η^6-

to two benzyl rings of adjacent molecular units, serving as a polymeric bridge in an analogous way to the η^5-, η^2- binding of potassium to the $N_{Pyrrolide}$ moieties observed in complex (2), *vide supra*. Complex (2) is, to the best of our knowledge, the first example of a bridging benzyl moiety in the chemistry of samarium.

Filtration and concentration of the red solution afforded by undertaking the reaction of (**XXII**) and excess potassium metal in benzene at 83 °C for 48 hours provides small red crystals of a self aggregated, Lewis-base unsolvated samarium(II) species, $[(Et_8N_4Me_2)Sm]$, (**3**), Equation 2-11.

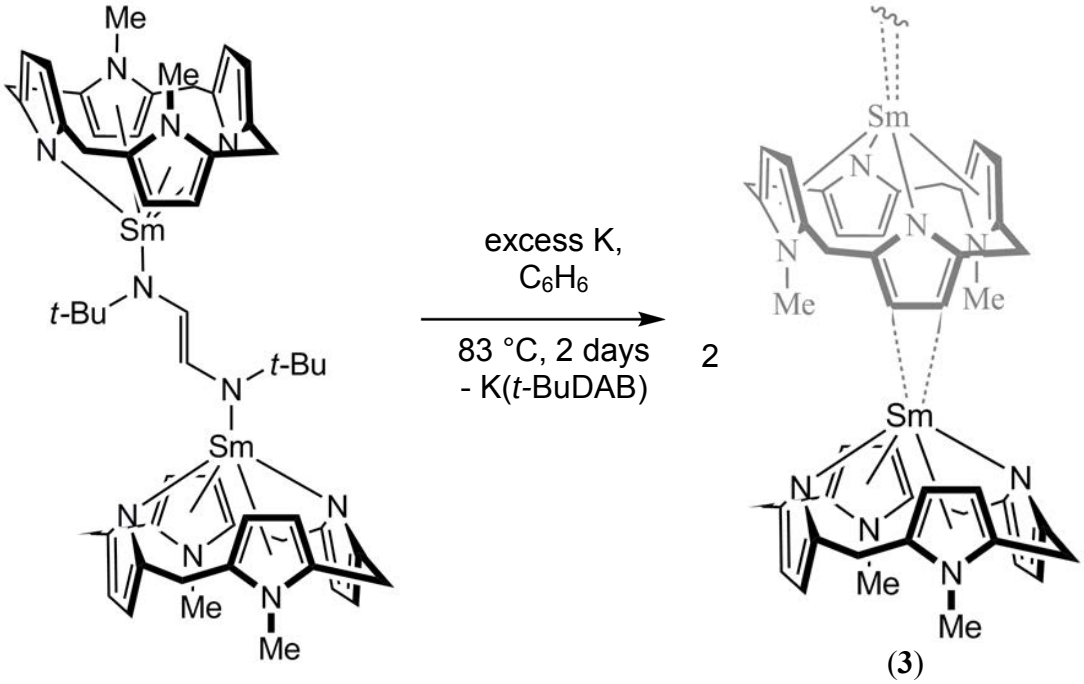

(**XXII**) (**3**)

Equation 2-11

The crystal structures of two forms of (**3**) contain benzene in the lattice, however the solvent is not involved in any coordination to the metal centre, unlike the toluene adduct (1). Instead, the samarium(II) centres show close contact (*ca*. 3.04 Å) to the *β*-carbons of one $N_{Pyrrolide}$ unit of another molecular unit of (**3**), as depicted in Figure 2-20, giving complex 1- or 2-D polymeric structures that are described in Section 2.3.2.3.

The reaction of (**XXII**) and potassium proceeds at a different rate according to the reaction solvent; a dark red/purple solution is obtained *via* heating the reaction at 83 °C in benzene after 48 hours, whereas six days are required to effect a similar colour change at the same temperature when the reaction is undertaken in toluene. Upon filtration to remove the orange precipitate from both reactions, a noticeable difference in the solution colour is observed, with the benzene reaction dark red/purple and the toluene reaction dark brown/orange in colour. During the final stages of candidature, satisfactory elemental analysis of (**3**) was obtained.

A third product isolated in low yield from the reaction of [{($Et_8N_4Me_2$)Sm}$_2$(*t*-BuDAB)], (**XXII**), and potassium in either toluene or benzene is the dimeric alkali metal oxide [{($Et_8N_4Me_2$)SmOK}$_2$], (**4**), Equation 2-12. Complex (**4**) was observed under varying conditions, particularly following prolonged periods of standing, and is thought to arise due to either incomplete removal of the oxide layer from the reacting potassium metal or from trace serendipitous oxygen due to imperfect sealing of the reaction vessel. Complex (**4**) forms pale orange, well formed crystalline plates in both PhMe and C_6H_6. Neither deliberate nor complete synthesis of (**4**) has been attempted as such a synthesis offers no apparent advantage to this work. The molecular structure is consistent with a samarium(III) centre, Section 2.3.2.3.

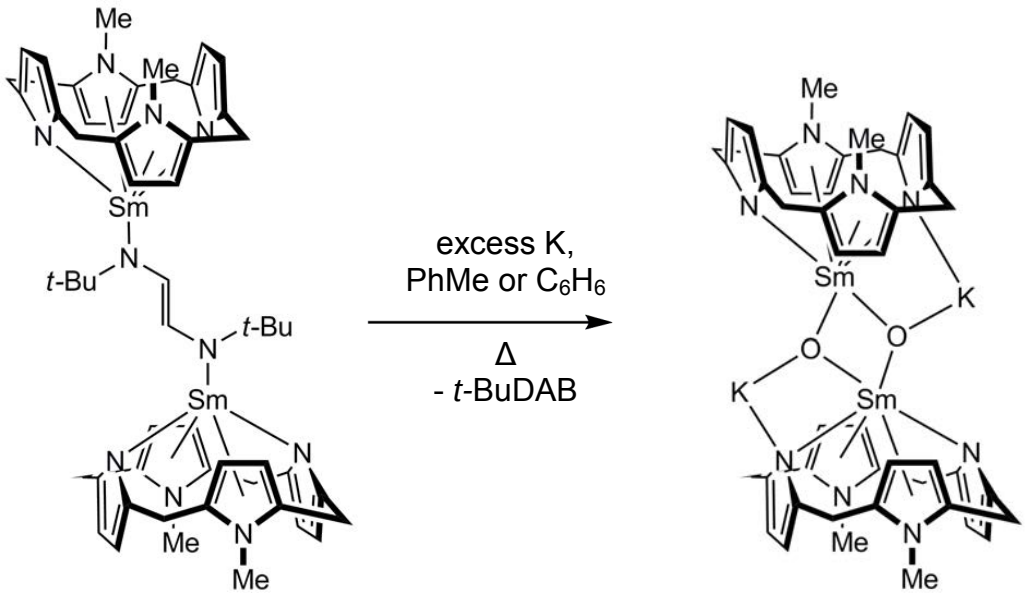

(**XXII**) (**4**)

Equation 2-12

The reaction between (**XXII**) and potassium in benzene to provide the unsolvated species, (**3**), Equation 2-11, has also provided red crystals of a 1:1:1 polymeric complex formed by the samarium macrocycle, *t*-BuDAB and potassium; $[\{(Et_8N_4Me_2)Sm(t\text{-BuDAB})(K)\}_n]$, (**5**). A third red crystalline product has been characterised by X-ray crystallography in the form of a 1:1 complex comprised of the samarium macrocycle and a partially protonated *t*-BuDAB ligand, $[\{(Et_8N_4Me_2)Sm\}_2(t\text{-BuDAB})]$, (**6**). Complex (**6**) is significantly different from (**5**); there is no evidence of potassium incorporation in (**6**).

The X-ray crystal structure of (**5**) yields an accurate refinement of high quality, Section 2.3.2.5, leading to confidence in the description of (**5**), despite the difficulty in reproducing its synthesis. The solid state structure reveals a linear polymer through the η^5- (depicted) and η^2- (abbreviated) macrocycle interactions to the *exo*- bound potassium atoms, Equation 2-13. The oxidation state and electronic configuration of (**5**) have been probed by DFT analysis, Section 2.3.3.1, and are indicative of a samarium(II) centre

η^1- bound to a delocalised radical anion in the *t*-BuDAB moiety that is also η^1-bound to the potassium cation.

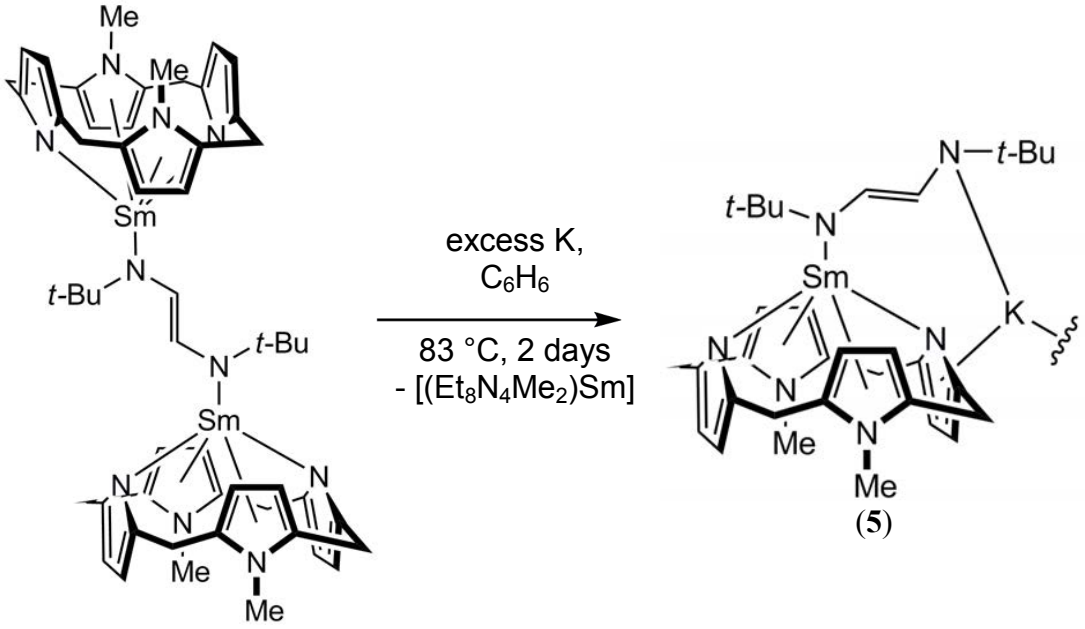

(**XXII**) (**5**)

Equation 2-13

Formation of complexes (**5**) and (**6**) is assumed to be in low yield based on ^{1}H NMR spectroscopy, Section 2.3.1.1, which does not support the presence of a soluble *t*-Bu moiety. The high solubility of the reaction filtrate and the paramagnetic effects of the Sm^{II} centre have not permitted purification and characterisation data, including relative yields. A balanced equation for formation of both (**3**) and (**5**) is not available when the initial co-formed precipitate is presumed to be [K(*t*-BuDAB)]. Incomplete precipitation of [K(*t*-BuDAB)] may lead to incorporation the K(*t*-BuDAB) moiety in the molecular structure of (**3**), giving rise to a small amount of (**5**). The synthesis of complexes (**5**) and (**6**) has not been reproducible and satisfactory elemental analysis of (**3**) has been obtained *via* the described synthesis, indicating that both (**5**) and (**6**) are minor side products.

Serendipitous protonation of *t*-BuDAB to the observed imines could account for the formation of (**6**), *vide infra*, however the irreproducibility of the synthesis has prevented

further characterisation of both the reaction product and the synthetic pathway. The X-ray crystal structure refinement of complex (**6**) is not sufficiently accurate to confidently assign, despite falling within the „publishable' range for measures of data (R_{int}) and refinement (R_1) accuracy. The particular area of difficulty in the refinement is the pendant end of the *t*-BuDAB moiety, consistent with the untethered nature of the ligand. Due to unsatisfactory crystal structure refinement, the crystal structure of (**6**) is not presented in this thesis.

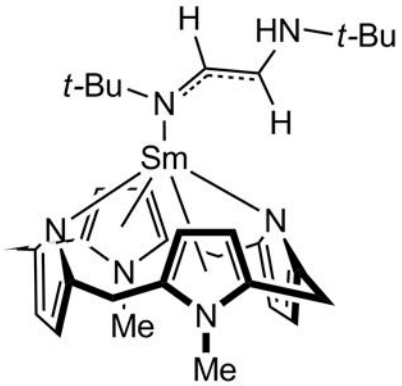

(**6**)

The identification of complexes (1) through (**6**) was achieved *via* X-ray crystallographic analysis and is supported by *in situ* ^{1}H NMR spectroscopic analysis, Section 2.3.1.1, and successful elemental analysis in the case of (**3**). As discussed, multiple products have been isolated from reaction of (**XXII**) and potassium in either toluene or benzene. Most of the complexes show a high degree of solubility and are obtained from complete ambient evaporation. These factors, and the breakthrough leading to this work falling at the end of the candidature, have prevented further characterisation being achieved despite repeated attempts to obtain separated products.

2.3.2.1 Molecular Structure of [$(Et_8N_4Me_2)Sm(PhMe)$], (1), and comparison with [$(Et_8N_4Me_2)Sm(THF)_2$], (XVI)

Complex (1) was obtained as a red crystalline precipitate from reaction of [{$(Et_8N_4Me_2)Sm$}$_2$(*t*-BuDAB)], (**XXII**), with potassium metal in PhMe, Figure 2-6.

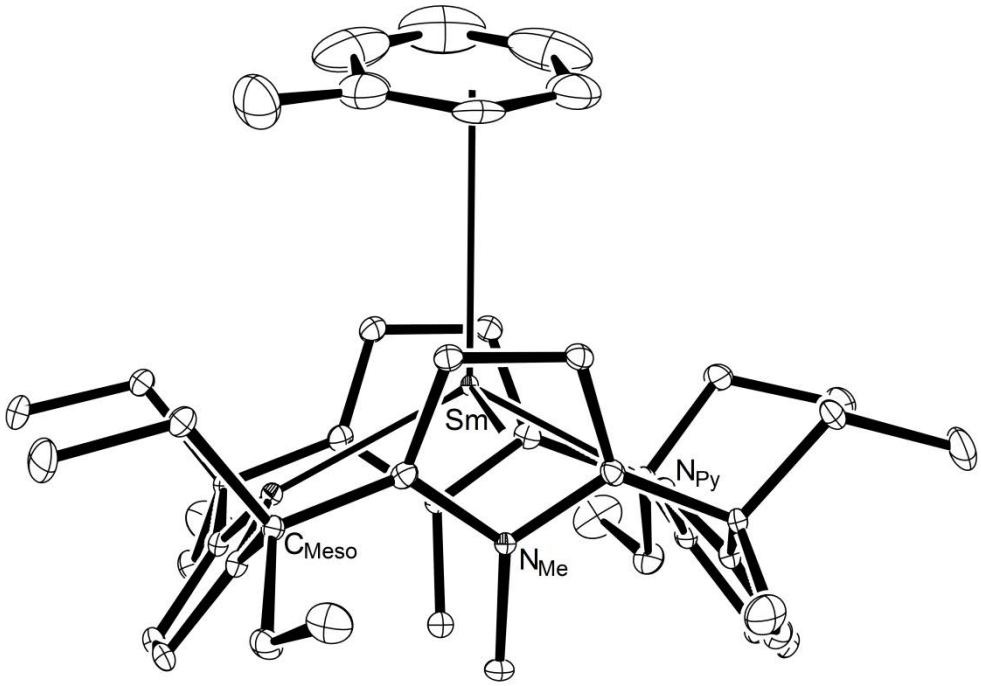

Figure 2-6 Molecular structure of (**1**) with thermal ellipsoids drawn at 50 % probability. Protons omitted for clarity.

The crystal belongs to the orthorhombic space group *Pnma* (No. 62), α = 9.992(2), *b* = 20.516(4), *c* = 18.558(3) Å, with four molecules in the unit cell. The asymmetric unit consists of one half of one molecule of (1), with C_s symmetry as depicted in Figure 2-6. The methyl group of the toluene molecule is disordered across the mirror plane.

The molecular structure of (1) exhibits 1,3-alternate conformation of the macrocycle, with η^1:η^5:η^1:η^5 binding of the Sm centre to the *N*-pyrrolide (N_{Py}) and *N*-methylpyrrole (N_{Me}) rings, respectively. This binding mode is enforced by the downward pointing *N*-methyl groups and is standard for all of the samarium macrocyclic compounds reported herein, unless otherwise noted, Figure 2-7.

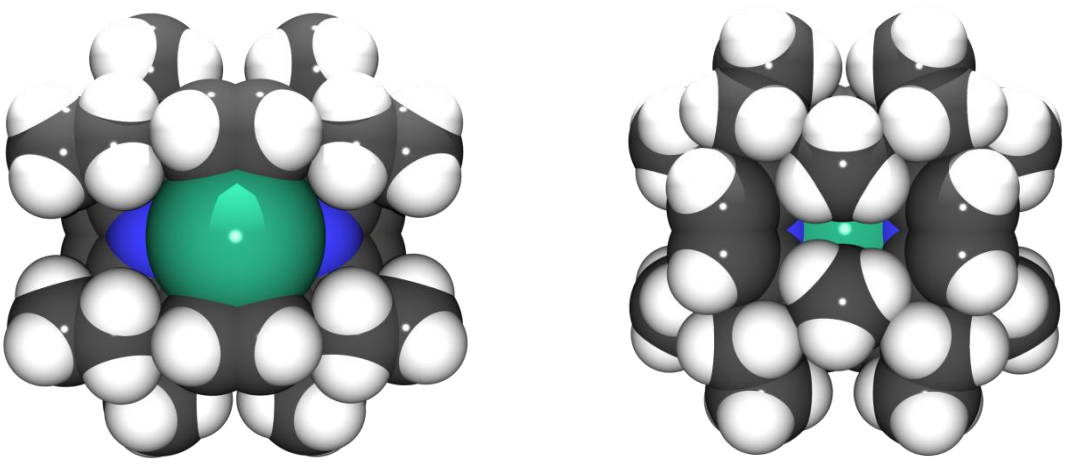

(a) (b)

Figure 2-7 Space filling representations of the molecular structure of $[(Et_8N_4Me_2)Sm(PhMe)]$, (**1**), viewed from the top, (a), and bottom, (b), of the molecule. Toluene omitted for clarity.

The binding groove of the molecule is clearly shown running from left to right in Figure 2-7a. The locked conformation of the macrocycle due to *trans-N,N'*-dimethylation, and shielding of the underside of the metal, Figure 2-7b, are established in Section 1.7.

The consistent $\eta^1{:}\eta^5{:}\eta^1{:}\eta^5$ binding observed for samarium complexes of the *N,N'*-dimethyl-*meso*-octaethylporphyrinogen allow for comparisons to be made between compounds in relation to steric effects, coordination number, affected metal radii and oxidation state. This allows the oxidation state of the metal to be established based on geometric features. Of interest to this thesis are the Sm-(η^1-N_{Py}) binding and Sm-(η^5-N_{Me}) ring centroid distances, Figure 2-8. The Sm-(η^1-N_{Py}) distance for (1) is 2.5324(4) Å and the Sm-(η^5-N_{Me}) distances are 2.65_0 and 2.66_7 Å. These distances are consistent with those observed for $[(Et_8N_4Me_2)Sm(THF)_2]$, (**XVI**), at 2.667(2) Å and 2.75_5 Å, respectively, given the higher coordination number and the effect of Lewis base coordination *via* O-donors for (**XVI**).

Further useful investigation of the Sm coordination environments across various complexes is achieved by defining a number of parameters relative to the least squares

plane defined by the four *meso*-carbon atoms of the macrocycle. Figure 2-8a shows a side on view of a samarium macrocycle complex with the *meso*- plane horizontal relative to the view angle. Figure 2-8b shows rotation of the molecule to show atoms above (white) and below (grey) the *meso*- plane.

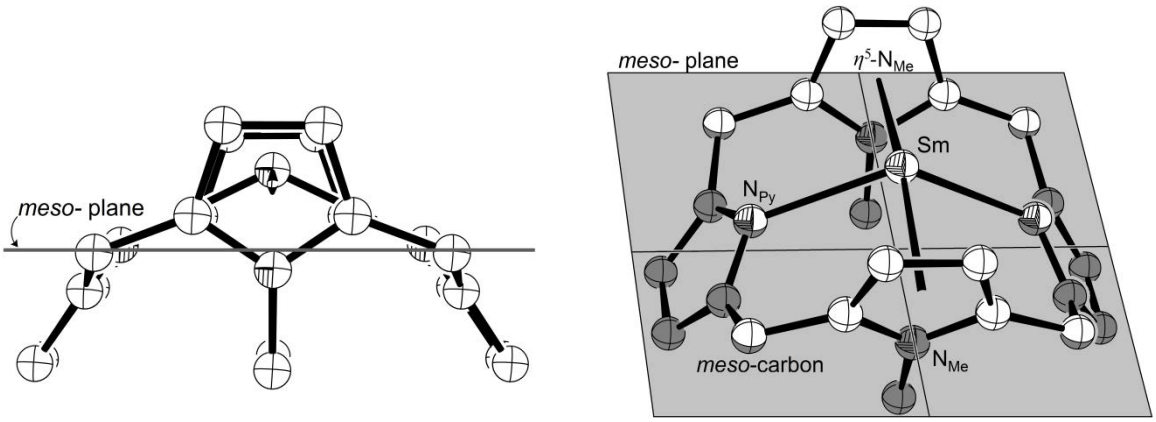

(a) (b)

Figure 2-8 Side-on (a) and tilted (b) view of "($H_8N_4Me_2$)Sm", showing the *meso*-plane, derived from [($Et_8N_4Me_2$)Sm(THF)$_2$], (**XVI**). For clarity, solvent molecules and protons are omitted, atoms are of arbitrary size.

The η^1- bound N_{Py} ring of (1) (defined by the five atoms of the N_{Py} ring) lies at an angle to the least squares plane of the four the *meso*- carbon atoms of the macrocycle, N_{Py}–*meso* = 53.67(1) °. Similarly, the planes of each N_{Me} ring (each defined by the five atoms of the heterocycle and excluding the *N*-Me group) form angles to the *meso*- plane, N_{Me}–*meso* = 75.71(1) and 83.25(1) °, respectively. The significant variation in angle arises due to the slipped η^3- bound toluene molecule, Figure 2-9. The samarium centre sits above the *meso*- plane of the macrocycle, Sm–*meso* = 1.3097(3) Å. The same N_{Py}–*meso* and N_{Me}–*meso* interplanar angles for (**XVI**) are smaller (N_{Py} = 49.92(7) ° and N_{Me} = 73.24(7) °) due to the much larger Sm–*meso* distance, 1.4794(17) Å, in (**XVI**). This variation between (1) and (**XVI**) is a consequence of the coordination of two molecules of THF in the case of (**XVI**); the oxophilic samarium is withdrawn from the macrocyclic cavity by the

coordination of the O-donor ligands. More generally, increasing coordination number increases the effective metal radii. In the absence of a Lewis base, as in (1), the metal draws deeper inside the macrocyclic cavity to better satisfy the coordination sphere of the metal.

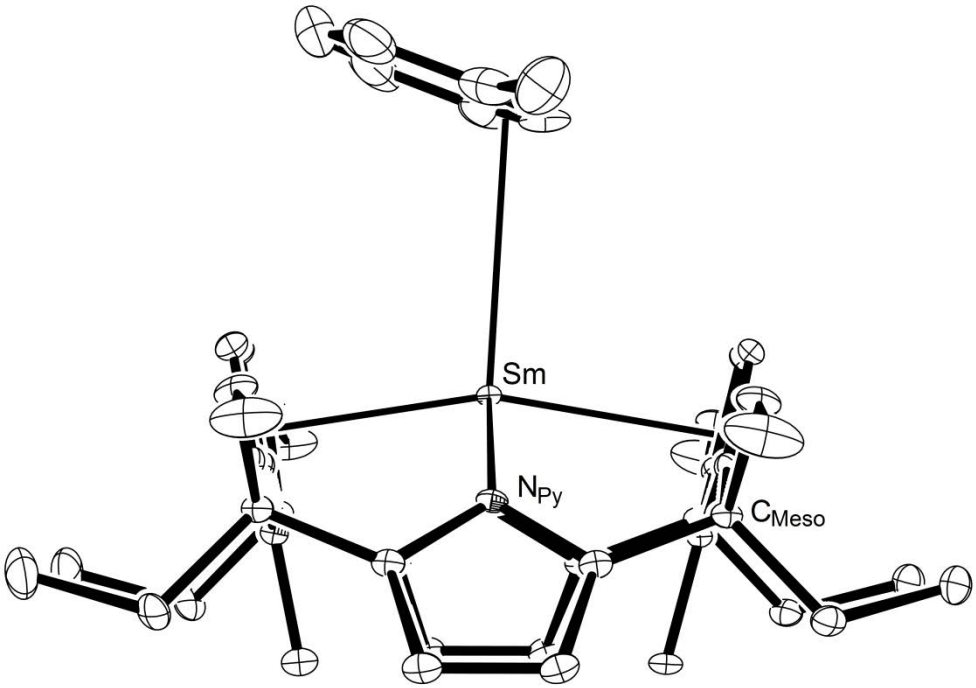

Figure 2-9 Molecular structure of (**1**) with thermal ellipsoids drawn at 50 % probability. Protons omitted for clarity.

Figure 2-9 clearly demonstrates the metallocene bend angle of (1), defined as the (η^5-N_{Me} ring centroid)−Sm−(η^5-N_{Me} ring centroid) angle. At 161.5_1 °, the metallocene bend angle of (1) is significantly larger (i.e. the geometry is less bent) than any decamethylsamarocene adduct, including $[(C_5Me_5)_2Sm(THF)_2]$, (**IV**, 136.7 °),[19] $[(C_5Me_5)_2Sm(THF)_1]$ (138.5 °),[86] and $[(C_5Me_5)_2Sm]$ (**V**, 140.1 °).[23] Table 2-2 compares the significant bond lengths and angles of (1) to related complexes of the macrocycle; the known Sm^{II} mono- and bis(THF) adducts and the Sm^{III} methyl complex. Data for (**XVI**) are reported for a structure obtained using the same crystallographic conditions as (1) and may show minor variation from reported values.[71]

	$M = Sm^{II}$ $L = PhMe$ (**1**)	$M = Sm^{II}$ $L = (THF)_2$ (**XVI**)	$M = Sm^{II}$ $L = THF$[72]	$M = Sm^{III}$ $L = Me$[75] (**XX**)
$M-(\eta^1\text{-}N_{Py})$	2.5324(4)	2.667(2)	2.566(2), 2.557(2)	2.478(3)
$M-(\eta^5\text{-}N_{Me})$	2.65_0, 2.66_7	2.75_5	2.66_8, 2.68_7	2.59_3, 2.60_9
$M-L_{donor\ atom}$	3.20_6 (as the $\eta^3\text{-}_{centroid}$)	2.6552(14)	2.544(2)	2.424(5)
M–*meso*	1.3097(3)	1.4794(17)	1.26_1	1.14_9
N_{Py}–*meso*	53.67(1)	49.92(7)	49.4_4, 55.6_0	50.1_5
N_{Me}–*meso*	75.71(1), 83.25(1)	73.24(7)	77.8_1, 78.3_0	78.8_1, 80.5_7
Metallocene bend	161.5_1	154.4_4	163.6_4	168.8_6

Table 2-2 Selected bond lengths (Å) and angles (°) for $[(Et_8N_4Me_2)M(L)]$.

The toluene molecule of $[(Et_8N_4Me_2)Sm(PhMe)]$, (1), adopts a slipped geometry, with an angle of 20.33(1) ° between the plane of the toluene molecule and the *meso*- plane of the macrocycle, Figure 2-9. The toluene molecule lies on a mirror plane, giving four inequivalent Sm–C distances; 3.103(7), 3.493(4), 4.177(5) and 4.477(8) Å. The two shortest lengths are consistent with η^3- coordination to the samarium(II) centre, where the $\eta^3\text{-}PhMe_{centroid}$–Sm distance is 3.20_6 Å.

2.3.2.2 Molecular Structure of $[\{(Et_8N_4Me_2)Sm\}_2(C_7H_7)K]\cdot 2(PhMe)$, (2)

Complex (2) was obtained as a red crystalline precipitate from reaction of (**XXII**) with potassium metal in PhMe, Figure 2-10. The rod shaped crystal belongs to the monoclinic space group $P2_1/c$ (No. 14) $a = 23.622(8)$, $b = 11.860(6)$, $c = 29.033(8)$ Å, $\beta = 91.886(6)$ °, with four dinuclear complexes in the unit cell. The asymmetric unit consists of one dinuclear complex of (2) and two molecules of toluene. Block shaped crystals of an orthorhombic crystal system, $a = 23.586(5)$, $b = 43.641(6)$, $c = 28.466(4)$ Å, were also observed. The initial solution in P shows isostructural molecules of (2) exhibiting a similar molecular geometry with no lattice solvent. The correct spacegroup assignment

cannot be made due to poor refinement quality, and thus this data will not be discussed further. Complex (2) forms a linear polymer through η^2- and η^5- bridging interactions between the *exo* bound potassium cation and the N_{Py} rings of one macrocycle, Figure 2-10.

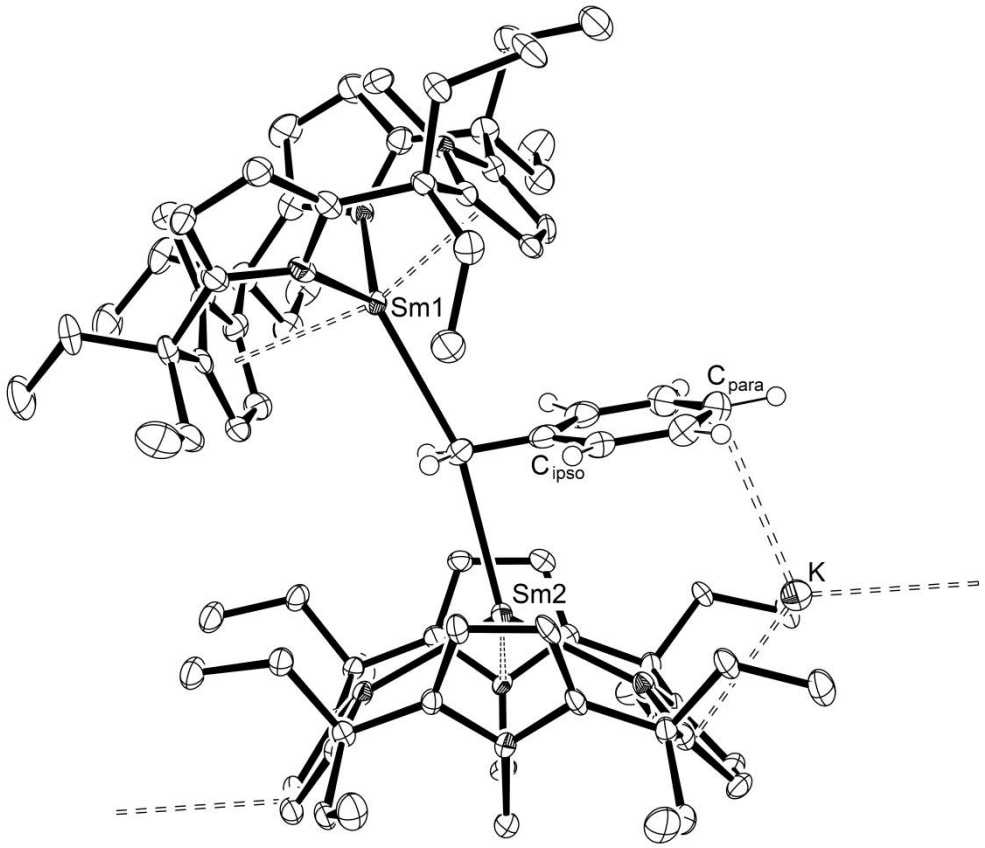

Figure 2-10 Molecular structure of (**2**) with thermal ellipsoids drawn at 50 % probability. Solvent molecules and macrocyclic protons omitted for clarity.

The molecular structure of (2) exhibits the standard η^1:η^5:η^1:η^5 macrocyclic binding mode. The Sm-(η^1-N_{Py}) distances are 2.534(4) and 2.543(4) Å for Sm1 and 2.619(4) and 2.589(4) Å for Sm2, with the latter being the distance to the nitrogen atom of the N_{Py} ring to which the potassium is bound *exo* at a distance of 2.83_5 Å to the N_{Py} centroid. The Sm-(η^5-N_{Me}) distances from the samarium centre to the N_{Me} ring centroids are 2.65_0 and 2.68_5, and 2.71_8 and 2.69_3 Å, respectively, with the samarium atoms sitting 1.297(2) and 1.393(2) Å above their respective *meso*-planes. The N_{Py}–*meso* interplanar angles are 51.29(16) and 56.54(14) ° for the potassium free macrocycle and 56.55(12) and 45.66(16) ° for the potassium coordinated macrocycle, with the latter N_{Py} plane significantly

deflected due to η^5- *exo*- coordination of the potassium cation. The N_{Me}−*meso* interplanar angles are 75.78(12) and 76.44(14), and 72.18(14) and 73.79(13) °, respectively. The dark red colour of the complex and the macrocycle geometries are consistent with the presence of Sm^{II} centres, Table 2-2. Further comparison between the molecular geometries of complexes (1), (2) and (**3**) is given below, Table 2-3, Section 2.3.2.3.

A molecule of toluene has been deprotonated at the methyl group to form a bridging benzyl unit with samarium contacts of 2.769(5) and 2.762(5) Å to the benzylic carbon for the top and bottom Sm^{II} atoms, respectively, Figure 2-10. The Sm−C_{ipso} distance shows significant variation (top 3.490(4), bottom 2.993(5) Å) due to the 'slip' angle of the benzyl unit relative to the *meso*-plane of each $(Et_8N_4Me_2)Sm$ unit (top 23.56(14), bottom 8.98(14) °). This angle cannot be expressed accurately because the benzyl plane is rotated in more than one axis relative to the defined *meso*-planes; thus, the angles reported are composite and only indicative of the true angle. Each of the seven benzyl protons was located in difference maps during structure refinement, indicating the site of deprotonation. Coordination of *exo*-bound cations to the macrocycle has previously been shown to occur η^5- to the pyrrolide face.[70] It is of interest that the potassium cation is not bound to the benzylic carbon, rather binding at a distance of 3.302(6) Å from the C_{para} atom and 3.542(6) Å from the nearer C_{meta} atom of the benzyl moiety, with a K− η^3- centroid distance of 3.44_6 Å. The coordination sphere of the potassium is completed by agostic interactions with *meso*- ethyl protons and the aforementioned η^2- and η^5- interactions to N_{Py} rings, Figure 2-10.

The C−C bond lengths of the benzyl moiety of complex (2) are consistent with the reported general trend of longer C_{Me}−C_{ipso} and C_{ipso}−C_{ortho} bonds and shorter C_{ortho}−C_{meta} and C_{meta}−C_{para} bonds,[127] Figure 2-11.

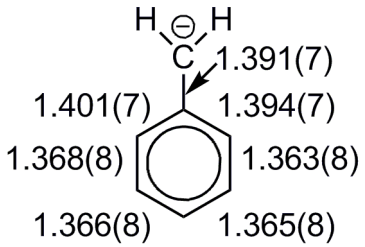

Figure 2-11 Bond lengths of the benzyl moiety of (**2**)

Toluene has previously been shown to bridge two copper centres in an η^2:η^2 fashion through C_{ortho}–C_{meta} and C_{para}–C_{meta} without deprotonation to benzyl functionality.[131] In 2007, Garcia *et al.* reported a molybdenum compound containing a bridging benzyl moiety (introduced *via* a pre-formed benzyl chloride) where asymmetric binding to two Mo atoms, with agostic interaction between one CH_2 proton and one Mo atom, is observed.[132]

2.3.2.3 Molecular Structure of $[\{(Et_8N_4Me_2)Sm\}_n]\cdot 0.875(C_6H_6)$, (3)

Crystals of (**3**) belong to the triclinic space group *P* (No. 2) a = 12.312(6), b = 25.211(7), c = 26.238(7) Å, α = 85.099(3), β = 81.513(3), γ = 77.014(9) °, with eight discrete molecules in the unit cell. The asymmetric unit consists of four units of $[(Et_8N_4Me_2)Sm]$ and three and a half molecules of benzene.

Four additional crystalline forms were obtained and show subtle variations in crystal packing whilst maintaining an overall structure similar to (**3**). A crystal belonging to the triclinic space group *P* (No. 2) a = 18.02(1), b = 24.907(2), c = 26.056(3) Å, α = 90.11(1), β = 92.85(2), γ = 90.81(2) °, with six molecules of $[(Et_8N_4Me_2)Sm]$ and four molecules of benzene in the asymmetric unit; a second crystal belonging to the triclinic space group *P* (No. 2) a = 18.588(5), b = 20.428(2), c = 28.276(4) Å, α = 90.578(8), β = 90.39(2), γ = 97.56(1) °, with six molecules of $[(Et_8N_4Me_2)Sm]$ in the asymmetric unit; a third crystal belonging to the monoclinic space group $P2_1/n$ (No. 14), a = 12.34(2), b = 24.409(6), c = 23.857(5) Å, β = 99.94(3) °, with two molecules of $[(Et_8N_4Me_2)Sm]$ in the asymmetric unit; and a fourth crystal belonging to the triclinic space group *P* (No. 2)

a = 23.595(4), b = 25.590(1), c = 26.371(1) Å, α = 97.030(5), β = 110.007(8), γ = 93.404(5) °, with eight molecules of [($Et_8N_4Me_2$)Sm] and two molecules of benzene in the asymmetric unit. Discussion will generally be restricted to the molecular structure of the first unit cell presented due to data and refinement quality.

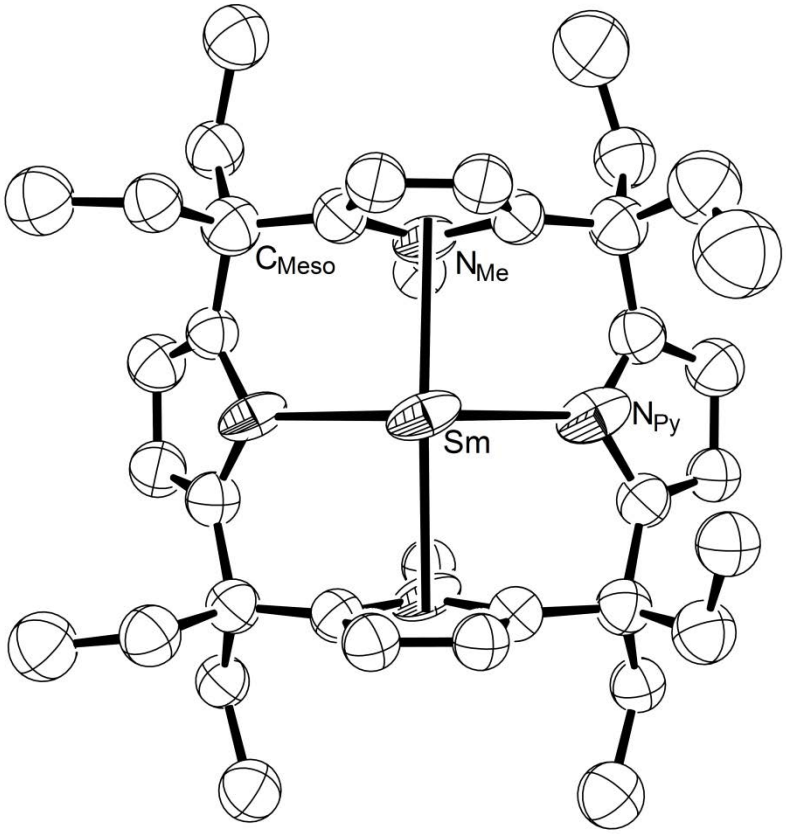

Figure 2-12 Molecular structure of (**3**) with thermal ellipsoids drawn at 50 % probability. Protons omitted for clarity. One of four molecules in the asymmetric unit.

The molecular structure of (**3**) exhibits the standard η^1:η^5:η^1:η^5 macrocyclic binding mode, Figure 2-12. The Sm-(η^1-N_{Py}) distances range from 2.48(3) to 2.633(15) Å and the Sm-(η^5-N_{Me}) distances range from 2.69_1 to 2.73_7 Å. The Sm−*meso* distances range between 1.27(1) and 1.366(8) Å. The N_{Py}–*meso* interplanar angles are clearly differentiated by coordination of a neighbouring samarium centre to the protons attached to the β-carbon at distances between 3.040(19) and 3.05(2) Å to the β-carbon, Figure 2-13.

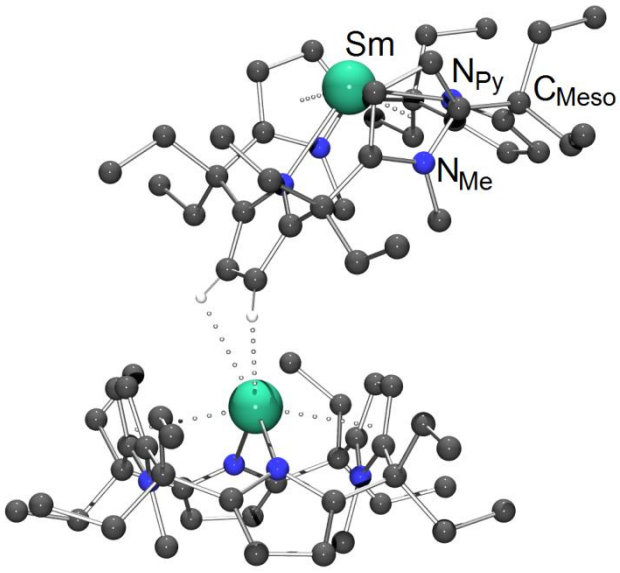

Figure 2-13 A portion of the extended structure of (**3**) illustrating a single example of the η^2- coordination of a samarium centre to the protons of a *β*-carbon of an adjacent N_{Py} ring.

Where intermolecular interactions through two Sm···H contacts occurs, the N_{Py}–*meso* interplanar angles range between 35.8(6) and 48.9(6) °; in the absence of this coordination, the N_{Py}–*meso* interplanar angles range from 52.4(4) to 75.7(6) °. The N_{Me}–*meso* interplanar angles consistently range from 74.29(0.50) to 78.32(0.54) °.

Aggregation of $[(Et_8N_4Me_2)Sm]$ units occurs between the samarium centre and the two protons of the *β*-carbons of a N_{Py} of an adjacent macrocycle, Figure 2-13. The Sm···H contacts range in length from 2.63_6 to 2.87_9 Å, with an average of 2.7_3 Å. Figure 2-14 shows the one-dimensional polymer of (**3**) is pseudo helical.

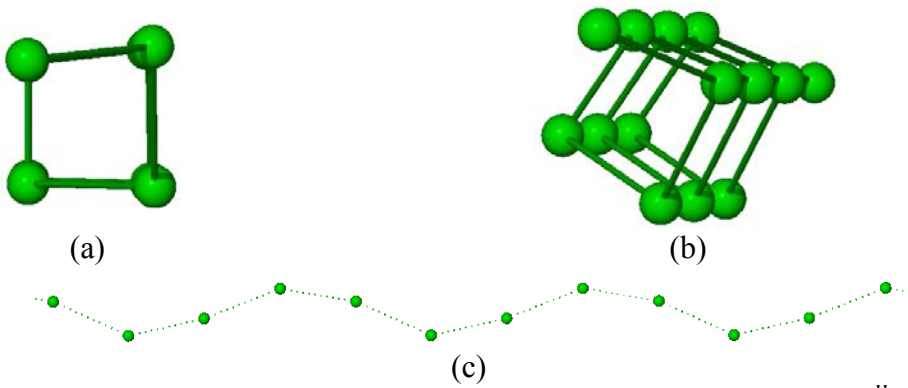

Figure 2-14 Two dimensional polymer network of (**3**) showing only the Sm^{II} atoms of six unit cells (a) end on, (b) staggered and (c) side on.

Comparison between the molecular geometry of (**3**) and the toluene adduct, (1), potassium benzyl included, (2) and known Sm^{III} methyl complex, (**XX**) reveals that the range of macrocycle geometries for the four macrocyclic units of (**3**) are consistent with Sm^{II} centres and similar to the toluene adduct, (1). The macrocyclic geometries of complex (2) are also shown to be consistent with two Sm^{II} centres, Table 2-3.

	M = Sm^{II} n = n L = - (**3**)	M = Sm^{II} n = $^1/_2$ L = $(C_7H_7)K$ (**2**)	M = Sm^{II} n = 1 L = PhMe (**1**)	M = Sm^{III} n = 1 L = Me[75] (**XX**)
M−(η^1-N_{Py})	2.48(3)-2.63(1)	2.543(4), 2.534(4) 2.619(4), 2.589(4)	2.5324(4)	2.478(3)
M−(η^5-N_{Me})	2.69_1-2.73_7	2.68_5, 2.65_0 2.69_3, 2.71_8	2.65_0, 2.66_7	2.59_3, 2.60_9
M−$L_{donor\ atom}$	2.63_6 - 2.87_9 Sm···H contacts	2.769(5) 2.761(5)	3.20_6 (as the η^3-$_{centroid}$)	2.424(5)
M−*meso*	1.27(1)-1.366(8)	1.297(4) 1.393(2)	1.3097(3)	1.14_9
N_{Py}−*meso*	35.8(5)-55.7(4)	51.29(16), 56.54(14) 56.55(12), 45.66(16)	53.67(1)	50.1_5
N_{Me}−*meso*	74.3(5)-78.3(5)	75.78(12), 76.44(14) 72.18(14), 73.79(13)	75.71(1), 83.25(1)	78.8_1, 80.5_7
Metallocene bend	159.5_4 -160.2_3	161.9_0 157.0_1	161.5_1	168.8_6

Table 2-3 Selected bond lengths (Å) and angles (°) for $[\{(Et_8N_4Me_2)M(L)\}_n]$.

Aggregation interactions between molecules of (**3**) *via* samarium and the *β*-carbon of a N_{Py} of a neighbouring macrocycle is consistently observed for each of the five molecular structures corresponding to the five reported unit cells, Figure 2-15, with one exception; the crystal belonging to the triclinic space group $P\bar{1}$ (No. 2) a = 18.588(5), b = 20.428(2), c = 28.276(4) Å, α = 90.578(8), β = 90.39(2), γ = 97.56(1) °, with six molecules of $[(Et_8N_4Me_2)Sm]$ in the asymmetric unit, shows an interaction between a samarium centre and the terminal protons of one *meso*-ethyl group at 2.67_5, 2.83_5 and 3.14_7 Å, respectively, Figure 2-15. This significantly shorter interaction is only observed once between only two molecules of the five crystallographically independent forms of (**3**) and indicates the

routinely observed Sm···H interaction to the *β*-protons of the N_{Py} ring are simply a weak aggregation due to the unsaturated coordination sphere of the metal, rather than a genuine, strong, π-bonding interaction.

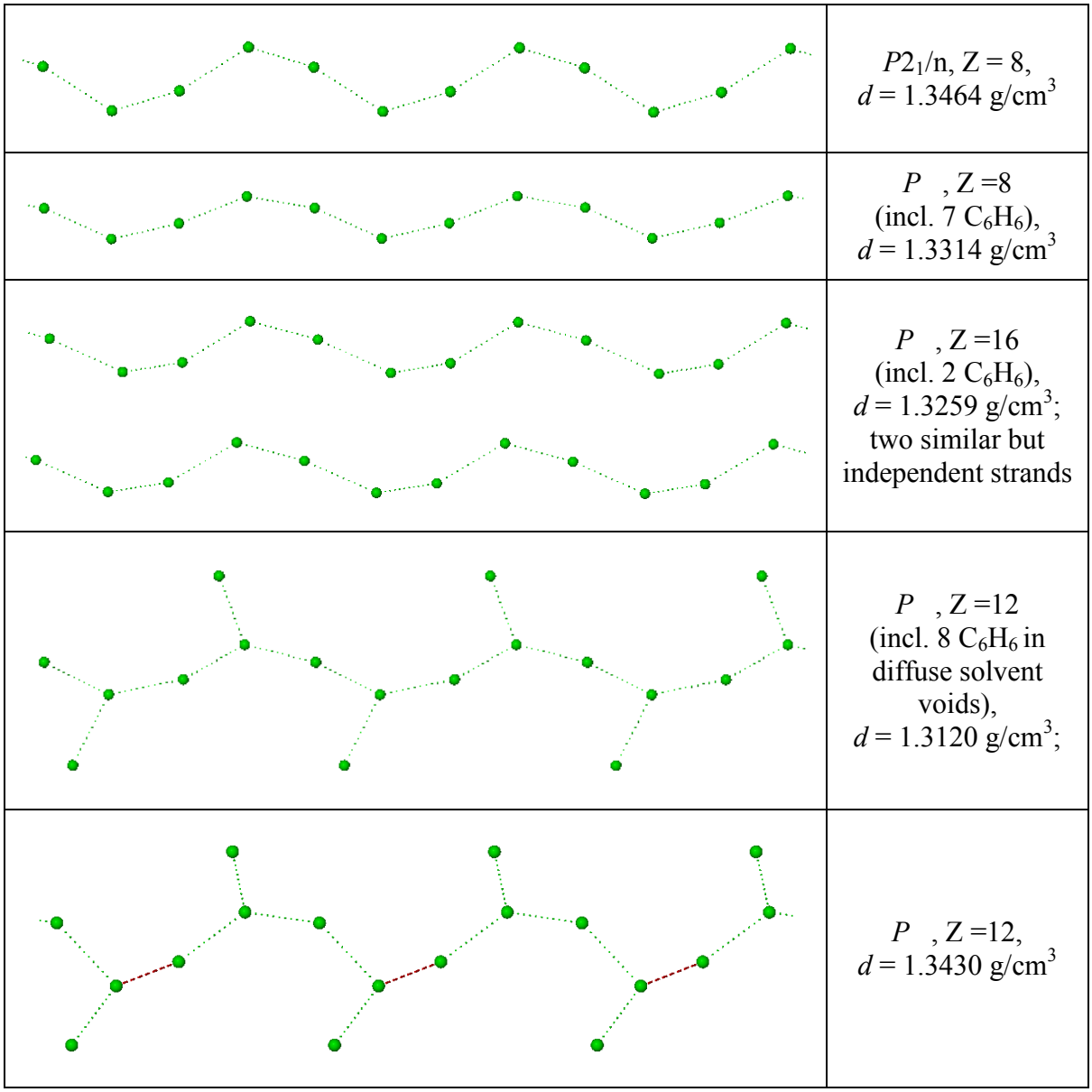

Figure 2-15 Representations of the 1D polymeric structures of the various polymorphs of [{($Et_8N_4Me_2$)Sm}$_n$], (**3**), in the solid state (and benzene solvates). Green spheres represent Sm centres, green and red bonds the Sm···Sm separations based on weak CH (β-pyrrolyl, 7.05_2 – 7.69_7 Å) and CH (methyl, 8.33_9 Å) interactions, respectively, viewed onto the chains. All complexes feature a head-to-tail association along the chains and similar 4-turn helical chains that stem from approximate alignment of the two-fold Sm−CH (β-pyrrolyl) interaction with the binding groove of the adjacent molecule. Branch points represent a chain molecule involving a second β-pyrrolyl unit bound to a Sm centre of a single side-chain molecule.

2.3.2.4 Molecular Structure of [{($Et_8N_4Me_2$)SmOK}$_2$], (4)

Complex (**4**) was obtained in low yield as a pale orange crystalline precipitate along with the Sm^{II} complexes (1) and (**3**) from several reactions between (**XXII**) and potassium metal in both C_6H_6 and PhMe. Samples of the pale orange plates were isolated and found to be suitable for X-ray crystal structure determination, Figure 2-16.

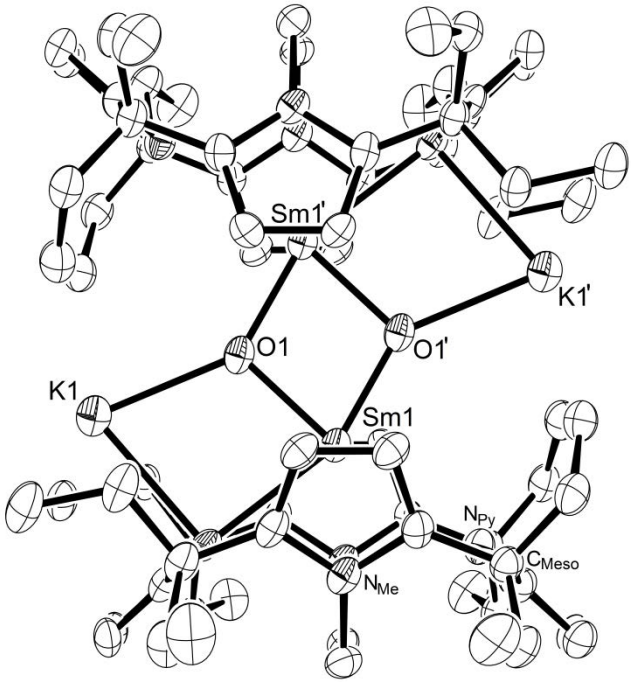

Figure 2-16 Molecular structure of (**4**) with thermal ellipsoids drawn at 50 % probability. Protons omitted and samarium, oxygen and potassium labelled for clarity.

The crystal belongs to the monoclinic space group *C*2/*c* (No. 15) a = 20.3945(15), b = 13.939(5), c = 26.3981(17) Å, β = 112.106(14) °, with four molecules in the unit cell. The asymmetric unit consists of one half molecule of dimeric (**4**), with molecules residing on inversion centres.

The molecular structure of (**4**) exhibits the standard η^1:η^5:η^1:η^5 macrocyclic binding mode. The Sm-(η^1-N_{Py}) distances are 2.911(3) and 2.716(4) Å. The Sm-(η^5-N_{Me}) distances are 2.81_4 and 2.86_3 Å, with a Sm−*meso* distance of 1.82(2) Å. The N_{Py}−*meso* interplanar angles are 42.77(14) and 43.20(13) °, whilst the N_{Me}−*meso* interplanar angles

are 77.43(13) and 75.28(15), respectively. The molecular geometry of the Sm^{III} species, (**4**), is compared with $[(Et_8N_4Me_2)Sm^{II}(THF)_2]$, (**XVI**), and $[(Et_8N_4Me_2)Sm^{III}Me]$, (**XX**), Table 2-4.

	$M = Sm^{III}$, n = 2 L = OK (**4**)	$M = Sm^{II}$, n = 1 $L = (THF)_2$ (**XVI**)	$M = Sm^{III}$, n = 1 L = Me[75] (**XX**)
$M-(\eta^1-N_{Py})$	2.716(4), 2.911(3)	2.667(2)	2.478(3)
$M-(\eta^5-N_{Me})$	2.81_4, 2.86_3	2.75_5	2.59_3, 2.60_9
$M-L_{donor\ atom}$	2.146(3)	2.6552(14)	2.424(5)
M–*meso*	1.82(2)	1.4794(17)	1.14_9
N_{Py}–*meso*	42.77(14), 43.20(13)	49.92(7)	50.1_5
N_{Me}–*meso*	77.43(13), 75.28(15)	73.24(7)	78.8_1, 80.5_7
Metallocene bend	141.3_3	154.4_4	168.8_6

Table 2-4 Selected bond lengths (Å) and angles (°) for $[\{(Et_8N_4Me_2)M(L)\}_n]$.

The molecular geometry of (**4**) is significantly affected by the presence of two O^{2-} ligands, causing the oxophilic Sm^{III} centre to rise significantly above the *meso*- plane of the macrocycle to bind closely to the oxygen centre, Table 2-4. The resulting molecular geometry metrics are significantly different from the known $Sm^{III}Me$ species, (**XX**) and in some cases more closely resemble the bis(THF) adduct, (**XVI**). Inspection of the space filling representation of (**4**) reveals that there is significant interaction between the protons of the *β*-carbons of the N_{Me} rings of each macrocycle, Figure 2-17. The extraordinarily large Sm^{III}–*meso* distance indicates that these inter-macrocyclic interactions are maximised.

The Sm1−O1 distance is 2.146(3), shorter than the Sm1−O1′ distance of 2.196(3) Å, and the oxygen atoms are separated by 2.688(6) Å. The samarium atoms are separated by 3.4102(5) Å, consistent with no significant Sm···Sm interaction. The samarium centre is

displaced from the centre of the macrocycle (approximate C_{2v} axis), as defined by the two nitrogen and two carbon atoms of the *N*Me fragments, by 0.135(8) Å towards the N_{Py}–K interaction. This displacement is a result of the strong Sm−O interaction.

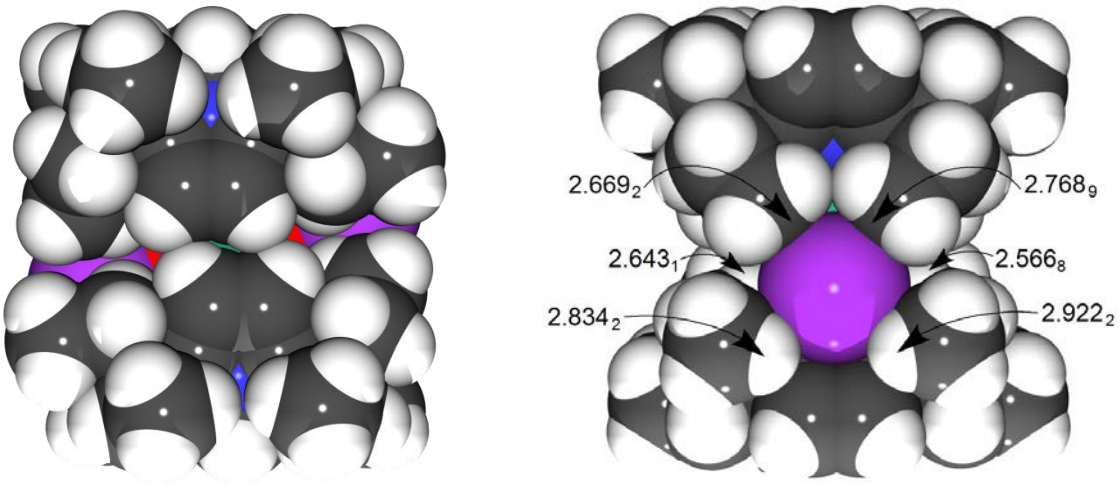

Figure 2-17 Space filling representations of (**4**) showing:
(a) significant macrocycle−macrocycle interaction;
(b) the six nearest $H_{agostic}$ interactions (Å).
Where the arrow points to carbon, the unseen hydrogen is intended.

The potassium cation engages the nitrogen atom of the N_{Py} ring in an η^1- interaction, with a N–K bond length of 2.839(3) Å, and is bound to an oxygen atom with an O − K distance of 2.616(3) Å. Inspection of the crystal packing structure reveals a weaker interaction with the *β*-hydrogens of the N_{Py} ring (that shows no other coordination of potassium) of a neighbouring molecule, Sm···H is 3.44_1, 3.44_4 Å. In addition, each potassium atom is enshrouded by *meso*- ethyl groups, with two ethyl groups of the macrocycle adopting an unusual arrangement in pointing up relative to the *meso*- plane, rather than away from it (Figure 2-16, *cf.* Figure 2-10), to accomplish the encapsulation. Significant agostic interactions are observed between *meso*- ethyl groups and the potassium centre, ranging from 2.566_8 to 2.922_2 Å, Figure 2-17.

2.3.2.5 Molecular Structure of [{($Et_8N_4Me_2$)Sm(*t*-BuDAB)(K)}$_n$], (5)

Crystals of (**5**) , Figure 2-18, belong to the orthorhombic space group *Pnma* (No. 62), a = 23.940(3), b = 17.374(2), c = 10.9210(18) Å, with four molecules in the unit cell. Due to a crystallographic mirror plane, the asymmetric unit consists of half a unit of the linear polymer [{($Et_8N_4Me_2$)Sm(*t*-BuDAB)(K)}$_n$]. The *t*-BuDAB moiety is partially disordered across the mirror plane and adopts a distinctly non-planar overall geometry, with the N−C−C−N plane lying at an angle to the ancillary ligand binding groove of the macrocycle, Figure 2-19.

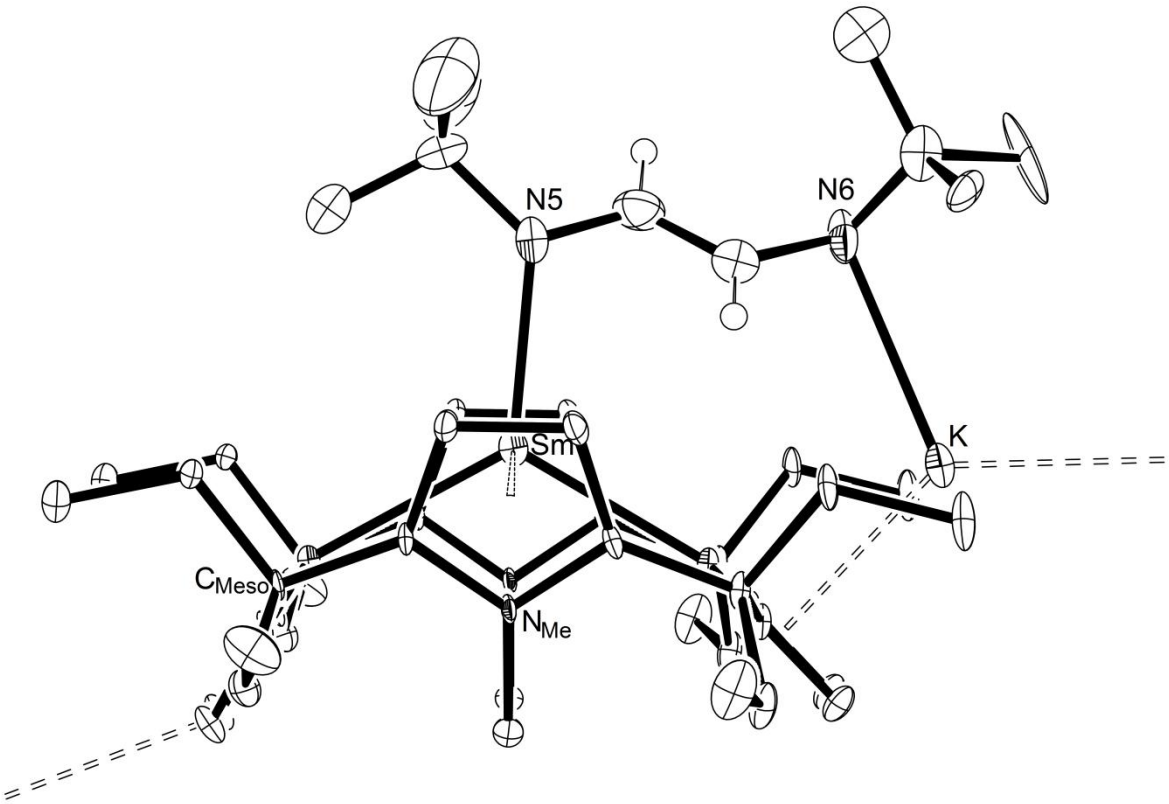

Figure 2-18 Molecular structure of (**5**) with thermal ellipsoids drawn at 50 % probability. Protons (excluding *t*-BuDAB chain protons) omitted for clarity.

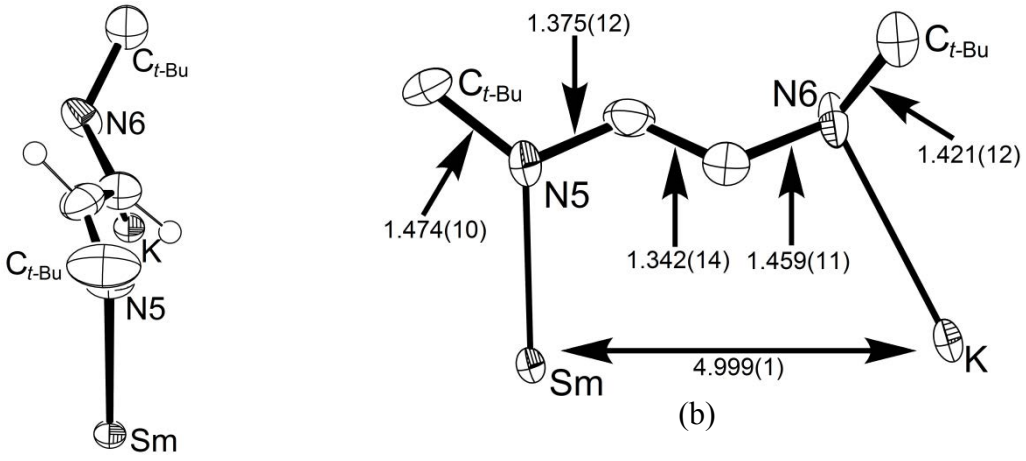

Figure 2-19 (a) Abbreviated view along the *t*-BuDAB moiety of (**5**)
(b) Selected bond lengths (Å) and errors of the *t*-BuDAB moiety of (**5**).

The molecular structure of (**5**) exhibits the standard η^1:η^5:η^1:η^5 macrocyclic binding mode. The molecule is polymeric, with the potassium atom bridging adjacent macrocycles through intramolecular η^5- (2.765(3) Å to the centroid of the N_{Py} ring) and intermolecular η^2- interactions (3.10_9 Å to the centroid of the N_{Py} β-carbons) of the N_{Py} moieties. At 2.646(5) and 2.722(5) Å, the Sm-(η^1-N_{Py}) distances show marked disparity due to asymmetric K coordination, with the former the Sm−N_{Py} distance for the N_{Py} ring η^5-coordinated to potassium, and the latter for the N_{Py} ring η^2- coordinated to potassium. The Sm-(η^5-N_{Me}) distance is 2.75_5 Å. The Sm−*meso* distance is 1.470(3) Å. The N_{Py}−*meso* interplanar angle for the N_{Py} ring bound η^5- to the potassium is 46.3(2) °, and for the η^2-bound N_{Py} ring is 60.38(16) °. The N_{Me}−*meso* angle is 74.85(13) °. These metrics are consistent with a formally Sm^{II} centre, however the redox active *t*-BuDAB ligand necessitated further investigation of the electronic structure of (**5**) *via* DFT analysis, Section 2.3.3.1.

The nitrogen donors of the *t*-BuDAB ligand are bound in η^1- fashion to both the samarium and potassium centres at 2.436(7) and 2.962(10) Å, respectively. The C−C and C−N bond lengths within the *t*-BuDAB moiety are consistent with partial delocalisation of

one electron over the ligand; this appears to be interrupted by strain in binding both metals, buckling the bridging ligand in coordinating both metal centres within their limited positional restrictions *endo*- and *exo*- to the macrocycle, Figure 2-19. The sum of bond angles around N5 indicate near planar geometry ($\Sigma = 357.3_5$ °), while N6 is pyramidal ($\Sigma = 322.2_8$ °). Density functional theory has been employed to ratify the conclusion drawn from these bond lengths and angles (and the Sm−macrocycle geometrical features); the samarium is present in the +2 oxidation state, the *t*-BuDAB moiety is present as a delocalised radical anion and the potassium centre is cationic, Section 2.3.3.1.

2.3.3 Introduction to DFT Analysis

Theoretical studies were undertaken to further investigate the electronic structure of [($Et_8N_4Me_2$)Sm(*t*-BuDAB)(K)], (**5**). The X-ray crystal structure refinement model was simplified (using GaussView[133] default settings for adding valence) at the *meso*- positions of the porphyrinogen (Et → H) and the *N*-methyl pyrrole (*N*Me → *N*H), as well as both *t*-Bu groups on the *t*-BuDAB moiety being simplified to Me groups (*Nt*-Bu → *N*Me). These groups are synthetically necessary, however it is assumed that they do not play a significant electronic role in the complex; their removal saves significant computational resources without sacrificing accuracy with regard to the analysis of the metals and contentious ligand fragments. This is particularly valid in this case, where geometry optimisations were not undertaken, and thus the steric influences of these groups are not crucial to the calculation. No attempt to optimise the geometry of the structure was undertaken to allow for direct analysis of the X-ray crystal structure geometry. Calculations were performed using Density Functional Theory with the B3LYP hybrid functional. The 6-31G(d) basis set[134-137] was applied to carbon, nitrogen, hydrogen and

potassium, whilst the Stuttgart RSC 1997 ECP[138-140] was applied to samarium. Where energy comparisons are made, they are comparisons of uncorrected SCF energies.

Calculations were performed to determine the Mulliken atomic spin density and Mulliken atomic charge distribution within the molecule. Atomic spin density correlates to unpaired electron population, allowing the assignment of five or six unpaired f- electrons of samarium(III) or samarium(II), respectively, and required to account for the additional electron provided by potassium as it oxidises to the cation. Energy comparisons are required to determine if the pairing energy (the energy barrier to placing a second electron in an already occupied orbital) is larger or smaller than the difference in energy between non-degenerate f- orbitals.

2.3.3.1 Theoretical Investigation of [($Et_8N_4Me_2$)Sm(*t*-BuDAB)(K)], (5)

Investigation of the calculated charge and spin density of (**5**) is necessary due to the unusual geometry observed in the *t*-BuDAB ligand in the complex and the difficulty in obtaining a pure product that limited the feasibility of further analyses. Due to the variable reduction states of *t*-BuDAB that can be adopted,[121] there are two likely formulations of (**5**); samarium assumes either +2 or +3 oxidation state, requiring the *t*-BuDAB fragment to adopt either a radical anionic or dianionic state (assuming cationic potassium).

Consideration of the formation of [($Et_8N_4Me_2$)Sm(*t*-BuDAB)(K)] reveals that the combination of unpaired electrons from samarium and potassium can occur in the molecular orbitals of the resulting complex in two possible ways; spin aligned or spin coupled, Figure 2-20. Additionally, if the spin coupled state is preferred, the coupled electrons may occupy a ligand (Sm^{III}) or metal (Sm^{II}) orbital, dictating the oxidation state of the samarium centre.

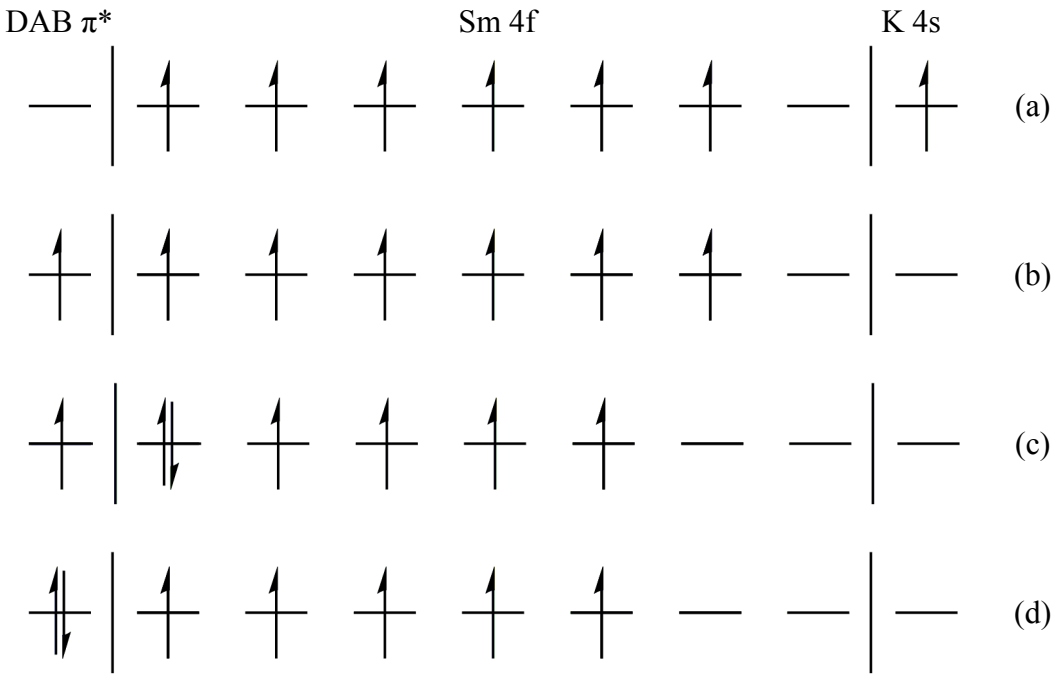

Figure 2-20 The molecular orbitals of [($Et_8N_4Me_2$)Sm(*t*-BuDAB)(K)], (**5**), showing the initial state prior to formation of (**5**), (a), and the three possible states upon formation of (**5**); Sm^{II} spin aligned, (b), Sm^{II} spin coupled, (c), and Sm^{III} spin coupled, (d).

Computational investigation revealed that the most stable state of [($Et_8N_4Me_2$)Sm(*t*-BuDAB)(K)], (**5**), is a paired state, (c), or (d), Figure 2-20. The energy difference between the two electronic states is 5.87 $kJmol^{-1}$, which is a sufficiently small energy barrier that both states are energetically realistic.

In calculations of both the seven- and five- unpaired electron structures, the spin density on the samarium centre is six (6.02 and 5.95, respectively), indicating that the samarium is present as samarium(II) and the *t*-BuDAB moiety is present as a radical anion, as per (c), Figure 2-20.

Figure 2-21 shows the unpaired electron population and atomic charge of the more stable five unpaired electron structure by individual atom. Figure 2-21b clearly shows that the nitrogen atoms of the *t*-BuDAB moiety bear the charge of the ligand whilst Figure 2-21a indicates that the unpaired electron is distributed across the ligand.

Figure 2-21 (a) Mulliken atomic spin density, and
(b) Mulliken atomic charge with hydrogens summed into heavy atoms for [{($Et_8N_4Me_2$)Sm(*t*-BuDAB)(K)}$_n$], (**5**).

2.3.4 End-on Binding of N_2 to a Samarium Complex

The successful isolation of the unsolvated samarium(II) complex (**3**) allowed investigation of the reactivity of [($Et_8N_4Me_2$)Sm] with a range of reagents that have previously shown no reactivity with the solvated analogue, [($Et_8N_4Me_2$)Sm(THF)$_2$], (**XVI**). This investigation is supported by the reasonable hypothesis that an unsolvated species will be more reactive than the solvated analogue; there is no competition with THF for coordination at the oxophilic Sm^{II} for an unsolvated species, allowing for coordination of other species, Section 2.1.1.

Satisfactory elemental analysis of (**3**) was obtained at the end of the candidature; prior to this, a pure sample of (**3**) could not be reproducibly isolated from the reaction between [{($Et_8N_4Me_2$)Sm}$_2$(*t*-BuDAB)], (**XXII**), and potassium metal in benzene, Equation 2-11, owing to the formation of low yielding by-products (**4**), (**5**) and (**6**) and the presumed high reactivity of (**3**), including potential decomposition to (**4**). However, crude reaction mixtures from the reaction of (**XXII**) and potassium in benzene were filtered to remove the orange precipitate and the resulting red solution exposed to a range of reagents. No reaction was observed between this solution and naphthalene, anthracene or *cis*-stilbene by ^{1}H NMR spectroscopy. Decamethylsamarocene, (**V**), has been shown to react with *cis*- and *trans*- stilbene and anthracene.[77, 141]

Allowing a filtered red benzene solution obtained *via* Equation 2-11 to sit, uncapped, overnight in a N_2 filled glovebox resulted in red crystals growing on the walls of the sample vial above the remaining solution. X-ray crystal structure determination revealed that the highly soluble unsolvated species had reacted with ambient pressure N_2 to form the first end-on dinitrogen complex of a lanthanoid metal, $[\{(Et_8N_4Me_2)Sm\}_2(\mu\text{-}\eta^1\text{:}\eta^1\text{-}N_2)]$, (**7**), Equation 2-14. The synthesis of (**7**) occurred very late in candidature and is difficult to isolate, leading to characterisation data limited to X-ray crystallography. Raman spectroscopic analysis has proved inconclusive at the time of writing. The red colour is consistent with the presence of Sm^{II}.

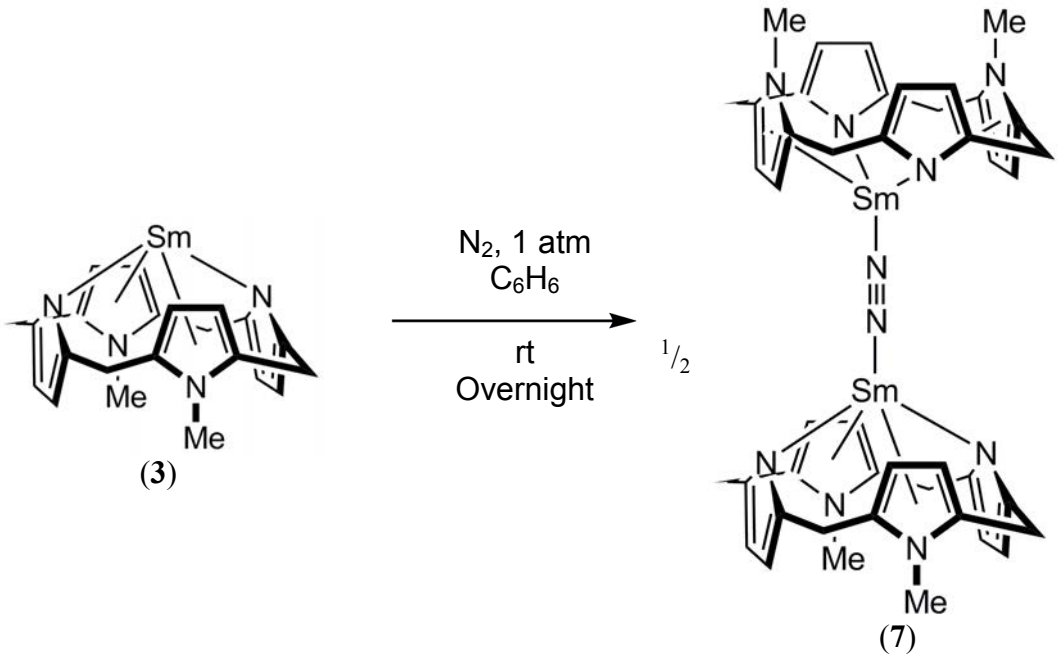

Equation 2-14

Throughout this thesis, serendipitous isolation of the oxo-bridged complex of the samarium macrocycle, $[\{(Et_8N_4Me_2)Sm\}_2(\mu\text{-}O)]$, (**8**), Figure 2-22, was noted in low yield as a by-product, presumably arising due to unintentional exposure of reaction mixtures to small amounts of O_2. The formation of complex (**8**) is thus analogous to reports of oxo-bridged complexes both by Evans[87] for the decamethylsamarocene system and Gambarotta[107] for the unsubstituted tetrapyrrolic macrocycle system. Complex (**8**) is

presented here as evidence to support the X-ray structure refinement of (**7**) by ruling out the most likely alternative interpretation of (**7**) as a $(\mu\text{-}\eta^1\text{:}\eta^1\text{-}O_2)^{2-}$ product from reaction with O_2. Indeed, only $(\mu\text{-}\eta^2\text{:}\eta^2\text{-}O_2)^{2-}$ side-on peroxo complexes of La, Pr, Sm, Eu and Lu by Bradley *et al*. in 1977[142] and Yb by Niemeyer[143] in 2002 are known. The dark red colour of (**7**) and DFT analysis of the molecular structure are consistent with a Sm^{II} species.

Section 2.1.2 discussed at length the ubiquity of side-on binding of dinitrogen to lanthanoid elements; those few cases where other binding modes are observed occur in addition to side-on coordination. The end-on coordination of bridging dinitrogen in the case of (**7**) is rationalised on steric grounds. Our group has previously reported the X-ray crystal structure of $[\{(Et_8N_4Me_2)SmCl\}_2]$ (**XVII**), Section 1.7).[71] Figure 2-22 shows that parallel alignment of the binding grooves in the case of $[\{(Et_8N_4Me_2)SmCl\}_2]$, (**XVII**), approaches the limit of steric possibility with these chloride ligands, with a *meso*···*meso* separation of 7.24_2 Å, *c.f.* 7.05_0 Å for the aligned binding grooves of $[\{(Et_8N_4Me_2)SmOK\}_2]$, (**4**), and 6.59_4 Å for the docked binding grooves of $[\{(Et_8N_4Me_2)Sm\}_2(\mu\text{-}O)]$, (**8**). Presumably, in the case of the smaller N_2 ligand, an analogous planar, non-linear Sm_2N_2 core (side on $\mu^2\text{-}N_2$) is not feasible due to increased interactions between macrocycles *via* the protons of the β-carbons of the N_{Me} rings, as reported for (**4**), Section 2.3.2.4. The weaker Sm···N interaction for (**7**) could not withdraw the Sm centre from the macrocycle analogously to the strong Sm··· O interaction with the O^{2-} ligand of (**4**). If elongated Sm−N distances were forced upon this side-on arrangement, the electronic saturation of each metal would be minimal at the distances allowed by the *β*-protons of the *N*Me rings. A 90 ° twist of one macrocycle, as is the case for the mono-atomic oxo- complex, (**8**) Figure 2-22, to allow closer docking of the macrocycles (with a Sm···Sm separation in (**8**) of 2.0699(7) Å) is not possible for a di-

atomic ligand as this would necessitate alignment of the N_2 unit perpendicularly across one of the two binding grooves of the macrocycles, Section 1.7. The only viable binding geometry for N_2 is thus end-on coordination with a Sm···Sm separation greatly increased to 6.25_9 Å, as observed in Figure 2-23.

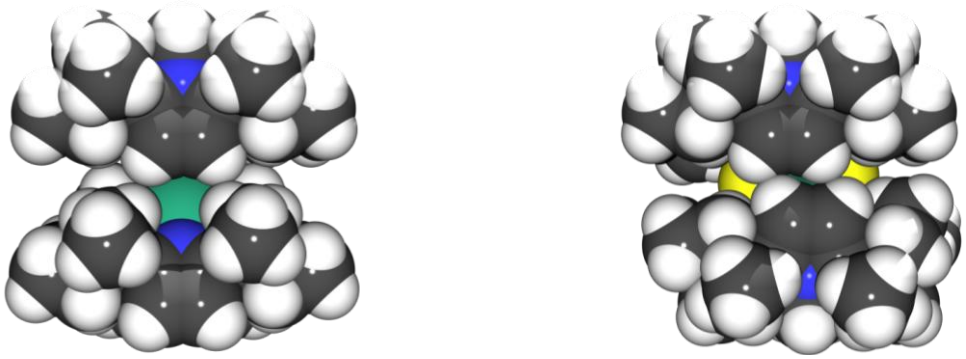

(8) **(XVII)**

Figure 2-22 Space filling representations of $[\{(Et_8N_4Me_2)Sm\}_2(\mu\text{-}O)]$, (**8**), and known complex $[\{(Et_8N_4Me_2)SmCl\}_2]$, (**XVII**), viewed onto the Sm_2Cl_2 core.

At 1.189(11) Å, the N−N bond length of the bound dinitrogen ligand is longer than the bond length in free dinitrogen, 1.0945 Å,[33] and the analogous N−N bond length in the side-on dinitrogen complex of decamethylsamarocene, $[\{(C_5Me_5)_2Sm\}_2(\mu\text{-}\eta^2\text{:}\eta^2\text{-}N_2)]$, (**VI**), 1.088(12) Å, Figure 2-23. Analogously to (**8**), the $(C_5Me_5)^-$ rings of (**VI**) dock together, resulting in a Sm···Sm separation of 4.58_8 Å for (**VI**).

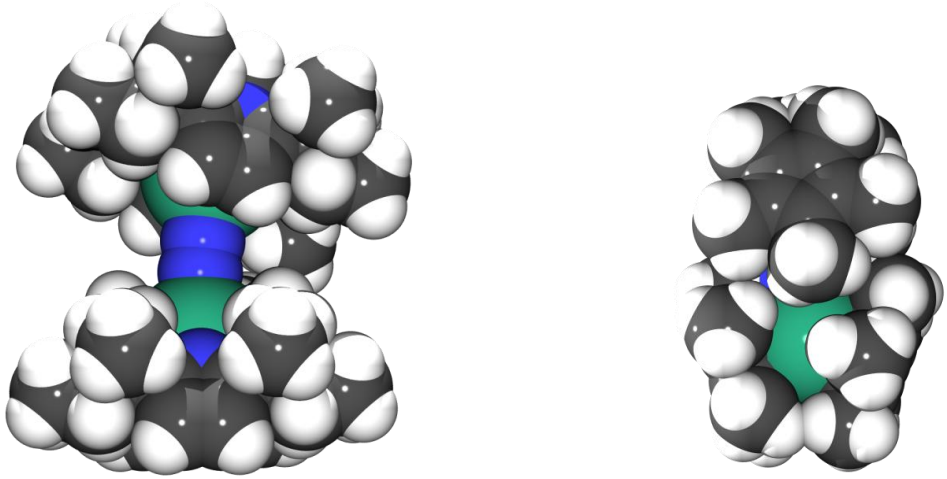

(7) **(VI)**

Figure 2-23 Space filling representations of $[\{(Et_8N_4Me_2)Sm\}_2(\mu\text{-}\eta^1\text{:}\eta^1\text{-}N_2)]$, (**7**), and $[(C_5Me_5)_2Sm\}_2(\mu\text{-}\eta^2\text{:}\eta^2\text{-}N_2)]$, (**VI**).

2.3.4.1 Molecular Structure of [{($Et_8N_4Me_2$)Sm}$_2$(μ-η^1:η^1-N_2)], (7)

Complex (**7**) was obtained as a pale red crystalline precipitate after overnight standing under a nitrogen atmosphere of a filtered solution obtained from the reaction between (**XXII**) and potassium metal, in C_6H_6. Crystals were observed to have formed on the walls of the sample vial above the remaining solution, in contrast to complexes (**3**), (**5**) and (**6**), which are very soluble and crystallise as a crust after near complete evaporation of the solution. The crystals were found to be suitable for X-ray crystal structure determination, Figure 2-24.

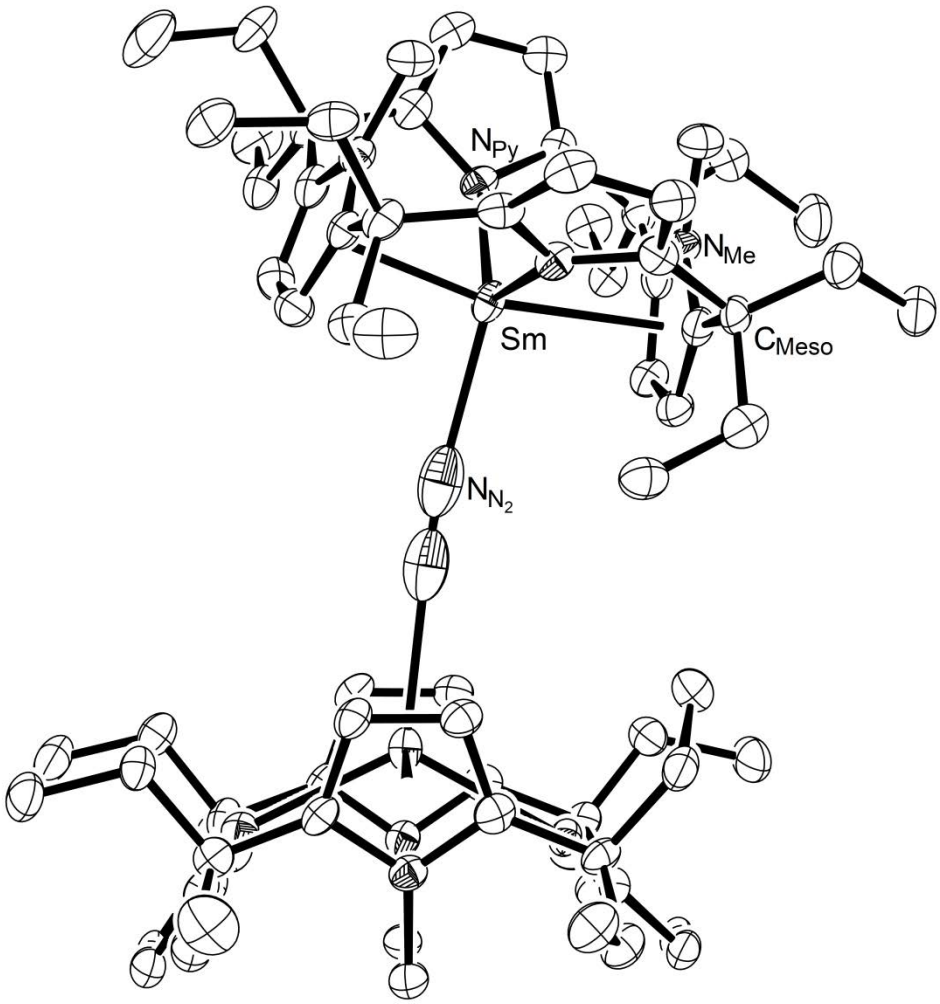

Figure 2-24 Molecular structure of (**7**) with thermal ellipsoids drawn at 50 % probability. Protons omitted for clarity.

Crystals of (**7**) belong to the monoclinic space group *C*2/*c* (No. 15) a = 29.339(6), b = 13.936(3), c = 17.864(5) Å, β = 105.246(12) °, with four molecules in the unit cell. The asymmetric unit consists of one half of the $[\{(Et_8N_4Me_2)Sm\}_2(\mu\text{-}\eta^1\text{:}\eta^1\text{-}N_2)]$ dimer with molecules residing on C_2 axes.

The molecular structure of (**7**) exhibits the standard $\eta^1\text{:}\eta^5\text{:}\eta^1\text{:}\eta^5$ macrocyclic binding mode. The Sm-(η^1-N_{Py}) distances are 2.525(4) and 2.509(4) Å and the Sm-(η^5-N_{Me}) distances are 2.63_2 and 2.61_5 Å. The Sm−*meso* distance is 1.218(2) Å. The Sm−N_2 distance is 2.547(6) Å and the N−N bond length of the bound dinitrogen ligand is 1.189(11) Å. The N_{Py}–*meso* interplanar angles are 55.50(14) and 42.81(15) °, whilst the N_{Me}–*meso* interplanar angles are 79.94(11) and 79.41(11). Table 2-5 compares the molecular geometry metrics of (**7**) with the unsolvated Sm^{II} species, (**3**), a 1:1 Sm^{II} nitrile adduct, (complex (**12**), Chapter 3), and a 1:1 Sm^{III} amide, (**XXXV**).

	M = Sm^{II} n = 2 L = N_2 (**7**)	M = Sm^{II} n = n L = - (**3**)	M = Sm^{II} n = 1 L = NC*t*-Bu (**12**)	M = Sm^{III} n = 1 L = $N(SiMe_3)_2$[71] (**XXXV**)
M−(η^1-N_{Py})	2.525(4), 2.509(4)	2.48(3)-2.63(1)	2.550(6) - 2.579(5)	2.51_3 – 2.60_4
M−(η^5-N_{Me})	2.63_2, 2.61_5	2.69_1-2.73_7	2.67_1 - 2.69_9	2.64_5 – 2.66_8
M−$L_{donor\ atom}$	2.547(6)	2.63_6 - 2.87_9 Sm··· H contacts	2.609(6), 2.612(7)	2.30_7 – 2.31_4
M−*meso*	1.218(2)	1.27(1)-1.366(8)	1.282(3), 1.289(3)	1.34_1 – 1.36_8
N_{Py}–*meso*	42.81(15), 55.50(14)	35.8(5)-55.7(4)	44.33(12) – 52.7(2)	n/a
N_{Me}–*meso*	79.94(11), 79.41(11)	74.3(5)-78.3(5)	76.4(2) – 79.2(2)	n/a
Metallocene bend	166.1_9	159.5_4 -160.2_3	162.7_5, 163.0_0	160.0_8 – 160.9_2

Table 2-5 Selected bond lengths (Å) and angles (°) for $[\{(Et_8N_4Me_2)M\}_n(L)]$.

Table 2-5 shows that the geometric properties of (**7**) are intermediate between lengths and angles characteristic of other Sm^{II} and Sm^{III} complexes that are not subject to steric influences.

The Sm−N_2 interaction in (**7**) is not linear, with both Sm−N−N angles being crystallographically the same at 174.5_2 ° The nitrogen centres of the dinitrogen moiety sit in neither the N_{Py}-Sm-N_{Py} plane nor the N_{Me}-Sm-N_{Me} plane, being displaced from each by 0.089(7) and 0.284(6) Å, respectively.

2.3.4.2 Molecular Structure of [{($Et_8N_4Me_2$)Sm}$_2$(μ-O)], (8)

Complex (**8**) was serendipitously isolated from multiple reactions presented later in this thesis, but is discussed here in relation to strengthening the identity assignment of (**7**). It forms as a colourless/pale yellow crystalline precipitate. The crystals were found to be suitable for X-ray crystal structure determination, Figure 2-25.

The crystal belongs to the tetragonal space group $I4_1/a$ (No. 88) a = 22.256(2), c = 13.439(4) Å, with four molecules in the unit cell. The asymmetric unit consists of one quarter of the [{($Et_8N_4Me_2$)Sm}$_2$(μ-O)] dimer, with molecules residing on 4 crystallographic sites, as viewed in Figure 2-25.

The molecular structure of (**8**) exhibits the standard η^1:η^5:η^1:η^5 macrocyclic binding mode. The Sm-(η^1-N_{Py}) distance is 2.511(4) Å and the Sm-(η^5-N_{Me}) distance is 2.65_1 Å. The Sm−*meso* distance is 1.227(3) Å. The N_{Py}−*meso* interplanar angle is 51.17(13) ° and the N_{Me}−*meso* interplanar angle is 51.17(13) °. The metallocene bend angle is 164.6_9 ° and the Sm-oxygen distance is 2.0699(7) Å.

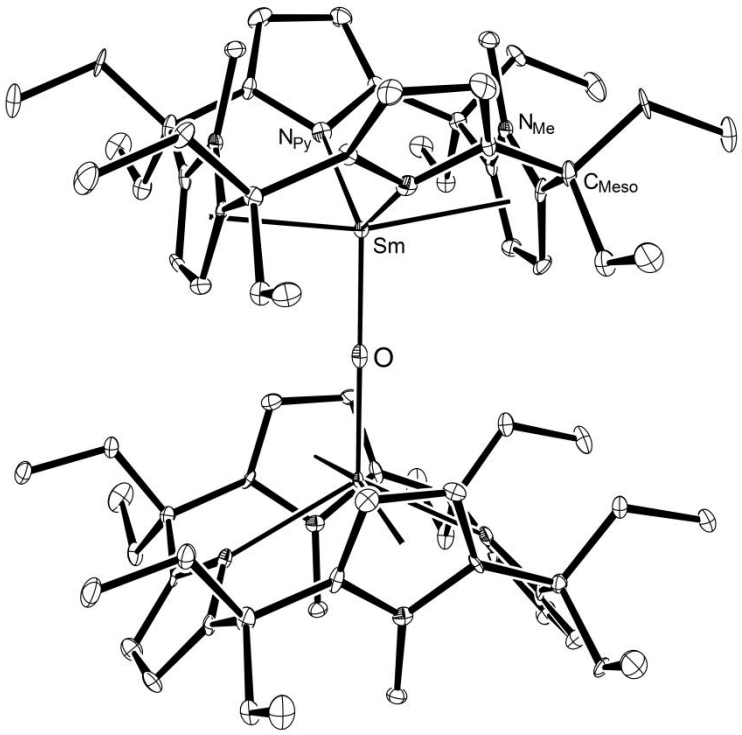

Figure 2-25 Molecular structure of (**8**) with thermal ellipsoids drawn at 50 % probability. Protons omitted for clarity.

The tightly bound bridging oxygen atom of (**8**) effectively withdraws the samarium centre from the macrocycle, giving the samarium(III) complex somewhat samarium(II)-like characteristics, Table 2-6.

	$M = Sm^{III}$ $n = 2$ $L = O^{2-}$ (**8**)	$M = Sm^{II}$ $n = 1$ $L = NC$*t*-Bu (**12**)	$M = Sm^{III}$ $n = 1$ $L = N(SiMe_3)_2$[71] (**XXXV**)	$M = Sm^{III}$ $n = 2$ $L = (OK)^-_2$ (**4**)
$M-(\eta^1-N_{Py})$	2.511(4)	2.550(6) - 2.579(5)	$2.51_3 - 2.60_4$	2.716(4), 2.911(3)
$M-(\eta^5-N_{Me})$	2.65_1	2.67_1 - 2.69_9	$2.64_5 - 2.66_8$	2.81_4, 2.86_3
$M-L_{donor\ atom}$	2.0699(7)	2.609(6), 2.612(7)	$2.30_7 - 2.31_4$	2.146(3)
M–*meso*	1.227(3)	1.282(3), 1.289(3)	$1.34_1 - 1.36_8$	1.82(2)
N_{Py}–*meso*	51.17(13)	44.33(12) – 52.7(2)	n/a	42.77(14), 43.20(13)
N_{Me}–*meso*	79.38(13)	76.4(2) – 79.2(2)	n/a	77.43(13), 75.28(15)
Metallocene bend	164.6_9	162.7_5, 163.0_0	$160.0_8 - 160.9_2$	141.3_3

Table 2-6 Selected bond lengths (Å) and angles (°) for $[\{(Et_8N_4Me_2)M\}_n(L)]$.

The limitation of assigning oxidation state based on molecular geometry alone is made clear by Table 2-6. Complexes that exhibit extreme steric duress show significant variation in macrocyclic geometry. Comparison between (**8**) and (**4**) reveal the significant difference in macrocyclic geometry resulting from either complimentary (90 °) macrocycle docking allowed when a single atom occupies both binding grooves, as in (**8**), Figure 2-22, or binding groove aligned docking, as necessitated by the presence of more than one atom in either binding groove, as in [{$(Et_8N_4Me_2)SmOK\}_2$], (**4**), Figure 2-17. Due to variation in coordination number and thus effective metal radii, quantification of this difference is not viable based on these complexes.

2.3.5 DFT Analysis of [{$(Et_8N_4Me_2)Sm\}_2(\mu\text{-}\eta^1\text{:}\eta^1\text{-}N_2)$], (7)

Density Function Theory analysis was undertaken to probe the electronic environment of [{$(Et_8N_4Me_2)Sm\}_2(\mu\text{-}\eta^1\text{:}\eta^1\text{-}N_2)$], (**7**), to gain an understanding of the degree of oxidation observed at the samarium atoms and subsequent reduction/activation of the dinitrogen moiety. The input geometry was obtained *via* a fully refined X-ray crystal structure and modified at the *meso*- carbons of the macrocycle to reduce the ethyl groups to protons using the GaussView Builder, as per the protocol established Section 2.3.3 using Density Functional Theory with the B3LYP hybrid functional. Unlike Section 2.3.3, the *N*-methyl groups were retained and the 6-31+G(d) basis set,[134-137, 144, 145] which additionally includes a diffusion coefficient, was applied to carbon, nitrogen, hydrogen and potassium, whilst the same Stuttgart RSC 1997 ECP[138-140] was applied to samarium. Where energy comparisons are made, they are comparisons of uncorrected SCF energies.

The NBO program performs the analysis of a many-electron molecular wavefunction in terms of the localised electron-pair bonding units. This method makes use of only the

first-order reduced density matrix of the wavefunction, rendering it useful to wavefunctions of general mathematical form.[146] NBO analysis is based on a method for optimally transforming a given wavefunction into localised form, corresponding to the one-center ("lone pair") and two-center ("bond") elements of the chemist's Lewis structure picture.[146] NBO analysis has been employed in this study and serves as a second and, perhaps, more valid interpretation of electron populations calculated from crystal structure geometries, compared with Mulliken atomic spin densities. Mulliken population analysis, rather than calculating natural orbitals, arbitrarily divides overlapping population equally between bonding atoms to arrive at a population for each atom. The Mulliken method is thus not reliable without the ratification of another technique. Both NBO analysis[146] and Mulliken electron population analysis techniques were employed for calculations on the X-ray structure geometry; no geometry optimisation was undertaken so as to better gain insight into the properties of the observed molecular structure.

The electron population of the 4f orbital of $[\{(Et_8N_4Me_2)Sm\}_2(\mu\text{-}\eta^1\text{:}\eta^1\text{-}N_2)]$, (**7**), was found to be 5.74 electrons by Mulliken analysis and 5.65 electrons by NBO analysis. Analogous calculations were undertaken on $[\{(C_5Me_5)_2Sm\}_2(\mu\text{-}\eta^2\text{:}\eta^2\text{-}N_2)]$ using coordinates obtained from the literature,[33] finding 4f populations of 5.34 electrons (by average of the two samarium centres at 5.30 and 5.39, respectively, due to minor variations in geometry) by Mulliken analysis and 5.40 electrons by NBO analysis (5.37 and 5.42, respectively).

Comparison of the values obtained for the electron populations of dinitrogen complexes with other calculations for $[(Et_8N_4Me_2)Sm(L)_n]$ complexes undertaken *via* the same method (Section 4.3.4) reveal that the values obtained for the end-on dinitrogen complex, (**7**), are neither consistent with purely Sm^{II} complexes nor purely Sm^{III}

complexes, Figure 2-26, but lie between those two states. Conversely, calculations show that the electron population of the 4*f* orbital in the case of the side-on bound dinitrogen complex of decamethylsamarocene, (**VI**), is consistent with a samarium(III) centre, as reported (based on ^{13}C NMR and X-ray crystal structure data).[33] These results are consistent with the proposal by Perrin *et al*. in 2003 that the N−N bond length in the $(N_2)^{2-}$ fragment in the X-ray crystal structure data for (**VI**) has been misrepresented due to crystallographic disorder of the $(N_2)^{2-}$ moiety.[99]

DFT analysis of the known Sm^{III} alkyl complex [$(Et_8N_4Me_2)SmMe$], (**XX**), was undertaken using coordinates obtained from a published X-ray crystal structure that was treated identically to (**7**).[75] Coordinates for the known Sm^{II} species [$(Et_8N_4Me_2)Sm(THF)_2$], (**XVI**), and a novel $Sm^{III}(L^{\bullet-})$ species, with the ligand adopting a radical anionic electronic state, [$(Et_8N_4Me_2)$Sm(2,2′-bipyridine)], (**27**), Chapter 4, were similarly modified from X-ray crystal structure data obtained in the same manner as (**7**). By the techniques employed for all of these calculations, there are 5.20 electrons on the formally Sm^{III} centre of the $Sm^{III}Me$ complex (**XX**), by both Mulliken and NBO analyses, and 5.45 and 5.44 electrons, by Mulliken and NBO analyses, respectively, on the formally Sm^{III} centre of the Sm^{III} radical anion species with 2,2′-bipyridine, (**27**). The additional electron density on the Sm^{III} centre for (**27**) is consistent with delocalised electron density on the singly reduced 2,2′-bipyridine fragment of (**27**) interacting with the samarium centre. By comparison, the electron populations of the bis(THF) adduct, [$(Et_8N_4Me_2)Sm(THF)_2$], (**XVI**), are 6.01 and 5.97 electrons by Mulliken and NBO analyses, respectively; a definitive result for a Sm^{II} species with formally six electrons in the 4f orbital.

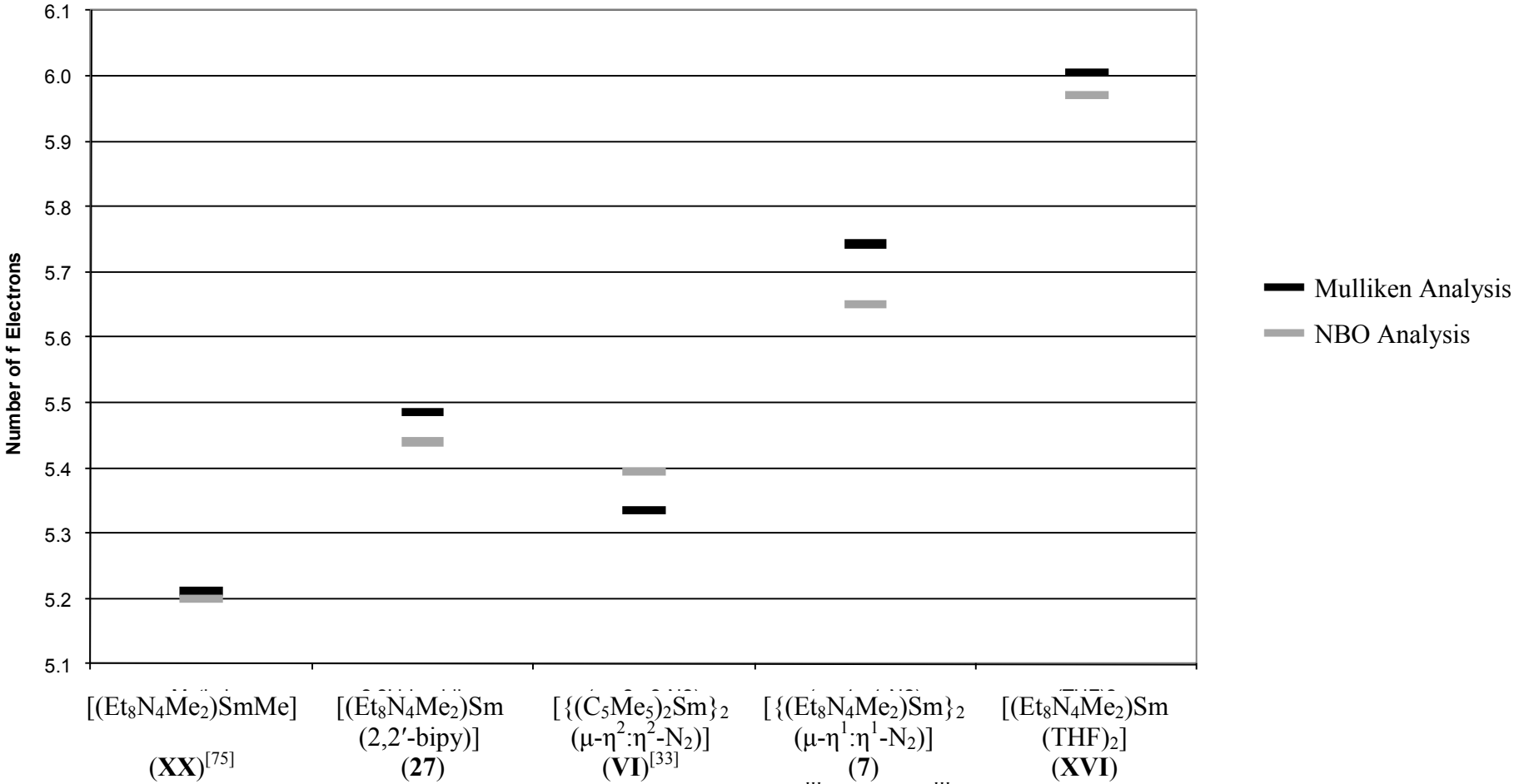

Figure 2-26 Chart showing the number of *f*-electrons on samarium for a Sm^{III}-alkyl, Sm^{III}-radical anion, two Sm-dinitrogen complexes and a Sm^{II}-bis(THF) adduct by Mulliken and NBO population analysis.

2.4 Experimental

The syntheses of the complexes described in this Chapter were primarily achieved *via* the reaction between [{($Et_8N_4Me_2$)Sm}$_2$(*t*-BuDAB)], (**XXII**), and potassium metal. The reaction proceeds differently depending on solvent choice, but in each case multiple products are isolated from each solvent system. The reaction proceeds more rapidly from the green colour of the starting material to the red/purple of the completed reaction in benzene rather than toluene. Isolation and further characterisation of the complexes described in this section, despite repeated attempts, has been difficult. As such, satisfactory ^{1}H NMR and ^{13}C NMR spectra, elemental analysis, and yield data have not generally been obtained and are thus unusually absent from the description of the synthesis of each of these complexes. Satisfactory elemental analysis of (**3**) is a notable exception. A number of individual, compound specific issues preventing full characterisation of these compounds are presented throughout this Chapter.

Synthesis of [($Et_8N_4Me_2$)Sm]·PhMe, (1)

A solution of [{($Et_8N_4Me_2$)Sm}$_2$(*t*-BuDAB)], (**XXII**), (6.24×10^{-6} mol, 10 mg) was prepared in toluene (0.5 mL). Cleaned potassium metal (7.67×10^{-5} mol, 3 mg) was added and the reaction heated at 83 °C for seven days, resulting in a very dark purple solution and an orange precipitate. The reaction solution was filtered and allowed to evaporate, providing red crystals of the title compound suitable for X-ray crystal structure determination. Two reactions were undertaken in parallel, differing only in atmosphere from dinitrogen to argon; both reactions were shown to provide (1) by X-ray crystal structure determination.

Synthesis of [{($Et_8N_4Me_2$)Sm}$_2$(C_7H_7)K], (2)

A solution of [{($Et_8N_4Me_2$)Sm}$_2$(*t*-BuDAB)], (**XXII**), (7.49 x 10^{-6} mol, 12 mg) was prepared in toluene (0.5 mL). Cleaned potassium metal (1.28 x 10^{-4} mol, 5 mg) was added and the reaction heated at 91 °C for seven days, resulting in an orange/brown solution over dark red rod- (and a miniscule amount of block-) shaped crystals. The dark red/purple crystalline rods and blocks were found to be the title compound by X-ray crystal structure determination. Due to the insolubility of (**2**), separation of the title complex from the concomitantly formed precipitate presumed to be K(*t*-BuDAB) has not been possible, preventing satisfactory elemental analysis.

Synthesis of [{($Et_8N_4Me_2$)Sm}$_n$], (3)

A solution of [{($Et_8N_4Me_2$)Sm}$_2$(*t*-BuDAB)], (**XXII**), (6.24 x 10^{-5} mol, 100 mg) was prepared in benzene (10 mL). Cleaned potassium metal (4.09 x 10^{-4} mol, 15 mg) was added. The reaction was heated for 48 hours at 76 °C resulting in a very dark purple solution and an orange precipitate. The reaction was filtered and allowed to evaporate, providing red crystals only upon almost complete evaporation of the benzene solution. The crystals were found to be the title compound by X-ray crystal structure determination. Satisfactory elemental analysis was obtained after complete evaporation at ambient temperature and pressure in the glovebox. On two separate occasions following independent repeats of this procedure, a single crystal of (**5**) and a single crystal of (**6**) were isolated from the reaction mixture afforded by this procedure.

Anal. Calcd.: C, 63.64; H, 7.59; N, 7.81 ($C_{38}H_{54}N_4Sm$)

Found: C, 63.51; H, 7.72; N, 7.53

Synthesis of [{($Et_8N_4Me_2$)SmOK}$_2$], (4)

Small amounts of pale orange crystalline plates of (**4**) were able to be identified in the various red/purple main products resulting from several reactions between (**XXII**) and potassium metal. A typical reaction from which (**4**) was isolated followed the preparation of a toluene solution (0.5 mL) of [{($Et_8N_4Me_2$)Sm}$_2$(*t*-BuDAB)], (**XXII**), (7.49×10^{-6} mol, 12 mg) and addition of freshly cleaned potassium metal (1.28×10^{-4} mol, 5 mg). The solution was subsequently heated at 83 °C for seven days, resulting in a very dark purple solution and an orange precipitate. The solution was filtered and allowed to evaporate, providing mainly red crystals of (**1**) and a relatively small number of pale orange crystalline plates of the title compound suitable for X-ray crystal structure determination.

Synthesis of [{($Et_8N_4Me_2$)Sm}$_2$(μ-η^1:η^1-N_2)], (7)

A solution of [{($Et_8N_4Me_2$)Sm}$_2$(*t*-BuDAB)], (**XXII**), (3.12×10^{-5} mol, 50 mg) was prepared in benzene (3 mL). Cleaned potassium metal (2.56×10^{-4} mol, 10 mg) was added. The reaction was heated for 48 hours at 76 °C resulting in a very dark purple solution and an orange precipitate. The reaction was filtered and allowed to evaporate overnight in an open vessel under an atmosphere of dinitrogen. The next day red crystals were observed on the walls of the flask above the remaining benzene solution. The crystals were found to be the title compound by X-ray crystal structure determination.

Synthesis of [{($Et_8N_4Me_2$)Sm}$_2$(μ-O)], (8)

Colourless crystalline plates of (**8**) were isolated from several reactions involving the samarium macrocycle. A typical reaction from which (**8**) was isolated followed the addition of pyrazine (2.50×10^{-5} mol, 2 mg) to a toluene solution (0.5 mL) of [($Et_8N_4Me_2$)Sm(THF)$_2$], (**XVI**), (1.16×10^{-5} mol, 10 mg). Serendipitous oxygenation resulting in identification and characterisation of colourless crystals from amongst the coloured crystals of the desired reaction product provided the title compound by X-ray crystal structure determination.

Chapter 3

Nitriles, Isonitriles and Samarium(II)

3.1 Introduction

Nitriles and isonitriles contain carbon-nitrogen triple bonds and differ only in substitution at the single-bond bound substituent of the carbon (nitriles) or nitrogen (isonitriles) and reciprocal location of the lone pair. Thus, nitriles and isonitriles are suitable for coordination to lanthanoids *via* the lone pair. Additionally, for Ln^{II} ions, reduction of the ligand provides additional incentive for coordination to the metal ions and a number of sequential reaction pathways are known.

A report by Jacobsen *et al.* in 1999 revealed that nitrile and isonitrile donor adduct complexation of tris(pentafluorphenyl)borane causes a shortening of the C≡N bond, characterised by a shift of the C≡N IR stretch to higher wavenumbers.[147] DFT analysis revealed that the bonding in these complexes is mainly dominated by electrostatic interactions.[147] A microreview by Choukroun and Lorber in 2005 ratifies the observation that the C≡N bond is strengthened upon coordination to a Lewis acid (in this case vanadium).[148]

A 1996 review entitled *Reactions of transition metal-coordinated nitriles* by Michelin, Mozzon and Bertani provides a rich overview of the transition metal chemistry of nitriles and the various reaction types, including insertion reactions, reactions involving metal-metal and metal-X (X=O,S) multiple bonds, coupling reactions, reduction to amines, nucleophilic attack and electrophilic attack.[149]

Several reports of adduct formation between nitriles or isonitriles and lanthanoids in both the Ln^{II} and Ln^{III} state can be found in the literature. Bis(nitrile) adducts of $(C_5H_5)_3Ln$ (Ln = La, Ce, Pr, Sm),[150] MeCN adducts of $(C_5H_5)_2Yb$ and several $(C_5H_5)_3Ln$ (Ln = Nd, Sm or Yb)[151] complexes have been reported for Ln^{III} ions. Additionally, Evans *et al.* showed in 2008 that MeCN reversibly coordinates as a neutral adduct in a Sm^{III} complex formed with deprotonated 1,3,4,6,7,8-hexahydro-2H-pyrimido[1,2-a]pyrimidine, Equation 3-1.[152] Such reactivity clearly exploits the slender, prolate shaped nature of these ligands.

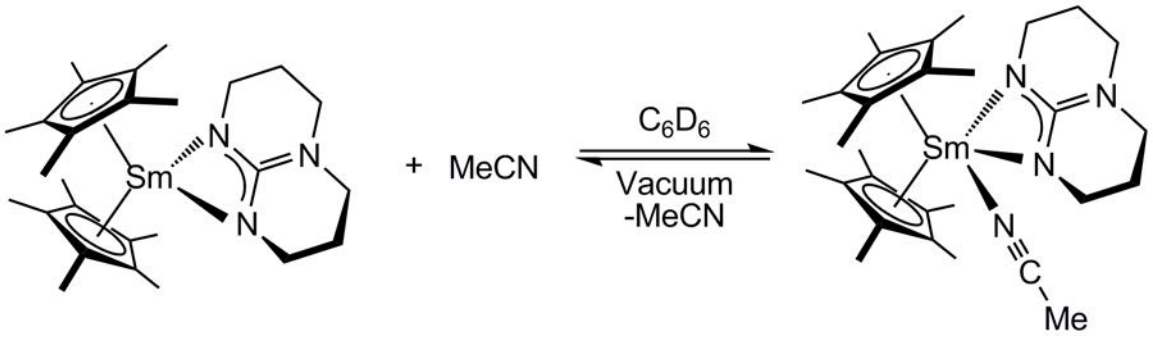

Equation 3-1

MeCN adducts of $(C_5H_5)_2Yb$,[151] and 2:1 or 1:1 isonitrile adducts of Yb^{II} and 1:1 isonitrile adducts of Sm^{II}, irrespective of stoichiometry, have been shown to form depending on the bulk of the supporting ligands, Equation 3-2.[153, 154]

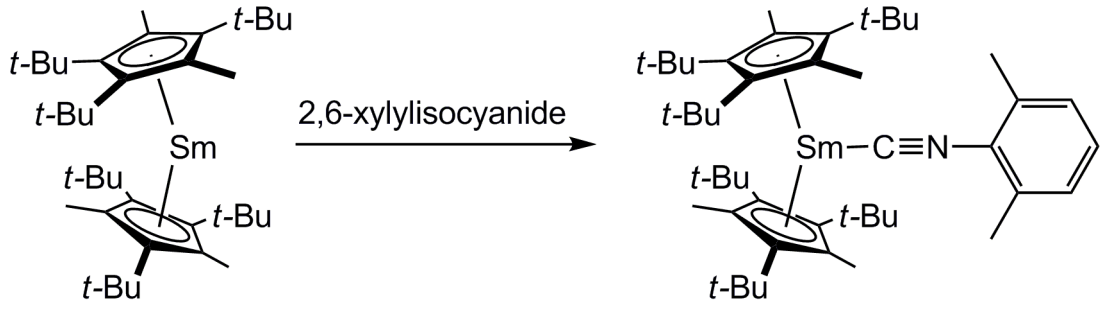

Equation 3-2

In 1988, Evans and Drummond reported an investigation into the reactivity of $[(C_5Me_5)_2Sm(THF)_2]$, (**IV**), with isonitriles; specifically *t*-BuNC and CyNC. It was found that reductive cleavage occurs to produce the samarium(III) cyclic trimer,

$[\{(C_5Me_5)_2Sm^{III}(CN)(CNR)\}_3]$, for R = *t*-Bu, Cy, where the cyanide ligands bridge the three metal centres and an additional molecule of unreacted isonitrile coordinates to each metal centre, Equation 3-3. It was noted that reductive cleavage of isonitriles had previously only been observed under harsh conditions.[155] A similar reaction outcome had earlier been observed by Gambarotta *et al*. in the reaction of *t*-BuNC with decamethylvanadocene.[156]

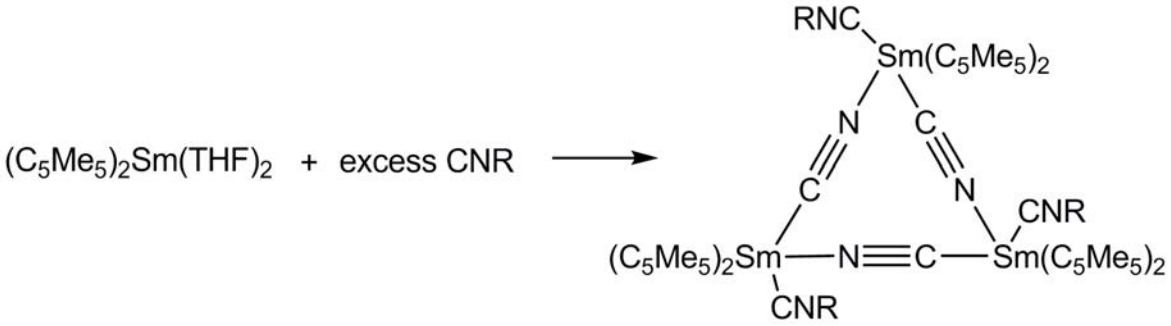

Equation 3-3

An alternate unsolvated samarocene cyanide complex was accessed *via* a different cyanide generation route in the absence of excess prolate shaped Lewis basic donor, and was shown to be a hexamer, $[((C_5Me_5)_2Sm(\mu\text{-}C{\equiv}N))_6]$, with a chair shaped $Sm_6C_6N_6$ 18-membered ring, Scheme 3-1.[157]

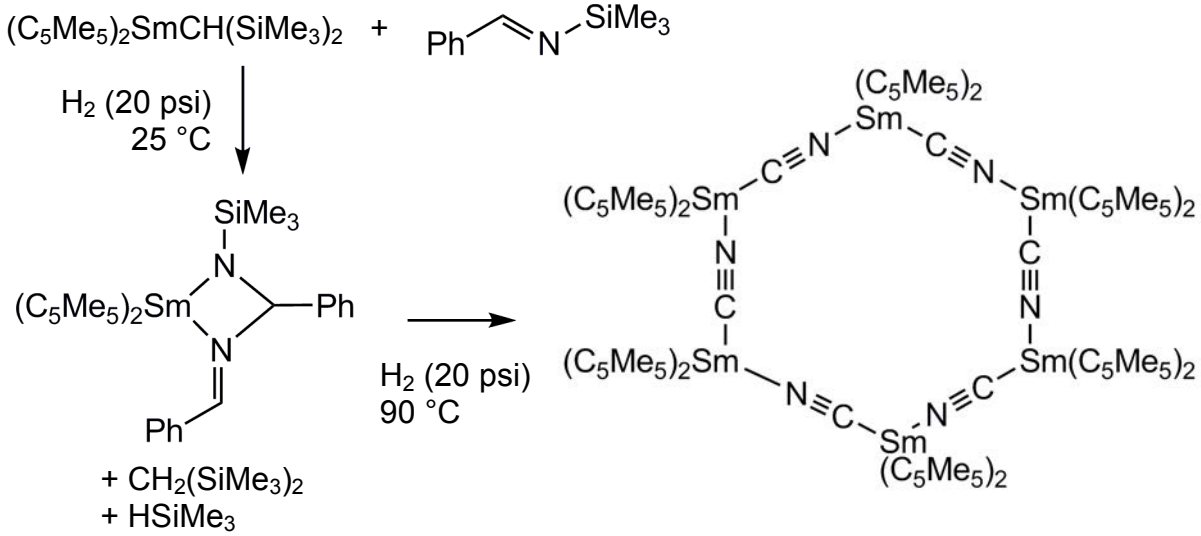

Scheme 3-1 Synthesis of a samarocene cyanide hexamer is achieved in the absence of excess prolate shaped Lewis basic donor. Adapted from Obora *et al*.[157]

Ten years after the initial isonitrile report, Evans, Forrestal and Ziller reported the reaction of $[(C_5Me_5)_3Sm]$, (**VII**), with nitriles and isonitriles. Benzonitrile was shown to insert into a $Sm(C_5Me_5)$ unit, with a second benzonitrile molecule coordinating to the metal centre, Equation 3-4. The observed reactivity was taken as strong evidence for the availability of an intermediate η^1-(C_5Me_5) type species in the $[(C_5Me_5)_3Sm]$ system that has subsequently been shown to be one of the characteristic reactivity patterns for this highly strained complex.[38]

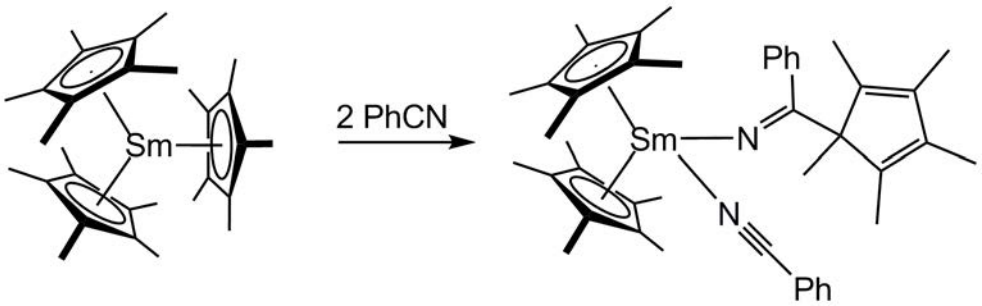

Equation 3-4

A *t*-BuNC adduct of $[(C_5Me_5)_3Sm]$, (**V**), was shown to form without further reaction, however the resulting complex could not be characterised by X-ray crystal structure analysis. Heating this reaction at 80 °C for one hour and X-ray characterisation of resulting material revealed the *t*-Bu analogue of the cyclic Sm^{III} cyanide trimer observed ten years previously (no satisfactory structure data had been obtained in the earlier work).[38]

Evans *et al.* reported in 2007 the reactivity of $[(C_5Me_5)_2Sm(THF)_2]$, (**IV**), with nitriles. It was shown that addition of two equivalents of *t*-BuCN to a THF solution of (**IV**) results in formation of the bis(*t*-BuCN) adduct of $(C_5Me_5)_2Sm$ with additional coordination of one molecule of THF, indicating that the nitrile outcompetes THF for coordination at the metal centre.[158] Undertaking the reaction over 24 hours in toluene results in isolation of insoluble orange $[(C_5Me_5)_2Sm(CN)]_n$ and a soluble yellow ketimide

complex, $[(C_5Me_5)_2Sm(N=C(H)t\text{-}Bu)(THF)]$. The latter complex presumably arises as a THF adduct of the product of inserting *t*-BuCN into the Sm−H bond of $[\{(C_5Me_5)_2Sm(\mu\text{-}H)\}_2]$; the independent synthesis of the ketimide complex was achieved *via* this route, Equation 3-5.[158] A third cyclic Sm^{III} trimer, this time as the *t*-BuCN adduct, was characterised by X-ray crystallography.[158]

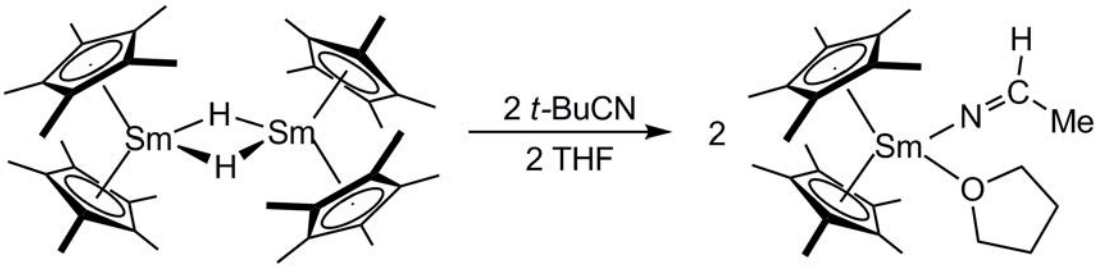

Equation 3-5

Formation of $[(C_5Me_5)_2Sm(CN)]_n$ *via* reaction of excess *t*-BuCN with $[(C_5Me_5)_2Sm(THF)_2]$, (**IV**), liberates a *t*-$Bu^{\bullet}$ group. ^1H NMR spectroscopic analysis of the reaction mixture was consistent with the presence of isobutene, indicating β-hydrogen elimination of *t*-$Bu^{\bullet}$ to form a hydride (required to generate the Sm^{III} hydride species) and isobutene.[158] Isobutane and isobutene are known decomposition products of the *t*-$Bu^{\bullet}$ fragment.[159]

In 1981, Chiu *et al.* reported methyl migration onto *t*-BuNC upon reaction with methyl complexes of tungsten, rhenium, zirconium, titanium and tantalum to form η^2-iminoacyl complexes.[160] Carrier *et al.* reported access to η^2-iminoacyl complexes of vanadocene by reaction with nitrilium salts.[161] Takenaka and Hou report the synthesis of terminal hydride species for Y, Nd, Sm, Dy and Lu with $(C_5Me_4SiMe_3)$ ligands. The reactivity of this yttrium complex was explored with *p*-methoxyphenylisocyanide, yielding a reductive dimerisation product between the isocyanide and the yttrium terminal hydride, possibly *via* an η^2-iminoacyl intermediate, Scheme 3-2.[162] In the 1988 paper by Evans

and Drummond, *vide supra*, elemental analysis consistent with the formation of $[(C_5Me_5)_2Sm(CyNCCy)]$ led to the suggestion of the presence of a potential η^2-iminoacyl complex arising from capture of the $^{\bullet}$Cy fragment resulting from reductive cleavage of the parent isonitrile by the Sm^{II} reactant, with concomitant formation of the Sm^{III} cyanide trimer.[155]

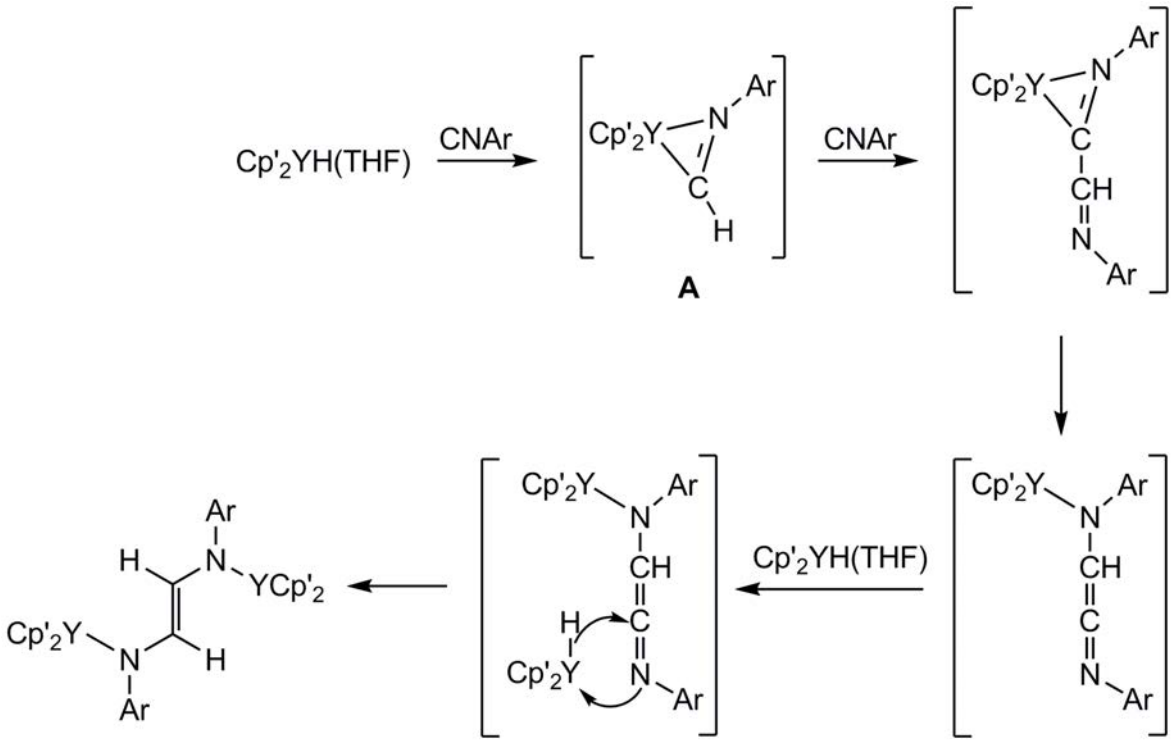

Scheme 3-2 Proposed reaction mechanism for the reaction of an yttrium hydride species with an isocyanide *via* an η^2-iminoacyl intermediate, A. Adapted from Takenaka and Hou.[162] Cp′ = ($C_5Me_4SiMe_3$), Ar = (C_6H_4OMe-*p*).

Hou, Nishiura and Shima showed that tetranuclear yttrium and lutetium dihydride complexes react with benzonitrile or acetonitrile to completely reduce the C≡N triple bond to a C−N single bond by double Ln−H addition, affording tetranuclear cubane-like imido complexes, $[\{(C_5Me_4SiMe_3)Ln(\mu_3\text{-}NCH_2Ph)\}_4]$ for Ln = Y and Lu.[163] Further reactivity of derivatives of the octahydrides was reported in the cyclotrimerisation of benzonitrile to form 2,4,6-triphenyl-1,3,5-triazine.[163] Benzonitrile had previously been shown to couple with pyridine, benzophenone and carbon dioxide.[164] Organolanthanoid-bound triazole

rings have also been achieved for *t*-BuCN by silyl migration for Sm and Ln, Equation 3-6.[165]

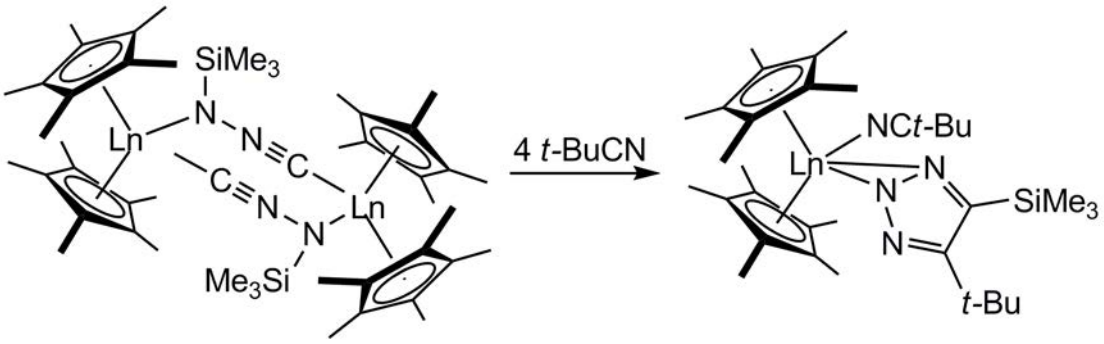

Equation 3-6

3.2 Research Aim

To investigate the coordination and reduction chemistry of *N*-heteroalkyne ligands with $[(Et_8N_4Me_2)Sm(THF)_2]$, (**XVI**). The viability of desolvation of isonitrile and nitrile adducts was the initial drive for this study; in accessing Sm^{II} Lewis base adducts that were potentially more labile than the oxygen donor adduct starting material, (**XVI**), an alternate route to Lewis base free samarium(II) species may be identified.

3.3 Results and Discussion

3.3.1 Reactions with Nitriles; N≡C−R, for R = Me

The bis(acetonitrile) adduct, $[(Et_8N_4Me_2)Sm(NCMe)_2]$, (**9**), was prepared by addition of excess acetonitrile to either benzene or toluene solutions of $[(Et_8N_4Me_2)Sm(THF)_2]$, (**XVI**). The complex precipitates within two minutes at room temperature as an insoluble dark green crystalline material that appears to undergo no visible change over ten days in either benzene or toluene. The reaction was shown to be reversible by addition of excess THF to an isolated sample of (**9**), effecting a purple solution shown by ^{1}H NMR spectroscopy to be $[(Et_8N_4Me_2)Sm(THF)_2]$, (**XVI**), Equation 3-7.

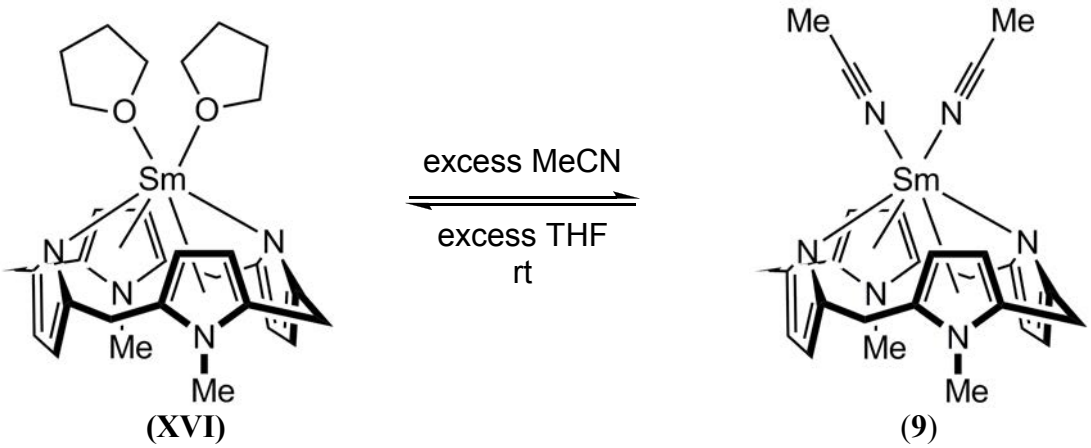

(XVI) **(9)**

Equation 3-7

Complex (**9**) was characterised by X-ray crystal structure determination. NMR analysis was not possible owing to the insolubility of (**9**) in hydrocarbyl solvents and the established ligand displacement reactivity with THF. Satisfactory elemental analysis could not be obtained due to the apparent instability of the isolated solid, *vide infra*.

Attempts to purify the samarium(II) bis(acetonitrile) adduct, (**9**), by washing an isolated sample of the dark green insoluble material with fresh benzene, resulted in a purple solution that bleached to colourless within five minutes. The soluble purple solution implies that MeCN is lost from (**9**) if excess MeCN is not present, presumably to give the mono(NCMe) adduct. Exploitation of the lability of MeCN by complete desolvation is not possible due to rapid bleaching of the purple solution, preventing isolation of the mono(adduct) due to its apparent instability. In contrast, preliminary results obtained in our lab by a co-worker indicate the complete desolvation *in vacuo* of a bis(acetonitrile) adduct of a related samarium(II) porphyrinogen.[166]

The bleached solution resulting from washing an isolated sample of (**9**) with fresh benzene was allowed to stand overnight, whereupon orange crystals formed and were shown by X-ray crystallography to be [{($Et_8N_4Me_2$)Sm(CN)}$_3$], (**10**). Clearly, in the absence of additional equivalents of MeCN, reductive cleavage of MeCN to give the Sm^{III} cyanide trimer, (**10**), occurs, most likely accompanied by the formation of the Sm^{III} methyl species, (**XX**), which is inferred *via* formation of (**10**) and supported by formation of (**11**), *vide infra*. The instability of isolated [($Et_8N_4Me_2$)Sm(NCMe)$_2$], (**9**), in non-coordinating solvents prevented appropriate sample preparation for elemental analysis, as the insoluble dark green solid could not be washed to remove excess residual NCMe without dissolving to a purple solution.

GC-MS analysis of the clear, colourless mother liquor above the green precipitate of (**9**), undertaken 96 hours after preparation and standing at room temperature, revealed only excess MeCN, C_6H_6 and THF, consistent with the visual observation that [($Et_8N_4Me_2$)Sm(NCMe)$_2$], (**9**), is stable at room temperature, *vide supra*. Heating a C_6H_6 suspension of crudely isolated (**9**) at 50 °C for 18 hours provided a yellow solution and an

insoluble orange crystalline material. X-ray crystal structure determination revealed that the orange crystalline material was the cyclic trimer of the Sm^{III} cyanide species, $[\{(Et_8N_4Me_2)Sm(CN)\}_3]$, (**10**), Equation 3-8. Due to the insolubility of the cyanide complex, (**10**), in PhMe, Et_2O, pet. ether and THF, NMR spectroscopic characterisation was unable to be performed; however satisfactory elemental analysis data were obtained.

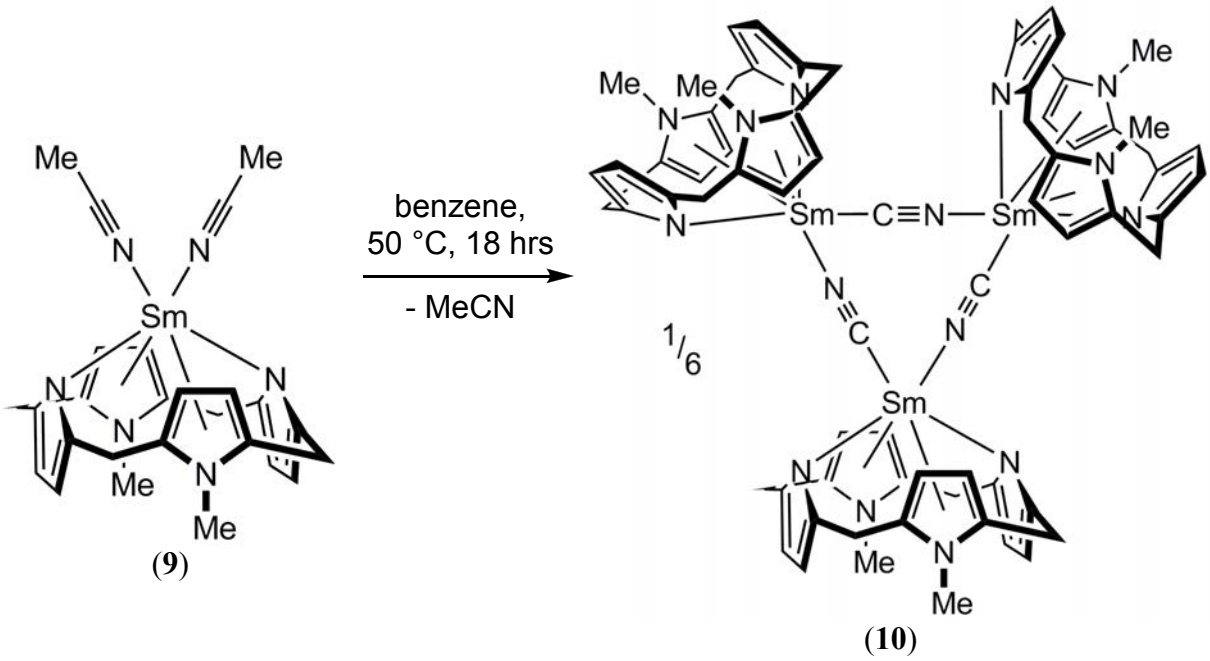

Equation 3-8

Formation of (**10**) implies reductive cleavage of MeCN to form the Sm^{III} cyanide complex and, presumably, residual $Me^{\bullet}$ which will either react further or decompose. The former is implied by the formation of a series of Sm^{III} derivatives and organic oligomeric products, *vide infra*.

The isolation of the trimeric samarium cyanide complex is consistent with previous reports in the literature. Decamethylsamarocene analogues of (**10**) show coordination of an additional neutral isonitrile/nitrile molecule, with a Sm···Sm separation reported for the CNCy coordinated trimer of 6.28 - 6.30 Å (*cf.* 6.23 Å for (**10**)).[38, 155] The absence of additional adduct coordination in the case of (**10**) is rationalised by the greater steric

requirements of the porphyrinogen. Near planar $M_3N_3C_3$ nine-membered ring planes are reported for all trimeric adducts of this type and (**10**) offers no exception.[38, 155, 167]

An unsolvated decamethylsamarocene cyanide complex has been accessed *via* a different cyanide generation route in the absence of an excess prolate shaped Lewis basic donor capable of binding to the Sm centre, and was shown to be a hexamer, $[\{(C_5Me_5)_2Sm(\mu\text{-}C{\equiv}N)\}_6]$, Section 3.1, Scheme 3-1. Each Sm−C≡N−Sm unit in this case is approximately linear, and an overall chair shaped $Sm_6C_6N_6$ 18-membered ring results, exhibiting a closer average Sm···Sm separation of 6.187 Å (*cf.* 6.23 Å for (**10**)).[157] In the case of (**10**), retention of the smaller trimeric unsolvated structure is likely to be dictated by the increased interactions between adjacent macrocycles that would exist for the larger oligomers by virtue of the decreased Sm···Sm···Sm exterior ring angle for expanded $(SmC{\equiv}N)_n$ rings, where n > 3 (255.2 ° for $[\{(C_5Me_5)_2Sm(\mu\text{-}C{\equiv}N)\}_6]$ *cf.* 240 ° for (**10**)).

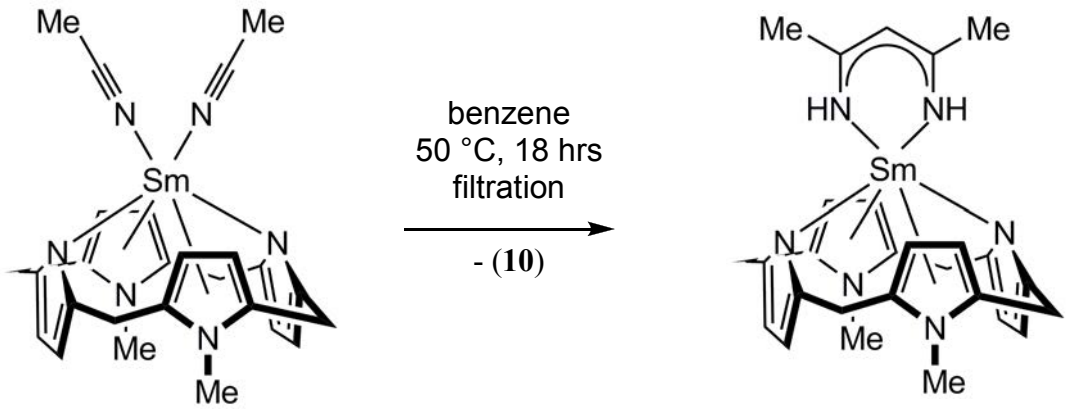

(**9**) (**11**)

Equation 3-9

In addition to the orange crystals of the Sm^{III} cyanide trimer, (**10**), which were isolated from the reaction undertaken at 50 °C for 18 hours, Equation 3-8, filtration followed by slow evaporation of the resulting supernatant solution provided yellow crystals of the samarium(III) *β*-diketiminate complex, $[(Et_8N_4Me_2)Sm(nacnac)]$, (**11**), on one occasion, Equation 3-9.

Formation of (**11**) from (**9**) is accompanied by concomitant formation of (**10**). Although the stoichiometry of the overall reaction is unknown, formation of (**10**) from (**9**) necessarily liberates both the $Me^{\bullet}$ fragment and sufficient MeCN from the starting material to satisfy the requirements for *in situ* formation of the "two-and-a-half units of MeCN" observed in the nacnac moiety of [$(Et_8N_4Me_2)$Sm(nacnac)], (**11**). GC-MS analysis of the solution from which (**11**) was obtained revealed the formation of dimerisation and trimerisation products of acetonitrile in addition to hydrolysed ligand, H(nacnac). These organic products are believed to result from subsequent reactivity relating to the mechanism of formation of the nacnac complex, (**11**), and will be discussed further, *vide infra*.

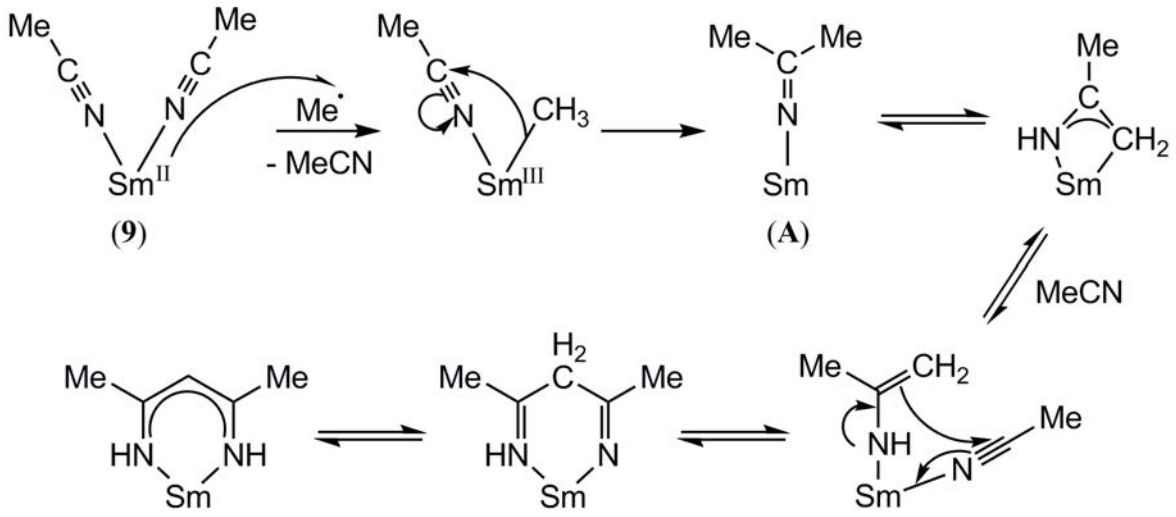

Figure 3-1 A possible mechanism for formation of (**11**). Macrocycle omitted for clarity.

A potential mechanism to rationalise the formation of (**11**) is presented, Figure 3-1. The mechanism assumes the $Me^{\bullet}$ fragment liberated by formation of (**10**) is reduced by a Sm^{II} complex to form the known complex [$(Et_8N_4Me_2)$SmMe], (**XX**).[75] Complex (**11**) has only been characterised by X-ray crystal structure analysis and inferred GC-MS analysis of the hydrolysed reaction mixture. The synthesis has not been reproduced as the formation of (**11**) is dependent on trapping $Me^{\bullet}$ by a Sm^{II} species that is low in

concentration (owing to the low solubility of (**9**)), and is presumably subject to subtle concentration and temperature effects.

The known samarium ketimide complex, $[(C_5Me_5)_2Sm(N=C(H)t\text{-}Bu)(THF)]$, is the implied intermediate analogous to (**A**), Figure 3-1.[158] A 1985 report by Bercaw, Davies and Wolcznaski noted the reaction of $[(C_5Me_5)_2ScR]$, for R = H, Me, *p*-tolyl, with nitriles, R′CN, to provide azomethine (or ketimide) complexes of the type $[(C_5Me_5)_2ScNC(R)R']$, as invoked by (**A**), Figure 3-1.[168] In the reaction between $[(C_5Me_5)_2ScMe]$ and acetonitrile, stoichiometry in excess of 1:1 resulted in further reaction of the second equivalent of MeCN to produce $[(C_5Me_5)_2Sc(nacnac)]$ as characterised by ^{1}H NMR, ^{13}C NMR and IR spectroscopies.[168] The proposed mechanism for the formation of $[(C_5Me_5)_2Sc(nacnac)]$ is analogous to Figure 3-1.[168] Similar reactivity is observed for a dimeric chromium complex, $[(C_5Me_5)(Me)Cr(\mu\text{-}Cl)]_2$, upon reaction with excess MeCN.[169] The mechanism in this case was probed by CD_3CN labelling experiments, which revealed the presence of D_6- (52 %), D_7- (11 %), D_8- (21 %) and D_9- (16 %) isomers, consistent with reversible proton exchange, as required by Figure 3-1.[169] A more recent report notes the high yield conversion of C,C-dimethylketimide complexes to a M(nacnac) complex, for M = Ti, over an extended time period (as invoked by the steps beginning at (**A**), Figure 3-1).[170]

Discussion to this point has focussed on the decomposition of (**9**) in the absence of excess acetonitrile. Investigation of the reaction of (**9**) with excess MeCN at 50 °C for 18 hours revealed organic products due to dimerisation and trimerisation of acetonitrile in the reaction mixture in addition to the presumed formation of the Sm^{III} cyanide, (**10**). Additional minor products were observed (each < 2 % relative to each of the main derivatives). Analysis of the reaction solution by GC-MS confirmed the dimerisation

product of acetonitrile to form both *cis*- and *trans*-aminocrotononitrile, (**XXXIII**), by comparison with a purchased sample. Presumably, this reactivity results from the initial loss of the nacnac ancillary ligand to generate a Sm^{III} hydride (*cf.* decamethylsamarocene hydride[171] and porphyrinogensamarium hydride[63]) that then reacts with MeCN in a similar fashion as (**9**), Figure 3-2. This structural change allows the necessary tautomeric shift to permit formation of aminocrotononitrile, a dimer of acetonitrile, that, due to the additional Me substituent in (**11**), is not possible from the implied $Sm^{III}Me$ intermediate, (**XX**). The fate of the nacnac ligand in (**11**) upon generation of the $Sm^{III}H$ species could not be established by GC-MS analysis.

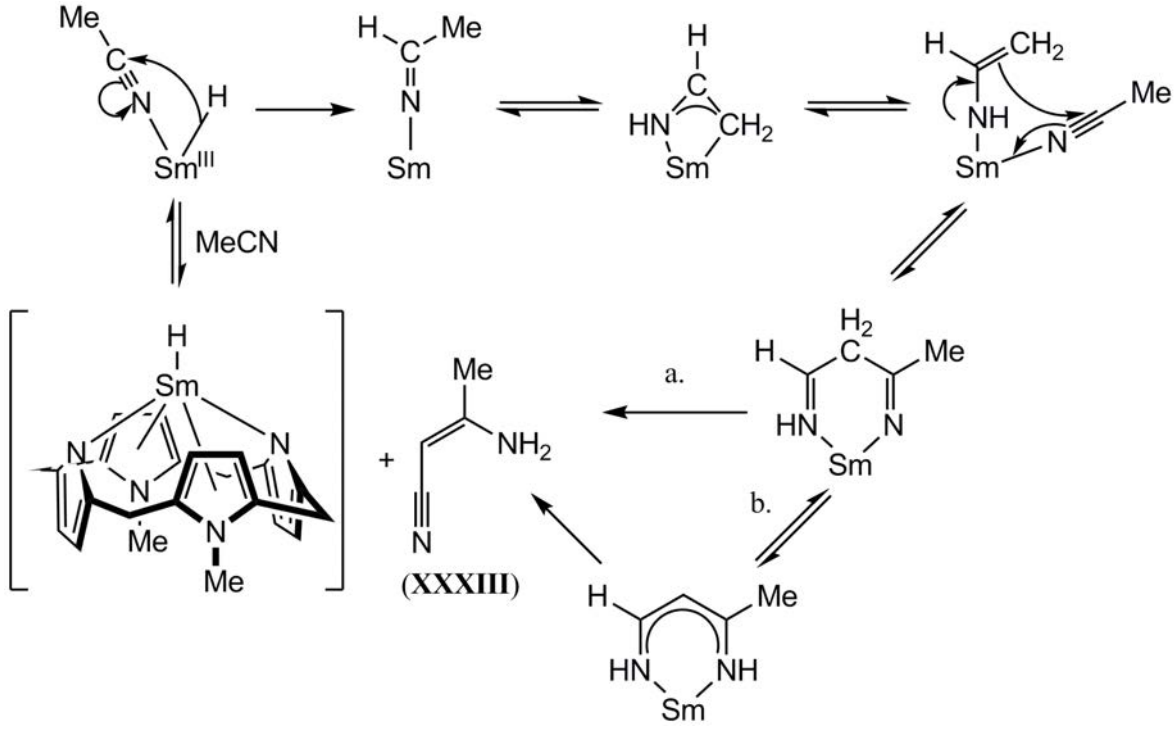

Figure 3-2 A possible mechanism for the catalytic formation of (**XXXIII**) assuming a samarium hydride species. Macrocycles throughout omitted for clarity.

The mechanism proposed in Figure 3-1, *vide supra,* to rationalise the synthesis of $[(Et_8N_4Me_2)Sm(nacnac)]$, (**11**), relies upon reaction of the known Sm^{III} methyl complex[75] with acetonitrile. Small scale, *in situ* generation of $[(Et_8N_4Me_2)SmMe]$, (**XX**), *via* addition of MeLi to $[\{(Et_8N_4Me_2)SmCl\}_2]$, (**XVII**), was undertaken according to published

procedure and subsequently exposed to acetonitrile under the conditions described by Equation 3-9.[75] A highly coloured fluorescent yellow solution was obtained and shown by GC-MS analysis to contain H(nacnac) and both the dimer aminocrotononitrile, (**XXXIII**) and trimer 4-amino-2,6-dimethylpyrimidine, (**XXXIV**), consistent with the hypothesis that formation of (**11**) proceeds *via* the Sm^{III} methyl complex. As this route does not involve redox chemistry (*c.f.* the initially discussed Sm^{II} reactivity), no evidence to support formation of the cyanide trimer, (**10**), was anticipated nor obtained under these conditions.

Formation of a nacnac moiety from acetonitrile has not previously been reported for any f element, however connectivity similar to the nacnac ligand has been observed upon reaction of acetonitrile with both U^{III} hydride and Th^{IV} hydride species, with a second nitrile insertion to form a trimerised acetonitrile complex, Equation 3-10. The uranium and thorium complexes are isomorphous.[172] The third unit of acetonitrile, included in addition to the „nacnac'-type intermediate implied earlier, is indicated in the product of Equation 3-10.

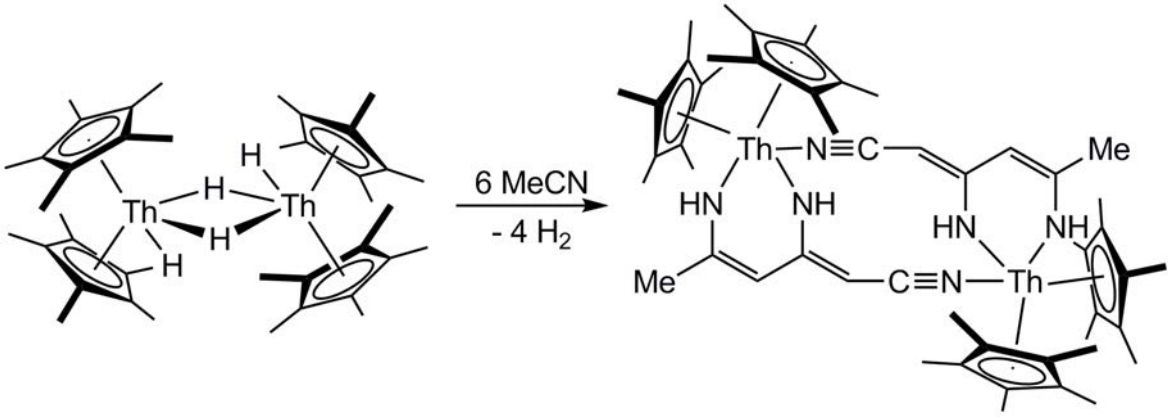

Equation 3-10

In addition to formation of the acetonitrile dimers, *cis*- and *trans*-aminocrotononitrile (**XXXIII**), GC-MS analysis of the reaction solution following the reaction between (**9**) and excess MeCN at 50 °C for 18 hours revealed the presence of a

single dominant trimerisation product, 4-amino-2,6-dimethylpyrimidine, (**XXXIV**). Complex (**XXXIV**) has previously been accessed *via* reaction of aminocrotononitrile, (**XXXIII**), and MeCN in the presence of hydroxide, Equation 3-11;[173] thus the role of the samarium centre in the reaction to produce the trimerisation product could not be unequivocally established and was deemed outside the scope of the project.

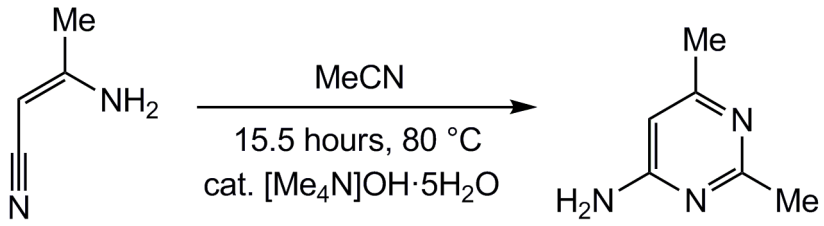

(**XXXIII**) (**XXXIV**)

Equation 3-11

GC-MS analysis of the reaction of excess MeCN and a benzene solution of (**XVI**) (0.3 mL benzene, 10 mg (**XVI**), 1.16 x 10^{-5} mol) at 50 °C for 18.5 hours and comparison with three concentration standards of (**XXXIII**) (0.96, 0.096 and 0.0096 mg.mL^{-1} *cis/trans*-aminocrotononitrile, linear fit with R = 0.999) indicated formation of 0.95 mg (**XXXIII**) (1.16 x 10^{-5} mol) and 2.13 mg (**XXXIV**) (1.73 x 10^{-5} mol). The yield of dimerisation and trimerisation products initially appears low in relation to the mass of samarium(II) material, however direct molar comparison between these catalytic products and the starting material is erroneous.

The reaction between [$(Et_8N_4Me_2)Sm(NCMe)_2$] and excess MeCN at 50 °C over 18 hours has been shown to proceed *via* a proportionally significant but undetermined (possibly in the order of 50 %, depending on the kinetics of the competing reactions) amount of Sm^{III}-cyanide trimer, (**10**), resulting in liberation of a $Me^{\bullet}$ fragment and subsequent formation of the Sm^{III}-nacnac complex, (**11**). Complex (**11**) must then dissociate to provide the Sm^{III}-hydride species required for formation of aminocrotononitrile, (**XXXIII**), as described by Figure 3-2, which may react with ambient

acetonitrile (independent of the samarium centre) to form 4-amino-2,6-dimethylpyrimidine, (**XXXIV**). Given GC-MS analysis reproducibly indicates H(nacnac), the concentration of which is dependent upon the initial cleavage of MeCN, is present in higher concentration than both (**XXXIII**) and (**XXXIV**); thus only a small fraction of the initial concentration of samarium can be present as the catalytically active hydride. As such, only a fraction of the initial 1.16×10^{-5} moles of samarium is available at any time to dimerise acetonitrile, and the total yield of dimer and trimer is significant. Quantification of this process, while desirable, is beyond the scope of this project.

Undertaking the reaction described by Equation 3-9 at 80 °C results in a significant decrease in relative concentration of *cis/trans*-aminocrotononitrile and H(nacnac) relative to the concentration of the trimerisation product, 4-amino-2,6-dimethylpyrimidine. This result is consistent with either higher catalytic activity at elevated temperature or the increased secondary conversion of dimer to trimer at this temperature. At 120 °C, an increase in the number of minor alternative products is observed.

3.3.2 Reactions with Nitriles; N≡C−R, for R = *t*-Bu

The reaction of excess *t*-BuCN with $[(Et_8N_4Me_2)Sm(THF)_2]$, (**XVI**), in benzene at room temperature initially results in a dark green solution. Removal of solvent and excess *t*-BuCN *in vacuo* at room temperature provides a green powder; redissolution of this powder in benzene provides a purple solution from which purple crystals of the Sm^{II} 1:1 adduct $[(Et_8N_4Me_2)Sm(NC\textit{t}\text{-Bu})]$, (**12**), were isolated following concentration of the solution, Equation 3-12.

Attempts to isolate the initial dark green complex were not successful, however addition of C_6D_6 to the dark green precipitate after removal of all volatiles *in vacuo* provided a purple solution shown by ^1H NMR spectroscopy to be consistent with the dark

green solid being the bis(adduct) by integration of the *t*-Bu proton resonance of the nitrile (1.66 ppm)/various macrocyclic proton resonances. The single resonance of the *t*-Bu group is indicative of rapid ligand exchange in solution. Concentration of this purple solution provided purple crystals of (**12**). Addition of C_6D_6 to an isolated sample of (**12**) confirms the loss of the second *t*-BuCN ligand by ^{1}H NMR spectroscopy at this stage to give the 1:1 adduct (3.55 ppm), consistent with the observation that the stability of the 2:1 adduct in benzene is dependent upon the presence of excess nitrile.

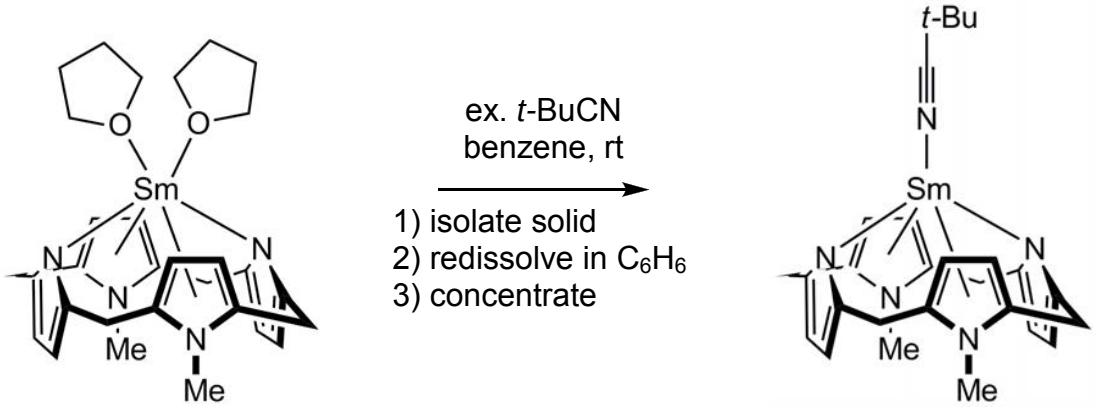

(**XVI**) (**12**)

Equation 3-12

Thermal decomposition of the *t*-BuCN adduct, (**12**), was investigated given the previously described reductive cleavage and catalytic C−C coupling reactivity of MeCN observed at elevated temperatures for the less bulky nitrile. Heating a C_6D_6 solution of the 1:1 *t*-BuCN adduct (**12**) at 52 °C was undertaken for 16 hours and shown to effect no change to the ^{1}H NMR spectrum. However, continued heating of the same solution for an additional 18 hours at 77 °C resulted in a red solution over orange crystals of the previously identified cyanide trimer, (**10**). GC-MS analysis of the reaction solution showed a complex mixture of oligomers of *t*-BuCN. Similarly, C_6D_6 solutions of (**12**) react with excess *t*-BuCN at 77 °C over two days to provide a complex mixture of *t*-BuCN oligomers by GC-MS analysis. Due to the large range of observed products, no further attempts were made to characterise these oligomerisation products. GC-MS analysis

showed that isobutane and isobutane are the dominant by-products derived from *t*-Bu radical decomposition under both sets of conditions, resulting from the initial reductive C−C cleavage of *t*-BuCN.[159]

The stability of the 1:1 *t*-BuCN adduct, (**12**), and instability of the 1:1 MeCN adduct, Section 3.3.1, is a result of the sterically restricted binding groove. Reductive cleavage of the respective nitrile to afford the Sm^{III} cyanide trimer, (**10**), and liberate *t*-$Bu^{\bullet}$ and $Me^{\bullet}$, respectively, is observed, *vide supra*. Reduction of $Me^{\bullet}$ by unreacted Sm^{II} results in the Sm^{III} methyl complex, (**XX**); the same reduction of *t*-$Bu^{\bullet}$ would result in formation of the Sm^{III} *tert*-butyl complex, $[(Et_8N_4Me_2)Sm(t\text{-}Bu)]$, of which there is no synthetic evidence. At Sm−alkyl bond lengths (*cf.* $[(Et_8N_4Me_2)SmMe]$[75]), the terminal methyl groups of the *t*-Bu moiety would not physically fit within the narrow, one-atom-wide binding groove. Hence, formation of $[(Et_8N_4Me_2)Sm(t\text{-}Bu)]$, and any subsequent nitrile insertion chemistry to form a *t*-Bu analogue of the nacnac moiety, are prevented on steric grounds. A similar rationalisation for the novel end-on binding of dinitrogen observed in $[\{(Et_8N_4Me_2)Sm\}_2(\mu\text{-}\eta^1\text{:}\eta^1\text{-}N_2)]$, (**7**), is presented in Section 2.3.4.

	MeCN	***t*-BuCN**
2:1 adduct	Isolated, (**9**)	Observed in solution
1:1 adduct	Decomposed, (**10**)	Isolated, (**12**)

Table 3-1 Reactivity of nitriles with $[(Et_8N_4Me_2)Sm(THF)_2]$, (**XVI**).

A summary of the observed adduct formation reactivity for acetonitrile and *tert*-butylnitrile with $[(Et_8N_4Me_2)Sm(THF)_2]$, (**XVI**), is given, Table 3-1. Reaction of (**XVI**) with excess nitrile for both MeCN and *t*-BuCN results in a dark green, insoluble precipitate of the bis(adduct) by X-ray crystallography, in the case of MeCN (**9**), and inferred from ^{1}H NMR spectroscopy, in the case of *t*-BuCN, *vide supra*. In both cases,

removal of all volatile materials (which includes any excess reagent) and addition of fresh aromatic solvent to the dark green solid results in a purple solution. Purple crystals of the 1:1 adduct of *t*-BuCN, (**12**), were isolated in this manner from this solution. For MeCN, conversely, the purple solution is fleeting, bleaching to a colourless solution over five minutes. Standing this solution at room temperature overnight provided orange crystals of the Sm^{III} cyanide trimer, (**10**), Section 3.3.1, by satisfactory elemental analysis. The initial formation of a purple solution is consistent with a 1:1 MeCN adduct.

3.3.3 Reactions with Isonitriles; C≡N−R, for R = *t*-Bu

Addition of a molar excess of *t*-butylisonitrile, *t*-BuNC, to a purple benzene solution of $[(Et_8N_4Me_2)Sm(THF)_2]$, (**XVI**), followed by heating at 77 °C results in an orange solution within two minutes. Overnight heating at 77 °C provided well-formed orange crystals of the samarium(III) cyanide trimer, (**10**), Equation 3-13, as previously observed, Section 3.3.1. Complex (**10**) is again a result of reductive cleavage, however in the case of the isonitrile, the cleavage occurs at the C−N bond rather than at the C−C bond, as observed for nitriles, *vide supra.*

GC-MS analysis of the quenched reaction solution obtained *via* Equation 3-13 revealed the remaining (excess) *t*-BuNC, *t*-BuCN (in approximately 1:1 ratio), a small amount of *t*-Bu(H)C=N−*t*-Bu, and both isobutane and isobutene as the dominant by-products derived from the *t*-Bu fragment. Observation of isobutane, isobutene and the isomerisation of the isonitrile to the nitrile has previously been reported for C−N cleavage of *t*-BuNC by a ruthenium complex.[159]

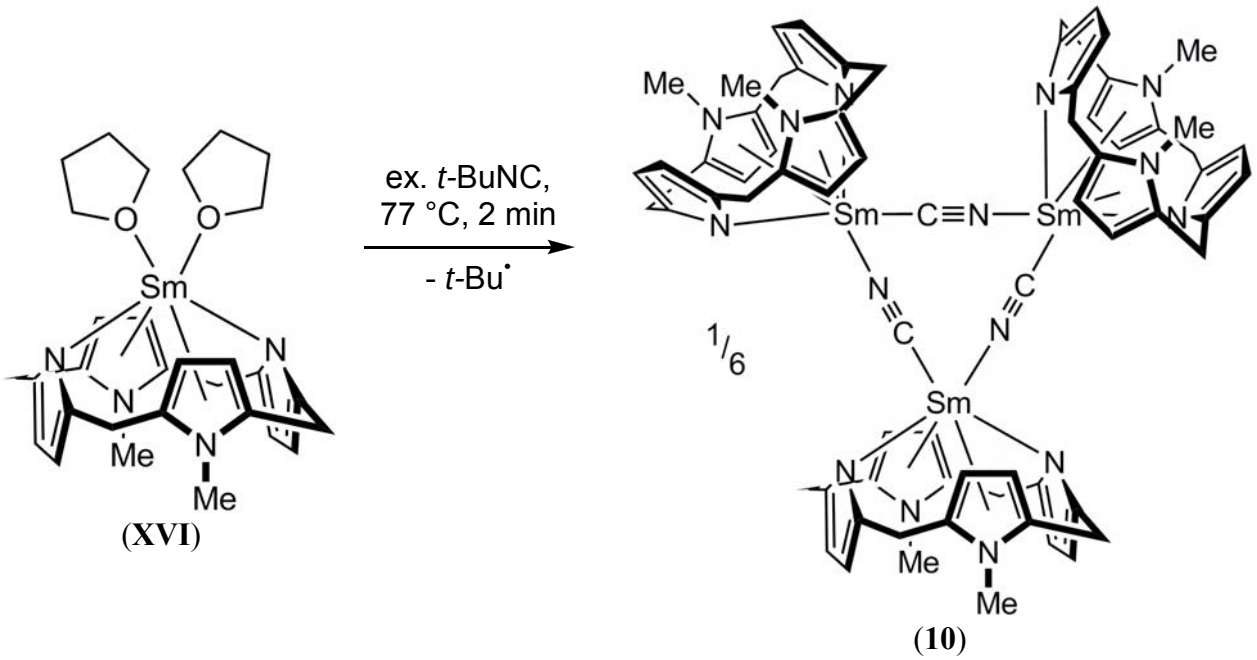

(**XVI**) (**10**)

Equation 3-13

As established in Section 3.1, homolytic cleavage of the N−R bond of isonitriles has previously been observed, for example upon reaction with decamethylsamarocene[155] and decamethylvanadocene[156]; however even at elevated temperature, the reaction described by Equation 3-13 proceeds significantly slower than reported for decamethylsamarocene at room temperature. The reduction in reaction rate is ascribed to the increase in steric bulk provided by the modified porphyrinogen employed; indeed, the only known stable Sm^{II} isonitrile adduct is observed in the heavily substituted $[\{C_5H_2(t\text{-}Bu)_3\}_2Sm(C{\equiv}N\text{-}2,6\text{-}Me_2C_6H_3)]$ system.[154]

The reaction of $[(Et_8N_4Me_2)Sm(THF)_2]$, (**XVI**) and *t*-BuNC at room temperature in benzene proceeds to completion slowly overnight, again providing the trimeric cyanide complex, (**10**), by satisfactory elemental analysis, in addition to variable yields of a red insoluble crystalline product. The latter product was identified by X-ray crystallography as the C−C coupled Sm^{III} iminoacyl complex $[(Et_8N_4Me_2)Sm(t\text{-}BuNCt\text{-}Bu)]$, (**13**), Equation 3-14. Complex (**13**) is insoluble in benzene, toluene, diethyl ether, pet. ether and

THF, precluding characterisation by NMR spectroscopy. A single crystal of (**13**) was submerged in deionised H_2O and observed through a polarising microscope to maintain colour and cyrstallinity overnight, presumably indicating stability.

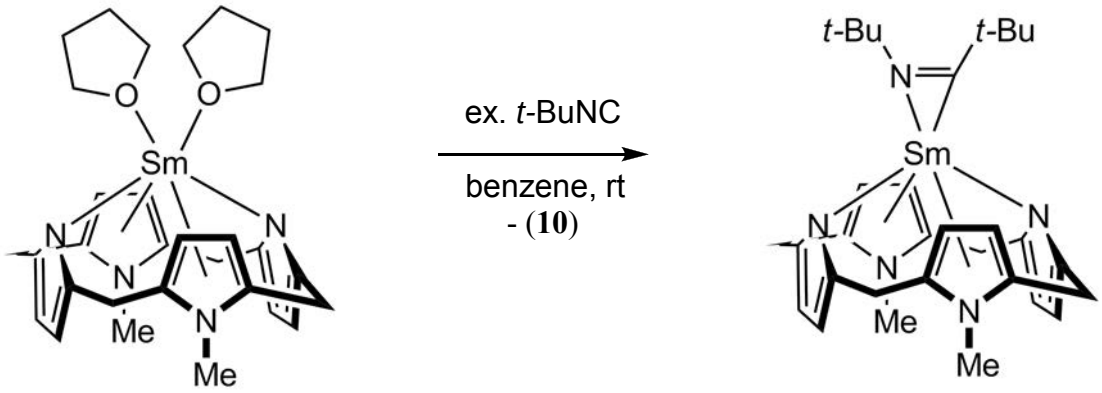

(**XVI**) (**13**)

Equation 3-14

The iminoacyl complex [($Et_8N_4Me_2$)Sm(*t*-BuNC*t*-Bu)], (**13**), is the first structurally characterised lanthanoid iminoacyl complex. A range of U^{IV} iminoacyl complexes have been reported *via* 1,1-addition to isonitriles, R′NC, of $(C_5H_5)_3UR$ for R = Me, R′ = Cy[174], R = *n*-Bu, R′ = *t*-Bu, Cy, 2,6-$Me_2C_6H_3$ (by IR and NMR spectroscopies only)[175]. 1,1- insertion between U^{IV} and a phenyl group has been reported for $(C_5Me_5)(COT)U(Ph)$ upon reaction with *t*-BuNC. Additionally, η^2-N,C binding of 2-metallated pyridine, $C_5H_4N^-$, in a U^{IV} complex has been reported.[176] Two yttrium iminoacyl complexes have been accessed *via* 1,1- insertion of both 2,6-$Me_2C_6H_3NC$ and *t*-BuNC into the Y−C bond of $(C_5Me_5)_2Y(CH_2C_6H_3Me_2\text{-}3,5)$.[177] In general, iminoacyl complexes have more commonly been accessed from lithium precursors prepared by the reaction of the appropriate isonitrile with an alkyl lithium reagent,[178] or by reaction with nitrilium salts, [RC≡NR′]X;[161] both routes allowing access to asymmetrically substituted complexes.

Literature precedent for trapping cleaved alkyl fragment, $R^{\bullet}$, from reductive cleavage of nitriles, RCN, rather than isonitriles, RNC, as is the case for (**13**), has been reported for

reactions of U^{III} with nitriles for R = Me, *n*-Pr, *i*-Pr *t*-Bu, which provide an equimolar mixture of $U^{IV}CN$ and the respective $U^{IV}R$ compounds.[179] Trapping of this nature has only been reported once in lanthanoid chemistry as the poorly characterised decamethylsamarocene analogue of (**13**), for R = Cy.[155] The reduction of *t*-BuCN with $[(C_5Me_5)_2Sm(THF)_2]$, (**IV**), resulted in formation of the ketimide complex $[(C_5Me_5)_2Sm(N{=}C(H)t\text{-Bu})(THF)]$ *via* formation of the intermediate Sm^{III} alkyl complex $[(C_5Me_5)_2Sm(t\text{-Bu})]$, with *β*-H elimination providing the required hydride intermediate, Scheme 3-3.[158] Independent synthesis of the ketimide from reaction of *t*-BuCN with $[\{(C_5Me_5)_2Sm(\mu\text{-H})\}_2]$ supports the hypothesis that nitrile addition occurs at the metal centre, Scheme 3-4.[158]

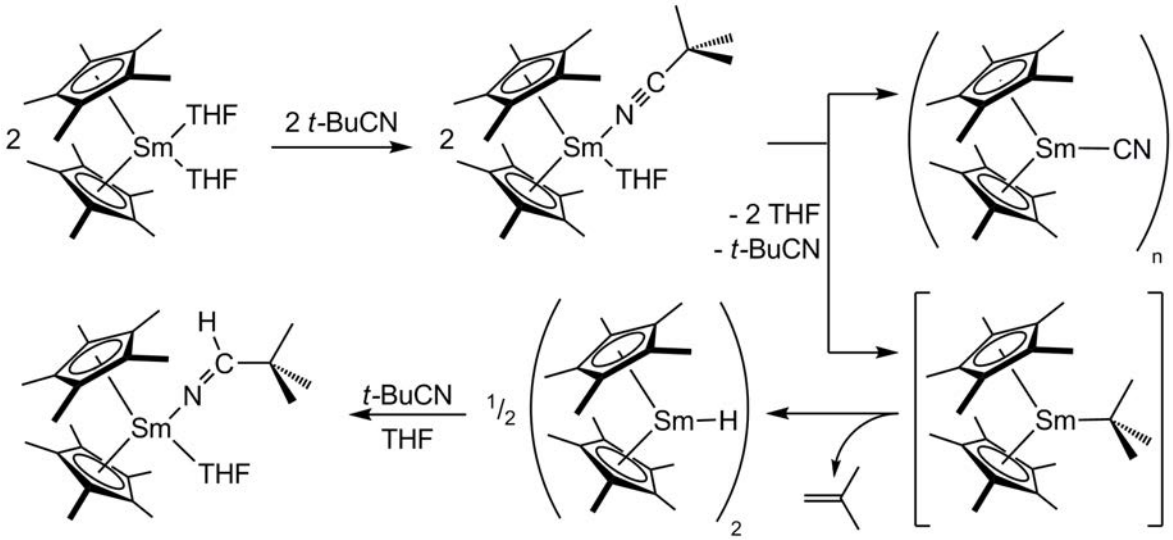

Scheme 3-3 Proposed synthesis of $[(C_5Me_5)_2Sm(NC(H)t\text{-Bu})(THF)]$, adapted from Evans *et al.*[158]

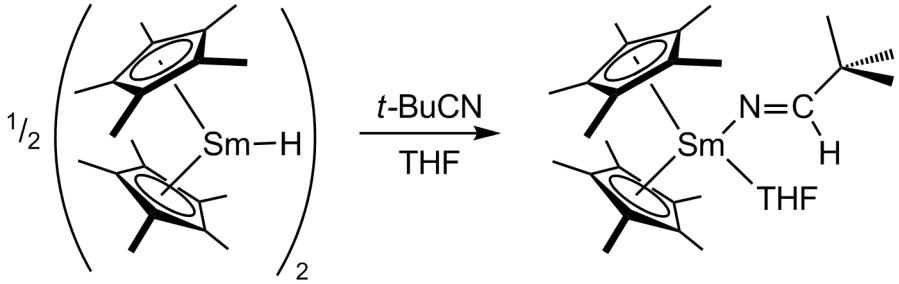

Scheme 3-4 Independent synthesis of $[(C_5Me_5)_2Sm(NC(H)t\text{-Bu})(THF)]$, adapted from Evans *et al.*[158]

At this stage, no detailed mechanistic information is available for the formation of [($Et_8N_4Me_2$)Sm(*t*-BuNC*t*-Bu)], (**13**). Thus, the reaction stoichiometry, stepwise or concerted nature, order of events, and specific involvement of the samarium centre are unknown, with many alternatives being possible in relation to the reaction conditions promoting single electron transfer, C−C bond formation and Sm coordination leading ultimately to the formation of the anionic (*t*-Bu−C=N−*t*-Bu)$^-$ ligand. However, as discussed above in relation to the stability of [($Et_8N_4Me_2$)Sm($NCMe)_2$], (**9**), *vs*. [($Et_8N_4Me_2$)Sm(NC*t*-Bu)], (**12**), Section 3.3.2, it is likely that steric restrictions would not permit the formation of [($Et_8N_4Me_2$)Sm(*t*-Bu)], the required intermediate to additionally coordinate *t*-BuNC, indicating that ligand formation may occur off-metal.

The absence of (**13**) at elevated temperature may relate to the reduced stability of the *t*-Bu$^\bullet$ fragment with regard to decay *via* established routes and/or the lower concentration of available Sm^{II} reagent due to rapid formation of the Sm^{III} cyanide trimer, (**10**).

3.3.4 Molecular Structures

3.3.4.1 Molecular Structure of [($Et_8N_4Me_2$)Sm($NCMe)_2$], (9)

Crystals of complex (**9**), Figure 3-3, belong to the orthorhombic space group *Cmcm* (No. 63), a = 22.412(5), b = 10.614(2), c = 17.762(4) Å, with four molecules in the unit cell. The asymmetric unit consists of one quarter of a molecule of (**9**) with the molecule lying on mm sites.

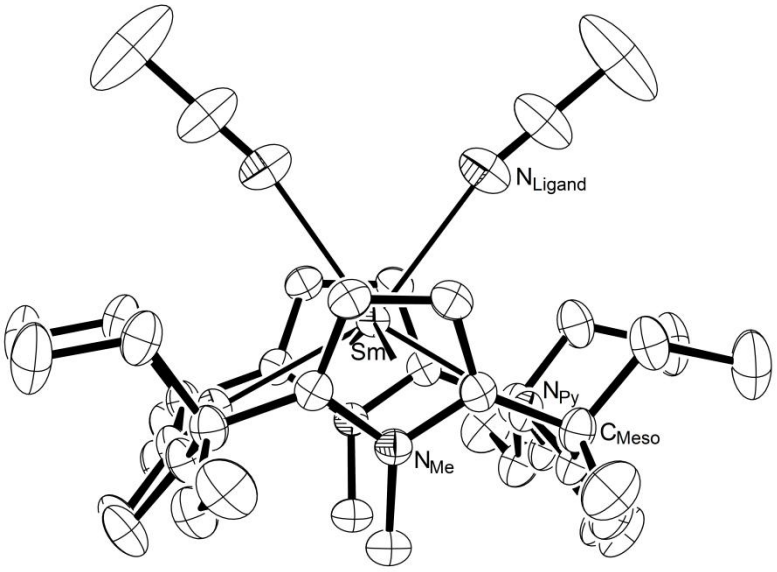

Figure 3-3 Molecular structure of (**9**) with thermal ellipsoids drawn at 30 % probability (protons omitted for clarity).

The molecular structure of (**9**) exhibits the standard η^1:η^5:η^1:η^5 macrocyclic binding mode. The Sm-(η^1-N_{Py}) distance is 2.624(3) Å and the Sm-(η^5-N_{Me}) distance is 2.72$_1$ Å, with a Sm−*meso* distance of 1.375(2) Å above the *meso*- plane of the macrocycle. The N_{Py}−*meso* and N_{Me}−*meso* interplanar angles are 52.18(13) and 77.07(9) °, respectively. Table 3-2 compares geometric features of the macrocycle for the bis(THF) adduct [($Et_8N_4Me_2$)Sm($THF)_2$], (**XVI**), and the bis(acetonitrile) adduct [($Et_8N_4Me_2$)Sm($NCMe)_2$], (**9**). Data for (**XVI**) are reported for a structure obtained using the same crystallographic conditions as (**9**) and may show minor variation from reported values.[71]

	$[(Et_8N_4Me_2)Sm(THF)_2]$ (**XVI**)	$[(Et_8N_4Me_2)Sm(NCMe)_2]$ (**9**)
$M-(\eta^1-N_{Py})$	2.667(2)	2.624(3)
$M-(\eta^5-N_{Me})$	2.75_5	2.72_1
$M-L_{donor\ atom}$	2.6491(18)	2.711(4)
L−M−L angle	69.89(8)	72.3(2)
M−*meso*	1.4794(17)	1.375(2)
N_{Py}−*meso*	49.92(7)	52.18(13)
N_{Me}−*meso*	73.24(7)	77.07(9)
Metallocene bend	154.4_4	158.9_2

Table 3-2 Comparison between geometric parameters of THF and acetonitrile adducts; L = ancillary ligand donor atom, bond lengths in (Å), bond angles in (°).

The Sm−N distance to the acetonitrile ligand (2.7 (4) Å) for (**9**) is consistent both with a neutral Lewis base donor interaction to the samarium(II) centre and demonstrates the weaker interaction observed for *N*-coordinating adducts compared to *O*-coordinating adducts, as per the bis(THF) adduct, (**XVI**), where $Sm-O_{THF}$ is 2.649(1) Å, Table 3-2. For the more weakly bound nitrile adduct, the metal centre resides deeper within the macrocyclic cavity, resulting in the observed increase in N_{Py}−*meso* and N_{Me}−*meso* interplanar and metallocene bend angles compared to the bis(THF) adduct, Table 3-2.

The acetonitrile ligands of (**9**) are not bound linearly to the samarium centre, with a Sm−N−C angle of 166.90(17) °, Figure 3-3, whilst the 1:1 *t*-BuCN adduct is linear, *vide infra*. The acetonitrile moiety, however, is linear (N−C−C = 179.9(9) °) with bond lengths typical of triple (N−C = 1.114(6) Å) and single (C−C = 1.444(8) Å) bonds, respectively.

3.3.4.2 Molecular Structure of $[\{(Et_8N_4Me_2)Sm(CN)\}_3]\cdot C_6H_6$, (10)

Formation of (**10**) was established through X-ray crystal structure determinations of several crystals owing to variability in visual crystal morphologies and synthetic routes to the complex, Sections 3.3.1-3. All crystal morphologies were found to be identical. Each cyanide ligand bridges two metal centres *via* ζ- bonding with the carbon and nitrogen atoms. Severe disorder is observed as the trimer resides on 3 symmetry sites.

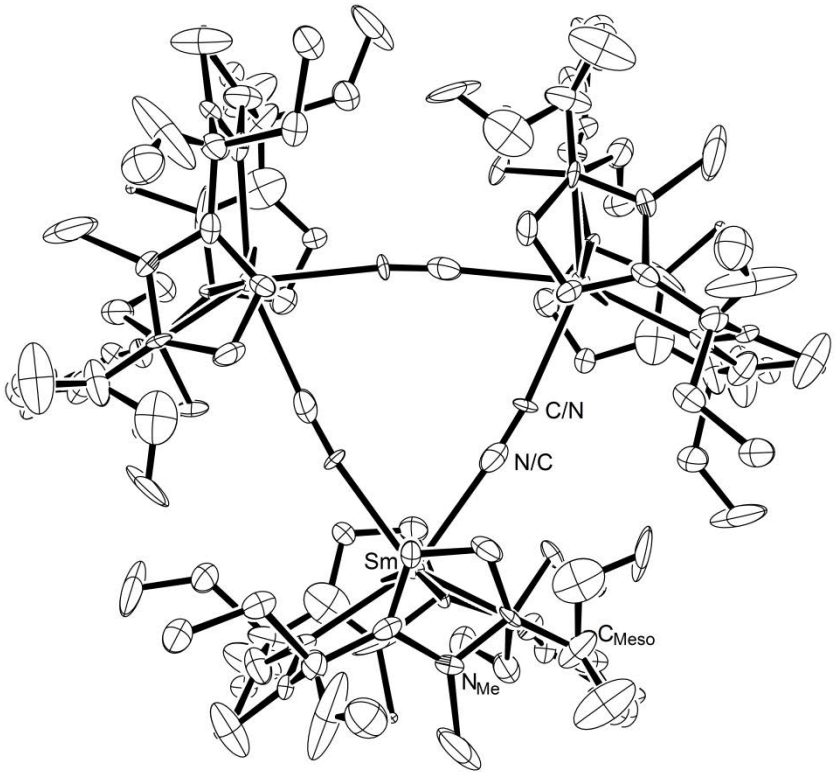

Figure 3-4 Molecular structure of (**10**) with thermal ellipsoids drawn at 50 % probability (Protons and extensive disorder omitted for clarity).

The severe disorder over sites relating to the inversion centre leads to many fractionally occupied and coincidental, or near so, C/N atom positions of the overlayed macrocycle orientations; as such, discussion is largely limited to connectivity of the complex that is nonetheless unequivocal, revealing the complex to be trimeric through bridging cyanide ligands. C/N linkage isomerism cannot be established owing to disorder on the $\bar{3}$ site. *C*-bound cyanides have been reported for terminally bound ligands in Ce^{III}

and U^{III} complexes[180]. The molecule exhibits the regular $\eta^1:\eta^5:\eta^1:\eta^5$ macrocyclic binding, with a Sm··· Sm separation of 6.23 Å.

3.3.4.3 Molecular Structure of $[(Et_8N_4Me_2)Sm(nacnac)]\cdot C_6H_6$, (11)

Crystals of (**11**) belong to the monoclinic space group $P2_1/n$ (No. 14), a = 14.14(5), b = 27.86(5), c = 23.24(4) Å, β = 107.709(11) °, with eight molecules in the unit cell. The asymmetric unit consists of two molecules of both (**11**) and benzene. Although satisfactory, the accuracy of the X-ray crystal structure refinement of (**11**) is not high, with a higher than desired R_{int} value of 0.1223. Both independent molecules in the asymmetric unit are similar in geometry, providing for the ranges of distances and angles quoted, *vide infra*.

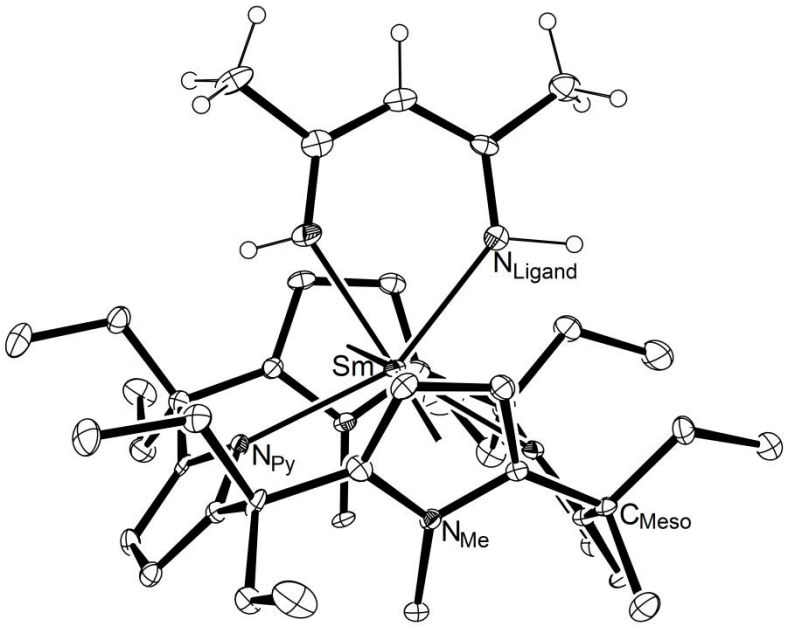

Figure 3-5 Molecular structure of (**11**). Thermal ellipsoids at 50 % probability (one molecule shown, macrocyclic protons and solvent omitted for clarity).

The molecular structure of (**11**) exhibits the standard $\eta^1:\eta^5:\eta^1:\eta^5$ macrocyclic binding mode, Figure 3-5. The Sm-(η^1-N_{Py}) distances range from 2.494(6) to 2.545(6) Å and the Sm-(η^5-N_{Me}) distances range from 2.61_6 to 2.65_4 Å. The Sm−*meso* distances range from 1.273(5) to 1.286(5) Å. The N_{Py}−*meso* interplanar angles are between 48.0(3) and

52.8(3) °, whilst the N_{Me}–*meso* interplanar angles are between 77.4(2) and 77.8(2) °. These metrics are consistent with the assigned Sm^{III} oxidation state.

Figure 3-6 N–C and C–C bond lengths of the nacnac moiety for both molecules of $[(Et_8N_4Me_2)Sm(nacnac)]$, (**11**).

The bond lengths within the nacnac moiety of (**11**) are consistent with delocalisation over the metallocycle, Figure 3-6. The bond lengths to the methyl groups are standard C(sp^2)–C(sp^3) single bond lengths, ranging from 1.478(8) to 1.518(8) Å. The nacnac ring approaches the binding groove at an angle of between 14.6(2) and 15.5(2) ° from vertical.

3.3.4.4 Molecular Structure of $[(Et_8N_4Me_2)Sm(tBuCN)]\cdot C_6H_6$, (12)

Crystals of (**12**) belong to the orthorhombic space group $Cmc2_1$ (No. 36), a = 17.460(6), b = 28.000(15), c = 18.760(4) Å, with eight molecules in the unit cell. The asymmetric unit consists of two half molecules of (**12**) and two half molecules of benzene residing on m centres.

The molecular structure of (**12**), Figure 3-7, exhibits the standard $\eta^1{:}\eta^5{:}\eta^1{:}\eta^5$ macrocyclic binding mode. The Sm-(η^1-N_{Py}) distances range from 2.550(6) to 2.579(5) Å and the Sm-(η^5-N_{Me}) distances range from 2.67_1 to 2.69_9 Å, with a Sm–*meso* distance of between 1.282(3) and 1.289(3) Å. The N_{Py}–*meso* interplanar angles are between 44.33(12) and 52.7(2) ° and the N_{Me}–*meso* interplanar angles are between 76.4(2) and 79.3(2) °, consistent with a Sm^{II} centre bound to one ancillary ligand.

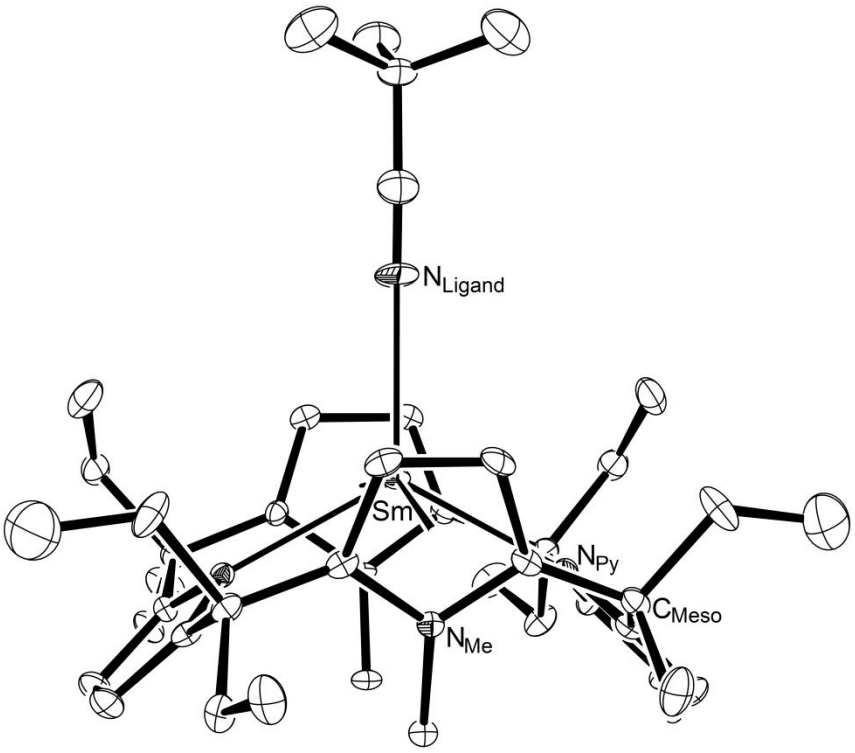

Figure 3-7 Molecular structure of (**12**) with thermal ellipsoids drawn at 50 % probability. One full molecule; solvent molecule and protons omitted for clarity.

The *t*-BuCN ligands bind directly from the top of the binding grooves (Sm−N−C are 176.1(9) and 179.5(9) °) and are pseudo-linear (N−C−C are 174.1(12) and 175.5(11) °). The bond lengths within the nitriles are consistent with triple (1.129(10) and 1.146(10) Å) and single bonds (1.458(10) and 1.461(10) Å). The Sm−N_{ligand} bond lengths, at 2.609(6) and 2.612(7) Å for (**12**), are much longer than the analogous Sm−N_{ligand} bond length reported for the Sm^{III} complex [$(Et_8N_4Me_2)Sm(N\{SiMe_3\}_2)$], at 2.314(2) Å,[181] and shorter than the Sm−N_{ligand} distance for the bis(acetonitrile) adduct, (**9**), at 2.711(4) Å, reflecting the reduction in effective nuclear radii with the reduction in coordination number.

3.3.4.5 Molecular Structure of [$(Et_8N_4Me_2)$Sm(*t*-BuNC*t*-Bu)], (13)

Crystals of [$(Et_8N_4Me_2)$Sm(*t*-BuNC*t*-Bu)], (**13**), Figure 3-8, belong to the orthorhombic space group *Cmcm* (No. 63), a = 21.06(6), b = 10.493(7), c = 19.3928(15) Å, with four molecules in the unit cell. The asymmetric unit consists of one quarter of one

molecule of (**13**) which sits on mm sites. Iminoacyl C/N disorder is present across a mirror plane and the *t*-Bu groups were refined isotropically due to their high thermal motion. The X-ray reflection data for (**13**) was collected on an Enraf Nonius TurboCAD4 spectrometer at -80 °C, Appendix A.

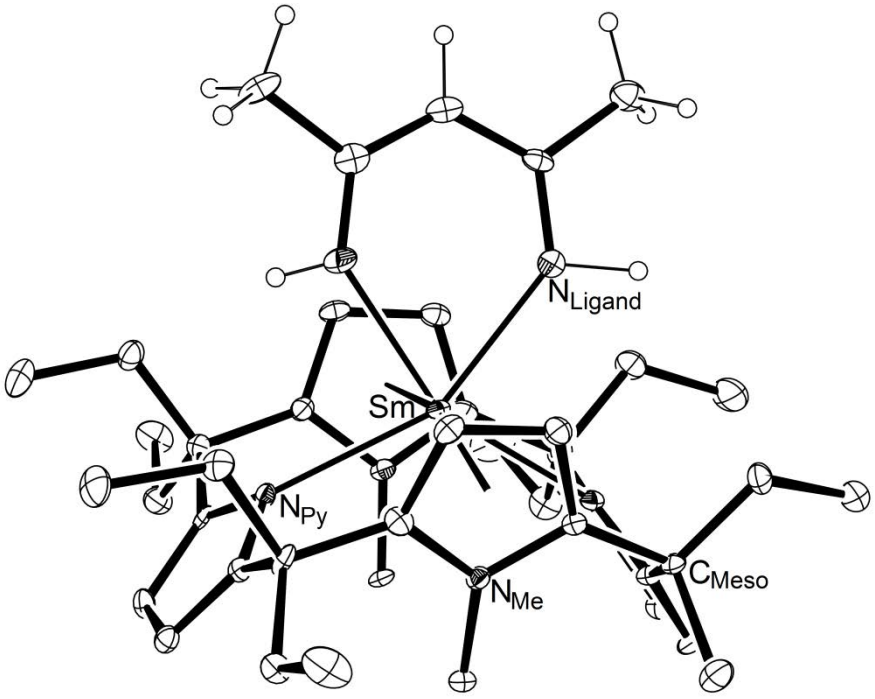

Figure 3-8 Molecular structure of (**13**) with thermal ellipsoids drawn at 50 % probability (protons omitted for clarity).

The molecular structure of (**13**) exhibits the standard $\eta^1{:}\eta^5{:}\eta^1{:}\eta^5$ macrocyclic binding mode. The Sm-(η^1-N_{Py}) distance is 2.581(11) Å and the Sm-(η^5-N_{Me}) distance is 2.64_6 Å, with a Sm−*meso* distance of 1.32(1) Å. The N_{Py}−*meso* and N_{Me}−*meso* interplanar angles are 47.9(4) °, and 77.0(4) °, respectively.

The Sm^{III}–$N_{iminoacyl}$ and Sm^{III}–$C_{iminoacyl}$ bond lengths are 2.397(13) Å, however this distance is likely an average due to disorder. The N=C bond length is 1.32(2) Å, consistent with a double bond; the N/C−*t*-Bu distance is as expected for a single bond, given the N/C disorder (1.468(18) Å).

3.4 Experimental

Synthesis of [($Et_8N_4Me_2$)Sm(NCMe)$_2$], (9)

Addition of excess acetonitrile (two drops) to a benzene solution (1 mL) of [($Et_8N_4Me_2$)Sm(THF)$_2$], (**XVI**), (1.16 x 10^{-2} mmol, 10 mg) immediately produces a dark green solution from which dark green insoluble material precipitates within 20 minutes at room temperature in quantitative yield (9 mg). A small, dark green crystal of the title compound suitable for X-ray crystal structure determination was obtained *via* this method. Removal of all volatiles *in vacuo* provides a dark green powder that is unstable in benzene and toluene, preventing NMR spectroscopic analysis and hindering elemental analysis as the isolated compound undergoes further reactivity upon washing.

Synthesis of [{($Et_8N_4Me_2$)Sm(CN)}$_3$]·C_6H_6, (10)

A solution of [($Et_8N_4Me_2$)Sm(THF)$_2$] (1.04 x 10^{-2} mmol, 9 mg) was prepared in benzene (1 mL). Neat *tert*-butylisocyanide (0.536 mmol, 22 mg) was added to the samarium solution. The reaction was heated at 77 °C for 18 hours, during which time small, single orange crystalline prisms of the title complex formed. The supernatant solution was removed and the insoluble crystals were washed with fresh benzene (2 x 0.2 mL) and dried *in vacuo* to reveal the title complex as insoluble orange blocks, preventing NMR characterisation (7 mg, 87 %).

Anal. Calcd.: C, 64.01; H, 7.34; N, 9.10 ($C_{117}H_{162}N_{15}Sm_3$•C_6H_6)

Found: C, 64.37; H, 7.06; N, 8.64

Synthesis of [($Et_8N_4Me_2$)Sm(nacnac)]·C_6H_6, (11)

Addition of excess acetonitrile (two drops) to a benzene solution (1 mL) of [($Et_8N_4Me_2$)Sm(THF)$_2$], (**XVI**), (1.16×10^{-2} mmol, 10 mg) and heating the reaction at 50 °C for 18 hours results in a pale yellow supernatant solution and small orange crystals of (**10**). Filtration of the supernatant followed by concentration of the solution by slow evaporation in the glovebox provided small yellow crystals of the title compound suitable for X-ray crystal structure determination. Due to contamination from the observed catalytic activity, small reaction scale, and the aforementioned subtle concentration and temperature effects in formation of (**11**) involving methyl radical trapping, Section 3.3.1, the isolation of (**11**) could not be repeated and further characterisation data could not be obtained.

Synthesis of [($Et_8N_4Me_2$)Sm(NC*t*-Bu)]·C_6H_6, (12)

A solution of [($Et_8N_4Me_2$)Sm(THF)$_2$] (1.04×10^{-2} mmol, 9 mg) was prepared in benzene (1 mL). To this solution was added *tert*-butyl nitrile (0.536 mmol, 22 mg). The solution was left at room temperature for 18 hours and then all volatiles were removed *in vacuo*. Fresh benzene was added (0.5 mL) to effect dissolution and then allowed to evaporate, providing purple crystals of the title compound (9 mg, 98%). Satisfactory elemental analysis could not be obtained.

^{1}H NMR (C_6D_6, 299.888 MHz, RT, ppm): δ = -26.42 (s, 4H, 2 CH_2), -10.06 (s, 12H, 4 CH_3), -8.07 (s, 4H, 2 CH_2), -0.62 (s, 12H, 4 CH_3), 0.62 (s, 4H, 2 CH_2), 1.73 (s, 4H, 4 CH), 3.55 (s, 9H, CCH_3), 5.56 (s, 4H, 2 CH_2), 13.77 (s, 4H, CH), 50.28 (s, 6H, 2 NCH_3)

Synthesis of [($Et_8N_4Me_2$)Sm(*t*-BuNC*t*-Bu)], (13)

A solution of [($Et_8N_4Me_2$)Sm(THF)$_2$] (1.16 x 10^{-2} mmol, 10 mg) was prepared in benzene (1 mL) and filtered through a glass wool plug in a small Pasteur pipette. Neat *tert*-butylisocyanide (0.536 mmol, 22 mg) was similarly filtered into the dark purple samarium solution. The reaction was allowed to stand at room temperature for 18 hours, whereupon large red crystalline blocks of the title compound formed concomitant with small orange crystalline prisms of (**10**). Large red crystals of the title compound were separated with a spatula and washed twice with fresh benzene (0.4 and 0.2 mL) and dried *in vacuo* (2 mg, 19 % based on total Sm). The complex is insoluble after initial precipitation, preventing NMR characterisation.

Anal. Calcd.: C, 65.83; H, 8.46; N, 8.17 ($C_{47}H_{72}N_5Sm$)

Found: C, 65.83; H, 8.45; N, 8.25

Chapter 4

Pyridines and Samarium(II)

4.1 Introduction

Pyridine is a six-membered aromatic *N*-heterocycle that is more basic than nitriles and furans.[182] It finds use as an aprotic aromatic solvent with the potential to ligate Lewis acidic metals and form coordination compounds *via* the lone pair centred on the nitrogen atom.

Pyridine has been used as a coordinating solvent in lanthanoid chemistry since the 1950s,[8, 9] and has been employed numerously since. Deacon *et al.,*[183] Froelich *et al*.,[184] Mashima *et al.,*[185] Leverd, Rinaldo and Nierlich,[186] and Cui *et al.*,[187] all provide examples of the use of pyridine as a solvent and subsequent coordination to form lanthanoid−pyridine adducts. Clark *et al.* reported stoichiometric addition of pyridine (py) to displace THF in complexes of the type $Sm(OAr)_3(THF)_{2-n}(py)_n$ and isolated complexes for n = 0, 2 and also a tris(pyridine) adduct (Ar = 2,6-diisopropylphenyl).[188] 12-membered mixed metal, isocarbonyl linked rings of molybdenum and either samarium or ytterbium were synthesised and shown to breakup upon addition of pyridine. The resulting pyridine adducts of the mixed metal complexes were not isolable.[189] Melman, Emge and Brennan substituted pyridine for THF ligands in their work on octonuclear lanthanoid sulfide cluster complexes in a failed attempt to stabilise their complexes at room temperature.[39] Freedman, Emge and Brennan found that pyridine can replace THF without disrupting the solid state structure of the $(L)_8Sm_8Se_6(SPh)_{12}$ cluster, L = py, THF. They also found that performing the reaction of $Sm(SePh)_3$ with elemental sulphur in

pyridine quadruples the yield of the same reaction performed in THF. They attributed the higher yield to the greater basicity of pyridine, which displaces bridging SePh from the inner coordination sphere of the metal more effectively than THF, facilitating reaction.[190] Pyridine has also been used to stabilise a samarium(II) tellurolate complex, $(py)_5Sm(TePh)_2$, which is synthesised *via* reduction of elemental samarium in pyridine with PhTeTePh.[191] A recent study reported by Agarwal and Kumar has investigated the effect of pyridine coordination on the stereochemistry of a series of lanthanoid complexes in the presence of different anions (Cl^-, NCS^- and ClO_4^-).[192]

As pyridine has been employed extensively as a ligand and solvent, so have more complex analogues of pyridine. Clegg *et al*. have investigated substituted pyridines (such as 4-dimethylaminopyridine) as potential ligands with samarium- and terbium$(acac)_3$ complexes for use as triboluminescent materials (compounds that emit light when fractured and have potential application as structural damage sensors).[193]

Alkyl- and arylation of pyridines leads to more sterically demanding ligands. Graddon and Watton found that the stability of divalent transition metal adducts of substituted pyridines decreases in the order 4-Mepy > py > 2-Mepy > 2,6-Me_2py.[194] Richardson, Wagner and Sands employed 2-, 4-, 2,4- and 2,6- methyl substituted pyridines in their study of $Ln(acac)_3 \cdot H_2O \cdot$py complexes, finding that, in all likelihood, the pyridines were interacting with coordinated water molecules rather than the metal itself.[195] Similarly, Weakley reported crystal structures of lanthanoid adducts of 4,4′-bipyridine in aqueous systems where the 4,4′-bipyridine ligand is hydrogen bonded to the ligating water molecules and is not directly coordinated to the metal.[196] 4-Phenylpyridine was employed by Brady *et al.* in 2002 in an attempt to replace coordinating THF and provide a more stable $[Sm\{N(SiMe_3)_2\}_2(4\text{-Phpy})_2]$ complex for X-ray crystal structure determination;

however, isolation of the desired compound was not achieved.[197] Sidorov *et al.* employed 2-phenylpyridine in rhodium "Chinese lantern" complexes, where 2-Phpy outcompeted solvent MeCN molecules to from an unsymmetrical "lantern dimer".[198]

Fedushkin *et al.* reported the reductive coupling of pyridine upon its addition to thulium diiodide, TmI_2, forming a dianionic bridge between two $TmI_2(py)_4$ units, Equation 4-1.[199] Similar reactivity has been observed for the less reducing decamethylsamarocene reagent, $[(C_5Me_5)_2Sm]$, (**V**), which shows similar reactivity to provide $[\{(C_5Me_5)_2Sm(py)\}_2(\mu\text{-}N_2C_{10}H_{10})]$ upon addition of pyridine.[200]

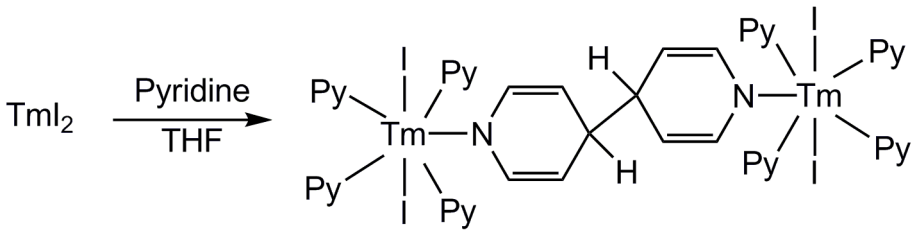

Equation 4-1

Durfee *et al.* reported reductive coupling of pyridine ligands, again through the 4-position, upon reaction with a titanium(II) complex intermediate.[201] Birch and Karakhanov showed that 4-alkylpyridines react with $Li{-}NH_3$ followed by an alkylating agent to reductively couple the alkylpyridine at the 4- position. Reductive coupling for both symmetric ($R^{1,2}$ = Me) and asymmetric (R^1 = Me, R^2 = H, Me, *n*-Pr and CO_2Me) substitutions show that limited alkyl steric bulk at the 4- position does not prevent coupling, Equation 4-2.[202] Dorogy Jr. and Schram also demonstrated reductive coupling of γ-picoline *via* reaction of the trimethylaluminium reagent $Me_3Al{\cdot}4\text{-}MePy$ with two equivalents of lithium.[203] The 1,1′-4,4′-tetrahydro-4,4′-dimethylbipyridine moiety was not able to be isolated, even *via* derivatisation to the previously reported *N*-carboxyethyl or *N*-methyl[202] analogues.

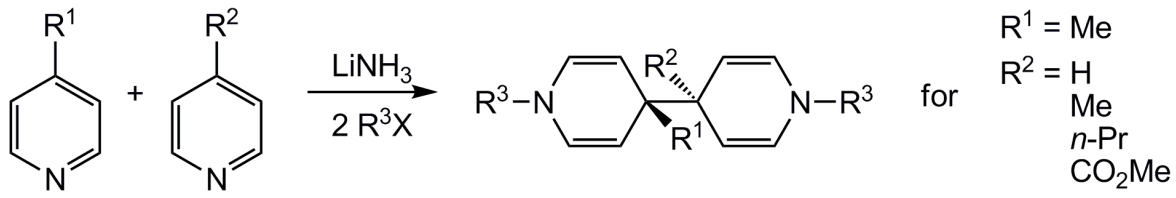

Equation 4-2

Ethyl-1,4-dihydropyridine-1-carboxylate (obtained *via* Birch reduction of pyridine and subsequent addition of diethyl carbonate) has been reduced by excess potassium *tert*-butoxide in DMSO under argon. The resulting potassium hydropyridide was stable at room temperature for approximately one hour, whereupon it converts to dimeric potassium 4,4-bis(hydridopyridide), presumably accompanied by loss of H_2, Equation 4-3.[204]

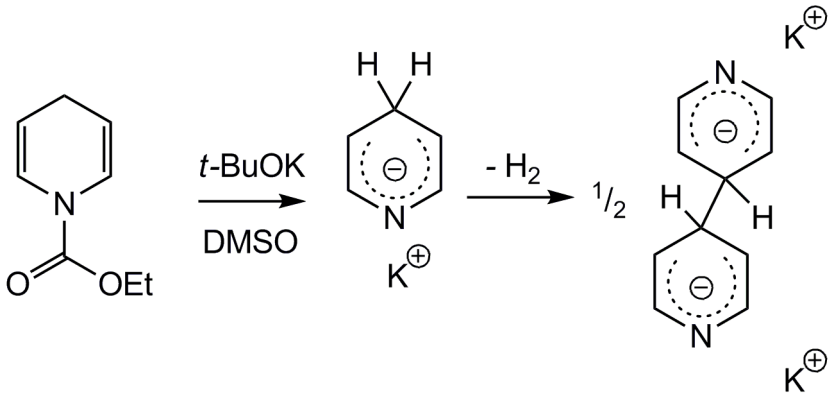

Equation 4-3

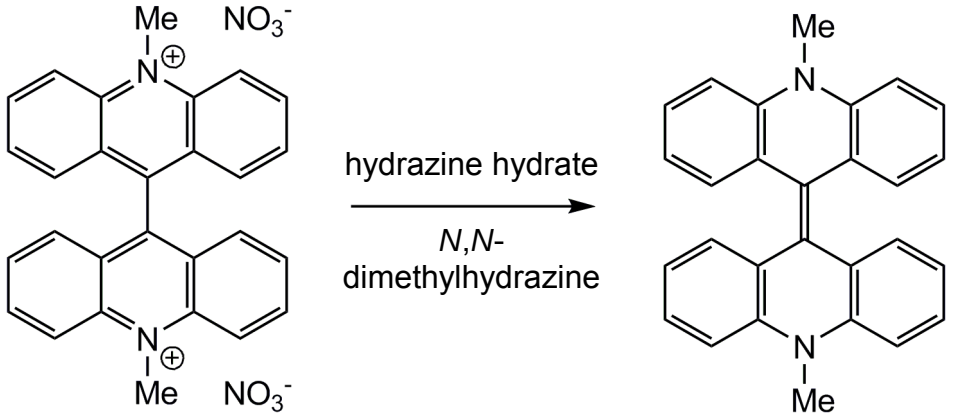

Equation 4-4

Papadopoulos and Nikokavouras showed that lucigenin, an analogue of 4,4′-bipyridine, could be reduced by two electrons (*via* nucleophilic addition of hydrazine

hydrate or *N*,*N*-dimethylhydrazine) to form N,N′-dimethyl-9,9′-biacridylidene, Equation 4-4.[205]

More complex pyridine based ligands include benzannulated examples such as monodentate quinoline based ligands and bidentate ligands based on 2,2′-bipyridine (2,2′-bipy) and 1,10-phenanthroline (phen). The chemistry of the lanthanoids and pyridines, quinolines, bipyridines and phenanthrolines was investigated in 1972 by Rohatgi and Sen Gupta, who observed a range of Ln^{III}–salicylaldehyde complexes which formed bis(pyridine), bis(quinoline), bipyridine and phenanthroline adducts.[206] Mixed metal aluminium/samarium complexes have been shown to form adducts of THF, pyridine and 1,10-phenanthroline.[207] Hasegawa *et al.* compared the emission properties of $Sm^{III}(hfa)_3(phen)_2$ (hfa = hexafluoroacetylacetonato) in pyridine, acetone and acetonitrile and found that crystals grown in pyridine had a lower coordination number as a molecule of pyridine had displaced 1,10-phenanthroline in the complex, causing significantly higher emissions. Kumar and Singh formulated Sm^{III} complexes with both 2,2′-bipy and phen bound as neutral adducts.[208]

The aqueous chemistry of 4,4′-bipyridine and samarium(III) has also been investigated by Czakis-Silikowska and Radwanska-Doczekalska, who formulated air stable bis(4,4′-bipy) adducts of lanthanoid complexes from lanthanoid bromides.[209] Czakis-Silikowska, Radwanska-Doczekalska and Markiewicz studied the thermal dehydration and subsequent decomposition of $Ln(NCS)_3(4,4'\text{-bipy})_2 \cdot 5H_2O$ for Ln = La, Pr, Nd, Sm, Eu and Y.[210]

Investigations of organic couplings by SmI_2 undertaken by Weitgenant, Mortison and Helquist showed that reactions between aldehydes or ketones and derivatives (benzylic

acetates) of 1,10-phenanthroline, quinoline, pyridine and 2,2′-bipyridine in the presence of SmI_2 resulted in a series of (2-hydroxyalkyl) heteroaromatics, Equation 4-5.[211]

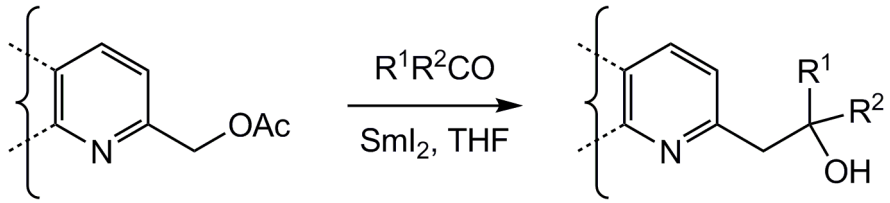

Equation 4-5

Birch and Lehman systematically studied metal-ammonia reductions of substituted quinolines in the presence of various alkylating agents, finding 2-, 3-, 4- and 8-methylquinolines behave similarly. They found no evidence for two electron reduction of a quinoline or reductive coupling of quinolines.[212] Crooks and Bard investigated the reductive dimerisation of quinoline and acridine by electrochemical techniques, finding that at elevated temperatures the dimerisation is reversible.[213] Grignon-Dubois *et al.* found that lithium reduction of 2-methylquinoline in the presence of Me_3SiCl in THF resulted in reductive coupling to give *N*,*N*′-bis(trimethylsilyl)-1,1′,4,4′-tetrahydro-4,4′-biquinaldine as a secondary product as the (*R*,*S*) isomer in 23% yield, Equation 4-6a. Undertaking the reaction with magnesium rather than lithium gave the (*S*,*S*) isomer of the same product in 80% yield, Equation 4-6b, although their attempts to isolate the compound (including *via* derivatisation) were unsuccessful.[214]

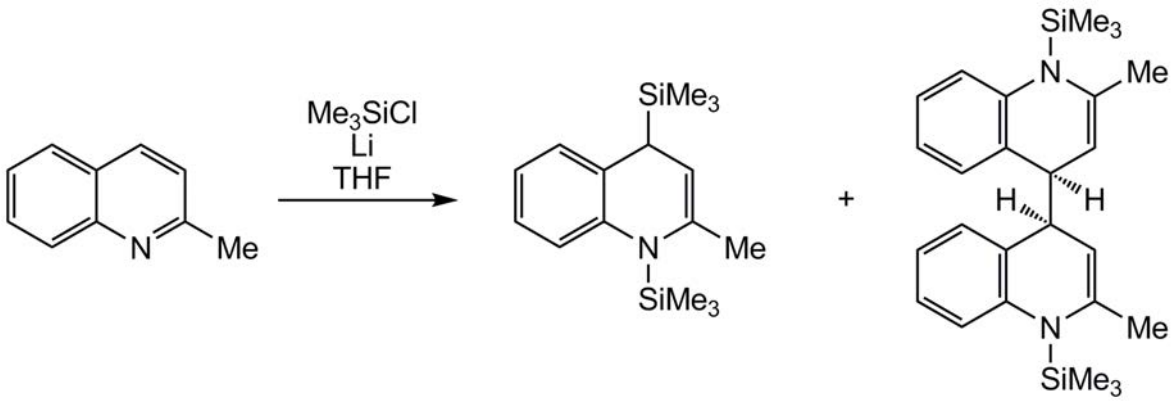

Equation 4-6a

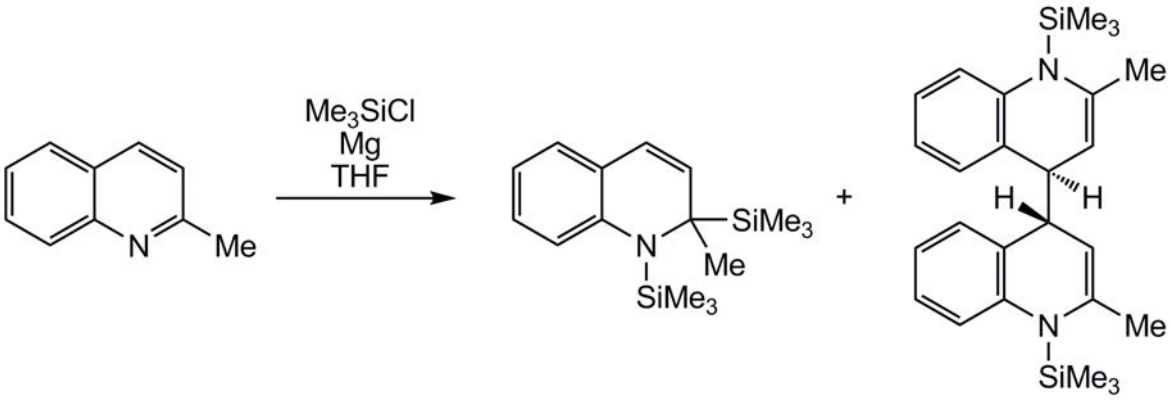

Equation 4-6b

A ruthenium silylyne complex stabilised by 1,10-phenanthroline was shown by Grumbine, Chadha and Tilley to reductively dimerise through the 4 position of the 1,10-phenanthroline ligand after nine days stirring over sodium amalgam to give a ruthenium silylene dimer in 90% yield, Equation 4-7.[215]

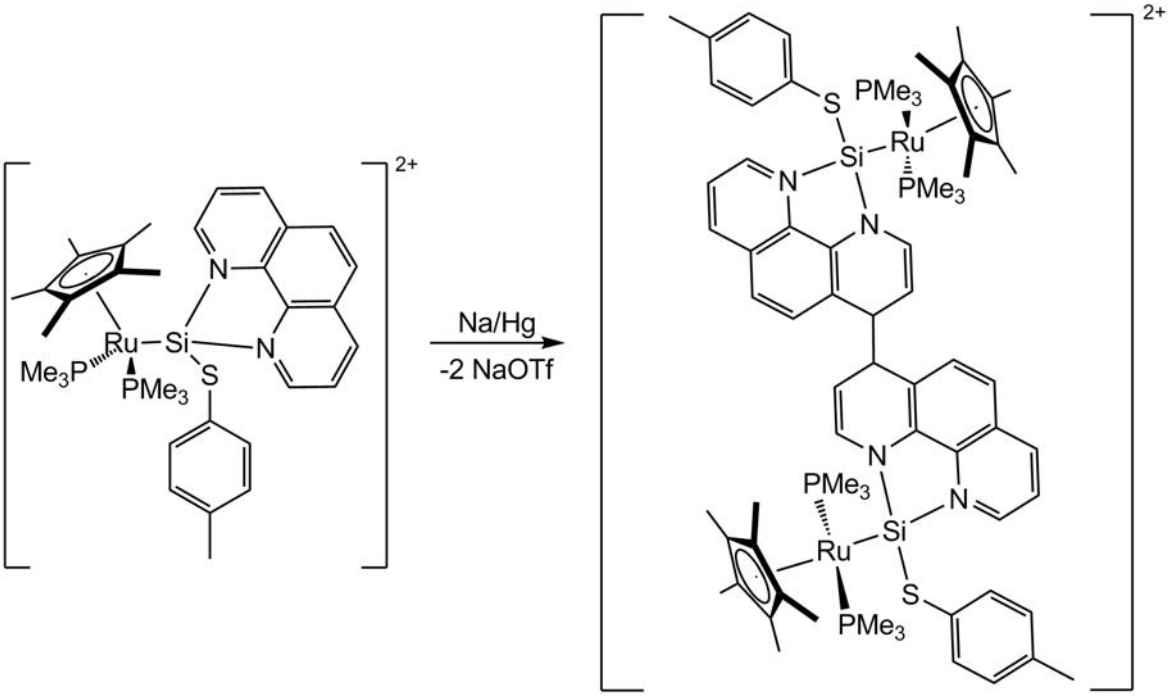

Equation 4-7

The reaction of 2,2′-bipyridine and $(C_5Me_5)_2Sm(THF)_2$, (**IV**), was reported by Evans *et al.* in 1989 and describes single electron reduction of the bipy ligand upon formation of $[(C_5Me_5)_2Sm^{III}(2,2'\text{-bipy})]$.[216] In the same paper, the reductive coupling of pyridazine (1,2-diazabenzene) is reported, Equation 4-8.

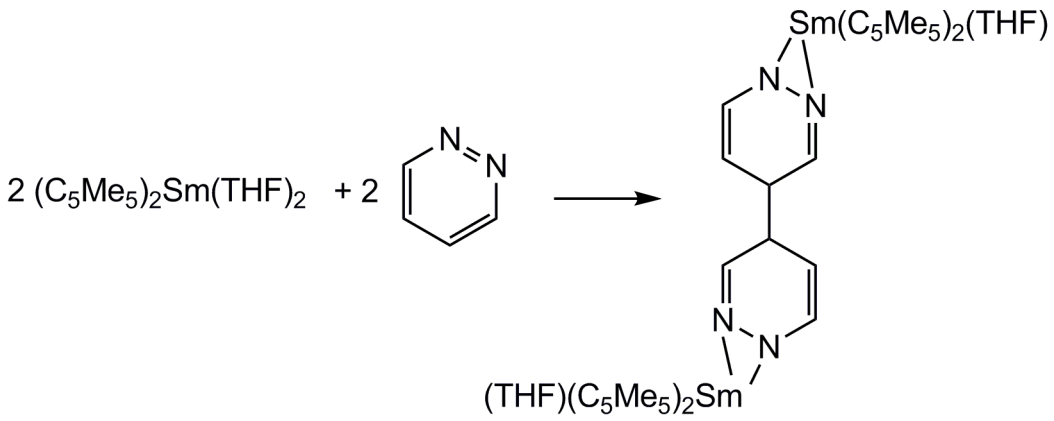

Equation 4-8

The reductive dimerisation product, $[\{(C_5Me_5)_2Sm(THF)\}_2(\mu\text{-}o\text{-}N_2C_4H_4)]$, shows each samarium atom is bound to one nitrogen atom *via* a formally single, $Sm{-}N_{amide}$ type bond (2.351(6) Å), and the other *via* the lone pair in a dative $Sm{-}N_{imine}$ type bond (2.430(6) Å).[216]

Following the paper by Evans *et al*.[216], Berg, Boncella and Anderson undertook a survey of the chemistry of a range of pyridine based ligands, including pyridazine, with $[(C_5Me_5)_2Yb(OEt)]$. It was found that, unlike $[(C_5Me_5)_2Sm]$, (**V**), $[(C_5Me_5)_2Yb]$ does not reduce pyridazine but instead forms the bis-adduct of pyridazine, $[(C_5Me_5)_2Yb(o\text{-}N_2C_4H_4)_2]$, in a manner analogous to the bis(pyridine) adduct.[217] Berg *et al.* also undertook the reaction with pyrazine (1,4-diazabenzene) and isolated a 1:1 adduct that is insoluble in toluene, $[(C_5Me_5)_2Yb(p\text{-}N_2C_4H_4)]$. The same ytterbocene complex was shown to form a 1:1 adduct with 4,4′-bipyridine.[217] Schultz *et al.* demonstrated that ytterbocene reacts with 2,2′-bipyridine and 1,10-phenanthroline to form a radical anion in each case; however they observe that the measured magnetic susceptibility suggests a complex interaction of metal and ligand spin. They also observed that modification of the substituents on the cyclopentadienide ring from electron donating alkyl groups to electron withdrawing trimethylsilyl groups inhibits the reduction, resulting in ytterbium(II)−neutral ligand adducts.[218] Da Re *et al.* followed up the Schultz paper in

the next year with further evidence (*via* cyclic voltammetry, UV-Vis-near-IR electronic absorption and resonance Raman spectroscopies) for the Yb^{III}–radical anion formulation for ytterbium complexes of 2,2′-bipyridine and 1,10-phenanthroline.[219] The intensity of investigation followed the measurement of the magnetic moment, which correlated poorly with the predicted magnetism of both an Yb^{II} and an Yb^{III} oxidation state, as expected for $[(C_5Me_5)_2Yb^{II}(L^0)]$ or $[(C_5Me_5)_2Yb^{III}(L^{\bullet})]$ for L = 2,2′-bipy or phen.

The literature reported herein demonstrates the variability of lanthanoid–heterocycle reactivity, with adducts, radical anions and reductive dimerisation reactivity available depending upon the system and metal reduction strength. The reducing strength of the metals clearly influence the reaction outcomes, however an extensive investigation of a range of heterocycles, to probe their steric and electronic influences, has not been presented.

4.2 Research Aim

Synthesis and X-ray crystal structure determination of complexes formed *via* reaction of $[(Et_8N_4Me_2)Sm(THF)_2]$, (**XVI**), with a range of mono-, bi- and tridentate pyridine-based ligands will reveal the characteristics of Lewis basic nitrogen coordination to divalent samarium or reduction by divalent samarium. Steric effects can be extensively probed by systematic investigation of X-ray crystal structure data, allowing a thorough description of the ligand binding properties. Additionally, whilst it is clear that the X-ray crystal structure metrics of a complex provide an indication of the oxidation state of the metal centre, confidence in an assigned oxidation state for ambiguous cases is increased with evidence obtained *via* a complimentary technique. The literature has shown that measurement of the magnetic moment of a complex is not necessarily definitive with regard to oxidation state due to subtle interactions between ligand and metal orbitals. This

thesis will present the results of density functional theory analysis as a technique complimentary to analysis of molecular geometries, allowing confident assignment of metal oxidation states. Where possible, further ratification will be provided *via* ^{1}H NMR spectroscopy.

4.3 Results and Discussion

The series of complexes investigated in this Chapter naturally fall into three subsets – substituted mono-pyridine ligands, systematically varied benzannulated pyridine ligands, and substituted 1,10-phenanthrolines (including 2,2′-bipyridine), Figure 4-1. It is useful to discuss each subset before broad and general comparisons are made across the entire series.

Many of the complexes reported herein are only sparingly soluble, preventing complete characterisation of the complexes reported. Additionally, in several cases where NMR spectroscopic analysis was undertaken, the resulting spectra are complicated by either extreme broadening due to the presence of a radical anionic heterocyclic ligand, paramagnetic metal centre, or significant peak overlap due to reduced molecular symmetry. In these cases, only partial resonance assignments could be made, leading to the broadest of generalisations made with regard to the oxidation state of the metal based on the extent of paramagnetic broadening indicating Sm^{II} or Sm^{III}, respectively. Satisfactory elemental analysis could only be obtained, despite multiple attempts, for a small number of complexes due to either sparing or extreme solubility; both issues hindering standard purification techniques. Without access to readily purified samples across the entire series, magnetic susceptibility measurement was deemed to be of reduced value and is extremely demanding for Sm^{II}/Sm^{III} systems. DFT analysis based on the molecular geometries derived from X-ray crystal structure data, however, provided a

convenient, quantitative and readily applicable technique for analysis of oxidation state for complexes where such assignment could be ambiguous.

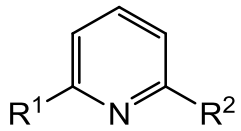

For $R^{1,2}$ = H, H; H, Me; Me, Me; H, Ph; Me, Ph; py, py

Substituted mono-pyridine ligands
Section 4.3.1

Tricyclic framework based on these extensions:

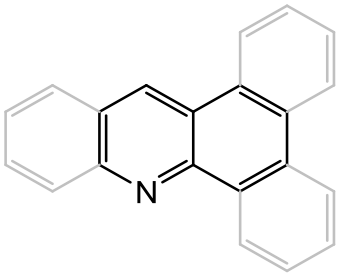

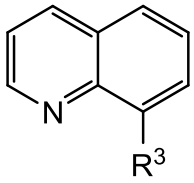

For R^3 = H; Me

Benzannulated pyridine ligands
Section 4.3.2

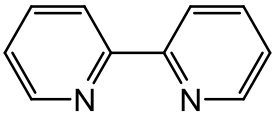

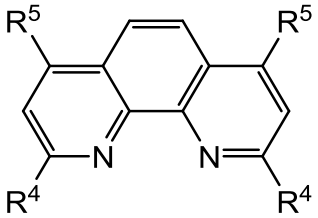

For $R^{4,5}$ = H, H; Me, H; H, Me; H, Ph

Substituted 1,10-phenanthroline ligands
Section 4.3.3

Figure 4-1: The three ligand types under investigation in this Chapter.

4.3.1 Coordination of Substituted Pyridine Ligands

The substituted pyridines employed in this study were selected based upon potential for steric interactions influencing their coordination within the binding groove of the samarium complex, Figure 4-2. The effect of steric bulk on the tendency of the ligand to form either 1:1 or 2:1 adducts, or be reduced to a radical anion or reductively couple with a second molecule, is of interest.

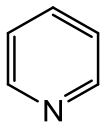

py
pyridine

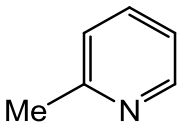

2-pic
2-methylpyridine

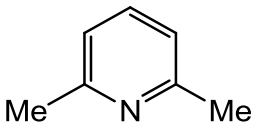

2,6-lut
2,6-dimethylpyridine

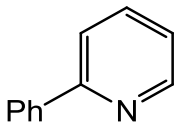

2-Phpy
2-phenylpyridine

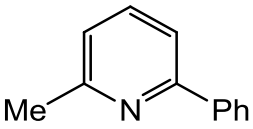

2-Me-6-Phpy
2-methyl-6-phenylpyridine

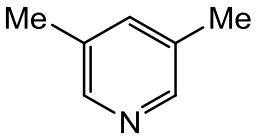

3,5-lut
3,5-dimethylpyridine

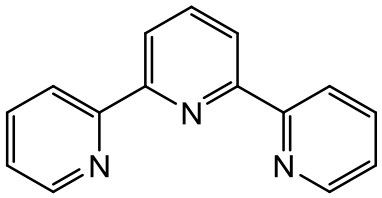

terpy
2,2′;6′,2″-terpyridine

Figure 4-2: The substituted pyridines employed in this study.

The synthesis of each complex described in this Section was achieved by addition of excess ligand to $[(Et_8N_4Me_2)Sm(THF)_2]$, (**XVI**), in either C_6H_6 or PhMe on a small scale (*ca*. 10 mg {**XVI**}). In all cases, the higher concentration of ligand was shown to displace the bound THF to form a new complex *via* ligand exchange reaction. Each product was isolated as crystalline material ranging in colour from red through purple to black.

A series of 1:1 substituted pyridine adducts were obtained *via* the method described above to form $[(Et_8N_4Me_2)Sm(2\text{-pic})]$, (**15**), $[(Et_8N_4Me_2)Sm(2,6\text{-lut})]$, (**16**), $[(Et_8N_4Me_2)Sm(2\text{-Phpy})]$, (**18**), and $[(Et_8N_4Me_2)Sm(2\text{-Me-6-Phpy})]$, (**20**). In each case, steric bulk is systematically increased throughout the series from the unsubstituted

bis(pyridine) adduct, [($Et_8N_4Me_2$)Sm(py)$_2$] (**14**), to the 2-methyl-6-phenylpyridine adduct, (**20**).

Reaction of [($Et_8N_4Me_2$)Sm(THF)$_2$], (**XVI**), with 3,5-lutidine was undertaken subject to the hypothesis that a 1:1 complex of a pyridine adduct with no steric strain at the binding groove could be achieved by preventing coordination of a second ligand *via* 3,5-dimethyl substitution whilst leaving the 2- and 6- positions unhindered. Such a complex would provide a valuable benchmark for comparison in this series of complexes. The desired outcome was not obtained and isolation of the bis(adduct) [($Et_8N_4Me_2$)Sm(3,5-lut)$_2$], (**17**), was achieved. Similarly, reaction of (**XVI**) with 4,4′-bipyridine was pursued to provide comparison with a reduced species with no steric bulk at the binding groove and isolation of [{($Et_8N_4Me_2$)Sm}$_2$(μ-4,4′-bipy)], (**21**), which incorporates a bridging dianionic 4,4′-bipyridyl moiety, was achieved.

Reaction of [($Et_8N_4Me_2$)Sm(THF)$_2$], (**XVI**), with 2,2′;6′,2″-terpyridine (terpy) was undertaken with the expectation that, should reaction occur, the binding groove of the samarium macrocycle would likely prohibit tridentate coordination of terpy and may lead to novel binding. The outcome of this reaction will be discussed in detail prior to further discussion of the outcomes of the reactions between substituted pyridines and (**XVI**).

4.3.1.1 Synthesis of [($Et_8N_4Me_2$)Sm(*N*-terpy)], (19)

The complex was synthesised *via* reaction of a benzene solution of (**XVI**) with excess 2,2′;6′,2″-terpyridine at room temperature, Equation 4-9. Black crystals suitable for X-ray crystal structure determination were obtained in 79 % yield in two crops after allowing the reaction to stand in a capped sample vial overnight. The black crystals were characterised by ^{1}H NMR spectroscopy, elemental analysis and X-ray crystallography.

^{13}C NMR spectroscopy was attempted, however the paramagnetic nature of the complex precluded acquisition of useful data.

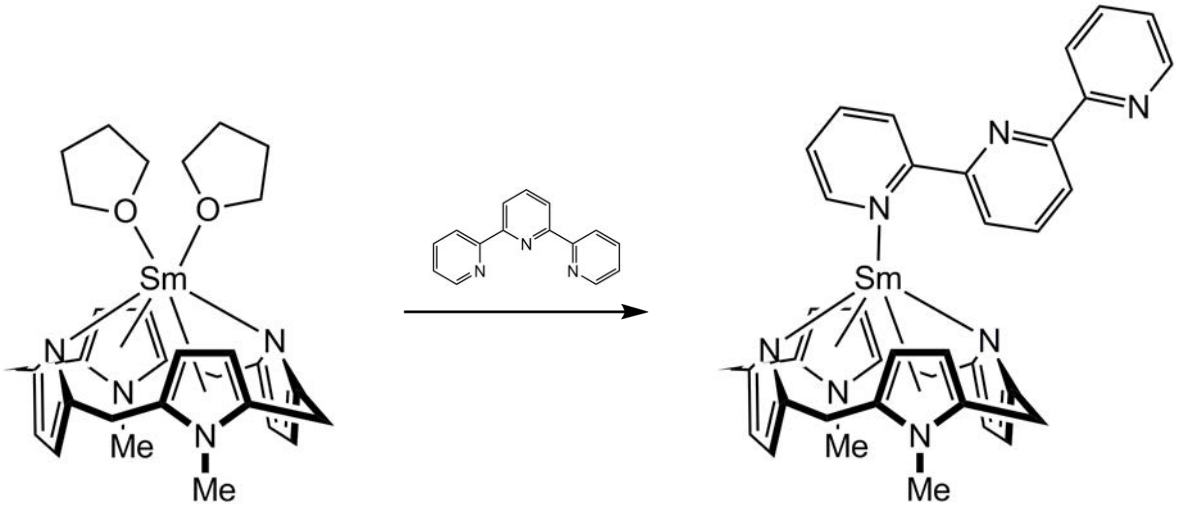

(**XVI**) **19**

Equation 4-9

The reaction described by Equation 4-9 was repeated with overnight heating at 65 °C to afford the same product by ^{1}H NMR spectroscopy. The complex is soluble in toluene and benzene and sparingly soluble in pet. ether. Washing the complex in pet. ether removed the solvating benzene (by satisfactory elemental analysis). [($Et_8N_4Me_2$)Sm(*N*-terpy)], (**19**), is, to the best of our knowledge, the first example of monodentate binding of 2,2′;6′,2″-terpyridine to a lanthanoid and also the first example involving a lanthanoid in the +2 oxidation state, *vide infra*.

^{1}H NMR spectroscopic analysis was undertaken and assignment of the resulting spectrum was achieved by comparison with [($Et_8N_4Me_2$)Sm(THF)$_2$], (**XVI**), Section 2.3.1.1. The spectrum shows a series of reproducibly widened and shifted resonances between -25 and 47 ppm at room temperature, consistent with a paramagnetic Sm^{II} centre (additionally supported by DFT analysis, Section 4.3.4). The singlet resonance at 46.9 ppm is assigned to the *N*-methyl groups; resonances at 18.3 and 1.5 ppm are due to the *β*-protons of the N_{Py} and N_{Me} rings. The multiplets at -24.4, -6.0, 0.9 and 5.3 ppm are

attributable to the CH_2 protons of the *meso*-ethyl groups, whilst the resonances at -7.9 and 0.4 ppm are attributable to the CH_3 protons of the *meso*-ethyl groups.

The appearance of the ^{1}H NMR spectrum of (**19**) is indicative of effective C_{2v} macrocyclic symmetry in solution at room temperature. Such symmetry is likely due to either rapid, fluxional decoordination of 2,2′;6′,2″-terpyridine or rapid spinning of the ligand with respect to the macrocycle. Ligand fluxionality *via* an associative mechanism involving a multidentate intermediate is unlikely due to steric interaction of the third, pendant ring of terpy with the macrocycle, Section 4.3.1.3. A reduction in effective macrocyclic symmetry from C_{2v}, as observed in the ^{1}H NMR spectrum of [($Et_8N_4Me_2$)Sm(*N*-terpy)], (**19**), to C_s has to date only been observed in Sm^{III} complexes of the macrocycle, such as the reduced diazabutadiene complex, [{($Et_8N_4Me_2$)Sm}$_2$(*t*-BuDAB)], (**XXII**).[76]

The chemical shifts of terpy resonances in the ^{1}H NMR spectrum of [($Et_8N_4Me_2$)Sm(*N*-terpy)], (**19**), are at 4.9, 5.2, 6.6 and from 10.8-12.3 ppm. The chemical shifts of these resonances are consistent with a neutral adduct of 2,2′;6′,2″-terpyridine with minor paramagnetic influences of some resonances due to proximity of those protons to the Sm^{II} centre and/or the π- bound N_{Me} rings. A report featuring both reduced and neutral terpy ligands bound to a Sm^{III} centre as a singly reduced radical anion, [(C_5Me_5)$_2$$Sm^{III}$(terpy$^{\bullet-}$)] and neutral adduct, [(C_5Me_5)$_2$$Sm^{III}$(terpy)][$PF_6$], respectively, indicate that the paramagnetic influences on the chemical shifts of terpy resonances in the ^{1}H NMR spectrum are dominated by the ligand centred radical rather than the paramagnetic samarium centre. For the reduced ligand, terpy$^{\bullet-}$, resonances are observed between -330 and 15 ppm, whereas for the neutral terpy ligand resonances are observed

between 0 and 8 ppm.[220] This is consistent with our assignment of a samarium(II) centre bound to a neutral 2,2′;6′,2″-terpyridine ligand for [($Et_8N_4Me_2$)Sm(*N*-terpy)], (**19**).

To better establish the novelty of both η^1- binding for 2,2′;6′,2″-terpyridine and coordination of terpy to a Ln^{II} centre, a brief review of the literature follows.

4.3.1.2 The Reported Chemistry of 2,2';6',2''-Terpyridine

The tridentate coordination of 2,2′;6′,2″-terpyridine is ubiquitous and spans d, p and f-block chemistry. A modest number of exceptions to the standard tridentate binding have been identified. The first credited postulation of bidentate binding of terpy was made by Ganorkar and Stiddard in 1965.[221] A number of subsequent papers throughout the 1970s proposed bidentate terpy binding to indium,[222] rhenium,[223] copper,[224] and manganese.[225] In 1981, Canty *et al.* showed bidentate binding of terpy in solution by ^{1}H NMR spectroscopy (tridentate in the solid state) for the methylmercury(II) complex [{MeHg(4,4′,4″-Et_3terpy)}NO_3],[226] however it wasn't until 984 that Deacon *et al.* crystallographically authenticated a bidentate complex of 2,2′;6′,2″-terpyridine in the form of [$RuBr_2(CO)_2$(*N*,*N*′-terpy)].[227]

A 2009 review of platinum complexes of terpyridine by Cummings contains a small section on unusual binding modes of terpy.[228] The discussion is based on a cluster of papers by Abel *et al.* in the early 1990s which report fluxional „tick-tock' bidentate terpy binding *via* an associative mechanism (through a seven coordinate, tridentate intermediate), Figure 4-3.[229-231] A dissociative mechanism (through a three-coordinate T-shaped intermediate, with terpy binding *via* only the central pyridine ring) was suggested by Rotondo *et al.*, but found to be unsatisfactory in relation to experimental evidence.[232]

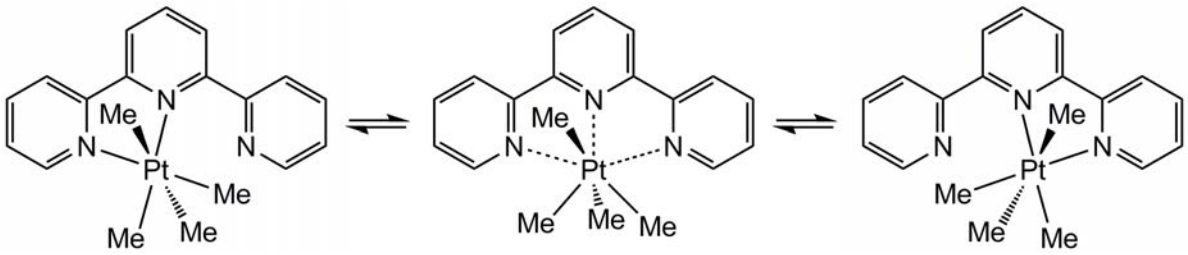

Figure 4-3 A "tick-tock" mechanism for fluxional bidentate coordination of terpy, adapted from Cummings.[228]

In 1995 Chotalia *et al.* found a 52.3 ° twist from the plane of the central, binding, pyridine ring of terpy for the ruthenium complex $[Ru(2,2'\text{-bipy})_2(N,N''\text{-terpy})][PF_6]_2$, to the third, pendant ring by X-ray crystal structure determination, Figure 4-4. They also compared their results to all prior entries in the Cambridge Crystallographic Data Centre for metal-terpy complexes.[233]

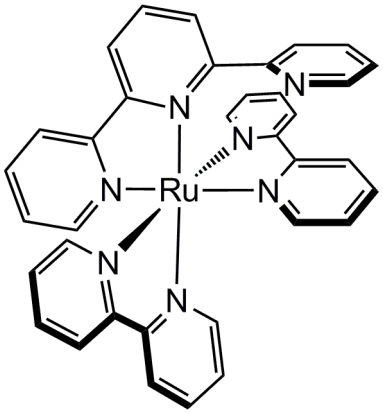

Figure 4-4 One enantiomer of the cation of $[Ru(2,2'\text{-bipy})_2(N,N''\text{-terpy})][PF_6]_2$, showing bidentate coordination of terpy.[233]

The twist of the pendant ring of bidentate terpy depends upon the situation; the degree of twist can support a „dangling' pendant ring[234] or, as found by Rao, Rao and Zacharias, in the case of a ruthenium complex, sufficient twist such that the face of the pyridine ring is exposed to the metal coordination sphere.[235] Inter- and intramolecular π-π stacking of the pendant ring of bidentate terpy has been observed with the pyridine rings of bipy and terpy ligands coordinated to ruthenium.[236]

In 2001, Doppiu *et al.* reported a dinuclear platinum(II) cyclometallation product where each platinum atom is bonded to a nitrogen of an outer pyridine and to a meta-carbon of the inner pyridine, Equation 4-10.[237] The DMSO ligand was shown to exchange with MeCN, CO, PPh_3 and tricyclohexylphosphine, PCy_3.[237] *Ortho*-metallation of 2-phenylpyridine by a platinum(II) reagent was first reported in 1984.[238]

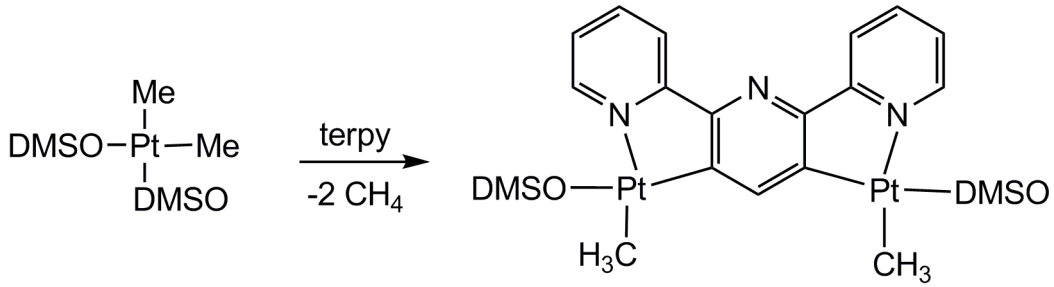

Equation 4-10

The first monodentate terpy complex was reported by Pruchnik *et al.* in 1996 for a rhodium(II)(μ-OAc)$_4$ dimeric paddle-wheel complex. Monodentate terpy binding occurs through a terminal pyridine and affords an anti-anti (nitrogen pointing up-down-up) conformation throughout the ligand, Figure 4-5.[239] A strikingly similar complex was reported in 2005 by Sidorov *et al.* for a rhodium(II)(μ-OC(*t*-Bu)O)$_4$ dimer with the same monodentate binding and conformation in terpyridine.[198]

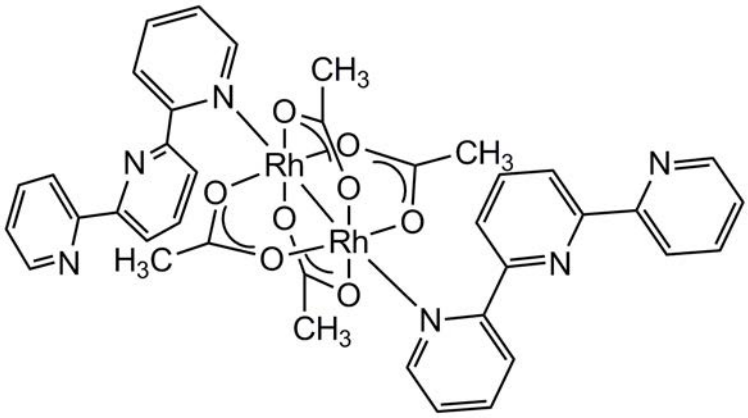

Figure 4-5 The first reported monodentate terpy complex, [$Rh_2(OAc)_4$(*N*-terpy)$_2$].[239]

In 2005 Aguado *et al.* employed 4′-ferrocenyl-2,2′:6′,2″-terpyridine to accommodate η^1- binding of three gold(I) atoms. This was achieved *via* significant twisting of the two

outer pyridine rings such that each pyridine ring is almost perpendicular to the next (i.e. +90 °: 0 °: -90 °) to accommodate the three metal centres, Equation 4-11.[240]

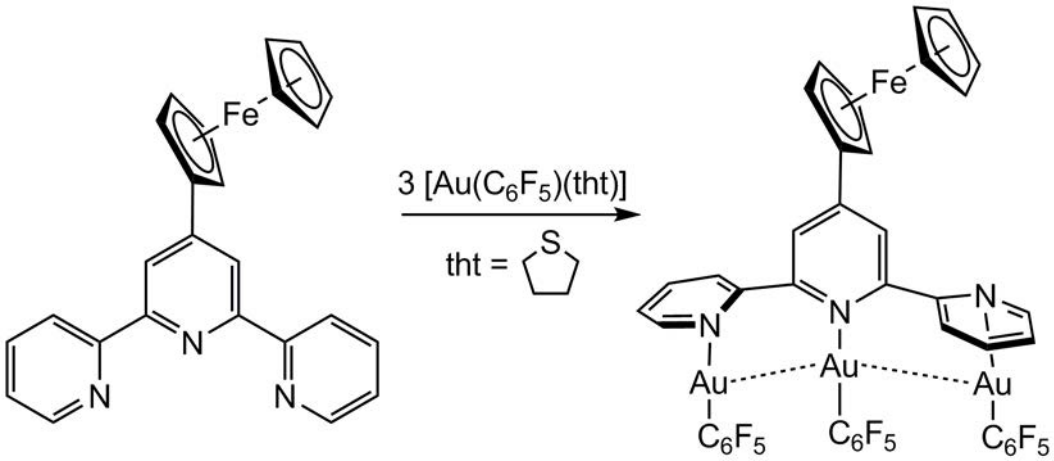

Equation 4-11

Reports of the chemistry of 2,2′;6′,2″-terpyridine and the lanthanoids begin as late as 1999, when Semenova and White undertook a series of investigations into hydrated 1:1 adducts of terpy in the form of $[(terpy)Ln(OH_2)_x]Br_3 \cdot yH_2O$[241] and $[(terpy)Ln(O_2NO)_2(OH_2)_y](NO_3)(\cdot zH_2O)$,[242] as well as tris(terpy) complexes with perchlorate anions.[243] The aqueous chemistry of terpy and the lanthanoids was also investigated by Drew *et al.* in 2000 as a viable technique for extraction and purification of lanthanoids from lanthanoid/actinoid mixtures that are found in nuclear waste.[244] Kumar and Singh employed several pyridine based ligands (terpy, 2,2′-bipy and phen) in reactions with $SmCl_3$, where the neutral ligand binds through all available nitrogen centres.[208]

Mixed metal systems with terpy and the lanthanoids have also been investigated by Figuerola *et al.* and Przchodzen *et al.* In 2006, Figuerola *et al.* used terpy to stabilise cyano-bridged Sm/Fe and Sm/Co complexes.[245] In 2006 and 2007, Przchodzen *et al.* synthesised a range of lanthanoid/tungsten complexes incorporating terpy, dimethylformamide, cyano and aqua ligands.[246, 247]

In 2007, Fukuda, Nakao and Hayashi synthesised a range of complexes of the general formula [Ln(terpy)(acac)$(NO_3)_2(H_2O)$]. In their study, they observed that the ionic radius of the metal has significant effects on the tridentate binding characteristics of terpy; Figure 4-6.[248] Consistent with the limited flexibility of the C−C bond geometries, it was rationalised that elongation of the metal−nitrogen bond occurs at the central ring of terpy for larger metals and at a terminal ring for smaller metals.

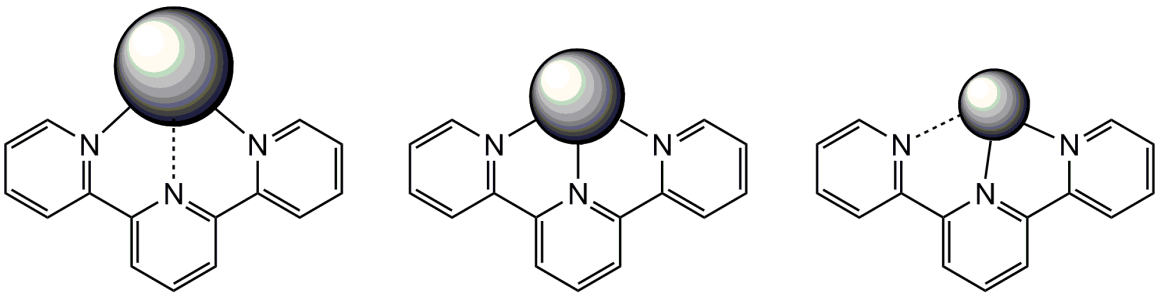

Figure 4-6: Variation in binding characteristics of 2,2′;6′,2″-terpyridine for large, moderate and small metal ions, left to right, respectively.[248]

Reports of incorporation of 2,2′;6′,2″-terpyridine in organolanthanoid chemistry began in 2003 with work by Kuehl *et al.*, following an earlier report on reactivity with bipy and phen,[219] who explored the reactivity of ytterbocene, $[(C_5Me_5)_2Yb(OEt_2)]$, with terpy and tetra-2-pyridinylpyrazine whilst investigating mixed-valence systems in the context of developing molecular wires and switches.[249] Terpy fits within the coordination wedge available for ancillary ligand binding of the bent ytterbocene, and binds in a tridentate fashion, Figure 4-7. Electrochemical and spectroscopic data suggest the ytterbium is present as ytterbium(III) and the terpy ligand carries one electron in the π* orbital.[249]

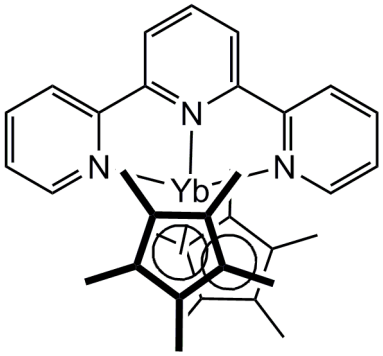

Figure 4-7 Tridentate binding of a terpy radical to decamethylytterbocene.[249]

In 2005 a paper by Veauthier *et al.* (indicating collaboration with most of the authors in the 2003 Kuehl paper) investigated the 4′-cyano substituted terpy ligand and its reactivity with ytterbocene. A tridentate $[(C_5Me_5)_2Yb^{III}(4'\text{-CN-}\eta^3\text{-terpy}^{\bullet-})]$ complex was reported, with terpy binding in a tridentate fashion to the ytterbium and the 4′-cyano group not involved in bonding. Oxidation of $[(C_5Me_5)_2Yb^{III}(4'\text{-CN-}\eta^3\text{-terpy}^{\bullet-})]$ with ferrocenium hexafluorophosphate in THF oxidised the heterocycle to a neutral tridentate terpy ligand whilst retaining the Yb^{III} centre. This reaction was achieved in 80 % isolated yield; a side reaction was also reported where the nitrile group is cleaved from terpy and C−C bond formation between terpy and a C_5Me_5 ring occurs (in less than 5 % yield). Reaction of the 4′-cyano-terpy ligand with $[(C_5Me_5)_2Yb^{III}I]$ provided monodentate coordination of the ligand through the nitrile; $[(C_5Me_5)_2Yb^{III}(\eta^1\text{-NCterpy})I]$. Reaction of unsubstituted terpy with $[(C_5Me_5)_2YbI]$ was undertaken to establish if $[(C_5Me_5)_2YbI]$ is a viable precursor to terpy complexes, resulting in the tridentate terpy salt $[(C_5Me_5)_2Yb^{III}(terpy)][(C_5Me_5)_2Yb^{III}I_2]$.[250] Carlson *et al*. expanded further on the charge separation chemistry of ytterbocene−terpy complexes in 2006[251] and 2007[252] without deviating from the tridentate ytterbium(III) chemistry already reported.

In 2008, Veauthier *et al.* reported samarium−terpy chemistry and compared it to the results reported in the earlier ytterbium−terpy paper. Terpy was found to bind in a tridentate fashion as a radical anion to samarocene, $[(C_5Me_5)_2Sm^{III}(terpy)]$. Oxidation with

ferrocenium hexafluorophosphate resulted in the Sm^{III} salt with a neutral, tridentate terpy ligand, Scheme 4-1. The paper establishes that samarium(II) more effectively transfers electron density to terpyridine than ytterbium(II), which is consistent with the respective M^{II}/M^{III} redox couple, Section 1.2.

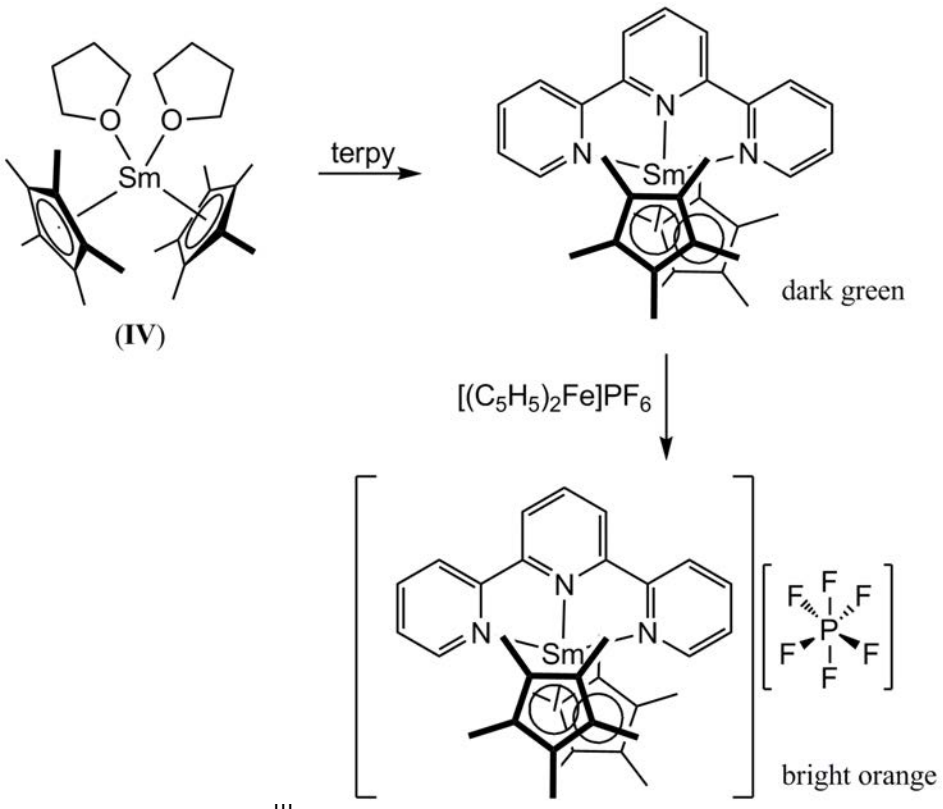

Scheme 4-1 Synthesis of Sm^{III} complexes of terpyridine, with terpy present as a radical anion and a neutral adduct.[220]

To the best of our knowledge, all lanthanoid−terpy complexes in the literature exclusively report tridentate binding of terpy to lanthanoid(III) metal centres.

4.3.1.3 Molecular Structure of [($Et_8N_4Me_2$)Sm(*N*-terpy)]·2.5(C_6H_6), (19)

Crystals of complex (**19**) belong to the monoclinic space group $P2_1/c$ (No. 14), $a = 18.3800(11)$, $b = 14.130(2)$, $c = 23.6000(8)$ Å, $\beta = 111.234(2)°$, with four molecules in the unit cell. The asymmetric unit consists of one molecule of [($Et_8N_4Me_2$)Sm(*N*-terpy)] and two and a half molecules of benzene, Figure 4-8.

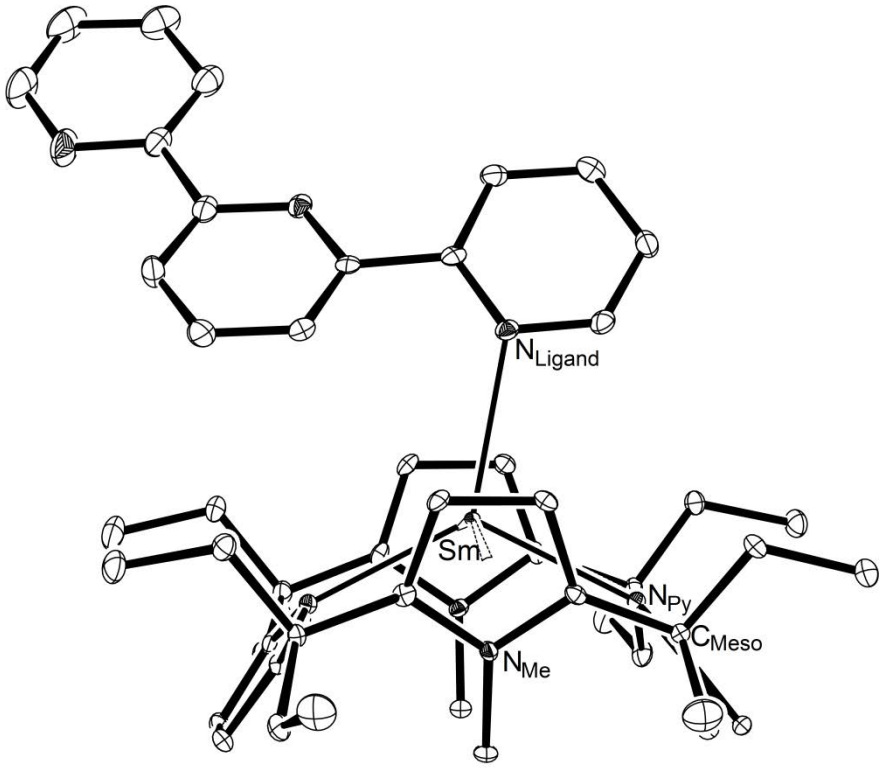

Figure 4-8: Molecular structure of (**19**) with thermal ellipsoids drawn at 50 % probability (solvent benzene omitted for clarity).

The molecular structure of (**19**) exhibits the standard $\eta^1{:}\eta^5{:}\eta^1{:}\eta^5$ macrocyclic binding mode. The Sm-$N_{Pyrrolide}$ distances are 2.5800(17) and 2.5748(18) Å and the distance from the samarium centre to the *N*-methylpyrrole ring centroids are 2.68_2 and 2.70_9 Å. The pyrrolide ring tilt angles are 50.15(7) and 55.71(7) °, and the *N*-methylpyridine ring tilt angles are 77.37(7) and 77.16(6) °. The asymmetric pyrrolide ring tilt is a result of steric effects imparted by the central pyridine ring of the terpy ligand, which increases the ring tilt angle as it effectively „pushes down' the pyrrolide ring. Table 4-1 compares the structural features of (**19**) with samarium(II) mono(THF) and mono(*t*-BuCN),

(**12**), adducts and the known samarium(III) bis(trimethylsilyl)amide complex $[(Et_8N_4Me_2)Sm\{N(SiMe_3)\}_2]$, (**XXXV**), revealing that the molecular geometry is generally consistent with a samarium(II) centre bound to a single ancillary nitrogen donor; variations observed with respect to the angle and coordination distance of the $N_{Pyrrolide}$ ring, are consistent with the effect of the bulky terpy ligand, *vide supra*.

	$M = Sm^{II}$ L = terpy (**19**)	$M = Sm^{II}$ L = THF[72]	$M = Sm^{II}$ L = NC*t*-Bu (**12**)	$M = Sm^{III}$ L = $N(SiMe_3)_2$ (**XXXV**)[71]
M−L	2.6771(19)	2.544(2)	2.609(6), 2.612(7)	$2.30_7 – 2.31_4$
M−(η^1-N_{Py})	2.580(2), 2.575(2)	2.566(2), 2.557(2)	2.550(6) – 2.579(5)	$2.51_3 – 2.60_4$
M−(η^5-N_{Me})	2.68_2, 2.70_9	2.668, 2.687	$2.67_1 – 2.69_9$	$2.64_5 – 2.66_8$
M−*meso*	1.2974(11)	1.26_1	1.282(3), 1.289(3)	$1.34_1 – 1.36_8$
N_{Py}−*meso*	50.15(7), 55.71(7)	49.4_4, 55.6_0	44.33(12) – 52.7(2)	n/a
N_{Me}−*meso*	77.16(6), 77.37(7)	77.8_1, 78.3_0	76.4(2) – 79.2(2)	n/a
Metallocene bend	162.7_0	163.6_4	162.7_5, 163.0_0	$160.0_8 – 160.9_2$

Table 4-1 Selected bond lengths (Å) and angles (°) for $[(Et_8N_4Me_2)M(L)]$.

The 2,2′;6′,2″-terpyridine ligand is bound in an η^1- fashion *via* the nitrogen atom of a terminal pyridine ring to the metal centre; the Sm−N_{ligand} distance is 2.6771(19) Å. The 2,2′;6′,2″-terpyridine ligand twists about the 2,2′ bond by 161.31(11) ° and by 176.08(12)° about the 6′,2″ bond, to give the anti-anti arrangement of terpy observed in (**19**), Figure 4-8.

The two samarium−terpy complexes reported by Veauthier *et al.* in 2008 show significantly different structural properties. The data from the molecular structures of $[(C_5Me_5)_2Sm^{III}(terpy)]$ and $[(C_5Me_5)_2Sm^{III}(terpy)][PF_6]$ are presented in Table 4-2.

	(**19**)	$[(C_5Me_5)_2Sm(terpy)]$	$[(C_5Me_5)_2Sm(terpy)][PF_6]$
$Sm-(C_5Me_5)$ centroid	-	2.504	2.472
$Sm-N_{terminal}$	2.6771(19)	2.498(2)	2.518[2]
$Sm-N_{central}$	-	2.449(3)	2.553(2)
Metallocene bend	162.7_0	139.0	142.4

Table 4-2 Comparison of the molecular characteristics $[(Et_8N_4Me_2)Sm(N\text{-terpy})]$, (**19**), with two reported samarium^{III} terpy complexes.[220]

The molecular structure of (**19**) varies significantly from the reported decamethylsamarocene-terpy complexes. Comparison of the closest Sm−N contact for these complexes reveals that terpyridine is bound more weakly as a neutral adduct than as a radical anion for these Sm^{III} complexes; however, in the case of (**19**), the same Sm−N distance is longer than observed in both of these Sm^{III} complexes, consistent with a Sm^{II} centre bound to a neutral adduct.

2,2′-bipyridine is reduced by $[(Et_8N_4Me_2)Sm(THF)_2]$, (**XVI**), to form a radical anion, *vide infra*, which occupies almost the entire binding groove length. Thus, the additional pyridine ring of 2,2′;6′,2″-terpyridine results in a ligand too long to bind as a tridentate ligand. In addition, bidentate coordination of terpy, as either a neutral adduct or reduced anion, is prohibited on steric grounds as the pendant 2-py ring would still be forced to lie in close proximity to the end of the binding groove (regardless of its orientation with respect to the other two rings of the ligand). Thus, monodentate coordination of 2,2′;6′,2″-terpyridine results, Figure 4-9.

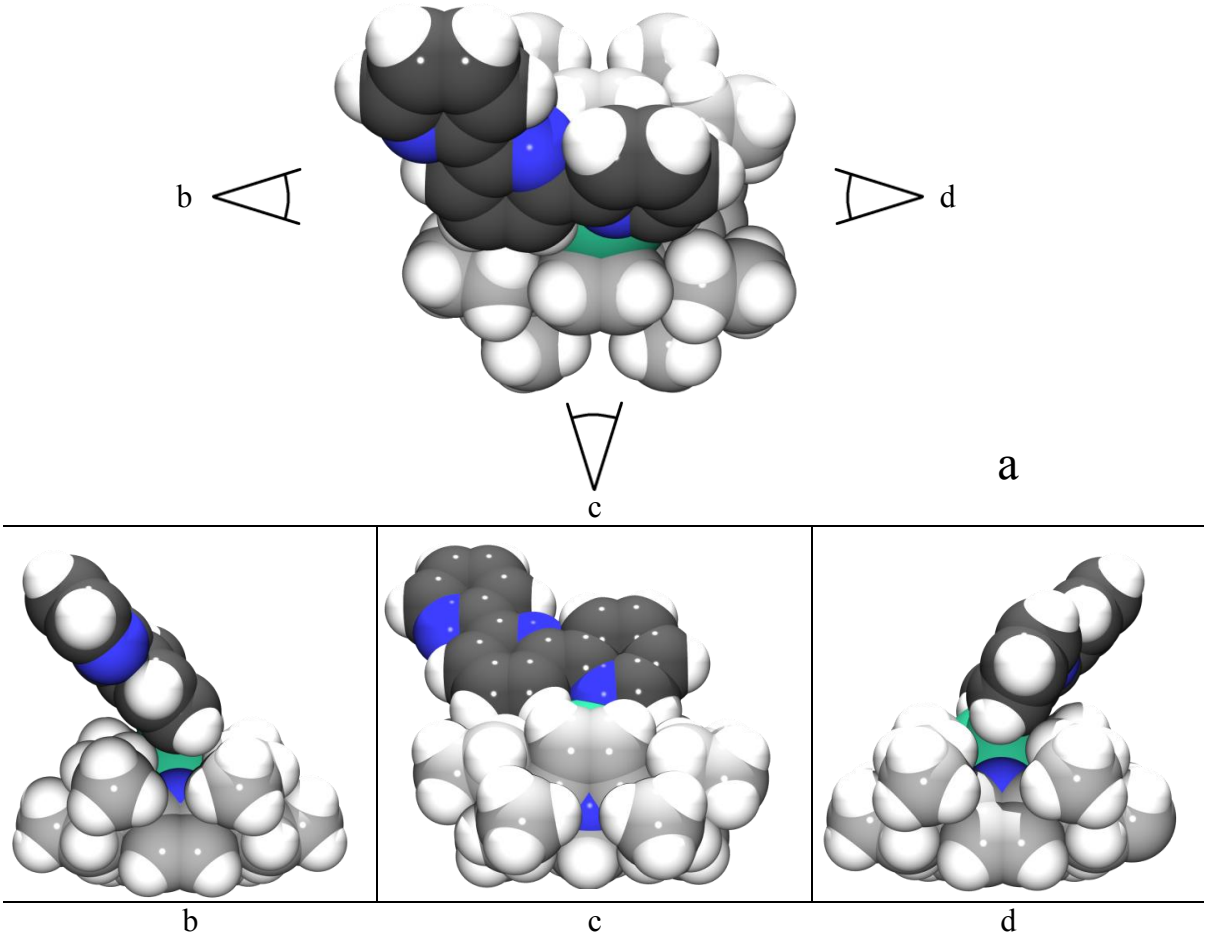

Figure 4-9 Space-filling representations of [($Et_8N_4Me_2$)Sm(*N*-terpy)],(**19**), looking down on the binding groove, *a*, and a series of views rotated by 90 ° in each case; viewing along the binding groove from the pendent terpy side, *b*, running from left-to-right, *c*, and from the coordinating pyridine side, *d*. Dark and light grey carbon atoms denote C_{terpy} and $C_{macrocycle}$, respectively.

The coordination of terpy within the binding groove of [($Et_8N_4Me_2$)Sm(*N*-terpy)], (**19**), is influenced by considerable steric interactions resulting in the terpy ligand being subject to rotations with respect to an internal Cartesian axis system defined by the symmetry features of the macrocycle, Figure 4-9. As such, to properly describe the geometry of coordination for (**19**), it is necessary to define and quantify the degrees of rotation about each axis. This definition will additionally allow proper description of all of the complexes formed between the substituted mono-pyridines and [($Et_8N_4Me_2$)Sm($THF)_2$] described in the following sections.

4.3.1.4 Definition of the Molecular Environment

Figure 4-9 demonstrates typical coordination of a significantly substituted pyridine ligand with the macrocyclic samarium species, clearly showing that steric bulk must lie within the binding groove; bulk across the cavity (at the level of coordination) will prohibit any encounter.

To meaningfully discuss and compare the coordination (and the effect on the macrocyclic geometry of that coordination) of this series of complexes, it is necessary to first define several relationships within the molecule. The foundations of this definition are the three least-squares planes defined by a) the four *meso*-carbon atoms of the macrocycle, b) the two nitrogens of the pyrrolide rings and the samarium, and c) the two nitrogens of the *N*-methylpyridine rings and the samarium, Figure 4-10. These three planes are approximately orthogonal to each other and thus define three spatial axes.

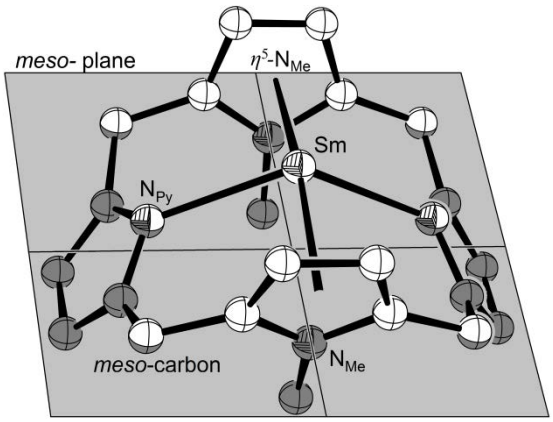

Figure 4-10 Tilted view of "$(H_8N_4Me_2)Sm$", showing the *meso*-plane, derived from $[(Et_8N_4Me_2)Sm(THF)_2]$, (**XVI**). For clarity, solvent molecules and protons are omitted, atoms are of arbitrary size.

Cursory visual inspection of the coordination environment reveals that it is usual for any 2,6- asymmetrically substituted coordinating pyridine to be subject to some angle of tilt within the binding groove. In addition, other analogues have exhibited more subtle angular deviation away from the approximate C_{2v} axis of the macrocycle.

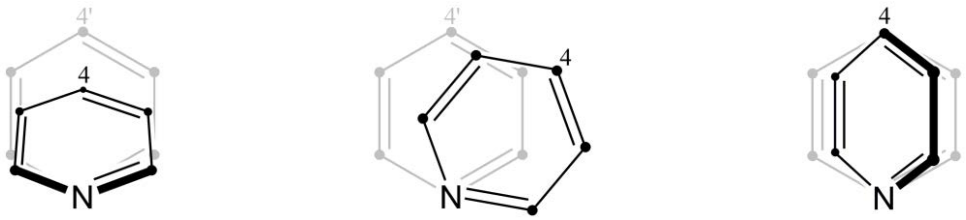

Incidence Tilt Twist

Figure 4-11: Rotation of the pyridine ring about the nitrogen atom in each dimension relative to the initial ring containing N′ and C4′. Viewed in such a direction that the binding groove runs from left to right.

Quantification of the twist angle (Figure 4-11) is obtained by finding the angle between the plane of the pyridine ring and the N_{Me}-Sm-N_{Me} plane. The angle of twist is the difference from orthogonal; any significant twist within the binding groove is sterically prohibited, thus the angle of twist is always small for this system.

The angle of incidence (Figure 4-11) is obtained by simply measuring the angle between the plane of the pyridine ligand and the N_{Py}-Sm-N_{Py} plane, and begins at zero for „vertical' attack down on the metal and increases in value as the attack angle departs from vertical.

The tilt angle (Figure 4-11) defies measurement *via* the simple relationship between ligand and macrocycle planes as no plane can be appropriately defined relative to the *meso*-plane for planar ligands. A complete derivation of the process of quantification of the molecular environment *via* trigonometric relationships is provided in Appendix B.

Having thus defined the rotation of a plane about the axis of all three spatial dimensions relative to the macrocycle, quantification of the molecular environment of the series of planar, pyridine based complexes formed with samarium *trans*-*N,N*′-dimethyl-*meso*-octaethylporphyrinogen complexes is provided in this Chapter.

4.3.1.5 Crystal Structure Comparison

Due to structural similarities between the crystal structures of complexes (**14** - **21**), data will be presented here *via* comparison, rather than *via* repetitious discussion of individual species. Crystal structure data for each species is supplied in .CIF format in Appendix C.

The samarium centre in compounds (**14** - **21**) exhibits the usual $\eta^1{:}\eta^5{:}\eta^1{:}\eta^5$ binding mode within its respective macrocycle. [$(Et_8N_4Me_2)$Sm(2,6-lut)], (**16**), has two individual molecules in the asymmetric unit; data for both are included. The data for [$(Et_8N_4Me_2)$Sm(Phpy)], (**18**), is not reliable as the crystal structure refinement is poor (R_{int} = 0.0972, R = 0.1851), however it is included for completeness and compares favourably with [$(Et_8N_4Me_2)$Sm(*N*-terpy)], (**19**), which can be viewed as analogous since the unbound terminal pyridine ring is not within the coordination sphere of the metal and the anti-anti conformation results in the central pyridine ring not presenting its nitrogen donor atom to the samarium centre. The crystallographic cell for complexes (**14** - **21**) is described in Table 4-3. Crystallographic disorder is present in the coordinating ligand of (**14**) and (**15**).

Ligand		Molecules in asymmetric unit	Lattice solvent per asym. unit (type, number)	Molecules in unit cell, Z	Crystal system, spacegroup
$(py)_2$	(**14**)	¼	-	4	ortho, *Cmcm*
(2-pic)	(**15**)	¼	-	4	ortho, *Cmcm*
(2,6-lut)	(**16**)	2 x ½	-	8	ortho, *Pnma*
$(3,5\text{-lut})_2$	(**17**)	$^1/_2$	-	2	mono, *P*2/*n*
(2-Phpy)	(**18**)	1	-	4	mono, $P2_1/n$
(terpy)	(**19**)	1	benzene, 2.5	4	mono, $P2_1/c$
(2-Me-6-Phpy)	(**20**)	1	-	4	ortho, $P2_12_12_1$
(4,4′-bipy)	(**21**)	$^1/_2$ dimer	benzene, 2	2	mono, $P2_1/n$

Table 4-3 X-ray crystallographic cell description for [$(Et_8N_4Me_2)$Sm(Ligand)]

Table 4-4, below, shows some key features of the macrocyclic geometries for each complex (**14** - **21**).

	$M = Sm^{II}$ $L = (py)_2$ (**14**)	$M = Sm^{II}$ $L = (3,5\text{-lut})_2$ (**17**)	$M = Sm^{II}$ L = (2-pic) (**15**)	$M = Sm^{II}$ L = (2-Phpy) (**18**)	$M = Sm^{II}$ L = (terpy) (**19**)	$M = Sm^{II}$ L = (2,6-lut) (**16**)	$M = Sm^{II}$ L = (2-Me-6-Phpy) (**20**)	$M = Sm^{III}$, n = 2 L = (μ-4,4′-bipy) (**21**)
M−L	2.77(1)	2.745(3)	2.609(3)	2.60(3)	2.6771(19)	2.724(4), 2.724(4)	2.844(3)	2.284(3)
$M-(\eta^1\text{-}N_{Py})$	2.668(6)	2.647(3)	2.5511(15)	2.58(2), 2.58(2)	2.580(2), 2.575(2)	2.580(3) - 2.596(4)	2.603(3), 2.632(3)	2.452(3), 2.479(3)
$M-(\eta^5\text{-}N_{Me})$	2.75_0	2.78_0	2.65_9	2.68_2, 2.70_9	2.68_2, 2.70_9	2.67_6, 2.66_8	2.69_0, 2.73_6	2.57_7, 2.58_9
M−*meso*	1.466(7)	1.465(2)	1.2334(15)	1.28(1)	1.2974(11)	1.310(2), 1.322(2)	1.4136(18)	1.1048(16)
N_{Py}−*meso*	52.2(2)	53.94(9)	55.25(7)	50.1(9) (H), 54.5(7) (Ph)	50.15(7) (H), 55.71(7) (Py)	51.2(1) – 57.0(1)	49.6(1) (Me), 57.9(1) (Ph)	43.22(7), 51.85(11)
N_{Me}−*meso*	75.7(3)	72.98(9)	79.88(5)	77.4(8), 76.2(8)	77.16(6), 77.37(7)	79.56(9), 79.55(9)	76.18(9), 77.2(1)	79.17(8), 81.12(7)
Metallocene bend	156.2_9	155.8_5	165.4_3	163.6_5	162.7_0	162.7_9, 162.5_5	158.6_2	170.8_2

Table 4-4 Selected bond lengths (Å) and angles (°) for $[\{(Et_8N_4Me_2)M\}_n(L)]$, highlighting bis(adducts) (**14, 17)**, 2-substituted adducts (**15, 18, 19)**, 2,6-disubstituted adducts (**16**, **20**) and a bridging bis(samarium(III)) complex, (**21**). Where relevant, asymmetric steric bulk affecting the N_{Py}−*meso* angle is described (**18**, **19, 20**).

Section 4.3.4 will report the results of DFT analyses, which indicate that the metal is present in the +2 oxidation state for each species (**14** - **20**). This assignment is consistent with the macrocyclic properties reported in Table 4-4 by comparison with the samarium(III) species (**21**) and various Sm^{II} species discussed earlier in this thesis. Table 4-4 demonstrates the effect of steric bulk directed into the macrocyclic binding groove on the geometry of the resulting samarium(II) adduct. The series of complexes (**14** - **20**) clearly falls into three subsets: 2:1 adducts, 1:1 adducts with substitution at the 2- position of the coordinating pyridine, and 2,6- disubstituted 1:1 adducts.

As discussed previously, direct metric comparison between 2:1 and 1:1 adducts is of limited value due to the change in effective metal radius as the coordination number increases; however, the generally long $Sm-N_{pyridine}$ bond lengths for the 2:1 adducts are comparible with the bis(nitrile) adduct of MeCN, (**9**), 2.711(4) Å. Maunder and Sella reported bond lengths for the 3,5-lutidine adduct of $Sm^{II}I_2$, $[SmI_2(3,5\text{-lut})_4]$, having comparable Sm−N bond lengths of 2.708(10) Å,[253] which compare well with $[(Et_8N_4Me_2)Sm(3,5\text{-lut})_2]$, (**17**), and further support the assignment of a samarium(II) centre based on structural parameters (Table 4-4) and DFT analysis (Section 4.3.4).

The $Sm-N_{pyridine}$ distance of the 1:1 adducts for 2-substituted pyridines is shorter than the 2:1 adducts, reflecting the change in effective ionic radius for samarium observed for bis(THF) to mono(THF) and bis(nitrile) to mono(nitrile) adducts, as previously discussed. The increase in bulk from 2-methyl to 2-phenyl or pyridyl (for η^1-terpy) affects a minimal change in structural parameters, Table 4-4. The 2-picoline ligand of (**15**) is crystallographically disordered across a mirror plane, resulting in an equal effect on the angle of the N_{Py} ring to *meso*- plane angle, whereas the 2-phenylpyridine and terpy ligand both tilt in the binding groove such that the bulky ligand minimises interaction with a N_{Py}

ring. Despite this tilt, the bulk of the ligand is clearly reflected in the variation in N_{Py}–*meso* angle for the N_{Py} ring adjacent to the substituted 2- and unsubstituted 6-positions, respectively, Table 4-4. The Sm–*meso* height also increases with the increase in bulk at the 2- position, consistent with the metal centre being balanced by coordination within the macrocycle and withdrawing towards the ancillary ligand when macrocycle-ancillary ligand interactions are present. The $Sm–N_{ligand}$ distance increases as the tilt angle increases to accommodate the steric bulk of the ligand within the narrow binding groove.

Increasing the steric interaction at the binding groove to 2,6- disubstituted pyridine ligands clearly places the system under significant strain, as reflected by the increase in the $Sm–N_{ligand}$ and Sm–*meso* lengths, even for the minimally substituted 2,6-lutidine ligand, Table 4-4. Introduction of the asymmetrically substituted 2-methyl-6-phenyl pyridine ligand further increased the steric bulk directed into the binding groove of the macrocycle and has been shown to result in extreme elongation of the $Sm–N_{ligand}$ and Sm–*meso* bond lengths and affects significant deviation in both N_{Py}–*meso* angles, despite the mitigation offered by the longer $Sm–N_{ligand}$ and Sm–*meso* lengths, Table 4-4. As a 1:1 adduct, complex (**20**) is clearly remarkable in its similarity to the two 2:1 adducts (**14**) and (**17**) with respect to metallocene bend angle and Sm–*meso* distance and elongated $Sm–N_{ligand}$ distance, despite the smaller effective metal radius arising from 1:1 rather than 2:1 adduct formation. Indeed, the 2-methyl-6-phenyl pyridine ligand clearly represents the limit of steric bulk that can be introduced at the binding groove; 2,6-diphenylpyridine is similar in structure to 2,2′;6′,2″-terpyridine without the additional coordination sites, and thus the novel η^1- binding of terpy clearly refutes any possibility of the coordination of 2,6-diphenylpyridine; accordingly, the reaction between $[(Et_8N_4Me_2)Sm(THF)_2]$, (**XVI**), and 2,6-diphenylpyridine was not attempted.

In addition to significantly affecting the macrocycle, the substituted mono(pyridine) ligands themselves are affected by the macrocycle resulting in non-trivial angles of incidence, twist and tilt, as defined in Section 4.3.1.4. Table 4-5 presents these affected ligand angles in the context of the height of the metal above the *meso*- plane and the Sm−N_{ligand} distance.

[{($Et_8N_4Me_2$)Sm}$_n$(L)]		Sm–*meso* distance	Sm – N_{ligand} distance	Angle of incidence	Angle of tilt	Angle of twist
M = Sm^{II}, L = $(py)_2$	(**14**)	1.465(6)	2.77(1)	n/a	n/a	n/a
M = Sm^{II}, L = $(3,5\text{-lut})_2$	(**17**)	1.465(2)	2.745(2)	n/a	n/a	n/a
M = Sm^{II}, L = (2-pic)	(**15**)	1.2334(15)	2.609(3)	-	20.49	-
M = Sm^{II}, L = (2-Phpy)	(**18**)	1.28(1)	2.60(2)	13.18	35.19	1.71
M = Sm^{II}, L = (*N*-terpy)	(**19**)	1.2974(11)	2.6771(19)	26.32	28.01	1.62
M = Sm^{II}, L = (2,6-lut) A M = Sm^{II}, L = (2,6-lut) B	(**16**)	1.310(2) 1.321(2)	2.724(4) 2.724(4)	-	2.26 4.04	-
M = Sm^{II}, L = (2-Me-6-Phpy)	(**20**)	1.4136(18)	2.844(2)	17.79	17.60	6.42
M = Sm^{III}, L = (μ-4,4'-bipy) n = 2	(**21**)	1.1048(16)	2.284(3)	3.97	3.35	4.62

Table 4-5 Ligand characteristics of [{($Et_8N_4Me_2$)Sm}$_n$(L)] by distance (Å) and angle (°).

Complexes formed with the mono-substituted pyridine ligands 2-pic (**15**), 2-PhPy (**18**) and *N*-terpy (**19**) demonstrate significant tilt as the ligand optimises within the binding groove of the macrocycle. Phenyl-sized 2-substituents result in a significant angle of incidence for both (**18**) and (**19**) and a small degree of twist to provide the greatest electron density to the samarium centre under the sterically crowded conditions. As apparent from the macrocyclic geometry metrics presented in Table 4-5, the 2-methyl-6-phenylpyridine complex is significantly strained, with the ligand rotating in all three axes (incidence, twist and tilt) to maximise the Sm−N_{ligand} interaction whilst minimising interactions between the

ligand and macrocycle, Figure 4-12. Superimposition of each of the 1:1 adducts, (**15**), (**16**), (**18**) - (**20**), allows the varying steric effects of the pyridine ligands to be compared visually, Figure 4-12.

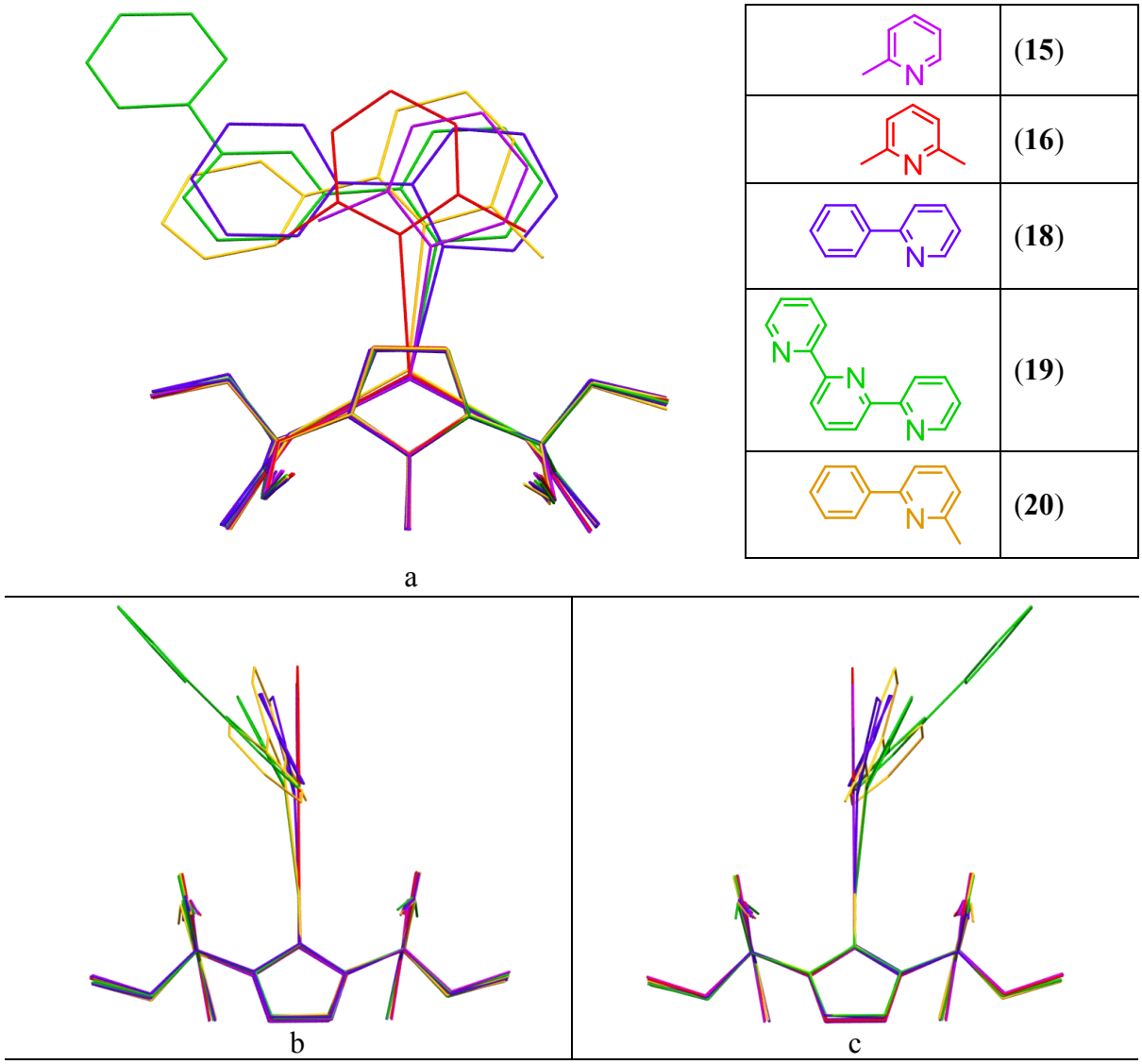

Figure 4-12 Molecular structures of $[(Et_8N_4Me_2)Sm(L)]$ for L = 2-pic, (**15**), 2,6-lut, (**16**), 2-Phpy, (**18**), terpy, (**19**), and 2-Me-6-Phpy, (**20**), superimposed at the four *meso*- carbons of the macrocycle of each complex. Viewed a) with the binding groove running from left to right, b) along the binding groove from the most substituted side of the ligand, and c) along the binding groove from the least substituted side of the ligand.

The limited coordination relief achieved *via* tilting the 2-methyl-6-phenylpyridine ligand in comparison to the 2-phenylpyridine ligand due to the opposing 2-methyl group of the former is demonstrated, Figure 4-12. This results in the longest $Sm{-}N_{ligand}$ distance in

this series for the complex formed with 2-Me-6-Phpy, (**20**). The extent of geometry deformation makes it apparent that the outcompeting of THF by the 2,6-disubstituted pyridine ligand for coordination in the formation of (**20**) must be verging on the limit of possibility due to sterics. Concentration effects resulting from a massive excess of reagent during precipitation are likely to have been influential in this competition. Binding strength studies were not undertaken. Greater $Sm{-}N_{ligand}$ distances and angular deformations have been observed for the Sm^{II} complex of 2,9-dimethyl-1,10-phenanthroline, Section 4.3.3. The bidentate coordination and different ligand shape in this case allow coordination at distances inaccessible to a 1:1 complex with a single donor atom, as per (**20**).

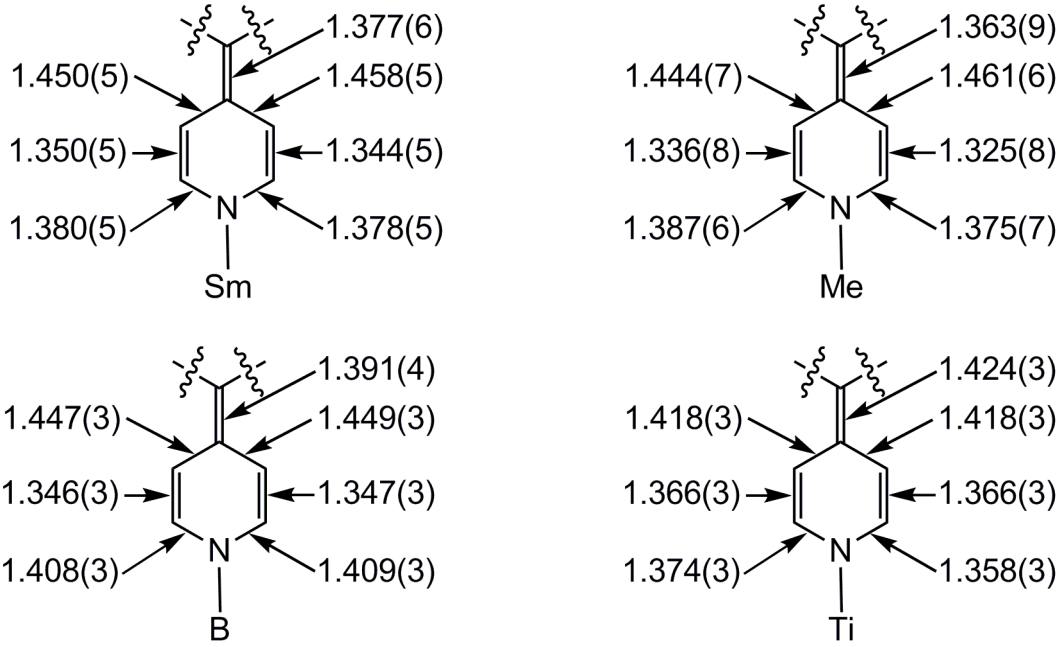

Figure 4-13 Bond lengths (Å) of the doubly reduced samarium 4,4′-bipyridine ligand (**21**) (top left), and reported complexes *N*,*N*′-dimethyl-4,4′-dihydrobipyridine (top right),[254] reduced 4,4′-bipyridine *via* boron reduction (bottom left),[255] and titanium reduction (bottom right).[256]

Although $[(C_5Me_5)_2Yb]$ has been shown to form a 1:1 neutral adduct of 4,4′-bipyridine,[217] the reduction of 4,4′-bipyridine by two molecules of $[(Et_8N_4Me_2)Sm(THF)_2]$ to form a doubly reduced bridging dianion between two Sm^{III} centres, $[\{(Et_8N_4Me_2)Sm\}_2(\mu\text{-}4,4'\text{-bipy})]$, (**21**), is expected for samarium(II), which has a

higher reduction potential than ytterbium(II), Section 1.2. The Sm−N_{ligand} and the intra-ligand bond lengths are both consistent with this assignment and compare well to a series of reported complexes, Figure 4-13.

4.3.2 Reactions with Benzannulated Pyridine Ligands

Following the reactivity investigated in Section 4.3.1, a benzannulated pyridine series was investigated to further study the effect of increasing steric bulk at the ancillary ligand. Benzannulated pyridines have reduced conformational freedom compared to substituted pyridines and, additionally, the effect of benzannulation on the electronic structure of the ligand was of interest, where increased resonance stabilisation of the reduced forms may influence the reactivity, providing a richer range of reaction outcomes dictated by both steric and electronic factors. The series of heterocycles studied is shown below, Figure 4-14.

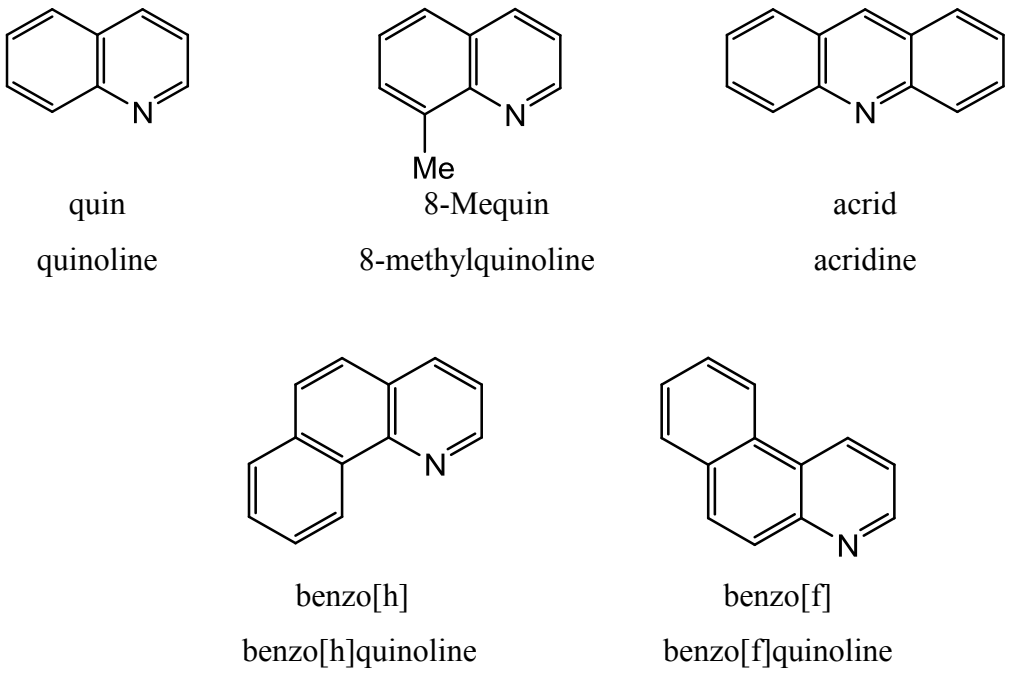

quin
quinoline

8-Mequin
8-methylquinoline

acrid
acridine

benzo[h]
benzo[h]quinoline

benzo[f]
benzo[f]quinoline

Figure 4-14: The substituted quinoline ligands employed in this study.

The synthesis of each complex described in this Section was achieved by addition of excess ligand to $[(Et_8N_4Me_2)Sm(THF)_2]$, (**XVI**) in either C_6H_6 or PhMe on a small scale

(*ca*. 10 mg [$(Et_8N_4Me_2)Sm(THF)_2$]). The outcomes of these reactions are described in turn below.

Addition of excess quinoline to a benzene solution of (**XVI**) at room temperature results immediately in a richly coloured dark purple solution. ^{1}H NMR spectroscopic analysis of the reaction within five minutes of addition reveals a complex spectrum consistent with a Sm^{III} centre (all resonances are located between -2 and 10 ppm) with reduced macrocyclic symmetry. Evaporation of the reaction solvent provides purple crystals of [$\{(Et_8N_4Me_2)Sm^{III}\}_2$(μ-4,4′-biquin)], (**22**), by X-ray crystal structure analysis, where the dianionic bridging (μ-4,4′-biquin) moiety arises due to reductive coupling at the 4- position of the quinoline ligand.

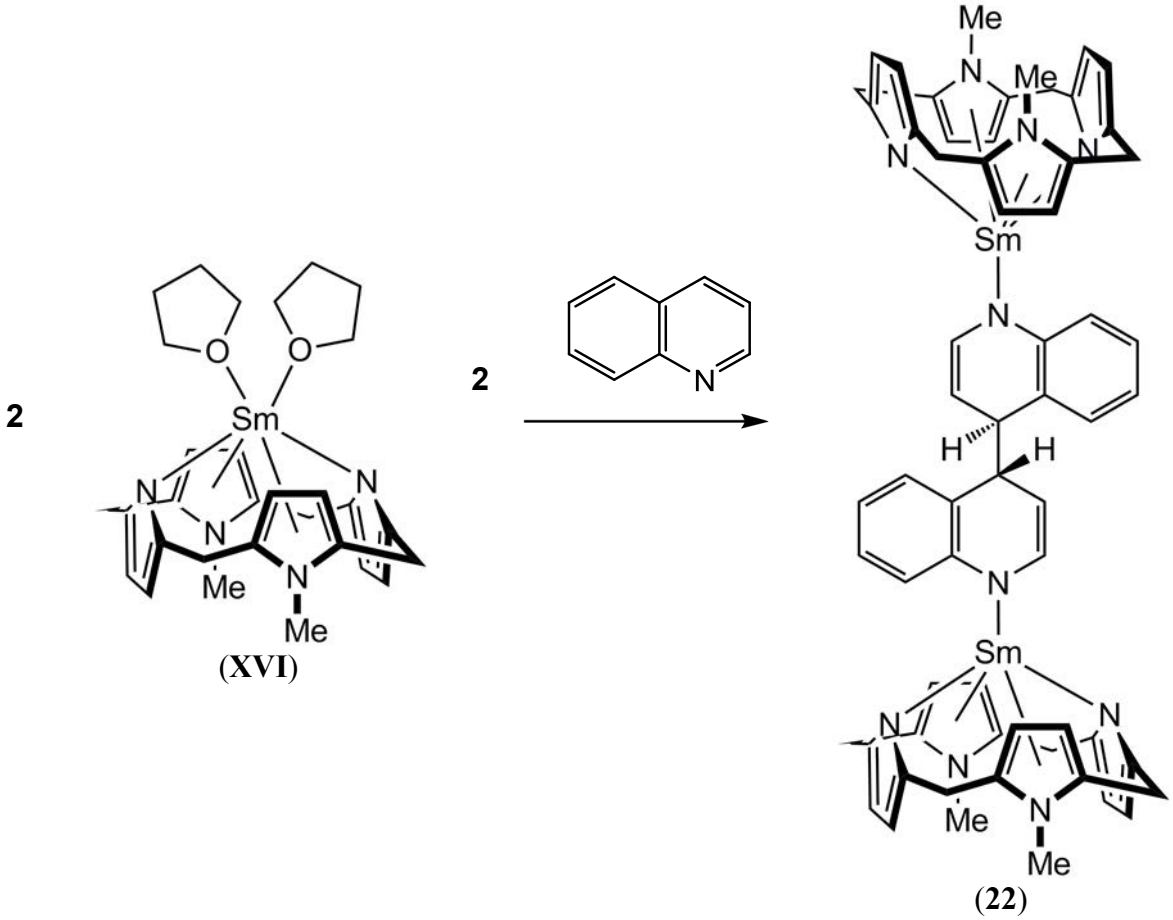

(**XVI**) (**22**)

Equation 4-12

Reductive dimerisation at the 4 position of the quinoline ligand leading to formation of (**22**) presumably indicates that the reaction proceeds *via* single electron reduction of quinoline to an initially formed complex of a singly reduced quinoline ligand, $[(Et_8N_4Me_2)Sm^{III}(quin^{\bullet-})]$. Detailed discussion of the X-ray crystal structure of the dimerised product, $[\{(Et_8N_4Me_2)Sm^{III}\}_2(\mu\text{-}4,4'\text{-biquin})]$, (**22**), is presented in Section 4.3.2.1; however the $Sm-N_{ligand}$ distance (2.285(7) – 2.325(5) Å) and macrocyclic geometry are consistent with the assigned samarium(III) oxidation state.

The structure of $[\{(Et_8N_4Me_2)Sm^{III}\}_2(\mu\text{-}4,4'\text{-biquin})]$, (**22**), is consistent with the complex appearance of the ^{1}H NMR spectrum. The stereogenic carbon centre at the 4-position of the quinoline, together with the annulated bicycle, removes all effective symmetry of the macrocycle if the complex is not fluxional with regard to the binding of the heterocycle within the binding groove.

Dimerisation of quinoline to form the 4,4′-dihydro-4,4′-diquinolinyl dianion has been shown electrochemically without structural assignment by Crooks and Bard;[213] work by Grignon-Dubois *et al.* reported two diastereomers of reductively dimerised quinoline *via* reaction with Me_3SiCl and either lithium or magnesium, where coupling similarly occurred at the 4 position of the ligand to give the (*R*,*S*) and (*S*,*S*) isomers, respectively.[214] The stereoselectivity of the reaction described by Equation 4-12 was deemed beyond the scope of this project and not pursued.

Reaction of 8-methylquinoline with $[(Et_8N_4Me_2)Sm(THF)_2]$, (**XVI**), resulted in formation of a sparingly soluble red 1:1 complex $[(Et_8N_4Me_2)Sm^{II}(8\text{-Mequin})]$, (**23**), which shows no evidence of reductive dimerisation. The reaction proceeds according to Equation 4-13 and the product is only sparingly soluble in either toluene or benzene; within 15 minutes at room temperature, large, dark crystals and only a trace of colour in the

supernatant solution is observed. Complex (**23**) was isolated in 67 % yield and shown to also be sparingly soluble in 40-60 ° petroleum spirits. ^{1}H NMR spectroscopic analysis of a C_6D_6 solution obtained within five minutes of reaction indicated loss of the resonances attributed to bound THF and an increase in resonances of free THF. This same ^{1}H NMR spectrum also showed wide, paramagnetic shifts characteristic of a samarium(II) species. Full characterisation by ^{1}H NMR and ^{13}C NMR spectroscopy of an isolated sample of [($Et_8N_4Me_2$)Sm(8-Mequin)], (**23**), was impeded by the insoluble nature of the complex.

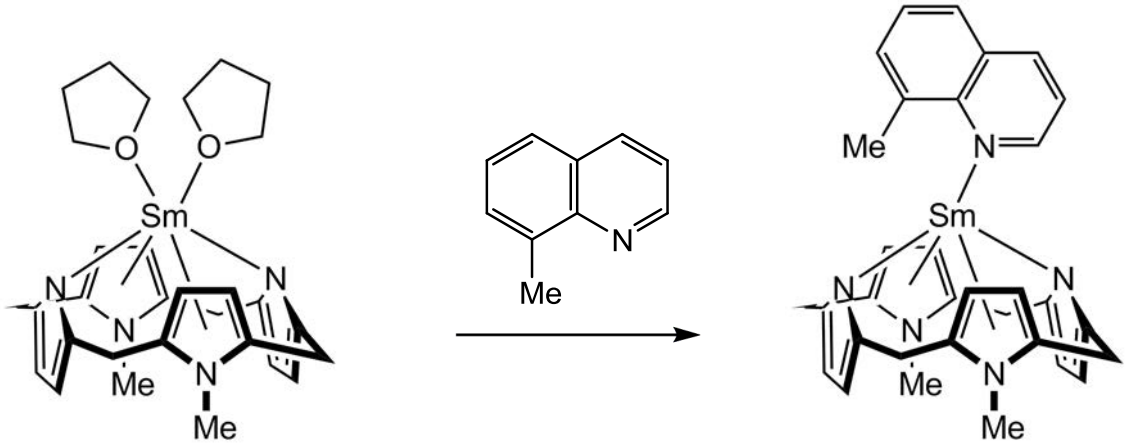

(**XVI**) (**23**)

Equation 4-13

The difference in reactivity observed for quinoline and 8-methyquinoline, with regard to the reductive dimerisation observed for (**22**) and adduct formation for (**23**), is noteworthy. DFT analysis was employed to investigate the oxidation state of (**23**) confirming the assigned Sm^{II} oxidation state based on ^{1}H NMR spectroscopic evidence. Additionally, the electron affinity of each ligand in the gas phase was calculated in an attempt to better understand the reaction outcomes; the conclusion drawn from this analysis is that the differing reaction outcomes are likely the result of a complex combination of both steric and electronic influences. Further discussion of these calculations is undertaken within the additional context of the entire series of complexes reported in Section 4.3.4.

Benzo[h]quinoline forms a soluble complex upon reaction with a benzene solution of (**XVI**) according to Equation 4-14. Dark purple crystals a 1:1 complex of $[(Et_8N_4Me_2)Sm^{II}(benzo[h])]$, (**24**), were isolated and characterised by X-ray crystallography. DFT analysis reveals that the metal in complex (**24**) is present as samarium(II). NMR analysis was deemed unnecessary given the lack of data available throughout the series.

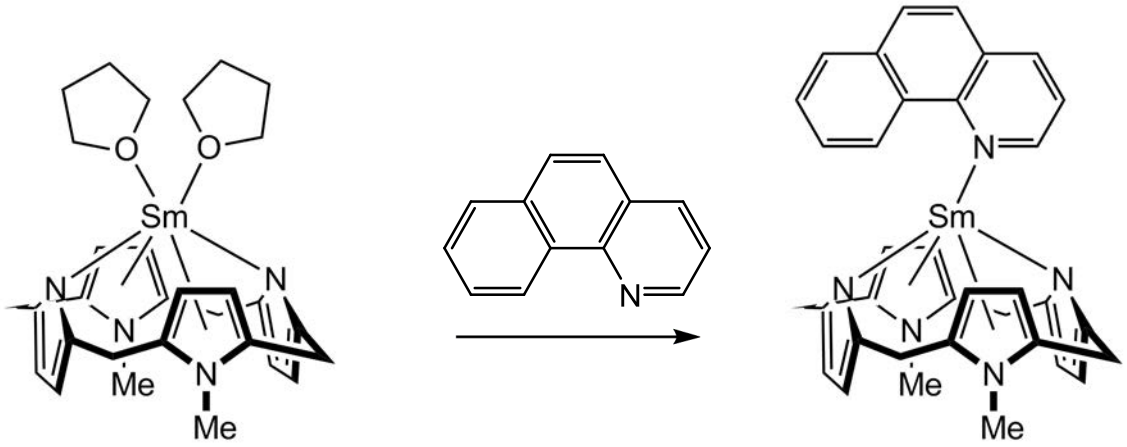

(**XVI**) (**24**)

Equation 4-14

Based on steric considerations, the synthesis of (**24**) is consistent with the analogous reactions with 8-methylquinoline and 2-phenylpyridine, which have similar steric influences to the benzo[h]quinoline ligand. This similarity is reflected in the geometry and metal oxidation state in each of the complexes and is discussed further in Sections 4.3.2.2 and 4.3.2.3

Benzo[f]quinoline reacts with a toluene solution of (**XVI**) to form a dark green solution, from which dark purple crystals were isolated of the 1:1 adduct after one week of standing at room temperature in the glovebox, Equation 4-15. Complex (**25**) is sparingly soluble in benzene and 40-60 ° petroleum spirits. The X-ray crystal structure refinement reveals one molecule of toluene in the crystal lattice; however washing (**25**) with benzene

provided a dark solid that was shown to contain no lattice solvent by satisfactory elemental analysis.

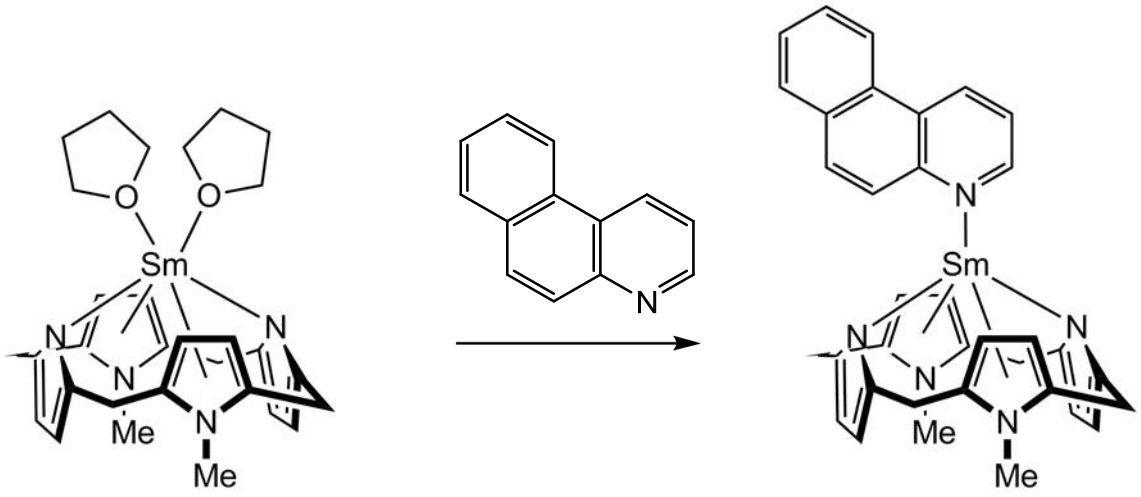

(**XVI**) (**25**)

Equation 4-15

The steric influence of the benzo[f]quinoline ligand on the macrocyclic binding groove are similar to an unsubstituted quinoline species, yet reductive dimerisation, as is the case for quinoline, (**22**), is not observed. This difference in reaction outcome for $[(Et_8N_4Me_2)Sm(THF)_2]$, (**XVI**), with quinoline (**22**) and benzo[f]quinoline (**25**) is thus ascribed to the electronic properties of the respective ligand. DFT analysis was undertaken to probe nature of these electronic properties, Section 4.3.4.

The reaction of acridine and (**XVI**) proceeds to the reductive dimerisation product $[\{(Et_8N_4Me_2)Sm\}_2(\mu\text{-}7,7'\text{-biacrid})]$, (**26**), according to Equation 4-16, where the dianionic bridging (μ-7,7′-biacrid) moiety arises due to reductive coupling at the 7- position of the acridine ligand. The reaction proceeds in THF, toluene and benzene *via* a very dark blue solution which subsequently changes to a clear solution above an insoluble bright purple precipitate. Efforts to crystallise the dark blue solution, presumably due to the $[(Et_8N_4Me_2)Sm^{III}(acrid^{\bullet-})]$ species, were unsuccessful both at lower temperatures and with the exclusion of light. The extremely insoluble complex (**26**) was isolated in 77 % yield

and characterised by X-ray crystal structure determination and satisfactory elemental analysis.

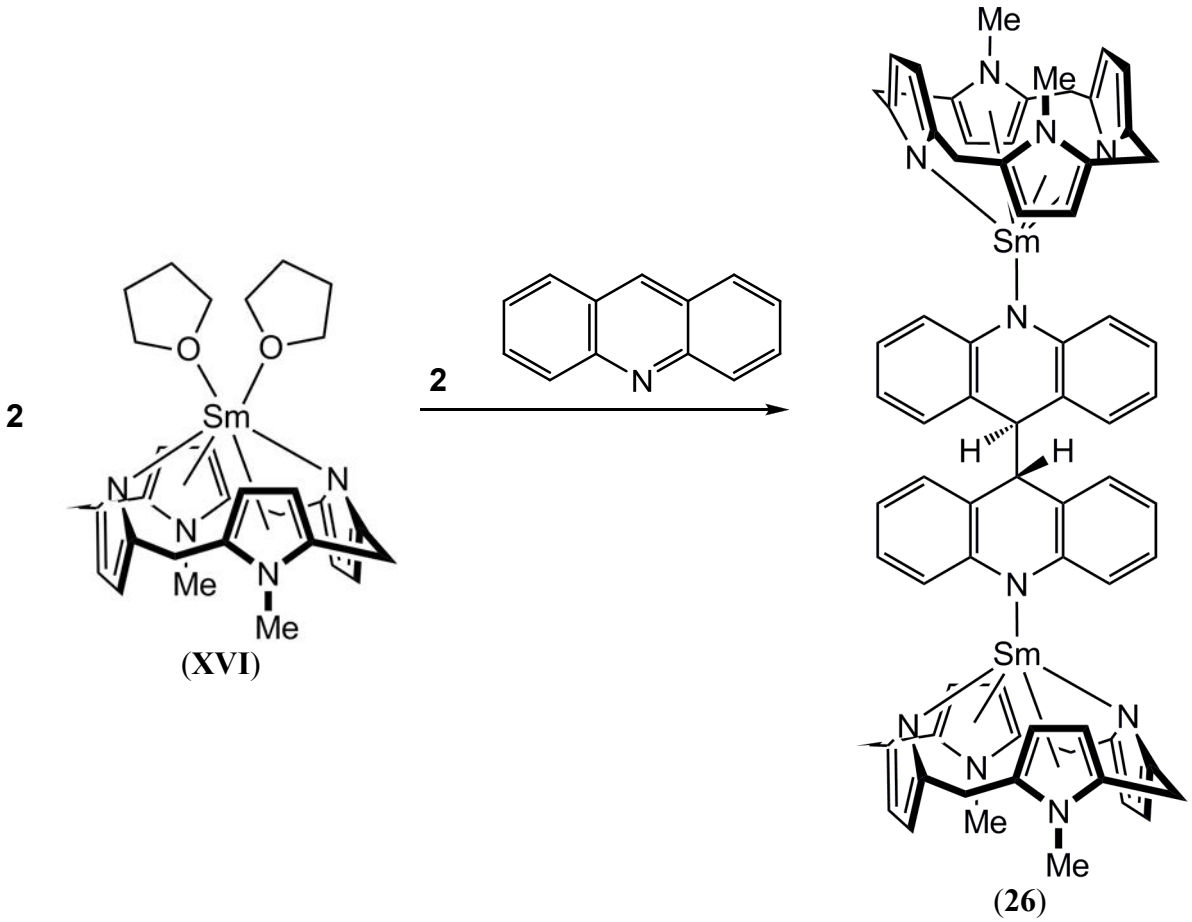

(**XVI**) (**26**)

Equation 4-16

As with [{($Et_8N_4Me_2$)Sm^{III}}$_2$(μ-4,4′-biquin)], (**22**), no evidence for dimerisation at any position other than the 7- position of the coordinating ring was observed for (**26**). NMR spectroscopic analysis could not be undertaken due to the sparing solubility of (**26**). A crystalline sample of (**26**) was submerged in a 5 % HCl solution with no change observed by eye over several hours; overnight, however, the complex was shown to deteriorate to a white precipitate. GC-MS and ESI analysis of (**26**) and the hydrolysed product provided no evidence of the hydrolysis product of the coupled acridine ligand, 9,9′-dihydro-9,9′-biacridinyl, or its protonated form. The absence of these species is consistent with a report by Crooks and Bard that the dimerisations of acridine and

quinoline become highly facile above 60 °C.[213] As per the reactivity patterns described in this Section, the reductive dimerisation outcome observed for acridine is investigated by DFT analysis, Section 4.3.4.

4.3.2.1 Molecular Structure of [{(Et$_8$N$_4$Me$_2$)Sm}$_2$(μ-4,4'-biquin)]·2.75(C$_6$H$_6$), (22)

Crystals of (**22**) belong to the triclinic space group *P* (No. 2), *a* = 15.090(3), *b* = 17.4024(17), *c* = 40.790(3) Å, α = 77.763(3), β = 85.506(8), γ = 68.731(4)°, with four dinuclear complexes in the unit cell. The asymmetric unit consists of two centrosymmetric and one [{(Et$_8$N$_4$Me$_2$)Sm}$_2$(μ-4,4′-biquin)] molecule, with five and a half molecules of benzene in the lattice, Figure 4-15.

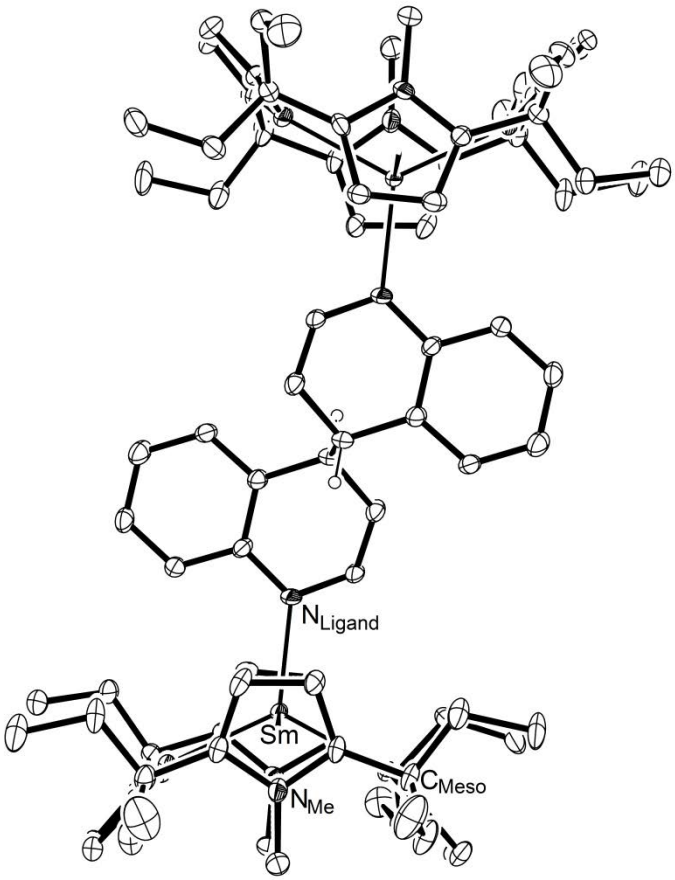

Figure 4-15 Molecular structure of (**22**) with thermal ellipsoids drawn at 50 % probability. One molecule; solvent molecules and protons (except the 4 and 4′ ligand protons) are omitted for clarity.

The molecular structure of (**22**) exhibits the standard $\eta^1{:}\eta^5{:}\eta^1{:}\eta^5$ macrocyclic binding mode. The Sm-(η^1-N_{Py}) distances range from 2.452(5) to 2.491(6) Å and the Sm-(η^5-N_{Me}) distances range from 2.58_6 to 2.61_5 Å. The N_{Py}–*meso* interplanar angles range from 46.9(3) to 52.4(2) ° and the N_{Me}–*meso* interplanar angles range from 79.8(2) to 81.7(2) °. The Sm–*meso* distances are between 1.138(3) and 1.162(4) Å. The molecular geometry of (**22**) compares favourably with [{($Et_8N_4Me_2$)Sm^{III}}$_2$(μ-4,4′-bipy)], (**21**), Table 4-6, indicating that the steric bulk of quinoline, as a benzannulated pyridine, has little effect on the macrocyclic coordination environment (noting both the similarity between the two as Sm^{III}-amide complexes and the difference in the presence or absence of 4,4′-dihydro functionality in (**22**) and (**21**), respectively).

	M = Sm^{III}, n = 2 L = (μ-4,4′-biquin) (**22**)	M = Sm^{III}, n = 2 L = (μ-4,4′-bipy) (**21**)	M = Sm^{II}, n = 1 L = (2-pic) (**15**)
M–L	2.285(7) – 2.325(5)	2.284(3)	2.609(3)
M–(η^1-N_{Py})	2.452(5) – 2.491(6)	2.452(3), 2.479(3)	2.5511(15)
M–(η^5-N_{Me})	2.58_6 – 2.61_5	2.57_7, 2.58_9	2.65_9
M–*meso*	1.138(3) – 1.162(4)	1.1048(16)	1.2334(15)
N_{Py}–*meso*	46.9(3) – 52.4(2)	43.22(7), 51.85(11)	55.25(7)
N_{Me}–*meso*	79.8(2) – 81.7(2)	79.17(8), 81.12(7)	79.88(5)
Metallocene bend	169.2_6	170.8_2	165.4_3

Table 4-6 Selected bond lengths (Å) and angles (°) for [{($Et_8N_4Me_2$)M}$_n$(L)].

The quinoline ligand is bound to the Sm^{III} centre in an η^1- fashion *via* the nitrogen atom; the Sm–N_{ligand} distances ranges from 2.285(7) to 2.325(5) Å. In the solid state, the molecule adopts an (*R,S*) racemic conformation with a H–C–C–H dihedral angle of 180 ° about the newly formed 4,4′- bond for the centrosymmetric molecules and $65._1$ ° for the full molecule in the asymmetric unit, Figure 4-16.

The angles of ligand incidence, twist and tilt with respect to the macrocyclic binding groove vary significantly between the two half molecules in the asymmetric unit, with one coupled quinoline unit subject to angles of incidence, twist and tilt of 6.7_1, 5.5_9 and 11.4_5 °, respectively, compared to the other with 28.9_9, 1.2_1 and 6.9_2 °, respectively. The non-centrosymmetric molecule in the asymmetric unit, Figure 4-16, also shows significant variation from one side of the molecule to the other, with incidence, twist and tilt angles of 18.4_6, 8.9_3, and 34.3_2 ° for one half of the dimer, respectively, compared to the other half of the dimer with 23.1_8, 4.2_5, and 14.3_7 °, respectively.

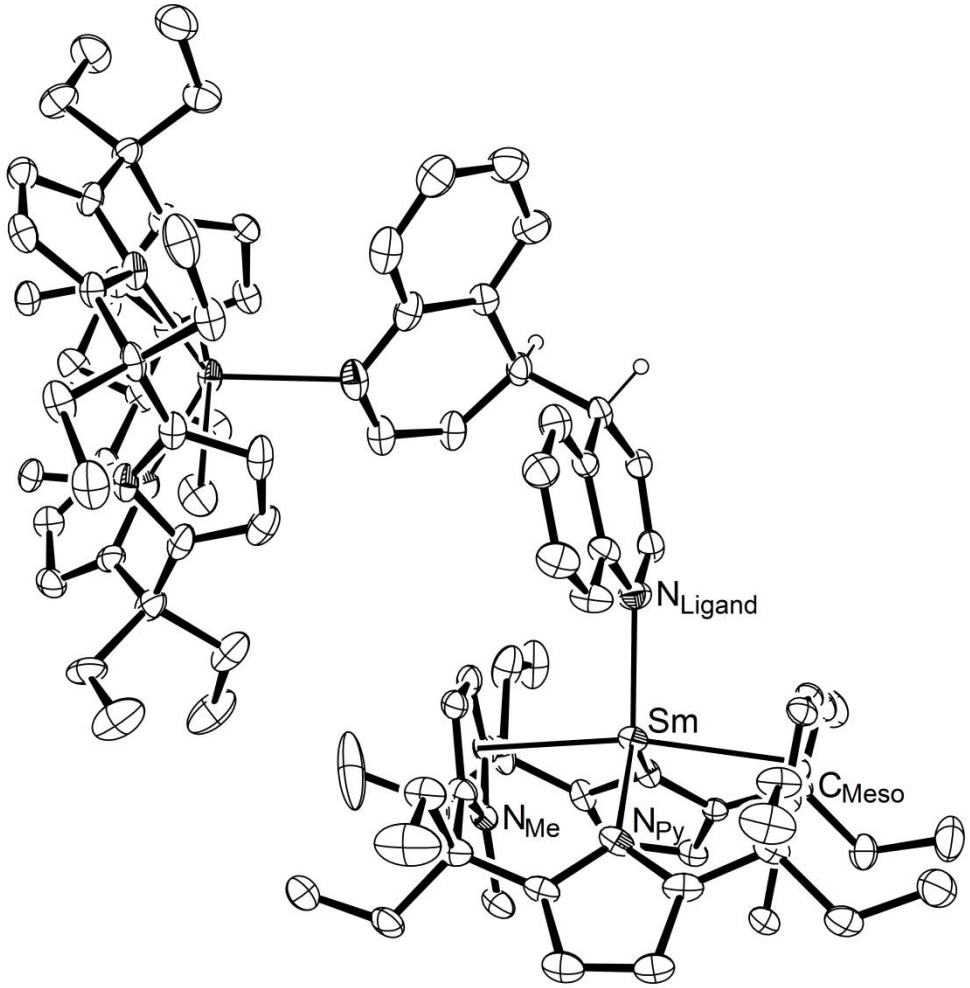

Figure 4-16 Molecular structure of the non-centrosymmetric molecule of (**22**) with thermal ellipsoids drawn at 50 % probability. One molecule; solvent molecules and protons (except the 4 and 4′ ligand protons) are omitted for clarity.

4.3.2.2 Molecular Structure of [($Et_8N_4Me_2$)Sm(8-Mequin)]·PhMe, (23)

Crystals of (**23**) belong to the monoclinic space group *Pn* (No. 7), a = 11.4090(7), b = 20.1660(6), c = 20.7300(6) Å, β = 94.125(4) °, with four molecules in the unit cell. The asymmetric unit consists of two molecules of (**23**) and two molecules of toluene. The 8-methylquinoline ligand is positionally disordered over two sites in both molecules, involving a flipping of the heterocycles along the binding groove and requiring isotropic refinement of two N_{ligand} and three $C_{solvent}$ atoms.

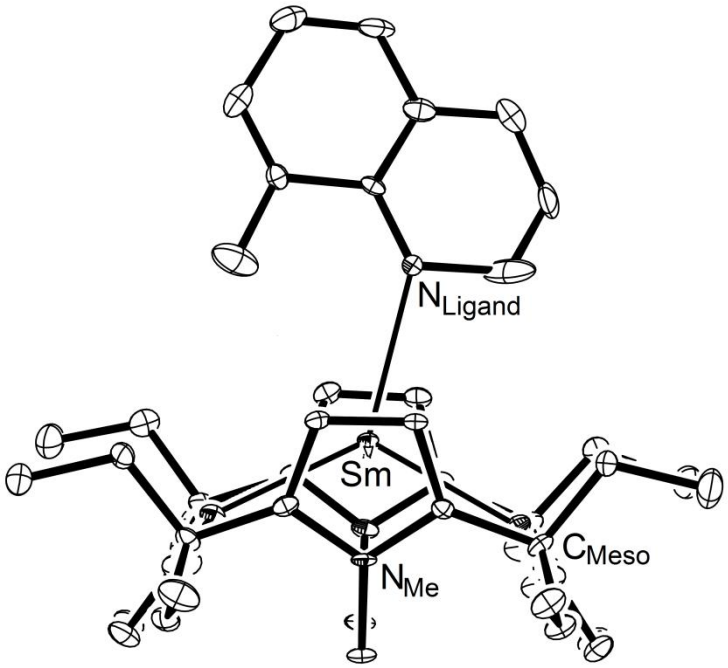

Figure 4-17 Molecular structure of (**23**) with thermal ellipsoids drawn at 50 % probability. One molecule; solvent toluene and protons omitted for clarity.

The molecular structure of (**23**), Figure 4-17, exhibits the standard $\eta^1{:}\eta^5{:}\eta^1{:}\eta^5$ macrocyclic binding mode. The Sm-(η^1-N_{Py}) distances range from 2.594(4) to 2.610(4) Å and the Sm-(η^5-N_{Me}) distances range from 2.69_2 to 2.70_4 Å. The N_{Py}–*meso* interplanar angles range from 54.6(1) to 55.7(1) °, and the N_{Me}–*meso* interplanar angles range from 77.0(1) to 78.0(1) °. The Sm–*meso* distances are 1.321(2) and 1.313(2) Å. Table 4-7 compares the molecular geometry of (**23**) with the 1:1 Sm^{II} adduct formed with 2-phenylpyridine, (**18**), and the Sm^{III}-quinoline dimer, (**22**).

	$M = Sm^{II}$, n = 1 L = (8-Mequin) (**23**)	$M = Sm^{II}$ L = (2-pic) (**15**)	$M = Sm^{II}$, n = 1 L = (2-Phpy) (**18**)
M−L	2.640(7) – 2.716(7)	2.609(3)	2.60(3)
M−(η^1-N_{Py})	2.594(4) – 2.610(4)	2.5511(15)	2.58(2), 2.58(2)
M−(η^5-N_{Me})	2.69_2 – 2.70_4	2.65_9	2.68_2, 2.70_9
M−*meso*	1.321(2), 1.313(2)	1.2334(15)	1.28(1)
N_{Py}−*meso*	54.6(1) – 55.7(1)	55.25(7)	50.1(9) (H), 54.5(7) (Ph)
N_{Me}−*meso*	77.0(1) – 78.0(1)	79.88(5)	77.4(8), 76.2(8)
Metallocene bend	161.8_0	165.4_3	163.6_5

Table 4-7 Selected bond lengths (Å) and angles (°) for $[\{(Et_8N_4Me_2)M\}_n(L)]$.

The slight variation between structural metrics observed for the 1:1 adducts of 8-methylquinoline and 2-picoline arise as a direct result of the steric interaction of the binding groove and the respective methyl groups. By comparison, the methyl group of 8-methylquinoline points more directly into the binding groove of the macrocycle, resulting in an increase in Sm−*meso* distance, which in turn affects the other structural metrics, Table 4-7. Similar variation between the structural metrics of the 1:1 adducts of 8-methylquinoline and 2-phenylpyridine are also observed. In this case, the position of the methyl carbon is approximately equal to the position of one *ortho*- carbon of the phenyl group. The small increase in M−L and M−*meso* distances for (**23**) compared to (**18**) is in accord with the small increase in bulk from the single proton of the phenyl ring of (**18**), which fits within the binding groove, to the three protons of the methyl group of (**23**), which will not fit within the binding groove. Accounting for this minor variation, both the molecular geometry and DFT analysis of (**23**) indicate that the samarium centres are present as samarium(II).

The 8-Methylquinoline ligand binds to the samarium(II) centre in (**23**) in an η^1-fashion through the nitrogen atom at a distance ranging from 2.640(7) to 2.716(7) Å. The

heterocycle is approximately flat, with angles of incidence, twist and tilt ranging from 6.9_1 - 18.2_0, 2.6_5 - 9.7_4, and 30.3_5 - 32.4_1 °, respectively.

4.3.2.3 Molecular Structure of [($Et_8N_4Me_2$)Sm(benzo[h])], (24)

Dark purple prismatic crystals of (**24**) belong to the orthorhombic space group $P2_12_12_1$ (No. 19), $a = 11.6950(11)$, $b = 17.0190(15)$, $c = 21.6040(14)$ Å with four molecules in the unit cell. The asymmetric unit consists of a single molecule of the 1:1 complex, Figure 4-18; there is neither solvent nor disorder present.

The molecular structure of (**24**) adopts the standard $\eta^1{:}\eta^5{:}\eta^1{:}\eta^5$ macrocyclic binding mode. The Sm-(η^1-N_{Py}) distances are 2.558(4) and 2.560(4) Å and the Sm-(η^5-N_{Me}) distances are 2.67_9 and 2.68_5 Å. The N_{Py}–*meso* interplanar angles are 54.7(1) and 55.3(1) °, and the N_{Py}–*meso* interplanar angles are 78.75(15) and 78.92(13) °. The Sm–*meso* distance is 1.227(3) Å.

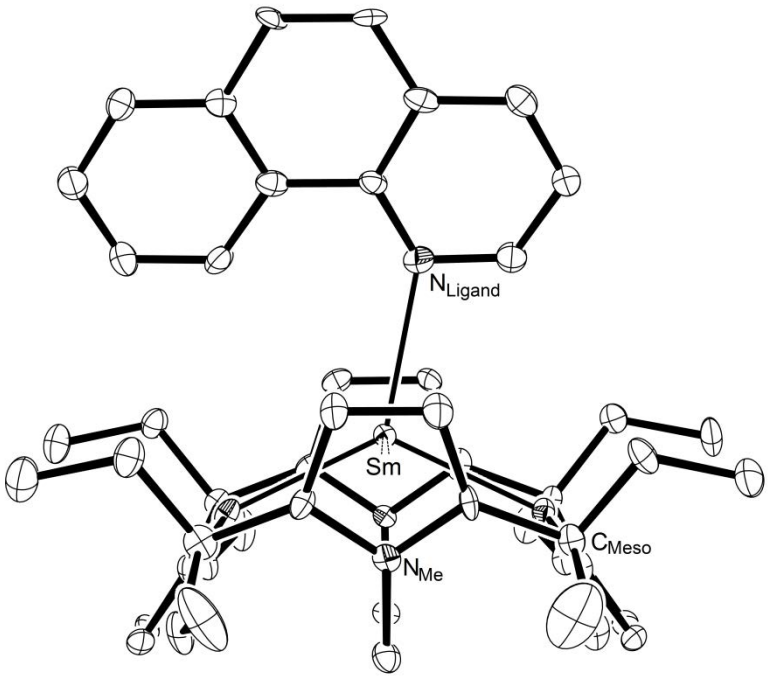

Figure 4-18 Molecular structure of (**24**) with thermal ellipsoids drawn at 50 % probability. Protons omitted for clarity.

Table 4-8 compares the structural metrics of (**24**) with 1:1 adducts of samarium(II) for 2-picoline, (**15**), 2-phenylpyridine, (**18**), and 8-methylquinoline, (**23**) revealing that the structures of (**15**), (**18**) and (**24**) are remarkably similar.

	$M = Sm^{II}$ L = (benzo[h]) (**24**)	$M = Sm^{II}$ L = (2-pic) (**15**)	$M = Sm^{II}$ L = (2-Phpy) (**18**)	$M = Sm^{II}$ L = (8-Mequin) (**23**)
M−L	2.605(4)	2.609(3)	2.60(3)	2.640(7) – 2.716(7)
$M-(\eta^1\text{-}N_{Py})$	2.558(4), 2.560(4)	2.5511(15)	2.58(2), 2.58(2)	2.594(4) – 2.610(4)
$M-(\eta^5\text{-}N_{Me})$	2.67_9, 2.68_5	2.65_9	2.68_2, 2.70_9	2.69_2 – 2.70_4
M−*meso*	1.227(3)	1.2334(15)	1.28(1)	1.321(2), 1.313(2)
N_{Py}−*meso*	54.7(1), 55.3(1)	55.25(7)	50.1(9) (H), 54.5(7) (Ph)	54.6(1) – 55.7(1)
N_{Me}−*meso*	78.75(15), 78.92(13)	79.88(5)	77.4(8), 76.2(8)	77.0(1) – 78.0(1)
Metallocene bend	165.7_7	165.4_3	163.6_5	161.8_0

Table 4-8 Selected bond lengths (Å) and angles (°) for $[(Et_8N_4Me_2)M(L)]$.

The observed structural similarity is a result of the similar ligand shape shared by these ligands, with the respective methyl, (**15**), phenyl, (**18**), and benzannulated, (**24**), bulk interacting with the binding groove of the macrocycle at approximately the same position for the three ligands. As noted, the methyl group of 8-methylquinoline is directed deeper into the binding groove with respect to the coordinating nitrogen for (**23**), resulting in the observed structural variation. Given that benzo[h]quinoline represents a conformationally locked 2-phenylpyridine ligand, the structural features of (**24**) may have been expected to more closely resemble the 2-phenylpyridine complex, (**18**), rather than the complex of 2-picoline, (**15**); Table 4-8 reveals that this is not the case. Both DFT analysis and the molecular structure of (**24**) indicate a samarium(II) species.

The benzo[h]quinoline ligand binds to the metal with an angle of incidence of 19.0_8 ° and 0.3_1 ° of twist. To accommodate the steric bulk directed into the binding groove, the

benzo[h]quinoline ligand is subject to a tilt of 31.2_6 °, which is consistent with the 30.3_5 - 32.4_1 ° tilt observed for the 8-methylquinoline ligand in (**23**).

4.3.2.4 Molecular Structure of [($Et_8N_4Me_2$)Sm(benzo[f])]·0.66(PhMe), (25)

Crystals of (**25**) belong to the orthorhombic space group $Pmn2_1$ (No. 31), a = 35.5300(14), b = 19.6600(6), c = 14.020(3) Å, with eight molecules in the unit cell. The asymmetric unit consists of a molecule of (**25**) with approximate C_2 symmetry (owing to a twist of the heterocycle and the conformation of two ethyl groups), two molecules of (**25**) residing on crystallographic mirror planes (one possessing a two component conformational disorder of an ethyl group), and two molecules of toluene.

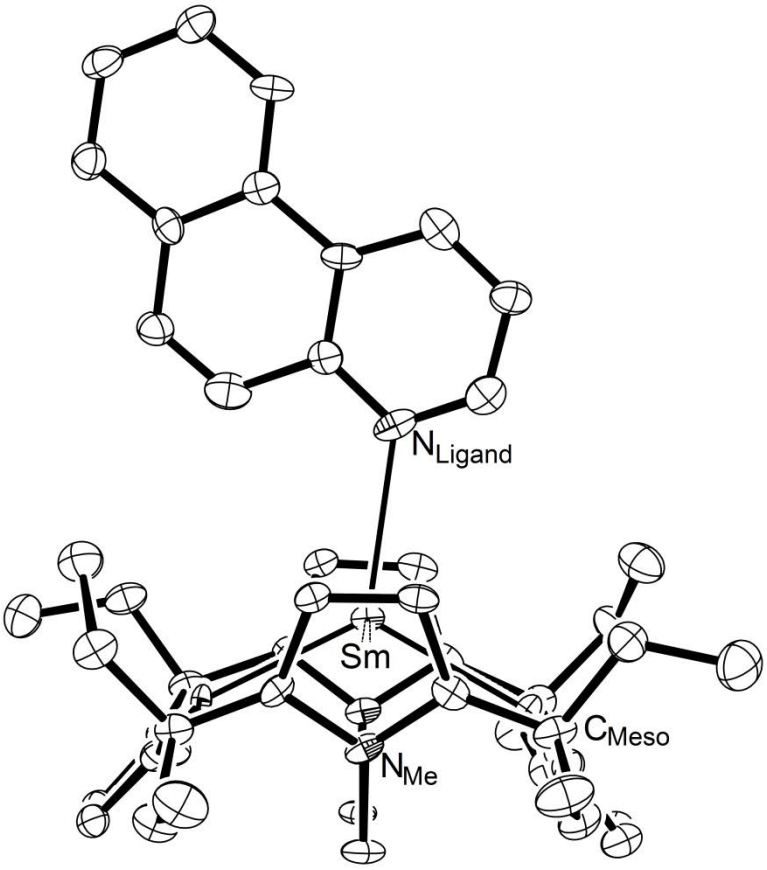

Figure 4-19 Molecular structure of (**25**) with thermal ellipsoids drawn at 50 % probability (one molecule depicted, solvent toluene and protons omitted for clarity).

The molecular structure of (**25**) adopts the standard $\eta^1{:}\eta^5{:}\eta^1{:}\eta^5$ macrocyclic binding mode, Figure 4-19. The Sm-(η^1-N_{Py}) distances range from 2.552(6) to 2.589(4) Å and the Sm-(η^5-N_{Me}) distances range from 2.65_2 to 2.66_3 Å. The N_{Py}–*meso* interplanar angles range from 47.7(2) to 59.2(3) °, and the N_{Me}–*meso* interplanar angles range from 77.02(18) to 79.81(19) ° . The Sm–*meso* distance is between 1.193(4) and 1.305(3) Å.

	M = Sm^{II} L = (benzo[f]) (**25**)	M = Sm^{II} L = (benzo[h]) (**24**)	M = Sm^{III}, n = 2 L = (μ-4,4′-biquin) (**22**)
M–L	2.639(7) – 2.716(5)	2.605(4)	2.285(7) – 2.325(5)
M–(η^1-N_{Py})	2.552(6) – 2.589(4)	2.558(4), 2.560(4)	2.452(5) – 2.491(6)
M–(η^5-N_{Me})	2.65_2 – 2.66_3	2.67_9, 2.68_5	2.58_6 – 2.61_5
M–*meso*	1.193(4) – 1.305(3)	1.227(3)	1.138(3) – 1.162(4)
N_{Py}–*meso*	47.7(2) – 59.2(3)	54.7(1), 55.3(1)	46.9(3) – 52.4(2)
N_{Me}–*meso*	77.02(18) – 79.81(19)	78.75(15), 78.92(13)	79.8(2) – 81.7(2)
Metallocene bend	165.4_7	165.7_7	169.2_6

Table 4-9 Selected bond lengths (Å) and angles (°) for $[\{(Et_8N_4Me_2)M\}_n(L)]$.

The molecular geometry of (**25**) is expected to provide an example of a sterically unhindered complex as the terminal C_6 ring is directed away from the binding groove of the macrocycle. Table 4-9 reveals that the relative geometries of the complexes formed with benzo[f]quinoline and benzo[h]quinoline ligands, (**25**) and (**24**), respectively, are not consistent with this expectation, with longer M–L and M–*meso* distances observed for (**25**). This reverse trend in structural metrics is likely due to electronic differences between the two benzannulated ligands. Additionally, it is likely that (**25**) represents a close structural analogue of the implied short-lived intermediate $[(Et_8N_4Me_2)Sm(quin^{\bullet-})]$ prior to C–C coupling to give $[\{(Et_8N_4Me_2)Sm\}_2$(μ-4,4′-biquin)], (**22**). The results of DFT

analysis on the molecular structure of [($Et_8N_4Me_2$)Sm(benzo[f])], (**25**), are consistent with a samarium(II) species.

The benzo[f]quinoline ligand lies on a mirror plane for the two half molecules in the asymmetric unit, however each is differentiated *via* a tilt angle of either 10.0_9 or 20.6_3 °. The full molecule in the asymmetric unit, Figure 4-19, exhibits an angle of incidence of 9.8_5 °, a ligand twist of 9.3_0 ° and a tilt angle of 10.4_5 °.

4.3.2.5 Molecular Structure of [{($Et_8N_4Me_2$)Sm}$_2$(μ-7,7'-biacrid)], (26)

Crystals of complex (**26**) belong to the monoclinic spacegroup $P2_1/c$ (No. 14), a = 12.301(3), b = 23.266(5), c = 15.312(3) Å, β = 97.53(3)° with two molecules in the unit cell. The asymmetric unit consists of one half of a centrosymmetric, reductively coupled dinuclear complex, Figure 4-20.

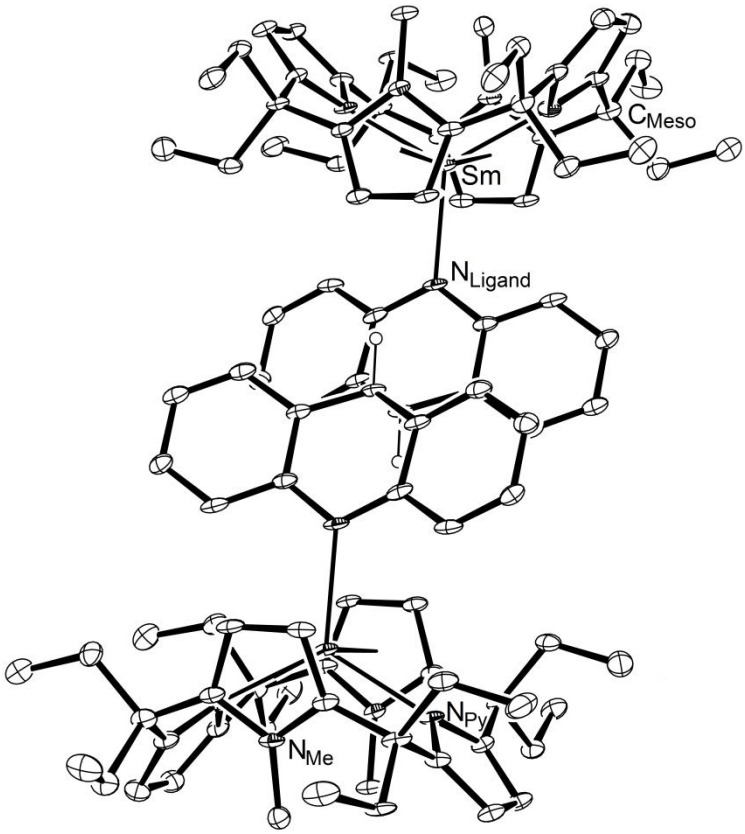

Figure 4-20 Molecular structure of (**26**) with thermal ellipsoids drawn at 50 % probability. Protons (except the 7 and 7′ ligand protons) omitted for clarity.

The molecular structure of (**26**) adopts the standard $\eta^1{:}\eta^5{:}\eta^1{:}\eta^5$ macrocyclic binding mode. The Sm-(η^1-N_{Py}) distances are 2.480(8) and 2.465(7) Å and the Sm-(η^5-N_{Me}) distances are 2.58_7 and 2.59_3 Å. The N_{Py}–*meso* interplanar angles are 46.4(3) and 52.1(3) °, and the N_{Me}–*meso* interplanar angles are 81.1(3) and 81.9(2) °. The Sm–*meso* distance is 1.185(4) Å.

The molecular geometry of (**26**), Table 4-10, is consistent with a samarium(III) species. The similarities in molecular geometry metrics to the reductively dimerised μ-4,4′-biquinoline complex, (**22**), are anticipated given the similar nature of the ligand. Small differences between (**22**) and (**26**) arise due to the symmetrical bulk about the coordinating central heterocyclic ring of acridine, resulting in slightly longer Sm–N_{ligand} and Sm–*meso* distances. This symmetrical coordination precludes tilting of the coupled acridine moiety within the binding groove; however a modest twist and significant angle of incidence, 2.8_5 and 24.7_2 °, respectively, are observed due to the steric bulk of the ligand and impossibility of strain relief through tilting.

	$M = Sm^{III}$, n = 2 L = (μ-7,7′-acrid) (**26**)	$M = Sm^{III}$, n = 2 L = (μ-4,4′-biquin) (**22**)	$M = Sm^{II}$ L = (benzo[f]) (**25**)
M–L	2.379(6)	2.285(7) – 2.325(5)	2.639(7) – 2.716(5)
M–(η^1-N_{Py})	2.480(8), 2.465(7)	2.452(5) – 2.491(6)	2.552(6) – 2.589(4)
M–(η^5-N_{Me})	2.58_7, 2.59_3	2.58_6 – 2.61_5	2.65_2 – 2.66_3
M–*meso*	1.185(4)	1.138(3) – 1.162(4)	1.193(4) – 1.305(3)
N_{Py}–*meso*	46.4(3), 52.1(3)	46.9(3) – 52.4(2)	47.7(2) – 59.2(3)
N_{Me}–*meso*	81.1(3), 81.9(2)	79.8(2) – 81.7(2)	77.02(18) – 79.81(19)
Metallocene bend	167.3_1	169.2_6	165.4_7

Table 4-10 Selected bond lengths (Å) and angles (°) for $[\{(Et_8N_4Me_2)M\}_n(L)]$.

4.3.3 Reactions with 1,10-Phenanthrolinoid Ligands

Following the reactivity investigated in sections 4.3.1 and 0, coordination of bidentate ligands based on pyridine, such as 2,2′-bipyridine, 1,10-phenanthroline and substituted 1,10-phenanthrolines, to $(Et_8N_4Me_2)Sm$ remains a valuable area for investigation. The 1,10-phenanthrolinoid ligands employed, Figure 4-21, were selected based upon potential for steric interaction at the binding groove of the samarium complex and additionally to examine the effect of both bidentate coordination and resonance stabilisation upon the reaction outcomes.

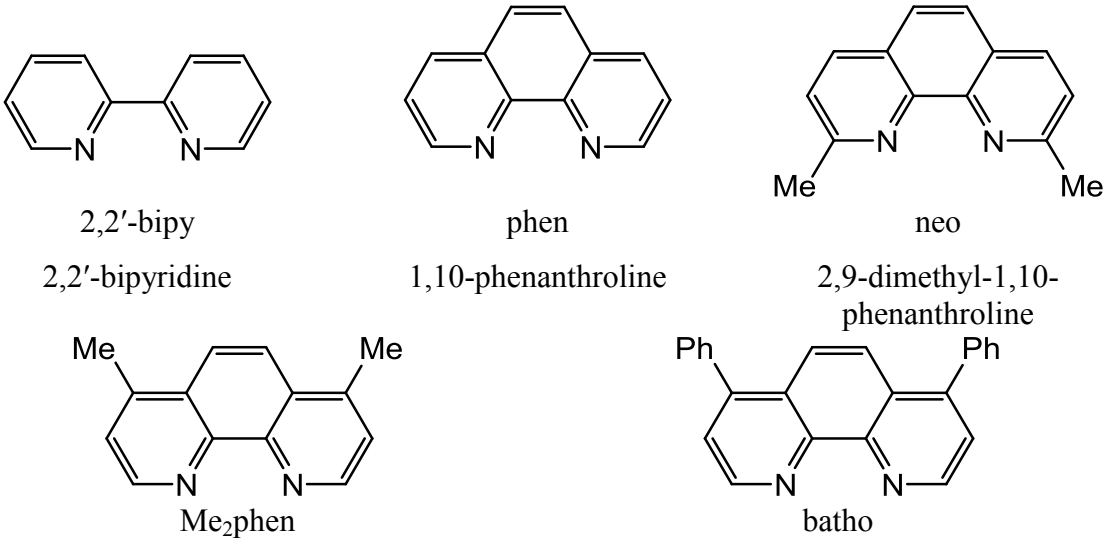

Figure 4-21 The 1,10-phenanthrolinoid ligands employed in this study.

The synthesis of each complex described in this Section was achieved by addition of excess ligand to $[(Et_8N_4Me_2)Sm(THF)_2]$, (**XVI**) in either C_6H_6 or PhMe on a small scale (*ca*. 10 mg $[(Et_8N_4Me_2)Sm(THF)_2]$).

Reaction of excess 2,2′-bipyridine with a benzene solution of $[(Et_8N_4Me_2)Sm(THF)_2]$ (10 mg (**XVI**) in 1 mL C_6H_6) immediately results in a red suspension of microcrystalline material due to single electron reduction of the 2,2′-bipy moiety to give $[(Et_8N_4Me_2)Sm^{III}(2,2'\text{-bipy}^{\bullet-})]$, (**27**), Equation 4-17. A small scale slow diffusion

experiment was undertaken in THF, leading to isolation of crystals suitable for X-ray crystal structure determination. Despite multiple attempts, satisfactory elemental analysis of [($Et_8N_4Me_2$)Sm(2,2′-bipy$^{\bullet-}$)], (**27**), could not be achieved. The complex is sparingly soluble in THF, toluene and benzene.

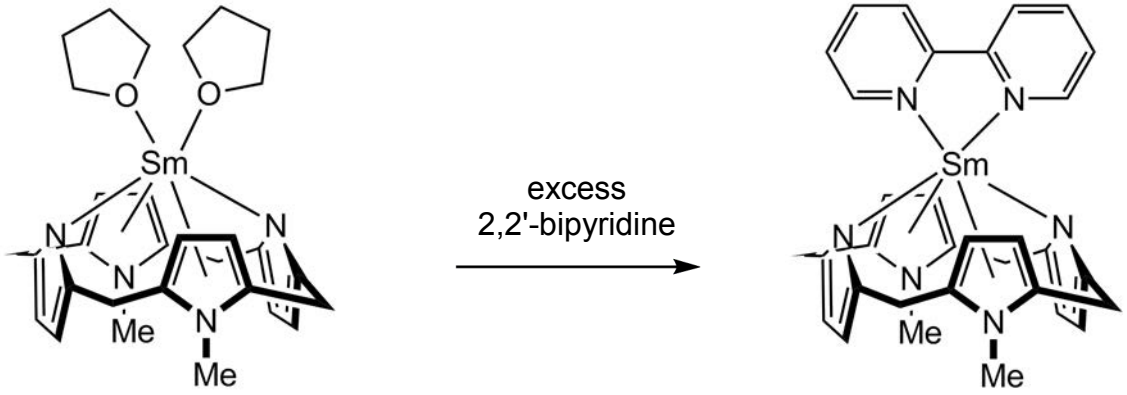

(**XVI**) (**27**)

Equation 4-17

DFT analysis and the molecular geometry of (**27**) are consistent with single electron reduction of the ligand to give a Sm^{III} species, Section 4.3.4. This reaction outcome is consistent with literature reports of the same reactivity for the bis(THF) solvated decamethylsamarocene complex, [(C_5Me_5)$_2$$Sm^{II}(THF)_2$], (**IV**), to give [($C_5Me_5$)$_2$$Sm^{III}$(2,2′-bipy)] upon reaction with 2,2′-bipyridine.[216]

In contrast to the reaction with 2,2′-bipyridine, reaction of a benzene solution of (**XVI**) with 1,10-phenanthroline immediately provided bright purple crystals of the reductively dimerised species [{($Et_8N_4Me_2$)Sm^{III}}$_2$(μ-4,4′-biphen)], (**28**), according to Equation 4-18, where the dianionic bridging (μ-4,4′-biphen) moiety arises due to reductive coupling at the 4- position of the 1,10-phenanthroline ligand. The reaction proceeds immediately *via* a highly coloured dark purple solution in both toluene and THF, with a bright purple precipitate visible in toluene within 15 minutes. Purple crystalline material

was visible in parallel reactions in both toluene and THF after one hour, although the volume of precipitated material appeared greater in the former case by visual comparison.

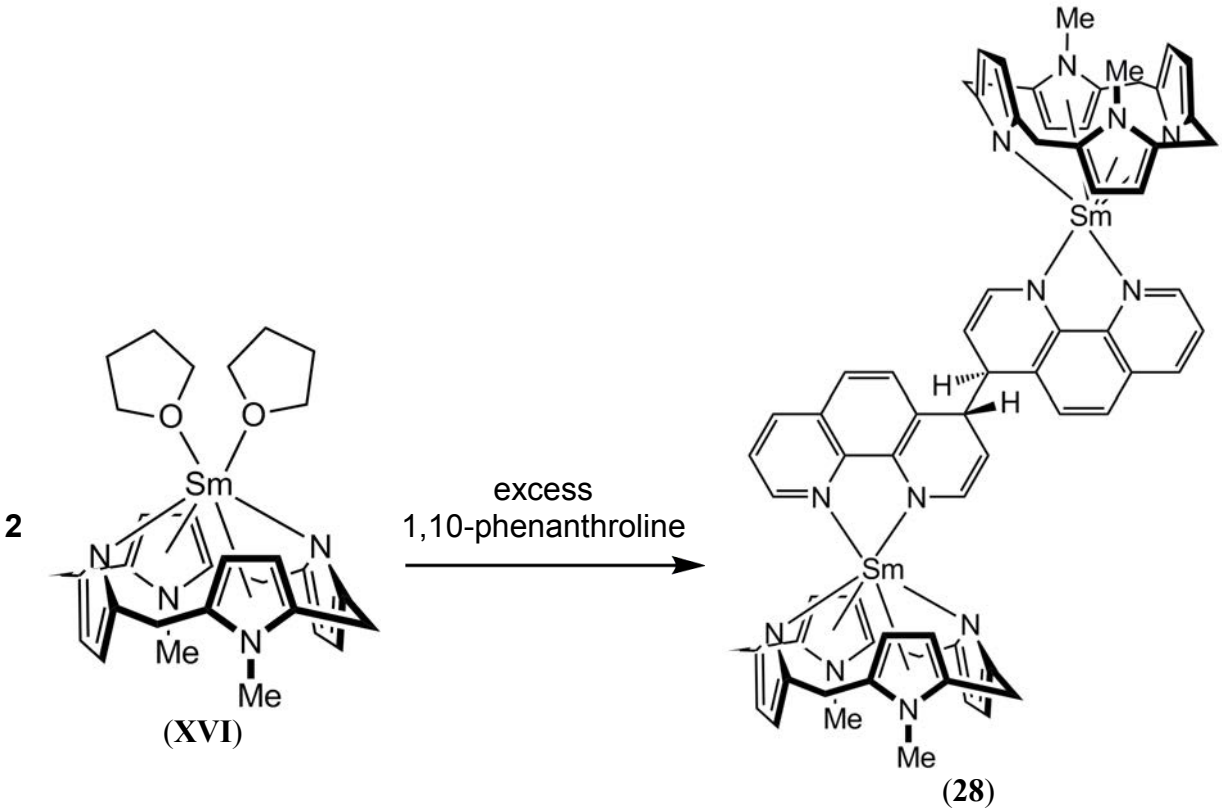

Equation 4-18

A ruthenium silylyne complex stabilised by 1,10-phenanthroline was shown by Grumbine, Chadha and Tilley to reductively dimerise through the 4 position of the 1,10-phenanthroline ligand after nine days stirring over sodium amalgam to give a ruthenium silylene dimer in 90% yield, Equation 4-7 Section 4.1.[215] As reported by Grumbine *et al*. and observed in the molecular structure of (**28**), reductive dimerisation of the bidentate ligand results in asymmetric coordination of the reductively coupled 1,10-phenanthroline ligand to each metal centre *via* distinct short $M-N_{amide}$ and longer $M-N_{adduct}$ interactions.

The reason for the difference in observed reaction outcome for the reaction of $[(Et_8N_4Me_2)Sm(THF)_2]$, (**XVI**), with 2,2′-bipyridine or 1,10-phenanthroline to form the

Sm^{III}-radical anion or reductively dimerised Sm^{III} complex, (**27**) and (**28**), respectively, is not immediately apparent. Da Re *et al.* undertook a study of the reactivity of these two, clearly related, ligands with decamethylytterbocene and reported differences in the electronic structure of the resulting products, $[(C_5Me_5)_2Yb^{III}(bipy^{\bullet-})]$ and $[(C_5Me_5)_2Yb^{III}(phen^{\bullet-})]$, leading them to comment:

> "However, none of the data reported here (electrochemical, electronic absorption, or resonance Raman) provide a clear differentiation between the electronic structure in the bipyridine versus phenanthroline ligand adducts that would readily explain the apparent difference in the extent of coupling of the spin states on the ligand radical anion and the f orbital manifold on the metal."[219]

The reasons for the formation of a ligand based radical anion in the case of (**27**) and a reductively coupled dimer in the case of (**28**) will be examined further based on DFT analysis, Section 4.3.4.

To further investigate the coupling tendency of the reduced 1,10-phenanthroline ligand *via* synthetic means, steric bulk was introduced at the coupling position *via* the 4,7-dimethyl-1,10-phenanthroline ligand. Undertaking the reaction of 4,7-Me_2phen with (**XVI**), under similar conditions to the unsubstituted reaction described above, resulted in the analogous reaction outcome; 4,7-dimethyl substitution of 1,10-phenanthroline does not hinder formation of $[\{(Et_8N_4Me_2)Sm^{III}\}_2(\mu\text{-}4,4'\text{-bis}(Me_2phen)]$, (**29**), *via* reductive dimerisation, Equation 4-19. The reaction proceeds in THF, toluene and benzene, with an immediate colour change upon addition of reagents to give a dark blue/violet solution in each solvent, followed by crystallisation of (**29**) upon standing over 96 hours.

Birch and Karakhanov reported the synthesis of *N*-substituted 1,4-hidydropyridines by metal-ammonia reactions, wherein pyridine and 4-methylpyridine were both shown to

reductively dimerise at the 4- position.[202] Thus, given the reductive dimerisation observed for (**28**), the same reactivity is both expected and observed for the 4,7-dimethyl substituted analogue and methyl substitution at the coupling site does not inhibit the reaction.

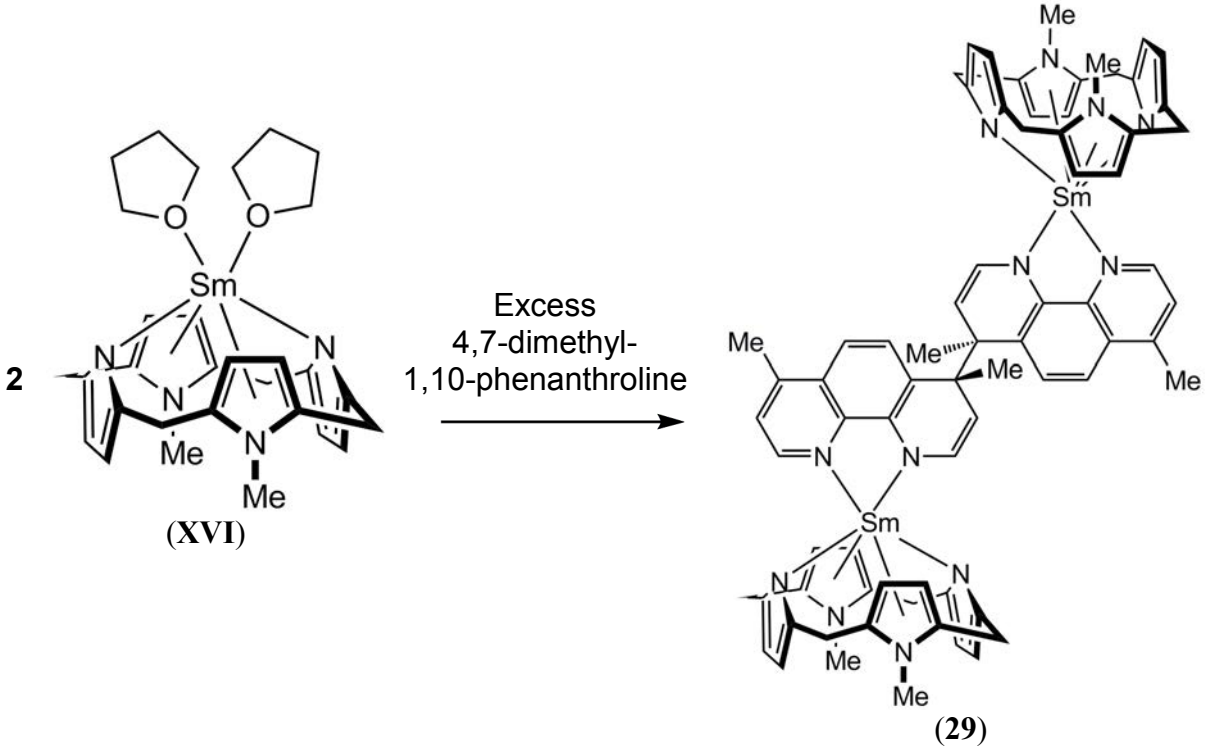

(**XVI**) (**29**)

Equation 4-19

Introduction of additional steric bulk by way of 4,7-diphenyl substitution of 1,10-phenanthroline offers a significant increase in steric bulk at the coupling site. Reaction of 4,7-diphenyl-1,10-phenanthroline (also known as „bathophenanthroline' and abbreviated „batho' herein) with a toluene solution of (**XVI**) immediately produces a dark blue/green solution. Slow evaporation of the reaction solution over one week in the glovebox provided dark blue/green crystals of a 1:1 Sm^{III}:radical anion complex, $[(Et_8N_4Me_2)Sm(batho^{\bullet-})]$, (**30**), Equation 4-20. Density functional theory calculations indicate that formation of (**30**) proceeds *via* single electron reduction of 4,7-diphenyl-1,10-phenanthroline to give a Sm^{III}-radical anion species, with delocalisation of the

unpaired electron over the chelate ring. Further discussion of (**30**) *via* DFT analysis is presented in Section 4.3.4.

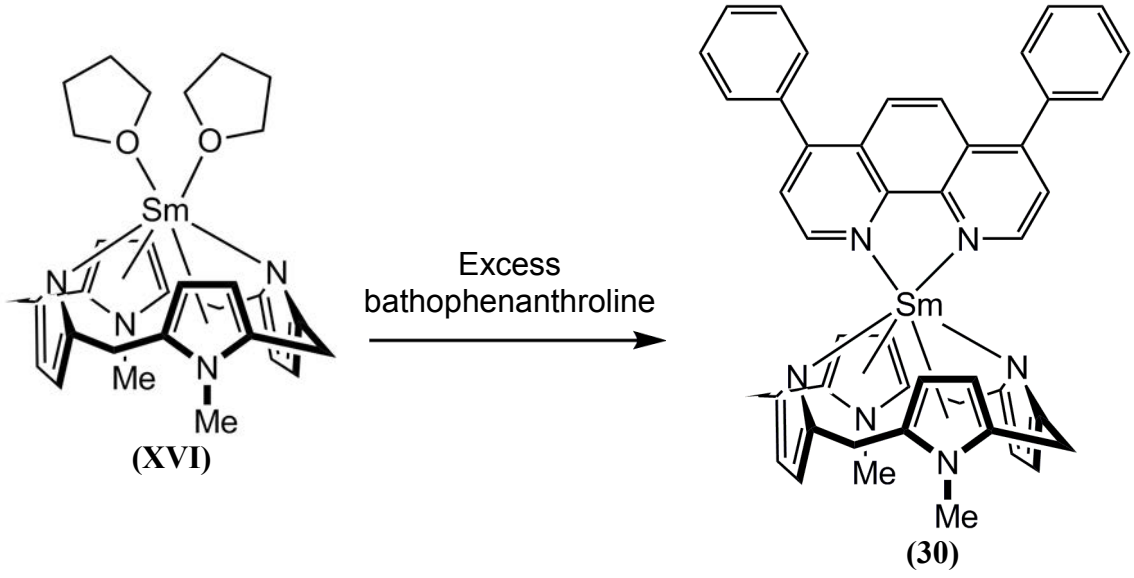

(XVI) **(30)**

Equation 4-20

Synthesis of the 1:1 Sm^{III}-radical anion, (**30**), indicates that with sufficient steric bulk in the coupling position, reductive dimerisation of 1,10-phenanthrolinoid ligands becomes energetically unfavourable. Presumably, (**30**) is a structural model for the assumed short lived [$(Et_8N_4Me_2)Sm(phen^{\bullet-})$] complex, prior to C−C bond formation. Having thus established the ability to alter reaction outcomes through of 4,7- disubstitution of 1,10-phenanthrolinoid ligands with (**XVI**), introduction of steric bulk directed towards the macrocyclic binding groove was undertaken *via* 2,9-dimethyl-1,10-phenanthroline, which is also known as „neocuproine' and will be abbreviated as „neo'. Reaction of neocuproine with a benzene solution of (**XVI**) provides a 1:1 Sm^{II} adduct, [$(Et_8N_4Me_2)Sm(neo)$], (**31**), according to Equation 4-21.

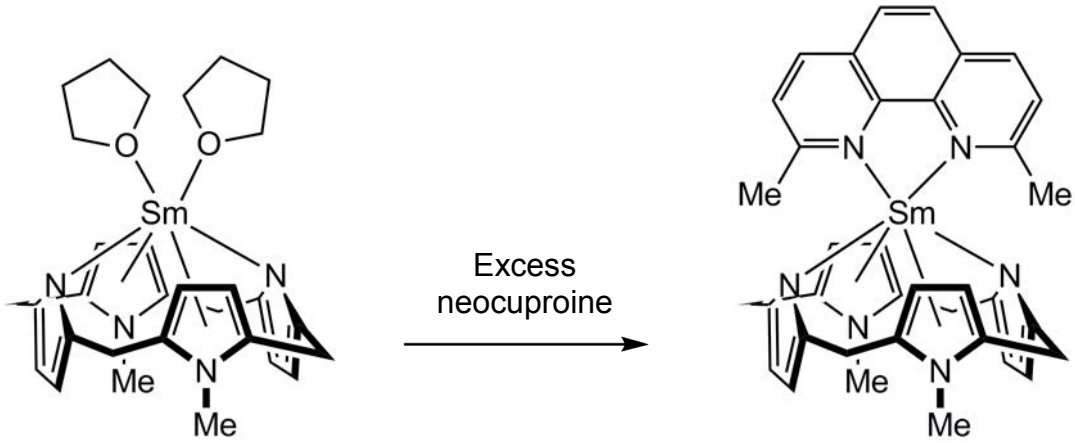

(XVI) **(31)**

Equation 4-21

The molecular structure of (**31**) is consistent with a Sm^{II} species with very long $Sm-N_{ligand}$ distances at 2.851(4) and 3.031(4) Å and displaying a very high angle of incidence (51.1_0 °); both indicative of a weak neutral heterocycle coordinated to a Sm^{II} species. DFT analysis confirms that (**31**) is a 1:1 adduct of samarium(II), rather than a Sm^{III}-radical anion as observed for the 4,7-diphenyl substituted analogue, (**30**).

4.3.3.1 Molecular Structure of [($Et_8N_4Me_2$)Sm(2,2'-bipy$^{\bullet-}$)], (27)

Crystals of (**27**) belong to the orthorhombic space group *Pnma* (No. 62), a = 10.764(7), b = 17.208(5), c = 21.718(6) Å, with four molecules in the unit cell. The asymmetric unit consists of one half molecule of (**27**), with both the ligand and binding groove lying on a crystallographic mirror plane.

The molecular structure of (**27**), Figure 4-22, exhibits the standard $\eta^1{:}\eta^5{:}\eta^1{:}\eta^5$ macrocyclic binding mode. The Sm-(η^1-N_{Py}) distances are 2.534(3) and 2.553(3) Å and the Sm-(η^5-N_{Me}) distance is 2.62_6 Å. The N_{Py}–*meso* interplanar angles are 48.72(1) and 49.8(1) °, and the N_{Me}–*meso* interplanar angle is 79.12(9) °. The Sm–*meso* distance is 1.312(2) Å.

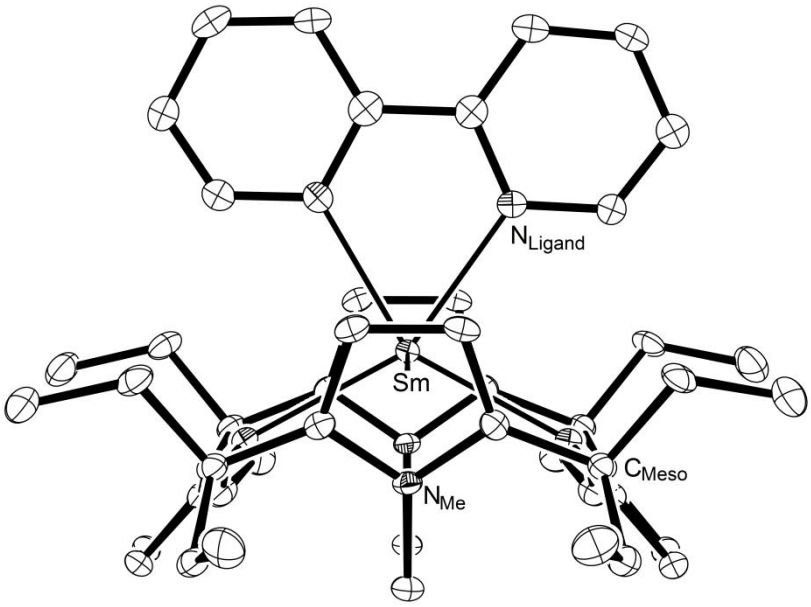

Figure 4-22 Molecular structure of (**27**) with thermal ellipsoids drawn at 50 % probability. Protons omitted for clarity.

Table 4-11 compares the molecular geometry of (**27**) with the 2:1 Sm^{II} adduct formed with pyridine, (**14**), and the Sm^{III}-quinoline dimer, (**22**), revealing that the molecular structure metrics of (**27**) are generally intermediate between the Sm^{II} adduct and the Sm^{III} species in a series devoid of protruding *ortho*-substitution. The effect of bidentate coordination on the effective metal radius limits the value of comparison between (**27**) and (**22**), however DFT analysis reveals that the electronic state of Sm^{III}-radical anion complexes is distinct from Sm^{III}-alkyl complexes due to delocalisation of the unpaired electron density over the metallocycle, Section 4.3.4.

Single electron reduction of 2,2′-bipyridine by a Sm^{II} species to give a 1:1 Sm^{III} radical anion has been reported for $[(C_5Me_5)_2Sm(THF)_2]$, (**IV**).[216] The resulting complex, $[(C_5Me_5)_2Sm(2,2'\text{-bipy}^{\bullet-})]$, has similar $Sm-N_{ligand}$ contacts at 2.427(2) and 2.436(2) Å, with a $N_{ligand}-Sm-N'_{ligand}$ angle of 67.05(9) ° and a metallocene bend of 138.0 °. By comparison, the slightly longer $Sm-N_{ligand}$ contacts of (**27**) are likely due to steric interaction of the reduced ligand with the macrocycle, resulting in a smaller $N_{ligand}-Sm-N'_{ligand}$ angle of 65.52(12) ° .

	M = Sm^{III}, n = 1 L = (2,2′-bipy) (**27**)	M = Sm^{II} L = $(py)_2$ (**14**)	M = Sm^{III}, n = 2 L = (μ-4,4′-biquin) (**22**)
M−L	2.443(4), 2.473(4)	2.77(1)	2.285(7) – 2.325(5)
M−(η^1-N_{Py})	2.534(3), 2.553(3)	2.668(6)	2.452(5) – 2.491(6)
M−(η^5-N_{Me})	2.62_6	2.75_0	2.58_6 – 2.61_5
M−*meso*	1.312(2)	1.466(7)	1.138(3) – 1.162(4)
N_{Py}−*meso*	48.72(1), 49.8(1)	52.2(2)	46.9(3) – 52.4(2)
N_{Me}−*meso*	79.12(9)	75.7(3)	79.8(2) – 81.7(2)
Metallocene bend	162.3_0	156.2_9	169.2_6

Table 4-11 Selected bond lengths (Å) and angles (°) for [{($Et_8N_4Me_2$)M}$_n$(L)].

4.3.3.2 Molecular Structure of [{($Et_8N_4Me_2$)Sm}$_2$(μ-4,4'-diphen)]·4(C_6H_6), (28)

Crystals of complex (**28**) belong to the monoclinic space group *C*2/*c* (No. 15), a = 20.084(4), b = 14.001(8), c = 38.880(6) Å, β = 91.052(8) ° with 4 molecules in the unit cell. The asymmetric unit contains one half of a centrosymmetric reductively coupled dinuclear molecule, one molecule of benzene constrained to hexagonal geometry and a second, badly disordered, molecule of benzene which was removed using the Squeeze card during refinement.

The molecular structure of (**28**), Figure 4-23, exhibits the standard η^1:η^5:η^1:η^5 macrocyclic binding mode. The Sm-(η^1-N_{Py}) distances are 2.532(5) and 2.551(6) Å and the Sm-(η^5-N_{Me}) distances are 2.62_6 and 2.64_4 Å. The N_{Py}−*meso* interplanar angles are 44.7(2) and 59.86(15) °, and the N_{Me}−*meso* interplanar angles are 81.5(2) and 81.8(2) °. The Sm−*meso* distance is 1.323(4) Å.

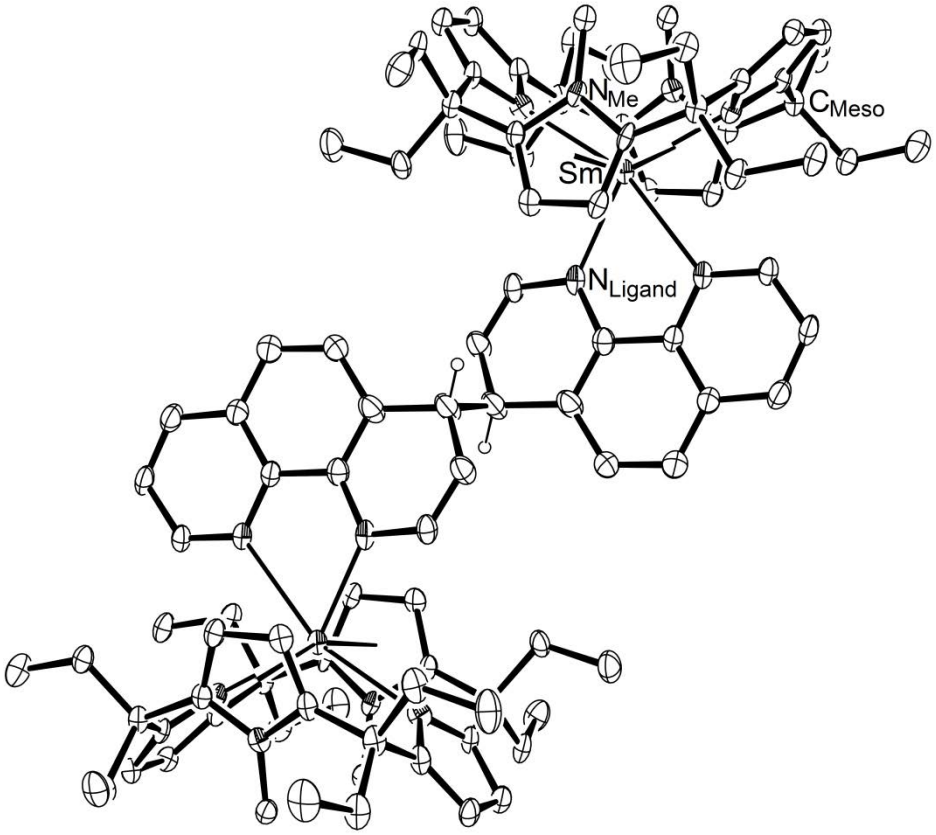

Figure 4-23 Molecular structure of (**28**) with thermal ellipsoids drawn at 50 % probability . Protons (excluding the 4,4′-ligand protons) and solvent omitted for clarity.

The molecular geometry of (**28**) is consistent with a Sm^{III} species, Table 4-12. Comparison with both (**27**) is particularly of interest given the 2,2′-bipyridine and 1,10-phenanthroline ligands are approximately the same shape and steric demand. Reaction of (**XVI**) with 1,10-phenanthroline results in reductive dimerisation, rather than adopting a 1:1 Sm^{III}-radical anion species as observed for 2,2′-bipyridine. Asymmetric coordination of the resulting μ-4,4′-bis(phenanthroline) ligand is observed, with significant variation between the Sm−N_{ligand} distance for the reduced and non-reduced rings, 2.358(6) and 2.603(5) Å, respectively.

	$M = Sm^{III}$, n = 2 L = (μ-4,4′-biphen) (**28**)	$M = Sm^{III}$, n = 1 L = (2,2′-bipy) (**27**)	$M = Sm^{III}$, n = 2 L = (μ-4,4′-biquin) (**22**)	$M = Sm^{II}$, n = 1 L = (2-Phpy) (**18**)
M−L	2.358(6), 2.603(5)	2.443(4), 2.473(4)	2.285(7) – 2.325(5)	2.60(3)
M−(η^1-N_{Py})	2.532(5), 2.551(6)	2.534(3), 2.553(3)	2.452(5) – 2.491(6)	2.58(2), 2.58(2)
M−(η^5-N_{Me})	2.62_6, 2.64_4	2.62_6	2.58_6 – 2.61_5	2.68_2, 2.70_9
M−*meso*	1.323(4)	1.312(2)	1.138(3) – 1.162(4)	1.28(1)
N_{Py}−*meso*	44.7(2), 49.86(15)	48.72(1), 49.8(1)	46.9(3) – 52.4(2)	50.1(9) (H), 54.5(7) (Ph)
N_{Me}−*meso*	81.5(2), 81.8(2)	79.12(9)	79.8(2) – 81.7(2)	77.4(8), 76.2(8)
Metallocene bend	161.9_0	162.3_0	169.2_6	163.6_5

Table 4-12 Selected bond lengths (Å) and angles (°) for $[\{(Et_8N_4Me_2)M\}_n(L)]$.

The major structural difference for complexes of 2,2′-bipyridine and 1,10-phenanthroline is limited to the Sm−N_{ligand} distances, with definitive Sm−N_{amide} and Sm−N_{adduct} distances observed for (**28**) due to reductive dimerisation of the ligand and absent due to delocalisation of the unpaired electron over the metallocycle in $[(Et_8N_4Me_2)Sm(2,2'\text{-bipy}^{\bullet-})]$, (**27**),. As both (**27**) and (**28**) are complexes of samarium(III), the Sm−macrocycle metrics are similar. Table 4-12 shows the Sm−N_{adduct} distance observed for (**28**) is consistent with the Sm−N_{ligand} distance for the complex formed with 2-phenylpyridine, (**18**), and the Sm−N_{amide} distance is consistent with the Sm−N_{ligand} distance for the complex resulting from reductive dimerisation of quinoline, (**22**), despite the change in coordination number observed for both and the additional change in oxidation state for the 2-phenylpyridine complex.

Due to asymmetry within the reduced 1,10-phenanthroline moiety, the angles of incidence, twist and tilt are not equal; the formally reduced ring has angles of 7.2_2, 3.6_3 and 36.9_6 °, respectively, whilst the lone pair coordinated ring has angles of 14.7_8, 3.1_9 and 26.6_5 °, respectively.

4.3.3.3 Molecular Structure of [{($Et_8N_4Me_2$)Sm}$_2$(μ-4,4'-bis(Me_2phen)] ·7(C_6H_6) , (29)

Crystals of (**29**) belong to the triclinic space group *P* (No. 2), a = 11.874(2), b = 16.0380(17), c = 18.627(2) Å, α = 69.259(8), β = 79.647(4), γ = 74.052(7) °, with one molecule in the unit cell. The asymmetric unit consists of one half of the centrosymmetric dinuclear molecule and three and a half molecules of benzene.

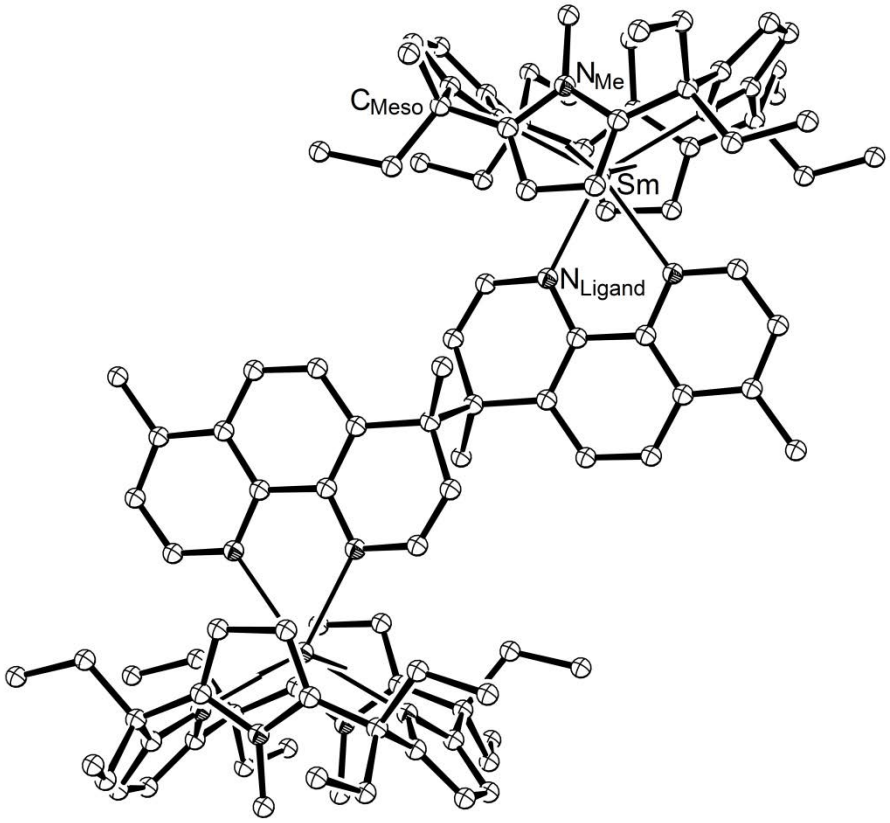

Figure 4-24 Molecular structure of (**29**) with thermal ellipsoids drawn at 50 % probability (protons and solvent omitted for clarity).

The molecular structure of (**29**) adopts the standard η^1:η^5:η^1:η^5 macrocyclic binding mode, Figure 4-24. The Sm-(η^1-N_{Py}) distances are 2.532(5) and 2.545(4) Å and the Sm-(η^5-N_{Me}) distances are 2.61_9 and 2.63_7 Å. The N_{Py}–*meso* interplanar angles are 47.1(2) and 48.2(2) °, and the N_{Me}–*meso* interplanar angles are 77.25(17) and 78.66(15) °. The Sm–*meso* distance is 1.312(3) Å. Table 4-13 compares the molecular structure of (**29**)

with (**28**) and (**27**), revealing that the macrocyclic geometry of (**28**) and (**29**) are approximately equivalent.

	$M = Sm^{III}$, n = 2 L = (μ-4,4′-bis{Me_2phen}) (**29**)	$M = Sm^{III}$, n = 2 L = (μ-4,4′-biphen) (**28**)	$M = Sm^{III}$, n = 1 L = (2,2′-bipy) (**27**)
M−L	2.369(6), 2.563(5)	2.358(6), 2.603(5)	2.443(4), 2.473(4)
M−(η^1-N_{Py})	2.532(5), 2.545(4)	2.532(5), 2.551(6)	2.534(3), 2.553(3)
M−(η^5-N_{Me})	2.61_9, 2.63_7	2.62_6, 2.64_4	2.62_6
M−*meso*	1.312(3)	1.323(4)	1.312(2)
N_{Py}−*meso*	47.1(2), 48.2(2)	44.7(2), 49.86(15)	48.72(1), 49.8(1)
N_{Me}−*meso*	77.25(17), 78.66(15)	81.5(2), 81.8(2)	79.12(9)
Metallocene bend	162.1_7	161.9_0	162.3_0

Table 4-13 Selected bond lengths (Å) and angles (°) for [{($Et_8N_4Me_2$)M}$_n$(L)].

As is the case for the unsubstituted ligand, (**28**), reductive dimerisation occurs at the 4- position of the 4,7-dimethyl-1,10-phenanthroline ligand upon reaction with (**XVI**), despite methyl- substitution at the coupling position. Table 4-13 reveals that the dative Sm−N_{ligand} distance for (**29**) is larger than the same distances for (**28**). With no notable difference in sterics, this difference is likely a result of the slight modification of electronic environment *via* 4,7-dimethyl substitution.

Due to asymmetry within the reduced 1,10-phenanthroline moiety, the angles of incidence, twist and tilt are not equal; the formally single bonded ring has angles of 4.1_8, 2.7_3 and 31.2_1 °, respectively, whilst the lone-pair coordinated ring has angles of 4.6_4, 1.8_5 and 31.6_4, respectively. Table 4-14 compares ligand binding angles for each coordinating ring of both [{($Et_8N_4Me_2$)Sm}$_2$(μ-4,4′-bis(phen)], (**28**), and the dimethyl substituted species [{($Et_8N_4Me_2$)Sm}$_2$(μ-4,4′-bis(Me_2phen)], (**29**).

	Incidence	Twist	Tilt
Reduced ring (**28**)	4.1_8	2.7_3	31.2_1
Dative ring (**28**)	4.6_4	1.8_5	31.6_4
Reduced ring (**29**)	7.2_2	3.6_3	36.9_6
Dative ring (**29**)	14.7_8	3.1_9	26.6_5

Table 4-14 Ligand characteristics of [{($Et_8N_4Me_2$)Sm(4,7-R_2phen)}$_2$] by angle (°), for R = H, (**28**), and R = Me, (**29**).

4.3.3.4 Molecular Structure of [($Et_8N_4Me_2$)Sm(batho$^{\bullet-}$)]·C_6H_6, (30)

Crystals of (**30**) belong to the monoclinic space group *C*2/*c* (No. 15), a = 21.402(4), b = 13.971(3), c = 38.209(5) Å, β = 106.114(8) ° with 8 molecules in the unit cell. The asymmetric unit consists of one molecule of (**30**) and one molecule of benzene.

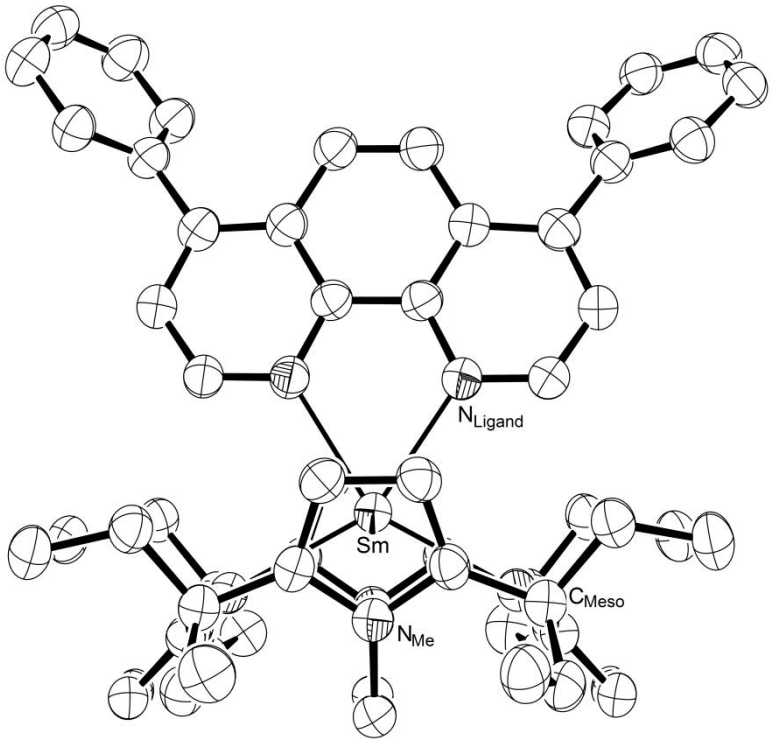

Figure 4-25 Molecular structure of (**30**) with thermal ellipsoids drawn at 50 % probability (solvent and protons omitted for clarity).

The molecular structure of (**30**) adopts the standard η^1:η^5:η^1:η^5 macrocyclic binding mode, Figure 4-25. The Sm-(η^1-N_{Py}) distances are 2.530(3) and 2.561 (3) Å and the Sm-(η^5-N_{Me}) distances are 2.63_1 and 2.65_4 Å. The N_{Py}–*meso* interplanar angles are

45.77(15) and 46.96(10) °, and the N_{Me}–*meso* interplanar angles are 76.68(13) and 77.41(11) °. The Sm–*meso* distance is 1.312(3) Å.

Increasing the steric bulk at the 4 and 7 positions of the 1,10-phenanthroline ligand to phenyl substitution results in a Sm^{III}-radical anion, [$(Et_8N_4Me_2)Sm^{III}(batho^{\bullet-})$], (**30**). The molecular structure of (**30**) is strikingly similar to the reduced 2,2′-bipyridine analogue, (**27**), and clearly distinct from the bis(pyridine) adduct of Sm^{II}, (**14**), which features much longer Sm–N_{ligand} distances, Table 4-15. DFT analysis indicates the complex (**30**) is present as a Sm^{III}-radical anion, Section 4.3.4.

	M = Sm^{III} L = ($batho^{\bullet-}$) (**30**)	M = Sm^{III} L = ($2,2'\text{-bipy}^{\bullet-}$) (**27**)	M = Sm^{II} L = $(py)_2$ (**14**)
M–L	2.467(3), 2.488(3)	2.443(4), 2.473(4)	2.77(1)
M–(η^1-N_{Py})	2.530(3), 2.561(3)	2.534(3), 2.553(3)	2.668(6)
M–(η^5-N_{Me})	2.63_1, 2.65_4	2.62_6	2.75_0
M–*meso*	1.312(3)	1.312(2)	1.466(7)
N_{Py}–*meso*	45.77(15), 46.96(10)	48.72(1), 49.8(1)	52.2(2)
N_{Me}–*meso*	76.68(13), 77.41(11)	79.12(9)	75.7(3)
Metallocene bend	161.7_9	162.3_0	156.2_9

Table 4-15 Selected bond lengths (Å) and angles (°) for [$(Et_8N_4Me_2)$M(L)].

Minor variation in N_{Py}–*meso* and N_{Me}–*meso* interplanar angles observed for (**30**) with respect to (**27**) arises as a result of the differing angle of incidence of the ligand; the reduced 2,2′-bipyridine ligand of (**27**) lies on a mirror plane, resulting in angles of incidence and twist of 0 °, whereas the reduced 4,7-diphenyl-1,10-phenanthroline ligand does not lie on a mirror plane and exhibits non-zero angles of incidence and tilt. As observed for complexes (**28**) and (**29**), small variation in each angle is observed (each angle is measured for the six atoms that define the coordinating pyridine ring). As such,

the angles of incidence, twist and tilt for (**30**) are 14.7_4, 5.0_0 and 30.6_8 °, and 13.1_5, 0.3_6 and 32.4_5 °, at each site of coordination, respectively.

4.3.3.5 Molecular Structure of [($Et_8N_4Me_2$)Sm(neo)]·C_6H_6) (31)

Crystals of (**31**) belong to the monoclinic space group *C*2/*c* (No. 15), a = 22.414(3), b = 18.9762(18), c = 22.8370(19) Å, β = 101.559(5) °,with 8 molecules in the unit cell. The asymmetric unit consists of one molecule of (**30**) and one molecule of benzene.

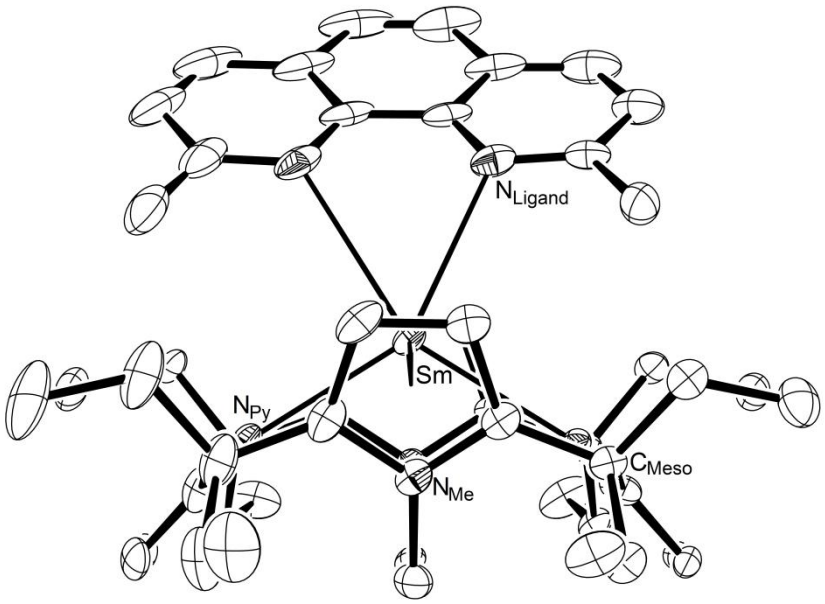

Figure 4-26 Molecular structure of (**31**) with thermal ellipsoids drawn at 50 % probability. Solvent and protons omitted for clarity.

The molecular structure of (**31**) adopts the standard η^1:η^5:η^1:η^5 macrocyclic binding mode, Figure 4-26. The Sm-(η^1-N_{Py}) distances are 2.658(4) and 2.751 (3) Å and the Sm-(η^5-N_{Me}) distances are 2.75_1 and 2.82_2 Å. The N_{Py}−*meso* interplanar angles are 45.10(15) and 47.46(12) °, and the N_{Me}−*meso* interplanar angles are 69.52(12) and 74.77(13) °. The Sm−*meso* distance is 1.588(2) Å. Table 4-16 compares the molecular structures of the bidentate 1:1 Sm^{II} adduct with neocuproine, (**31**), to the 2:1 Sm^{II} bis(pyridine) adduct, (**14**), and the 1:1 reduced Sm^{III}-batho radical anion, (**30**).

	$M = Sm^{II}$ L = (neo) (**31**)	$M = Sm^{II}$ $L = (py)_2$ (**14**)	$M = Sm^{III}$ $L = (batho^{\bullet-})$ (**30**)
M−L	2.851(4), 3.031(4)	2.77(1)	2.467(3), 2.488(3)
$M-(\eta^1\text{-}N_{Py})$	2.658(4), 2.751 (3)	2.668(6)	2.530(3), 2.561(3)
$M-(\eta^5\text{-}N_{Me})$	2.75_1, 2.82_2	2.75_0	2.63_1, 2.65_4
M−*meso*	1.588(2)	1.466(7)	1.312(3)
N_{Py}−*meso*	45.10(15), 47.46(12)	52.2(2)	45.77(15), 46.96(10)
N_{Me}−*meso*	69.52(12), 74.77(13)	75.7(3)	76.68(13), 77.41(11)
Metallocene bend	150.8_8	156.2_9	161.7_9

Table 4-16 Selected bond lengths (Å) and angles (°) for $[(Et_8N_4Me_2)M(L)]$.

The metrics of (**31**) are remarkable. At 2.851(4) Å, the closest $Sm-N_{ligand}$ contact is the same, within experimental error, as the $Sm-N_{ligand}$ interaction observed for the 1:1 Sm^{II} adduct of 2-methyl-6-phenylpyridine, (**20**), 2.844(3) Å. The weaker interaction to the second nitrogen, at 3.031(4) Å, is reminiscent of the interaction observed between Sm^{II} and the *β*-carbons of an adjacent N_{Me} ring for the unsolvated species, (**3**), 3.040(19) and 3.05(2) Å. In addition to these larger $Sm-N_{ligand}$ distances, to accommodate the 2,9-dimethyl substituted 1,10-phenanthroline, the incoming ligand is forced to adopt an extreme angle of incidence that, at 51.1_0 °, is hitherto unprecedented in this thesis, Figure 4-27. For comparison, a side view of $[(Et_8N_4Me_2)Sm(batho^{\bullet-})]$, (**30**) is provided, Figure 4-28.

Space-filling representations of the molecular structure of (**31**) demonstrate that coordination of 2,9-dimethyl-1,10-phenanthroline is at the very limit of capability of the macrocycle, with the 2,9-dimethyl moieties firmly against the *meso*- ethyl and *β*-N_{Me} protons on one side of the binding groove, and the rings of the 1,10-phenanthroline moiety firmly against the *meso*- ethyl and *β*-N_{Me} protons on the other side of the binding groove, Figure 4-29.

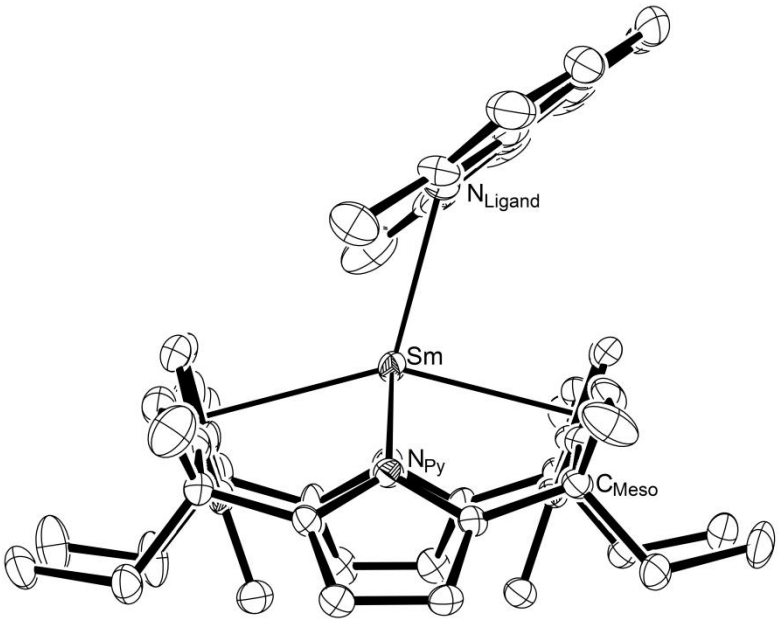

Figure 4-27 Molecular structure of (**31**), viewed from side on. Thermal ellipsoids drawn at 50% probability (solvent and protons omitted for clarity).

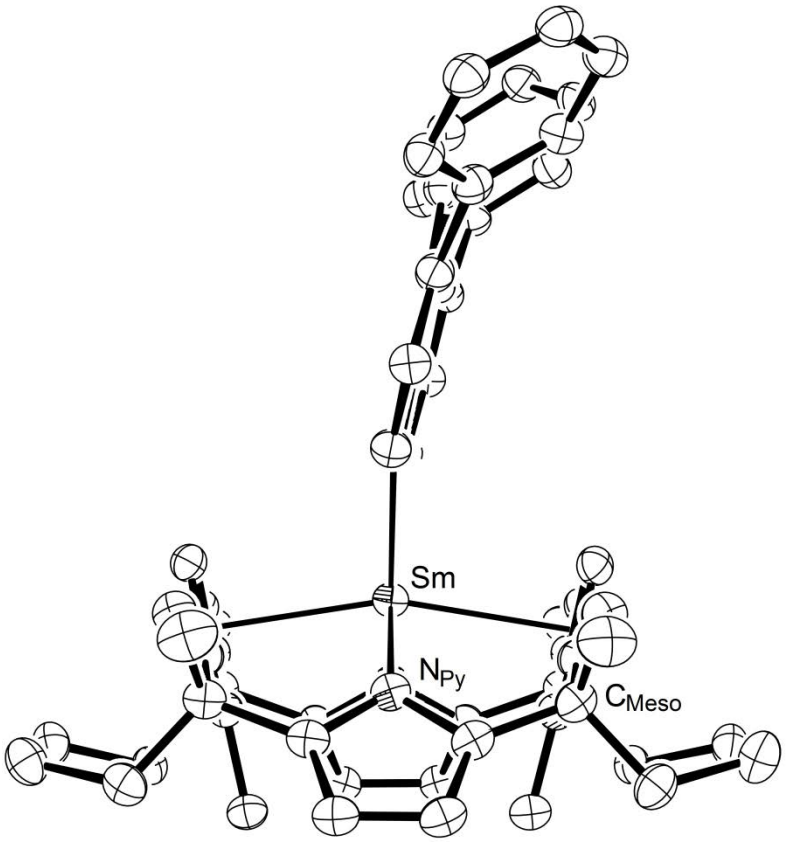

Figure 4-28 Molecular structure of (**30**), viewed from side on. Thermal ellipsoids drawn at 50% probability (solvent and protons omitted for clarity).

DFT analysis ratifies the assignment of the +2 oxidation state for samarium, which is apparent from the molecular geometry. Given the extreme metrics of coordination upon formation of (**31**), it is clear that reduction of 2,9-dimethyl-1,10-phenanthroline by the Sm^{II} centre is unfavoured due to the associated reduction in physical size of the metal centre, which would further add to the strain of the system.

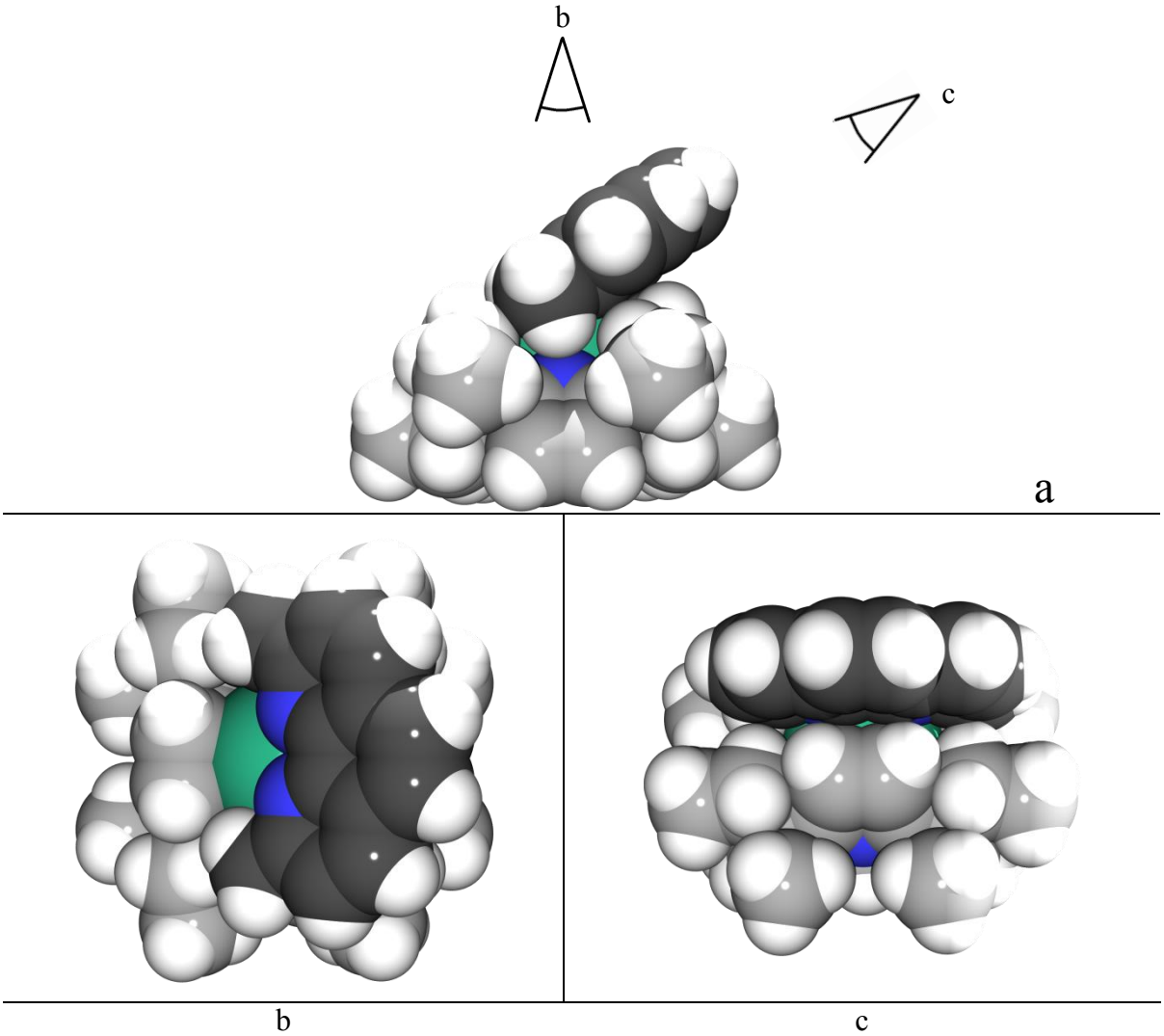

Figure 4-29 Space-filling representations of $[(Et_8N_4Me_2)Sm(neo)]$,(**31**), looking along the binding groove, *a*, looking down on the binding groove, *b*, and at the intersection of the 2,9-dimethyl-1,10-phenanthroline and N_{Me} planes, *c*. Dark and light grey carbon atoms denote C_{neo} and $C_{macrocycle}$, respectively.

4.3.4 Calculation of Electron Populations

The assignment of oxidation states for the series of complexes described in this Chapter is not always trivial. Simple cases, such as the doubly reduced bridging dianionic complex formed *via* reduction of 4,4′-bipyridine with $[(Et_8N_4Me_2)Sm(THF)_2]$, (**21**), can be confidently assigned based on the characteristic bond lengths of the reduced ligand. Where a bis-adduct is formed, as is the case with $[(Et_8N_4Me_2)Sm(py)_2]$, (**14**), and $[(Et_8N_4Me_2)Sm(3,5\text{-lut})_2]$, (**17**), it is obvious that, given equivalent bond lengths, reduction of both ligands would require two electrons; there is no evidence of either a second molecule of samarium in the crystal structure or of the samarium(IV) oxidation state (which should be considered impossible to reach under the conditions of these experiments, Section 1.2). Assigning oxidation states for mono-adducts of substituted pyridines becomes a more difficult task. Two possible states exist; $f^6\text{-}L^0$ or $f^5\text{-}L^{\bullet-}$, which correspond to samarium(II)-neutral ligand, as in the case of (**14**) and (**17**), or samarium(III)-radical anion. The issue has previously been resolved by Berg, Boncella and Andersen by analysis of the magnetic susceptibility of complexes.[217] Da Re *et al.* employed cyclic voltammetry, UV-vis-near-IR electronic absorption and resonance Raman spectroscopies to enhance the information acquired by Berg, Boncella and Anderson.[217] We have undertaken to employ Density Functional Theory analysis to investigate the spin state of these molecules; application of alternate characterisation techniques across the whole series was deemed unfeasible due to the issues previously outlined.

Calculations of this type are not computationally demanding (by today's standards), as the crystal structure can be imported to provide the geometry for a single point energy calculation. This avoids the time and expense of undertaking geometrical optimisation calculations on the computationally large molecules and, given the availability of accurate

molecular geometry *via* crystal structure determination techniques, is a valid geometry for such a calculation. In the case of [($Et_8N_4Me_2$)Sm(ligand)], the *meso*- ethyl groups are considered to have no significant effect on the electronic characteristics of the system and have been replaced with H atoms to further simplify the calculation. GaussView v5.0.8 and GaussView v3.0 make replacing ethyl groups with appropriate (with regard to position and bond length, i.e. sp^3) protons simple, and the calculated molecule is thus $H_8N_4Me_2Sm(L)$. A standard energy calculation requires the charge and multiplicity (unpaired electron count) of the complex as well as the geometry; in either the f^6-L^0 or the f^5-$L^{\bullet -}$ case, the charge of the complex does not vary (overall neutral) and possess six unpaired electrons which enter the system from the 4f shell of the samarium(II) centre. The final output file reports the self-consistent field converged unpaired electron orbital populations using Mulliken atomic spin densities[257] by default and, additionally, Natural Bond Order (NBO) analysis[146] is available by addition of a keyword.

Figure 4-30 shows the Mulliken and NBO analysis results for the substituted pyridine complexes reported in Section 4.3.1. Results for [($Et_8N_4Me_2$)Sm(2,2′-bipy)], (**27**), and the reported samarium(III) alkyl complex [($Et_8N_4Me_2$)SmMe], (**XX**)[75] are included.

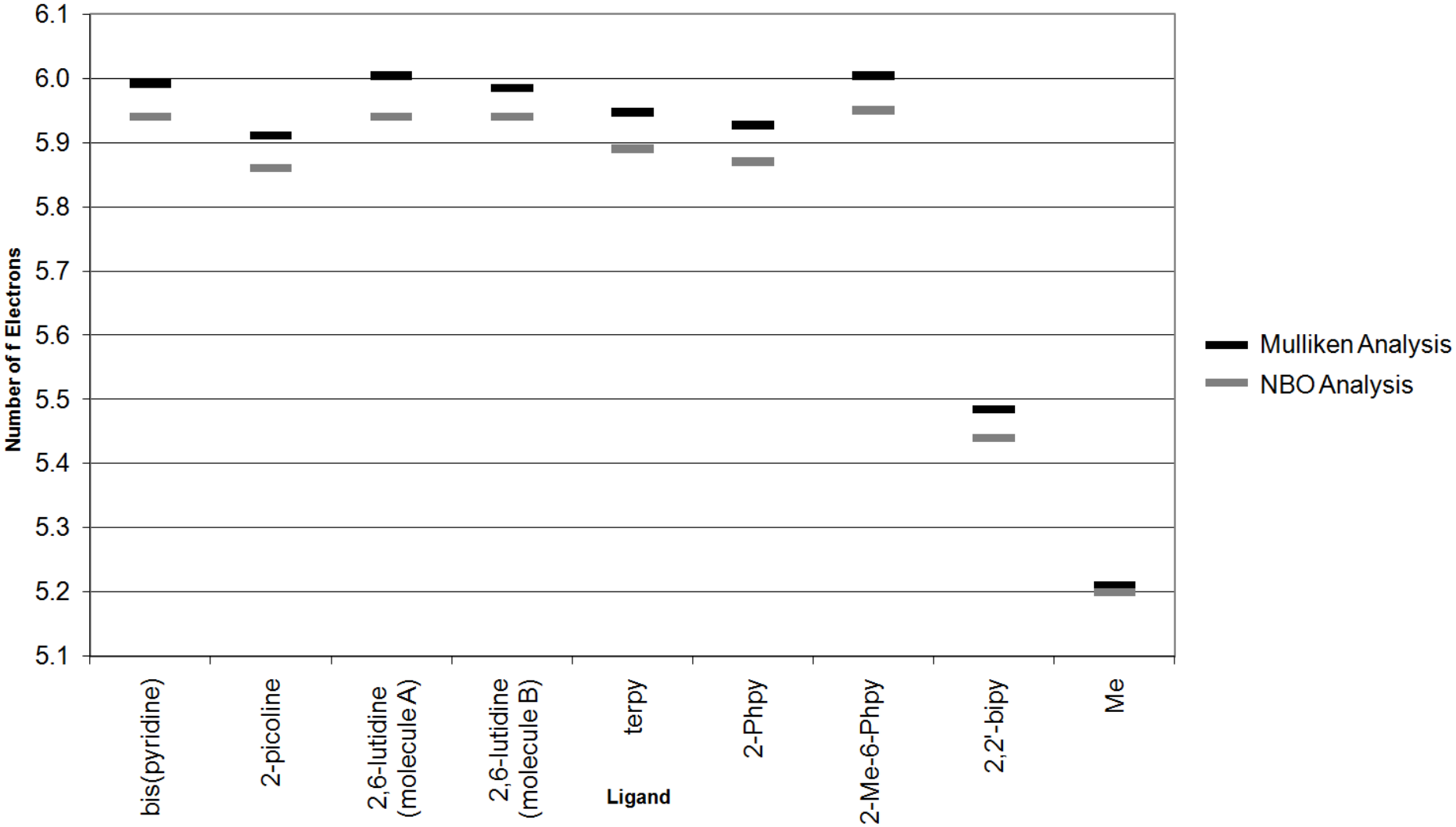

Figure 4-30 Chart showing the number of *f*-electrons on samarium for the range of $[(Et_8N_4Me_2)Sm(L)]$ complexes discussed in Section 4.3.1.

Figure 4-30 clearly shows that divalent samarium is present in complexes [($Et_8N_4Me_2$)Sm($py)_2$], (**14**), [($Et_8N_4Me_2$)Sm(2-pic)], (**15**), [($Et_8N_4Me_2$)Sm(2,6-lut)], (**16**), [($Et_8N_4Me_2$)Sm(terpy)], (**19**), and [($Et_8N_4Me_2$)Sm(2-Me-6-Phpy)], (**20**), with [($Et_8N_4Me_2$)Sm(2-Phpy)], (**18**) included, despite being a poor crystal structure refinement for the calculation to be performed upon, as per Section 4.3.1. Inclusion of the results found for the 2,2′-bipyridine system (**27**) and [($Et_8N_4Me_2$)SmMe], (**XX**), demonstrate the clear distinction between samarium(II) adducts, samarium(III) delocalised radical anions and samarium(III) alkyl type complexes.

Electron populations for complexes reported in Sections 0 and 4.3.3 were also calculated where the oxidation state is unclear *i.e.* where reductive dimerisation has not occurred. ($Et_8N_4Me_2$)Sm complexes of 8-methylquinoline (**23**), benzo[h]- (**24**) and benzo[f]quinoline (**25**) reported 6.26, 5.94 and 5.91 electrons on samarium by Mulliken analysis and 5.95, 5.89 and 5.85 by NBO analysis. The outlying result for (**23**) by Mulliken analysis (6.26 e^- on samarium) appears to be caused by spin contamination; the cause of this result would be interesting to investigate further, however it is beyond the scope of this thesis to do so. Each of these complexes is consistent with the samarium(II) formulation. ($Et_8N_4Me_2$)Sm complexes of 2,2′-bipyridine, (**27**), bathophenanthroline, (**30**) and neocuproine, (**31**), report samarium electron populations of 5.48, 5.52 and 5.98 by Mulliken analysis and 5.44, 5.45 and 5.93 by NBO analysis respectively. Thus, complexes (**27**) and (**30**) are samarium(III)-radical anion type complexes, whilst (**31**) is formally an adduct of samarium(II). The range of Sm−N_{ligand} distances show clear correlation with the Sm^{II}/Sm^{III} oxidation state assignment based on DFT analysis of the unpaired electron population of each complex.

In attempting to shed light on the reason why [($Et_8N_4Me_2$)Sm(2,2′-bipy$^{\bullet-}$)], (**27**), forms a samarium(III)-radical anion type complex and 1,10-phenanthroline affords the reductively coupled complex [{($Et_8N_4Me_2$)Sm}$_2$(μ-4,4′-biphen)], (**28**), it is useful to further investigate the electron population of the complexes in more detail. Due to the reductive dimerisation apparent in (**28**), it is not possible to generate data comparable to the radical anion species (**27**), since no model for [($Et_8N_4Me_2$)Sm^{III}(phen$^{\bullet-}$)] exists and computational optimisation has not been employed for any other calculation. However, [($Et_8N_4Me_2$)Sm(batho$^{\bullet-}$)] (**30**) has been shown to exist as a radical anion-samarium(III) system analogous to the 2,2′-bipyridine case (**27**), and will serve as a useful comparison in this case.

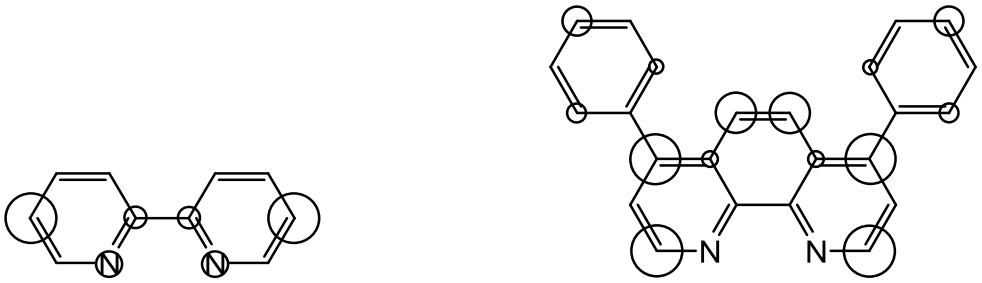

Figure 4-31 The unpaired electron population as a percentage of the largest site of spin in the radical anion of each molecule, 2,2′-bipyridinide (*left*) and bathophenanthrolinide (*right*).

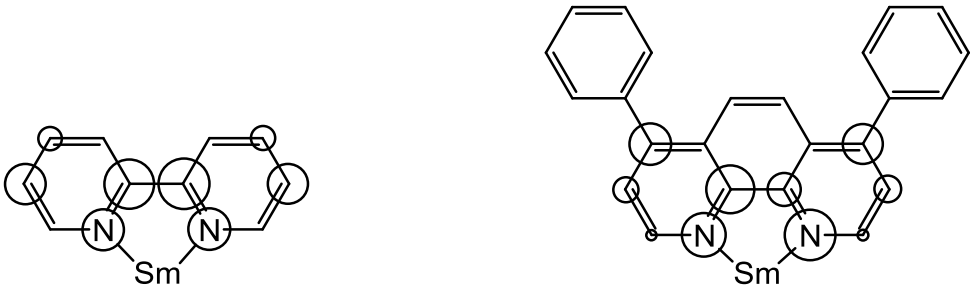

Figure 4-32 The unpaired electron population of the ligand as a percentage of the largest site of spin for $H_8N_4Me_2Sm$ analogues of (**27**) (*left*) and (**30**) (*right*).

Figure 4-31 and Figure 4-32 show the electron population of the isolated radical anionic forms of ligands (Figure 4-31) and samarium(III) bound radical anions (Figure 4-32) of 2,2′-bipyridine and bathophenanthroline, as computational analogues of complexes (**27**) and (**30**), respectively. The circles show the unpaired electron population

scaled within each molecule. Figure 4-31 and Figure 4-32 may not be directly compared based on this qualitative description, since each molecule has a different starting point; however, qualitative conclusions may be drawn. Figure 4-31 is included to show that calculation of a single electron reduced species without coordination of a metal is not relevant to the systems under investigation; the effect of the metal is significant and must be accounted for. Figure 4-32 shows that unpaired electron spin population for [($H_8N_4Me_2$)Sm(2,2′-bipy$^{\bullet-}$)], (**27**), is centred about the N−C−C−N chelate ring of the ligand and only minimal unpaired spin is present in the C4 positions, which have been shown as the site of coupling for molecules of this type. The unpaired electron spin population for [($H_8N_4Me_2$)Sm(batho$^{\bullet-}$)], (**30**), however, has significant presence at the C4 position, indicating coupling would be favourable if sterically allowed (as is the case for (**28**) and (**29**)). The data indicate that the 1,10-phenanthroline based ligands are better able to delocalise unpaired electron density around the ligand than 2,2′-bipyridine, leading to reductive dimerisation at the C4 position of the 1,10-phenanthroline ligands if the C4 position is not blocked. Interestingly, coupling at C3 may be feasible for the 2,2′-bipy system based on Figure 4-32; however coupling at C3 is likely to be sterically prohibited by ($Et_8N_4Me_2$)Sm. No experimental evidence for coupling at this position for any [($Et_8N_4Me_2$)Sm(L)] species has been obtained.

The cause of reductive dimerisation of quinoline and acridine complexes of ($Et_8N_4Me_2$)Sm, (**22**) and (**26**) respectively, and formation of adducts with 8-methylquinoline, benzo[h]- and benzo[f]quinoline (**23**), (**24**) and (**25**) respectively, is also not immediately obvious. Quinoline and 8-methylquinoline have two fused rings, whilst acridine and the benzoquinolines all have three fused rings. The 8-methylquinoline ligand is tilted *ca*. 30 ° from „flat', where the quinoline ligand is not, possibly preventing orbitals from overlapping, but benzo[f]quinoline is similarly not tilted and doesn't reductively

dimerise. Investigation of the electron affinity of each species, where a positive electron affinity indicates that the A^- ion has a lower, more favourable energy than the neutral species, A,[3] was undertaken.

The electron affinity of benzo[h]quinoline in the gas phase is 41.1 kJ mol^{-1}. For benzo[f]quinoline, it is 46.1 kJ mol^{-1} and for 8-methylquinoline it is 30.8 kJ mol^{-1}. The electron affinities for ligands shown to reductively dimerise are 39.5 kJ mol^{-1} for quinoline and 105.5 kJ mol^{-1} for acridine. With a positive value of electron affinity for each of these five ligands, it is clear that reduction is feasible. Given that there is no discernable cut-off or pattern to the electron affinity with respect to the observed tendency to reductive dimerise or not, it is necessary to concede that there is likely a complex interplay between sterics and electronics that governs the interactions of the species reported in Section 4.3.2.

4.4 Experimental

The syntheses of the complexes described in this Chapter were achieved *via* the reaction between $[(Et_8N_4Me_2)Sm(THF)_2]$, (**XVI**), and the relevant *N*-heterocycle. Given the significant number of products described and the emphasis placed on characterisation *via* X-ray crystal determination and Density Functional Theory analysis, NMR spectroscopic analysis, elemental analysis and yield data were only pursued in a small number of cases, as described below.

Synthesis of $[(Et_8N_4Me_2)Sm(py)_2]$, (14)

A solution of $[(Et_8N_4Me_2)Sm(THF)_2]$, (**XVI**), (1.16×10^{-5} mol, 10 mg) was prepared in benzene (0.5 mL). Neat pyridine (12.64×10^{-5} mol, 10 mg) was added *via* pipette. The reaction was allowed to stand at room temperature overnight, whereupon purple/black crystals were observed. All volatiles were removed *in vacuo*, providing crystals of the title compound (8 mg, 79%).

^{1}H NMR (C_6D_6, 299.888 MHz, RT, ppm): δ = -22.33 (s, 4H, 2 CH_2), -8.27 (s, 12H, 4 CH_3), -5.21 (s, 4H, 2 CH_2), 0.91 (s, 12H, 4 CH_3), 1.20 (b, s, 8H, 2 CH_2 and 4 =CH pyrMe or pyr), 5.34 (s, 4H, 2 CH_2), 6.44 (b, s, 2H, py), 8.59 (s, 4H, py), 8.83 (s, 4H, py), 20.49 (s, 4H, =CH pyrMe or pyr), 46.30 (s, 6H, 2 NCH_3)

Synthesis of $[(Et_8N_4Me_2)Sm(2\text{-pic})]$, (15)

A solution of $[(Et_8N_4Me_2)Sm(THF)_2]$, (**XVI**), (1.04×10^{-5} mol, 9 mg) was prepared in benzene (0.5 mL). Two drops of neat 2-methylpyridine was added *via* pipette. After 20 minutes, a dark, sparingly soluble precipitate was evident under a weakly purple supernatant solution. The solid was observed by polarising microscopy as a purple/red

crystalline material resembling an elongated hexagonal prism. The crystals were characterised by X-ray crystallography.

Synthesis of [($Et_8N_4Me_2$)Sm(2,6-lut)], (16)

A solution of [($Et_8N_4Me_2$)Sm(THF)$_2$], (**XVI**), (1.16×10^{-5} mol, 10 mg) was prepared in benzene (0.5 mL). Two drops of neat 2,6-dimethylpyridine was added *via* pipette. After one hour a red solution and crystalline rods was apparent. The crystalline rods were investigated by polarising microscopy and found to be red/purple in colour. The crystals were characterised by X-ray crystallography.

Synthesis of [($Et_8N_4Me_2$)Sm(3,5-lut)], (17)

A solution of [($Et_8N_4Me_2$)Sm(THF)$_2$], (**XVI**), (1.16×10^{-5} mol, 10 mg) was prepared in benzene (0.5 mL). Two drops of neat 3,5-dimethylpyridine was added *via* pipette. No immediate colour change was observed and the reaction was allowed to stand at room temperature for three days, whereupon the purple supernatant was decanted and brown crystalline plates were isolated and characterised by X-ray crystallography.

Synthesis of [($Et_8N_4Me_2$)Sm(2-Phpy)], (18)

A solution of [($Et_8N_4Me_2$)Sm(THF)$_2$], (**XVI**), (1.39×10^{-5} mol, 12 mg) was prepared in benzene (0.5 mL). Neat 2-phenylpyridine was added *via* pipette (5.15×10^{-5} mol, 8 mg). The reaction immediately produced purple/red solid and was allowed to stand at room temperature for one hour, whereupon many small, very dark purple/black crystals were observed. The reaction was allowed to stand overnight. The following day, the supernatant solution was decanted and the remaining solid washed with petroleum ether (40-60 °C) and dried *in vacuo*, providing crystals of the title compound (9 mg, 74 %).

Satisfactory elemental analysis was obtained of the toluene, benzene and petroleum ether insoluble title compound:

Anal. Calc: C, 67.46; H, 7.28; N, 8.03 ($C_{49}H_{63}N_5Sm$)

Found: C, 67.18; H, 7.39; N, 7.64

Synthesis of [($Et_8N_4Me_2$)Sm(*N*-terpy)]·2.5(C_6H_6), (19)

A solution of [($Et_8N_4Me_2$)Sm(THF)$_2$], (**XVI**), (1.39×10^{-5} mol, 12 mg) was prepared in benzene (0.5 mL). Excess solid 2,2′;6′,2″-terpyridine was added (4.29×10^{-5} mol, 10 mg). Upon addition, the solution immediately became black with a dark precipitate. The reaction was allowed to stand at room temperature overnight. The supernatant solution was decanted and the remaining solid dried *in vacuo*, providing black crystals that appear, by microscopy, red under a polarising filter. The title compound was isolated in two crops (12 mg, 79 %) and characterised by ^{1}H NMR spectroscopy, elemental analysis (as a desolvated species) and X-ray crystallography:

^{1}H NMR (C_6D_6, 299.888 MHz, RT, ppm): δ = -24.43 (s, 4H, 2 CH_2), -7.90 (s, 12H, 4 CH_3), -5.97 (s, 4H, 2 CH_2), 0.35 (s, 12H, 4 CH_3), 0.94 (s, 4H, 2 CH_2), 1.50 (s, 4H, =CH pyrMe or pyr), 4.88 (b, s, 2H, terpy), 5.20 (b, s, 2H, terpy), 5.33 (b, s, 4H, 2 CH_2), 6.63 (s, 2H, terpy), 10.8-12.3 (broad m, 5H, terpy), 18.31 (s, 4H, =CH pyrMe or pyr), 46.88 (s, 6H, 2 NCH_3)

Anal. Calc: C, 66.97; H, 6.89; N, 10.32 ($C_{53}H_{65}N_7Sm$)

Found: C, 67.09; H, 6.96; N, 10.33

Synthesis of [($Et_8N_4Me_2$)Sm(2-Me-6-Phpy)], (20)

A solution of [($Et_8N_4Me_2$)Sm(THF)$_2$], (**XVI**), (1.04 x 10^{-5} mol, 9 mg) was prepared in benzene (0.5 mL). Two drops of neat 2-methyl-6-phenylpyridine was added *via* pipette. No colour change or precipitate was observed after one hour and the reaction was allowed to stand at room temperature overnight. The supernatant solution was allowed to evaporate, providing purple crystalline blocks of the title compound by X-ray crystallography.

Synthesis of [{($Et_8N_4Me_2$)Sm}$_2$(μ-4,4′-bipy)]·2(C_6H_6), (21)

A solution of [($Et_8N_4Me_2$)Sm(THF)$_2$], (**XVI**), (1.16 x 10^{-5} mol, 10 mg) was prepared in benzene (0.5 mL). Solid 4,4′-bipyridine was added (1.92 x 10^{-5} mol, 3 mg), effecting an immediate colour change of the solution to intense dark red/orange. The reaction was allowed to stand at room temperature overnight, whereupon red crystals were sampled *via* spatula and characterised by X-ray crystallography.

Synthesis of [{($Et_8N_4Me_2$)Sm}$_2$(μ-4,4′-biquin)]·2.75(C_6H_6), (22)

A solution of [($Et_8N_4Me_2$)Sm(THF)$_2$], (**XVI**), (1.16 x 10^{-5} mol, 10 mg) was prepared in benzene (0.5 mL). Three drops of neat quinoline was added *via* pipette, immediately effecting a colour change in the solution as the dark purple starting material became a much lighter purple solution. The reaction was allowed to stand at room temperature overnight, whereupon the lavender purple supernatant was decanted and purple crystalline blocks were isolated and characterised by X-ray crystallography.

Synthesis of [($Et_8N_4Me_2$)Sm(8-Mequin)]·PhMe, (23)

A solution of [($Et_8N_4Me_2$)Sm(THF)$_2$], (**XVI**), (1.04 x 10^{-5} mol, 9 mg) was prepared in benzene (0.5 mL). Two drops of 8-methylquinoline were carefully layered onto the [($Et_8N_4Me_2$)Sm(THF)$_2$] solution, immediately producing a very dark solution from which large, dark crystals precipitated over 15 minutes. Under the same conditions, the reaction proceeds in benzene to provide similar dark crystals and a very pale supernatant solution, indicating the product is only sparingly soluble in benzene after 15 minutes. The crystals obtained *via* reaction in toluene were more suited to X-ray crystallography, leading to characterisation of the title compound.

Synthesis of [($Et_8N_4Me_2$)Sm(Benzo[h])], (24)

A solution of [($Et_8N_4Me_2$)Sm(THF)$_2$], (**XVI**), (1.04 x 10^{-5} mol, 9 mg) was prepared in benzene (0.5 mL). Excess solid benzo[h]quinoline was added (2.23 x 10^{-5} mol, 4 mg) with no immediately discernable effect. The reaction was allowed to stand at room temperature overnight, whereupon the supernatant was decanted and dark purple crystalline prisms were isolated and characterised by X-ray crystallography.

Synthesis of [($Et_8N_4Me_2$)Sm(Benzo[f])]·0.66(PhMe), (25)

A solution of [($Et_8N_4Me_2$)Sm(THF)$_2$], (**XVI**), (1.04 x 10^{-5} mol, 9 mg) was prepared in toluene (0.5 mL). Excess solid benzo[f]quinoline was added (1.67 x 10^{-5} mol, 3 mg), immediately effecting a dark green solution with no sign of precipitation after 15 minutes. The reaction was allowed to stand at room temperature for 12 days, whereupon large purple crystals of the title complex were precipitated. The dark supernatant was decanted and the crystals were washed with benzene and petroleum ether (40 - 60 °C) and characterised via X-ray crystallography and elemental analysis. The reaction was repeated

in benzene and precipitation of dark green/orange crystalline material proceeded within seven minutes at room temperature. This material appeared reddish/orange after one hour.

Anal. Calc: C, 69.80; H, 7.19; N, 7.31 $3(C_{51}H_{63}N_5Sm), 2(C_7H_8)$

Found: C, 70.14; H, 6.87; N, 7.35

Synthesis of [{$(Et_8N_4Me_2)Sm$}$_2$(μ-7,7′-biacrid)$_2$], (26)

A solution of $[(Et_8N_4Me_2)Sm(THF)_2]$ (1.16×10^{-5} mol, 10 mg) was prepared in toluene (0.5 mL). Excess solid acridine was added (2.23×10^{-5} mol, 4 mg), immediately effecting a very dark purple solution. After 15 minutes, a violet precipitate was observed. Allowing the reaction to stand at room temperature for one hour provides a colourless solution and violet precipitate. Undertaking the reaction in THF under the same conditions proceeds *via* a very dark blue solution from which no precipitation is visible after 15 minutes. After one hour, the same colourless solution over violet precipitate is observed. Crystals of the title compound suitable for X-ray crystallography were obtained from reaction in THF; satisfactory elemental analysis was obtained from reaction in toluene in 77 % yield (8 mg).

Anal. Calc: C, 68.33; H, 7.08; N, 7.81 $(C_{51}H_{63}N_5Sm)$

Found: C, 68.58; H, 6.77; N, 7.43

Synthesis of [$(Et_8N_4Me_2)Sm(2,2'\text{-bipy}^{\bullet-})$], (27)

A solution of $[(Et_8N_4Me_2)Sm(THF)_2]$ (1.04×10^{-5} mol, 9 mg) was prepared in toluene (0.5 mL). Excess solid 2,2′-bipyridine was added (2.79×10^{-5} mol, 5 mg), immediately effecting an intense red suspension. The reaction was repeated on a THF solution of $[(Et_8N_4Me_2)Sm(THF)_2]$ (5.80×10^{-5} mol, 50 mg) with excess 2,2′-bipyridine

(16.8 x 10^{-5} mol, 30 mg) in a small-scale wine-bottle experiment. After two weeks, large, rhombus shaped red crystals were isolated and characterised by X-ray crystallography. The title compound is insoluble in THF, toluene, benzene, diethyl ether and petroleum ether (40 - 60 °C). Satisfactory elemental analysis could not be obtained, despite multiple attempts.

Synthesis of [{($Et_8N_4Me_2$)Sm}$_2$(μ-4,4′-diphen)]·4(C_6H_6), (28)

A solution of [($Et_8N_4Me_2$)Sm(THF)$_2$] (1.28 x 10^{-5} mol, 11 mg) was prepared in toluene (0.5 mL). Excess solid 1,10-phenanthroline was added (3.33 x 10^{-5} mol, 6 mg), resulting in an immediate colour change of the solution to an intense violet purple colour. After 15 minutes, purple precipitate was visible; after one hour, a significant amount of purple precipitate was visible. Undertaking the reaction in THF results in an intense purple solution with limited precipitation over one hour. Crystals suitable for X-ray crystallography were obtained from the benzene reaction and shown to flash red (from purple) under a polarising microscope.

Synthesis of [{($Et_8N_4Me_2$)Sm}$_2$(μ-4,4′-bis(Me_2phen)]·7(C_6H_6), (29)

A solution of [($Et_8N_4Me_2$)Sm(THF)$_2$] (1.16 x 10^{-5} mol, 10 mg) was prepared in toluene (0.5 mL). Solid 4,7-dimethyl-1,10-phenanthroline was added (1.92 x 10^{-5} mol, 4 mg), resulting in an immediate colour change of the solution to an intense dark blue/purple colour. The reaction was also undertaken in THF and toluene; all three proceeded to yield a dark purple crystalline precipitate under a purple supernatant after three days standing at room temperature. Crystals of the title compound suitable for X-ray crystallography were obtained from the reaction undertaken in benzene.

Synthesis of [($Et_8N_4Me_2$)Sm(batho$^{\bullet-}$)], (30)

A solution of [($Et_8N_4Me_2$)Sm(THF)$_2$] (1.28 x 10^{-5} mol, 11 mg) was prepared in toluene (0.5 mL). Solid 4,7-diphenyl-1,10-phenanthroline was added (1.81 x 10^{-5} mol, 6 mg), resulting in an immediate colour change of the solution to an intense blue/green colour. The reaction was allowed to stand for one week, whereupon dark green crystals of the title compound were obtained after decanting the highly coloured supernatant solution. Crystals of the title compound were characterised by X-ray crystallography.

Synthesis of [($Et_8N_4Me_2$)Sm(neo)]•(C_6H_6), (31)

A solution of [($Et_8N_4Me_2$)Sm(THF)$_2$] (1.16 x 10^{-5} mol, 10 mg) was prepared in toluene (0.5 mL). Excess solid 2,9-dimethyl-1,10-phenanthroline was added (2.88 x 10^{-5} mol, 6 mg) , resulting in an immediate colour change of the solution to olive green/brown colour. The reaction was allowed to stand for one month, whereupon large pale yellow crystals of the title compound were obtained after near-complete evaporation of the supernatant solution. The yellow crystals were characterised by X-ray crystallography.

Chapter 5

Concluding Remarks

5.1 Conclusion

This thesis describes the synthesis, characterisation and reactivity of a range of samarium(II) and samarium(III) complexes of the dimetallated modified macrocycle *trans*-*N,N'*-dimethyl-*meso*-octaethylporphyrinogen, $(Et_8N_4Me_2)^{2-}$.

Chapter 1 provided a broad introduction and relevant background on the properties of samarium with respect to the other lanthanoids, general aspects of the organometallic chemistry of the lanthanoid elements, important recent advances in reactivity studies arising from studying sterically crowded systems, relevant and related chemistry of the porphyrinogen systems, and general considerations of computational techniques employed in this study.

Chapter 2 outlined the synthesis of a Lewis base free (unsolvated) samarium(II) porphyrinogen complex and its subsequent reactivity, including deprotonation of toluene to form a bridging benzyl complex; a result indicative of the highly reactive nature of the unsolvated species, as supported by the synthesis of several other unusual complexes. The unprecedented binding of dinitrogen to provide the first example of end-on binding of dinitrogen to a lanthanoid element was reported. The novel binding mode is rationalised by steric and electronic arguments and probed by theoretical investigation, providing a richer understanding of the degree of dinitrogen activation in this, as well as other, samarium-based systems.

The reaction between the samarium porphyrinogen and simple *N*-heteroalkynes was described in Chapter 3. The chemistry of simple 2:1 and 1:1 adducts of nitriles was reported and shown to be complicated at higher temperature, with oligomerisation and reductive cleavage of nitriles reported. Similar reductive cleavage of an isonitrile provided the first structurally characterised lanthanoid iminoacyl complex *via tert*-butyl radical trapping.

A systematic investigation of the interaction between substituted pyridines, benzannulated pyridines and substituted 1,10-phenanthrolines (including 2,2′-bipyridine) by X-ray crystallography was detailed in Chapter 4. Reaction outcomes including mono- and bis- adduct formation, single electron ligand reduction and reductive dimerisation were reported. A thorough analysis of the geometric properties of the X-ray crystal structure data was provided and informs future analysis of similar systems. Computational techniques were employed to analyse singly occupied molecular orbital populations, providing satisfactory assignment and rationalisation of the oxidation state of the samarium centre for these complexes *in lieu* of magnetic susceptibility data. A working protocol has been established for future computational analysis of similar compounds.

5.2 Future Directions

The synthesis of the end-on dinitrogen complex, (**7**), simultaneously provides a clearly significant result amid a veritable minefield of difficulties with regard to convenient isolation based on the current synthetic approach. Full characterisation of this complex is highly sought. Synthesis of (**7**) *via* potassium reduction of the sterically strained complex, [{($Et_8N_4Me_2$)Sm}$_2$(*t*-BuDAB)], (**XXII**), has provided invaluable insight into the properties of unsolvated samarium(II) complexes of *trans-N,N*′-dimethyl-*meso*-octaethylporphyrinogen by way of demonstrating that the unsolvated species is extremely

soluble in both toluene and benzene. Knowledge of the solubility of the unsolvated species suggests that a re-examination of the reaction between unsolvated decamethylsamarocene and the lithium salt of the macrocycle is warranted. The reaction is reported to produce the mono(THF) adduct in 5 % yield due to incomplete desolvation of the reagents, Equation 2-8.[72]

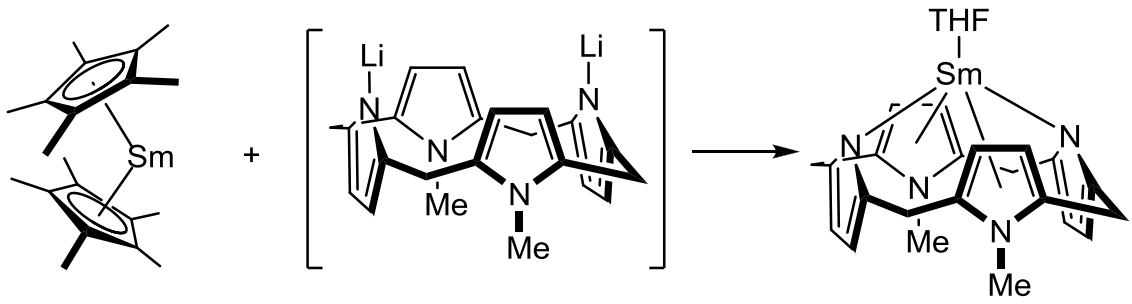

Equation 2-8

Given the high solubility of unsolvated [$(Et_8N_4Me_2)$Sm] and the low solubility of Li(C_5Me_5), the reaction suggested by Equation 2-8, following complete desolvation of the reagents, is likely to prove a far superior route to access unsolvated species following filtration and concentration. This synthetic route may provide a stable starting point to investigate potassium assisted toluene metallation chemistry, as demonstrated by isolation of (2), and to shed light on the equilibrium between the unsolvated species and *t*-BuDAB and K(*t*-BuDAB) incorporated complexes. Additionally, such a solution would be ideal to investigate the effect of either bubbling N_2 gas through it, or employing apparatus suited to high pressures of N_2 gas, to access the less soluble end-on dinitrogen complex, (**7**). Further characterisation of the dinitrogen complex should be sought *via* Raman spectroscopic analysis and ^{15}N- labelling experiments.

Given the steric control of reductive cleavage reactivity outcomes observed for mono(nitrile) adducts, Chapter 3, the reaction between benzonitrile, PhCN, and [$(Et_8N_4Me_2)$Sm$(THF)_2$], (**XVI**), may provide outcomes worthy of investigation.

Presumably, excess PhCN will result in the formation of a bis(benzonitrile) adduct. Isolation of such an adduct and subsequent redissolution in a non-coordinating solvent, such as benzene or toluene solutions, may allow access to the 1:1 adduct as inferred for MeCN and observed for *t*-BuCN, (**XVI**). Reductive cleavage of this 1:1 benzonitrile adduct would presumably lead to either the Sm^{III} cyanide trimer, (**10**), and a novel Sm^{III}-phenyl complex, as observed for the 1:1 acetonitrile adduct, or a samarium diphenylimine complex *via* addition of the phenyl anion to the liberated nitrile. This latter species would be unable to progress to the proposed further C−C coupled nacnac system and hence provide significant mechanistic evidence. The synthetic viability of a novel Sm^{III}-phenyl complex could be established *via* reaction of $[\{(Et_8N_4Me_2)SmCl\}_2]$, (**XVII**), with PhLi; this reaction has not been pursued in our laboratory at this stage. The steric environment of the macrocyclic binding groove, which has been shown in this thesis to not allow the unstrained binding of the *t*-butyl anion to a Sm^{III} centre, is likely to accommodate a planar phenyl ring.

Chapter 4 details the synthesis of a number of sterically hindered Sm^{II} and Sm^{III} *N*-heterocyclic complexes. Exploration of the potential for these strained species to either act as synthons for the unsolvated Sm^{II} species, $(Et_8N_4Me_2)Sm$, (**3**), by virtue of the absence of THF from the system and, in some cases, highly soluble complexes, or demonstrate ligand based reduction in the form of SIR chemistry to alleviate the significant steric strain, may provide for valuable areas of future enquiry.

References

[1] G. J. Leigh, *Chem. Int.* **2009**, *31*, 4.

[2] H. C. Aspinall, *Chemistry of the f-Block Elements*, **2001**, 176.

[3] D. F. Shriver and P. W. Atkins, *Inorganic Chemistry*, Oxford University Press, Oxford, **1999**, 321.

[4] T. J. Kealy and P. L. Pauson, *Nature* **1951**, *168*, 1039.

[5] P. F. Eiland and R. Pepinsky, *J. Am. Chem. Soc.* **1952**, *74*, 4971.

[6] G. Wilkinson, P. L. Pauson, J. M. Birmingham and F. A. Cotton, *J. Am. Chem. Soc.* **1953**, *75*, 1011.

[7] G. Wilkinson and F. A. Cotton, *Chem. Ind.* **1954**, 307.

[8] G. Wilkinson and J. M. Birmingham, *J. Am. Chem. Soc.* **1954**, *76*, 6210.

[9] J. M. Birmingham and G. Wilkinson, *J. Am. Chem. Soc.* **1956**, *78*, 42.

[10] E. O. Fischer and H. Fischer, *Angew. Chem.* **1964**, *76*, 52.

[11] F. Calderazzo, R. Pappalardo and S. Losi, *J. Inorg. Nucl. Chem.* **1966**, *28*, 987.

[12] G. W. Watt and E. W. Gillow, *J. Amer. Chem. Soc.* **1969**, *91*, 775.

[13] A. Streitwieser, Jr. and U. Mueller-Westerhoff, *J. Am. Chem. Soc.* **1968**, *90*, 7364.

[14] A. Streitwieser, Jr., U. Muller-Westerhoff, G. Sonnichsen, F. Mares, D. G. Morrell, K. O. Hodgson and C. A. Harmon, *J. Am. Chem. Soc.* **1973**, *95*, 8644.

[15] K. O. Hodgson, F. Mares, D. F. Starks and A. Streitwieser, Jr., *J. Am. Chem. Soc.* **1973**, *95*, 8650.

[16] R. E. Maginn, S. Manastyrskyj and M. Dubeck, *J. Am. Chem. Soc.* **1963**, *85*, 672.

[17] S. Manastyrskyj, R. E. Maginn and M. Dubeck, *Inorg. Chem.* **1963**, *2*, 904.

[18] R. G. Hayes and J. L. Thomas, *J. Am. Chem. Soc.* **1969**, *91*, 6876.

[19] W. J. Evans, I. Bloom, W. E. Hunter and J. L. Atwood, *J. Am. Chem. Soc.* **1981**, *103*, 6507.

[20] J. L. Namy, P. Girard and H. B. Kagan, *Nouv. J. Chim.* **1977**, *1*, 5.

[21] P. Girard, J. L. Namy and H. B. Kagan, *J. Am. Chem. Soc.* **1980**, *102*, 2693.

[22] W. J. Evans, J. W. Grate, H. W. Choi, I. Bloom, W. E. Hunter and J. L. Atwood, *J. Am. Chem. Soc.***1985**, *107*, 941.

[23] W. J. Evans, L. A. Hughes and T. P. Hanusa, *J. Am. Chem. Soc.* **1984**, *106*, 4270.

[24] W. J. Evans, L. A. Hughes and T. P. Hanusa, *Organometallics* **1986**, *5*, 1285.

[25] M. Schultz, C. J. Burns, D. J. Schwartz and R. A. Andersen, *Organometallics* **2000**, *19*, 781.

[26] J. C. Green, D. Hohl and N. Roesch, *Organometallics* **1987**, *6*, 712.

[27] R. L. DeKock, M. A. Peterson, L. K. Timmer, E. J. Baerends and P. Vernooijs, *Polyhedron* **1990**, *9*, 1919.

[28] M. Guido and G. Gigli, *J. Chem. Phys.* **1976**, *65*, 1397.

[29] T. V. Timofeeva, J.-H. Lii and N. L. Allinger, *J. Am. Chem. Soc.* **1995**, *117*, 7452.

[30] T. K. Hollis, J. K. Burdett and B. Bosnich, *Organometallics* **1993**, *12*, 3385.

[31] L. C. Pauling, *The Nature of the Chemical Bond and the Structure of Molecules and Crystals. An Introduction to Modern Structural Chemistry. 3rd ed*, **1960**, 644

[32] R. A. Andersen, R. Blom, J. M. Boncella, C. J. Burns and H. V. Volden, *Acta Chem. Scand., Ser. A* **1987**, *A41*, 24.

[33] W. J. Evans, T. A. Ulibarri and J. W. Ziller, *J. Am. Chem. Soc.* **1988**, *110*, 6877.

[34] W. J. Evans, S. L. Gonzales and J. W. Ziller, *J. Am. Chem. Soc.* **1991**, *113*, 7423.

[35] W. J. Evans and T. A. Ulibarri, *J. Am. Chem. Soc.* **1987**, *109*, 4292.

[36] W. J. Evans, K. J. Forrestal, J. T. Leman and J. W. Ziller, *Organometallics* **1996**, *15*, 527.

[37] W. J. Evans, J. M. Perotti, S. A. Kozimor, T. M. Champagne, B. L. Davis, G. W. Nyce, C. H. Fujimoto, R. D. Clark, M. A. Johnston and J. W. Ziller, *Organometallics* **2005**, *24*, 3916.

[38] W. J. Evans, K. J. Forrestal and J. W. Ziller, *J. Am. Chem. Soc.* **1998**, *120*, 9273.

[39] J. H. Melman, T. J. Emge and J. G. Brennan, *Inorg. Chem.* **1999**, *38*, 2117.

[40] T. D. Tilley, R. A. Andersen, B. Spencer, H. Ruben, A. Zalkin and D. H. Templeton, *Inorg. Chem.* **1980**, *19*, 2999.

[41] H. Schumann, J. A. Meese-Marktscheffel and L. Esser, *Chem. Rev.* **1995**, *95*, 865.

[42] W. J. Evans, *Coord. Chem. Rev.* **2000**, *206-207*, 263.

[43] W. J. Evans, D. K. Drummond, L. R. Chamberlain, R. J. Doedens, S. G. Bott, H. Zhang and J. L. Atwood, *J. Am. Chem. Soc.* **1988**, *110*, 4983.

[44] W. J. Evans, D. K. Drummond, S. G. Bott and J. L. Atwood, *Organometallics* **1986**, *5*, 2389.

[45] W. J. Evans, K. J. Forrestal and J. W. Ziller, *Angew. Chem., Int. Edit.* **1997**, *36*, 774.

[46] W. J. Evans, C. A. Seibel and J. W. Ziller, *J. Am. Chem. Soc.* **1998**, *120*, 6745.

[47] W. J. Evans, B. L. Davis and J. W. Ziller, *Inorg Chem.* **2001**, *40*, 6341.

[48] W. J. Evans, G. W. Nyce, R. D. Clark, R. J. Doedens and J. W. Ziller, *Angew. Chem., Int. Edit.* **1999**, *38*, 1801.

[49] S. Shinkai, *Tetrahedron* **1993**, *49*, 8933-8968.

[50] D. Jacoby, C. Floriani, A. Chiesi-Villa and C. Rizzoli, *Chem. Commun.* **1991**, 790.

[51] P. A. Gale, *Coord. Chem. Rev.* **2001**, *213*, 79.

[52] L. Bonomo, E. Solari, R. Scopelliti and C. Floriani, *Angew. Chem., Int. Edit.* **2001**, *40*, 2529.

[53] J. Jubb and S. Gambarotta, *J. Am. Chem. Soc.* **1994**, *116*, 4477.

[54] J.-I. Song and S. Gambarotta, *Angew. Chem., Int. Edit.* **1995**, *34*, 2141.

[55] T. Dubé, S. Gambarotta and G. P. A. Yap, *Angew. Chem., Int. Edit.* **1999**, *38*, 1432.

[56] W. J. Evans, D. S. Lee, J. W. Ziller and N. Kaltsoyannis, *J. Am. Chem. Soc.* **2006**, *128*, 14176.

[57] W. J. Evans, D. S. Lee, D. B. Rego, J. M. Perotti, S. A. Kozimor, E. K. Moore and J. W. Ziller, *J. Am.Chem. Soc.* **2004**, *126*, 14574.

[58] W. J. Evans, D. S. Lee, C. Lie and J. W. Ziller, *Angew. Chem., Int. Edit.* **2004**, *43*, 5517.

[59] W. J. Evans, D. S. Lee, M. A. Johnston and J. W. Ziller, *Organometallics* **2005**, *24*, 6393.

[60] W. J. Evans, S. E. Lorenz and J. W. Ziller, *Inorg. Chem.* **2009**, *48*, 2001.

[61] M. G. Gardiner and D. N. Stringer, *Materials* **2010**, *3*, 841.

[62] T. Dubé, S. Gambarotta and G. P. A. Yap, *Organometallics* **2000**, *19*, 817.

[63] T. Dubé, S. Gambarotta and G. P. A. Yap, *Organometallics* **2000**, *19*, 121.

[64] T. Dubé, J. Guan, S. Gambarotta and G. P. A. Yap, *Chem.-Eur. J.* **2001**, *7*, 374.

[65] J. Guan, T. Dubé, S. Gambarotta and G. P. A. Yap, *Organometallics* **2000**, *19*, 4820.

[66] E. Campazzi, E. Solari, C. Floriani and R. Scopelliti, *Chem. Commun.* **1998**, 2603.

[67] E. Campazzi, E. Solari, R. Scopelliti and C. Floriani, *Chem. Commun.* **1999**, 1617.

[68] E. Campazzi, E. Solari, R. Scopelliti and C. Floriani, *Inorg. Chem.* **1999**, *38*, 6240.

[69] Y. Furusho, H. Kawasaki, S. Nakanishi, T. Aida and T. Takata, *Tetrahedron Lett.* **1998**, *39*, 3537.

[70] J. Wang, M. G. Gardiner, E. J. Peacock, B. W. Skelton and A. H. White, *Dalton Trans.* **2003**, 161.

[71] J. Wang, A. K. J. Dick, M. G. Gardiner, B. F. Yates, E. J. Peacock, B. W. Skelton and A. H. White, *Eur. J. Inorg. Chem.* **2004**, 1992.

[72] A. K. J. Dick, A. S. P. Frey, M. G. Gardiner, M. Hilder, A. N. James, P. C. Junk, S. Powanosorn, B. W. Skelton, J. Wang and A. H. White, *J. Organomet. Chem.* **2010**, *695*, 2761.

[73] W. J. Evans, J. M. Perotti and J. W. Ziller, *J. Am. Chem. Soc.* **2005**, *127*, 3894.

[74] N. W. Davies, A. S. P. Frey, M. G. Gardiner and J. Wang, *Chem. Commun.* **2006**, 4853.

[75] J. Wang, M. G. Gardiner, B. W. Skelton and A. H. White, *Organometallics* **2005**, *24*, 815.

[76] J. Wang, R. I. J. Amos, A. S. P. Frey, M. G. Gardiner, M. L. Cole and P. C. Junk, *Organometallics* **2005**, *24*, 2259.

[77] W. J. Evans, T. A. Ulibarri and J. W. Ziller, *J. Am. Chem. Soc.* **1990**, *112*, 219.

[78] W. J. Evans, D. G. Giarikos, C. B. Robledo, V. S. Leong and J. W. Ziller, *Organometallics* **2001**, *20*, 5648.

[79] F. G. N. Cloke and P. B. Hitchcock, *J. Am. Chem. Soc.* **2002**, *124*, 9352.

[80] W. J. Evans, S. A. Kozimor and J. W. Ziller, *J. Am. Chem. Soc.* **2003**, *125*, 14264.

[81] A. S. P. Frey, M. G. Gardiner, D. N. Stringer, B. F. Yates, A. V. George, P. Jensen and P. Turner, *Organometallics* **2007**, *26*, 1299.

[82] D. Young, *Computational Chemistry*, Wiley Interscience, New York, **2001**, 8

[83] W. J. Evans, *Adv. Organomet. Chem.* **1985**, *24*, 131.

[84] W. J. Evans, T. T. Peterson, M. D. Rausch, W. E. Hunter, H. Zhang and J. L. Atwood, *Organometallics* **1985**, *4*, 554.

[85] P. L. Watson, *Chem. Commun.* **1980**, 652.

[86] W. J. Evans, G. Kociok-Koehn, S. E. Foster, J. W. Ziller and R. J. Doedens, *J. Organomet. Chem.* **1993**,*444*, 61.

[87] W. J. Evans, J. W. Grate, I. Bloom, W. E. Hunter and J. L. Atwood, *J. Am. Chem. Soc.* **1985**, *107*, 405.

[88] D. J. Berg, C. J. Burns, R. A. Andersen and A. Zalkin, *Organometallics* **1989**, *8*, 1865.

[89] A. Recknagel, M. Noltemeyer and F. T. Edelmann, *J. Organomet. Chem.* **1991**, *410*, 53.

[90] W. J. Evans, T. A. Ulibarri, L. R. Chamberlain, J. W. Ziller and D. Alvarez, Jr., *Organometallics* **1990**, *9*, 2124.

[91] W. J. Evans, S. A. Kozimor and J. W. Ziller, *Inorg. Chem.* **2005**, *44*, 7960.

[92] G. Jeske, H. Lauke, H. Mauermann, P. N. Swepston, H. Schumann and T. J. Marks, *J. Am. Chem. Soc.* **1985**, *107*, 8091.

[93] M. Tsutsui and N. Ely, *J. Am. Chem. Soc.* **1975**, *97*, 3551.

[94] W. J. Evans, T. M. Champagne and J. W. Ziller, *Organometallics* **2007**, *26*, 1204.

[95] H. Sitzmann, T. Dezember, O. Schmitt, F. Weber, G. Wolmershäuser and M. Ruck, *Z. Anorg. Allg.Chem.* **2000**, *626*, 2241.

[96] M. Visseaux, D. Barbier-Baudry, O. Blacque, A. Hafid, P. Richard and F. Weber, *New J. Chem.* **2000**, *24*, 939.

[97] W. J. Evans and H. Katsumata, *Macromolecules* **1994**, *27*, 2330.

[98] A. D. Allen and C. W. Senoff, *Chem. Commun.***1965**, 621.

[99] L. Perrin, L. Maron, O. Eisenstein, D. J. Schwartz, C. J. Burns and R. A. Andersen, *Organometallics* **2003**, *22*, 5447.

[100] M. D. Fryzuk, T. S. Haddad and S. J. Rettig, *J. Am. Chem. Soc.* **1990**, *112*, 8185.

[101] E. A. MacLachlan and M. D. Fryzuk, *Organometallics* **2006**, *25*, 1530.

[102] A. L. Odom, P. L. Arnold and C. C. Cummins, *J. Am. Chem. Soc.* **1998**, *120*, 5836.

[103] N. Kaltsoyannis and P. Scott, *Chem. Commun.***1998**, 1665.

[104] P. Roussel and P. Scott, *J. Am. Chem. Soc.* **1998**, *120*, 1070.

[105] P. Roussel, W. Errington, N. Kaltsoyannis and P. Scott, *J. Organomet. Chem.* **2001**, *635*, 69.

[106] M. Ganesan, M. P. Lalonde, S. Gambarotta and G. P. A. Yap, *Organometallics* **2001**, *20*, 2443.

[107] J. Guan, T. Dube, S. Gambarotta and G. P. A. Yap, *Organometallics* **2000**, *19*, 4820.

[108] T. Dubé, S. Conochi, S. Gambarotta, G. P. A. Yap and G. Vasapollo, *Angew. Chem., Int. Edit.* **1999**, *38*, 3657.

[109] W. J. Evans, D. K. Drummond, H. Zhang and J. L. Atwood, *Inorg. Chem.* **1988**, *27*, 575.

[110] W. J. Evans, D. K. Drummond, H. Zhang and J. L. Atwood, *Inorg. Chem.* **1988**, *27*, 2904.

[111] C. D. Bérubé, M. Yazdanbakhsh, S. Gambarotta and G. P. A. Yap, *Organometallics* **2003**, *22*, 3742.

[112] M. N. Bochkarev, I. L. Fedushkin, A. A. Fagin, T. V. Petrovskaya, J. W. Ziller, R. N. R. Broomhall-Dillard and W. J. Evans, *Angew. Chem., Int. Edit.* **1997**, *36*, 133.

[113] W. J. Evans, N. T. Allen and J. W. Ziller, *J. Am. Chem. Soc.* **2000**, *122*, 11749.

[114] M. N. Bochkarev, I. L. Fedushkin, S. Dechert, A. A. Fagin and H. Schumann, *Angew. Chem., Int. Edit.* **2001**, *40*, 3176.

[115] W. J. Evans, G. Zucchi and J. W. Ziller, *J. Am. Chem. Soc.* **2003**, *125*, 10.

[116] F. T. Edelmann, *Synthetic Methods of Organometallic and Inorganic Chemistry, Vol 6*, **1997**, 37.

[117] W. J. Evans, D. S. Lee and J. W. Ziller, *J. Am. Chem. Soc.* **2004**, *126*, 454.

[118] W. J. Evans and D. S. Lee, *Can. J. Chem.* **2005**, *83*, 375.

[119] G. Guillemot, B. Castellano, T. Prange, E. Solari and C. Floriani, *Inorg. Chem.* **2007**, *46*, 5152.

[120] W. J. Evans, M. Fang, G. Zucchi, F. Furche, J. W. Ziller, R. M. Hoekstra and J. I. Zink, *J. Am. Chem. Soc.* **2009**, *131*, 11195.

[121] G. Van Koten and K. Vrieze, *Adv. Organomet. Chem.* **1982**, *21*, 151.

[122] M. G. Gardiner, G. R. Hanson, M. J. Henderson, F. C. Lee and C. L. Raston, *Inorg. Chem.* **1994**, *33*, 2456.

[123] C. D. Broaddus, *J. Am. Chem. Soc.* **1966**, *88*, 4174.

[124] C. D. Broaddus, *J. Org. Chem.* **1970**, *35*, 10.

[125] A. J. Chalk and T. J. Hoogeboom, *J. Organomet. Chem.* **1968**, *11*, 615.

[126] P. C. Andrikopoulos, D. R. Armstrong, D. V. Graham, E. Hevia, A. R. Kennedy, R. E. Mulvey, C. T. O'Hara and C. Talmard, *Angew. Chem., Int. Edit.* **2005**, *44*, 3459.

[127] D. R. Baker, W. Clegg, L. Horsburgh and R. E. Mulvey, *Organometallics* **1994**, *13*, 4170.

[128] T. Del Giacco, E. Baciocchi and S. Steenken, *J. Phys. Chem.* **1993**, *97*, 5451.

[129] W. J. Evans, T. A. Ulibarri and J. W. Ziller, *Organometallics* **1991**, *10*, 134.

[130] A. Mandel and J. Magull, *Z. Anorg. Allg. Chem.* **1996**, *622*, 1913.

[131] Y. M. Badiei and T. H. Warren, *J. Organomet. Chem.* **2005**, *690*, 5989.

[132] M. E. Garcia, A. Ramos, M. A. Ruiz, M. Lanfranchi and L. Marchio, *Organometallics* **2007**, *26*, 6197.

[133] GaussView, Version 5, R. Dennington, T. Keith and J. Millam, *Semichem Inc*., Shawnee Mission KS, **2009**.

[134] W. J. Hehre, R. Ditchfield and J. A. Pople, *J. Chem. Phys.* **1972**, *56*, 2257.

[135] J. D. Dill and J. A. Pople, *J. Chem. Phys.* **1975**, *62*, 2921.

[136] M. M. Francl, W. J. Petro, W. J. Hehre, J. S. Binkley, M. S. Gordon, D. J. DeFrees and J. A. Pople, *J.Chem. Phys.* **1982**, *77*, 3654.

[137] P. C. Hariharan and H. Jacobsen, *Theor. Chim. Acta* **1973**, *28*, 213.

[138] A. Bergner, M. Dolg, W. Kuechle, H. Stoll and H. Preuss, *Mol. Phys.* **1993**, *80*, 1431.

[139] M. Kaupp, P. v. R. Schleyer, H. Stoll and H. Preuss, *J. Chem. Phys.* **1991**, *94*, 1360.

[140] M. Dolg, H. Stoll, H. Preuss and R. M. Pitzer, *J. Phys. Chem.* **1993**, *97*, 5852.

[141] W. J. Evans, S. L. Gonzales and J. W. Ziller, *J. Am. Chem. Soc.* **1994**, *116*, 2600.

[142] D. C. Bradley, J. S. Ghotra, F. A. Hart, M. B. Hursthouse and P. R. Raithby, *Dalton Trans.* **1977**, 1166.

[143] M. Niemeyer, *Z. Anorg. Allg. Chem.* **2002**, *628*, 647.

[144] V. Rassolov, J. A. Pople, M. Ratner and T. L. Windus, *J. Chem. Phys.* **1998**, *109*, 1223.

[145] T. Clark, J. Chandrasekhar, G. W. Spitznagel and P. v. R. Schleyer, *J. Comp. Chem.* **1983**, *4*, 294.

[146] E. D. Glendening, J. K. Badenhoop, A. E. Reed, J. E. Carpenter, J. A. Bohmann, C. M. Morales and F.Weinhold in *NBO 5.0 Vol.* Theoretical Chemistry Institute, University of Wisconsin, Madison, **2001**.

[147] H. Jacobsen, H. Berke, S. Döring, G. Kehr, G. Erker, R. Fröhlich and O. Meyer, *Organometallics* **1999**, *18*, 1724.

[148] R. Choukroun and C. Lorber, *Eur. J. Inorg. Chem.* **2005**, 4683.

[149] R. A. Michelin, M. Mozzon and R. Bertani, *Coord. Chem. Rev.* **1996**, *147*, 299.

[150] L. Xing-Fu, S. Eggers, J. Kopf, W. Jahn, R. D. Fischer, C. Apostolidis, B. Kanellakopulos, F. Benetollo, A. Polo and G. Bombieri, *Inorg. Chim. Acta* **1985**, *100*, 183.

[151] G. B. Deacon, C. M. Forsyth, R. H. Newnham and T. D. Tuong, *Aust. J. Chem.* **1987**, *40*, 895.

[152] W. J. Evans, E. Montalvo, D. J. Dixon, J. W. Ziller, A. G. DiPasquale and A. L. Rheingold, *Inorg. Chem.* **2008**, *47*, 11376.

[153] M. Schultz, C. J. Burns, D. J. Schwartz and R. A. Andersen, *Organometallics* **2001**, *20*, 5690.

[154] F. Weber, H. Sitzmann, M. Schultz, C. D. Sofield and R. A. Andersen, *Organometallics* **2002**, *21*, 3139.

[155] W. J. Evans and D. K. Drummond, *Organometallics* **1988**, *7*, 797.

[156] S. Gambarotta, C. Floriani, A. Chiesi-Villa and C. Guastini, *Inorg. Chem.* **1984**, *23*, 1739.

[157] Y. Obora, T. Ohta, C. L. Stern and T. J. Marks, *J. Am. Chem. Soc.* **1997**, *119*, 3745.

[158] W. J. Evans, E. Montalvo, S. E. Foster, K. A. Harada and J. W. Ziller, *Organometallics* **2007**, *26*, 2904.

[159] W. D. Jones and W. P. Kosar, *Organometallics* **1986**, *5*, 1823.

[160] K. W. Chiu, R. A. Jones, G. Wilkinson, A. M. R. Galas and M. B. Hursthouse, *Dalton Trans.* **1981**, 2088.

[161] A. M. Carrier, J. G. Davidson, E. K. Barefield and D. G. Van Derveer, *Organometallics* **1987**, *6*, 454.

[162] Y. Takenaka and Z. Hou, *Organometallics* **2009**, *28*, 5196.

[163] Z. Hou, M. Nishiura and T. Shima, *Eur. J. Inorg. Chem.* **2007**, 2535.

[164] A. Mendiratta and C. C. Cummins, *Inorg. Chem.* **2005**, *44*, 7319.

[165] W. J. Evans, E. Montalvo, T. M. Champagne, J. W. Ziller, A. G. DiPasquale and A. L. Rheingold, *J.Am. Chem. Soc.* **2008**, *130*, 16.

[166] A. J. Wilson and M. G. Gardiner, *unpublished results*.

[167] W. J. Evans, T. J. Mueller and J. W. Ziller, *Chem. -Eur. J.* **2010**, *16*, 964.

[168] J. E. Bercaw, D. L. Davies and P. T. Wolczanski, *Organometallics* **1986**, *5*, 443.

[169] D. S. Richeson, J. F. Mitchell and K. H. Theopold, *Organometallics* **1989**, *8*, 2570.

[170] P. D. Bolton, M. Feliz, A. R. Cowley, E. Clot and P. Mountford, *Organometallics* **2008**, *27*, 6096.

[171] W. J. Evans, I. Bloom, W. E. Hunter and J. L. Atwood, *J. Am. Chem. Soc.* **1983**, *105*, 1401.

[172] W. J. Evans, K. A. Miller and J. W. Ziller, *Angew. Chem., Int. Edit.* **2008**, *47*, 589.

[173] N. R. Smyrl and R. W. Smithwick, III, *J. Heterocycl. Chem.* **1982**, *19*, 493.

[174] P. Zanella, G. Paolucci, G. Rossetto, F. Benetollo, A. Polo, R. D. Fischer and G. Bombieri, *Chem. Commun.* **1985**, 96.

[175] A. Dormond, A. A. Elbouadili and C. Moïse, *Chem. Commun.* **1984**, 749.

[176] R. Boaretto, P. Roussel, N. W. Alcock, A. J. Kingsley, I. J. Munslow, C. J. Sanders and P. Scott, *J. Organomet. Chem.* **1999**, *591*, 174.

[177] K. H. den Haan, G. A. Luinstra, A. Meetsma and J. H. Teuben, *Organometallics* **1987**, *6*, 1509.

[178] G. E. Niznik, W. H. Morrison, III and H. M. Walborsky, *J. Org. Chem.* **1974**, *39*, 600.

[179] R. Adam, C. Villiers, M. Ephritikhine, M. Lance, M. Nierlich and J. Vigner, *J. Organomet. Chem.* **1993**, *445*, 99.

[180] J. Maynadié, J.-C. Berthet, P. Thuéry and M. Ephritikhine, *Organometallics* **2007**, *26*, 2623.

[181] J. Wang and G. Gardiner Michael, *Chem. Commun.* **2005**, 1589.

[182] V. Gutmann, *Coord. Chem. Rev.* **1976**, *18*, 225.

[183] G. B. Deacon, B. M. Gatehouse, S. N. Platts and D. L. Wilkinson, *Aust. J. Chem.* **1987**, *40*, 907.

[184] N. Froelich, P. B. Hitchcock, J. Hu, M. F. Lappert and J. R. Dilworth, *Dalton Trans.* **1996**, 1941.

[185] K. Mashima, Y. Nakayama, T. Shibahara, H. Fukumoto and A. Nakamura, *Inorg. Chem.* **1996**, *35*, 93.

[186] P. C. Leverd, D. Rinaldo and M. Nierlich, *Eur. J. Inorg. Chem.* **2001**, 2021.

[187] Y. Cui, H. L. Ngo, P. S. White and W. Lin, *Chem. Commun.* **2002**, 1666.

[188] D. L. Clark, J. C. Gordon, J. G. Watkin, J. C. Huffman and B. D. Zwick, *Polyhedron* **1996**, *15*, 2279.

[189] A. C. Hillier, A. Sella and M. R. J. Elsegood, *Dalton Trans.* **1998**, 3871.

[190] D. Freedman, T. J. Emge and J. G. Brennan, *Inorg. Chem.* **1999**, *38*, 4400.

[191] D. Freedman, A. Kornienko, T. J. Emge and J. G. Brennan, *Inorg. Chem.* **2000**, *39*, 2168.

[192] R. K. Agarwal and V. Kumar, *Phosphorus, Sulfur Silicon Relat. Elem.* **2010**, *185*, 1469.

[193] W. Clegg, I. Sage, I. Oswald, P. Brough and G. Bourhill, *Acta Crystallogr C* **2000**, *C56*, 1323.

[194] D. P. Graddon and E. C. Watton, *J. Inorg. Nucl. Chem.* **1961**, *21*, 49.

[195] M. F. Richardson, W. F. Wagner and D. E. Sands, *J. Inorg. Nucl. Chem.* **1969**, *31*, 1417.

[196] T. J. R. Weakley, *Inorg. Chim. Acta* **1982**, *63*, 161.

[197] E. D. Brady, D. L. Clark, D. W. Keogh, B. L. Scott and J. G. Watkin, *J. Am. Chem. Soc.* **2002**, *124*, 7007.

[198] A. A. Sidorov, G. G. Aleksandrov, E. V. Pakhmutova, A. Y. Chernyad'ev, I. L. Eremenko and I. I. Moiseev, *Russ. Chem. Bull.* **2005**, *54*, 588.

[199] I. L. Fedushkin, V. I. Nevodchikov, M. N. Bochkarev, S. Dechert and H. Schumann, *Russ. Chem. Bull.* **2003**, *52*, 154.

[200] W. J. Evans, *personal communication* **1999**.

[201] L. D. Durfee, P. E. Fanwick, I. P. Rothwell, K. Folting and J. C. Huffman, *J. Am. Chem. Soc.* **1987**, *109*, 4720.

[202] A. J. Birch and E. A. Karakhanov, *Chem. Commun.* **1975**, 480.

[203] W. E. Dorogy Jr and E. P. Schram, *Inorg. Chim. Acta* **1983**, *73*, 31.

[204] G. A. Olah and R. J. Hunadi, *J. Org. Chem.* **1981**, *46*, 715.

[205] K. Papadopoulos and J. Nikokavouras, *Tetrahedron Lett.* **1993**, *34*, 1371.

[206] K. K. Rohatgi and S. K. Sen Gupta, *J. Inorg. Nucl. Chem.* **1972**, *34*, 3061.

[207] M. G. Schrems, H. M. Dietrich, K. W. Toernroos and R. Anwander, *Chem. Commun.* **2005**, 5922.

[208] R. Kumar and U. P. Singh, *J. Mol. Struct.* **2008**, *875*, 427.

[209] D. M. Czakis-Sulikowska and J. Radwanska-Doczekalska, *J. Inorg. Nucl. Chem.* **1979**, *41*, 1299.

[210] D. Czakis-Sulikowska, J. Radwanska-Doczekalska and M. Markiewicz, *J. Therm. Anal.* **1994**, *41*, 81.

[211] J. A. Weitgenant, J. D. Mortison and P. Helquist, *Org. Lett.* **2005**, *7*, 3609.

[212] A. J. Birch and P. C. Lehman, *Perkin Trans. 1* **1973**, 2754.

[213] R. M. Crooks and A. J. Bard, *J. Electroanal. Chem.* **1988**, *240*, 253.

[214] M. Grignon-Dubois, M. Fialeix, M. Laguerre, J.-M. Léger and J.-C. Gauffre, *J. Org. Chem.* **1993**, *58*, 1926.

[215] S. D. Grumbine, R. K. Chadha and T. D. Tilley, *J. Am. Chem. Soc.* **1992**, *114*, 1518.

[216] W. J. Evans and D. K. Drummond, *J. Am. Chem. Soc.* **1989**, *111*, 3329.

[217] D. J. Berg, J. M. Boncella and R. A. Andersen, *Organometallics* **2002**, *21*, 4622.

[218] M. Schultz, J. M. Boncella, D. J. Berg, T. D. Tilley and R. A. Andersen, *Organometallics* **2002**, *21*, 460.

[219] R. E. Da Re, C. J. Kuehl, M. G. Brown, R. C. Rocha, E. D. Bauer, K. D. John, D. E. Morris, A. P. Shreve and J. L. Sarrao, *Inorg. Chem.* **2003**, *42*, 5551.

[220] J. M. Veauthier, E. J. Schelter, C. N. Carlson, B. L. Scott, R. E. Da Re, J. D. Thompson, J. L. Kiplinger, D. E. Morris and K. D. John, *Inorg. Chem.* **2008**, *47*, 5841.

[221] M. C. Ganorkar and M. H. B. Stiddard, *J. Chem. Soc.* **1965**, 5346.

[222] G. B. Deacon and J. C. Parrott, *Aust. J. Chem.* **1974**, *27*, 2547.

[223] C. C. Addison, R. David and N. Logan, *Dalton Trans.* **1974**, 2070.

[224] A. L. Crumbliss and A. T. Poulos, *Inorg. Chem.* **1975**, *14*, 1529.

[225] D. M. W. Buck and P. Moore, *Dalton Trans.* **1976**, 638.

[226] A. J. Canty, N. Chaichit, B. M. Gatehouse, E. E. George and G. Hayhurst, *Inorg. Chem.* **1981**, *20*, 2414.

[227] G. B. Deacon, J. M. Patrick, B. W. Skelton, N. C. Thomas and A. H. White, *Aust. J. Chem.* **1984**, *37*, 929.

[228] S. D. Cummings, *Coord. Chem. Rev.* **2009**, *253*, 449.

[229] E. W. Abel, N. J. Long, K. G. Orrell, A. G. Osborne, H. M. Pain and V. Sik, *Chem. Commun.* **1992**, 303.

[230] E. W. Abel, V. S. Dimitrov, N. J. Long, K. G. Orrell, A. G. Osborne, V. Sik, M. B. Hursthouse and M. A. Mazid, *Dalton Trans.* **1993**, 291.

[231] E. W. Abel, K. G. Orrell, A. G. Osborne, H. M. Pain, V. Sik, M. B. Hursthouse and K. M. A. Malik, *Dalton Trans.* **1994**, 3441.

[232] E. Rotondo, G. Giordano and D. Minniti, *Dalton Trans.* **1996**, 253.

[233] R. Chotalia, E. C. Constable, M. J. Hannon and D. A. Tocher, *Dalton Trans.* **1995**, 3571.

[234] S. Ramdeehul, L. Barloy, J. A. Osborn, A. De Cian and J. Fischer, *Organometallics* **1996**, *15*, 5442.

[235] K. M. Rao, C. R. K. Rao and P. S. Zacharias, *Polyhedron* **1997**, *16*, 2369.

[236] D. H. Gibson, J. G. Andino and M. S. Mashuta, *Organometallics* **2005**, *24*, 5067.

[237] A. Doppiu, G. Minghetti, M. A. Cinellu, S. Stoccoro, A. Zucca and M. Manassero, *Organometallics* **2001**, *20*, 1148.

[238] L. Chassot, E. Müller and A. von Zelewsky, *Inorg. Chem.* **1984**, *23*, 4249.

[239] F. P. Pruchnik, F. Robert, Y. Jeannin and S. Jeannin, *Inorg. Chem.* **1996**, *35*, 4261.

[240] J. E. Aguado, M. J. Calhorda, M. C. Gimeno and A. Laguna, *Chem. Commun.* **2005**, 3355.

[241] L. I. Semenova and A. H. White, *Aust. J. Chem.* **1999**, *52*, 539.

[242] L. I. Semenova and A. H. White, *Aust. J. Chem.* **1999**, *52*, 507.

[243] L. I. Semenova, A. N. Sobolev, B. W. Skelton and A. H. White, *Aust. J. Chem.* **1999**, *52*, 519.

[244] M. G. B. Drew, P. B. Iveson, M. J. Hudson, J. O. Liljenzin, L. Spjuth, P.-Y. Cordier, A. Enarsson, C. Hill and C. Madic, *Dalton Trans.* **2000**, 821.

[245] A. Figuerola, J. Ribas, X. Solans, M. Font-Bardia, M. Maestro and C. Diaz, *Eur. J. Inorg. Chem.* **2006**, 1846.

[246] P. Przychodzen, K. Lewinski, R. Pelka, M. Balanda, K. Tomala and B. Sieklucka, *Dalton Trans.* **2006**, 625.

[247] P. Przychodzen, R. Pelka, K. Lewinski, J. Supel, M. Rams, K. Tomala and B. Sieklucka, *Inorg. Chem.* **2007**, *46*, 8924.

[248] Y. Fukuda, A. Nakao and K. Hayashi, *Dalton Trans.* **2002**, 527.

[249] C. J. Kuehl, R. E. Da Re, B. L. Scott, D. E. Morris and K. D. John, *Chem. Commun.* **2003**, 2336.

[250] J. M. Veauthier, E. J. Schelter, C. J. Kuehl, A. E. Clark, B. L. Scott, D. E. Morris, R. L. Martin, J. D. Thompson, J. L. Kiplinger and K. D. John, *Inorg. Chem.* **2005**, *44*, 5911.

[251] C. N. Carlson, C. J. Kuehl, R. E. Da Re, J. M. Veauthier, E. J. Schelter, A. E. Milligan, B. L. Scott, E. D. Bauer, J. D. Thompson, D. E. Morris and K. D. John, *J. Am. Chem. Soc.* **2006**, *128*, 7230.

[252] C. N. Carlson, B. L. Scott, R. L. Martin, J. D. Thompson, D. E. Morris and K. D. John, *Inorg. Chem.* **2007**, *46*, 5013.

[253] G. H. Maunder and A. Sella, *Polyhedron* **1997**, *17*, 63.

[254] T. M. Bockman and J. K. Kochi, *J. Org. Chem.* **1990**, *55*, 4127.

[255] A. Lichtblau, H.-D. Hausen, W. Schwarz and W. Kaim, *Inorg. Chem.* **1993**, *32*, 73.

[256] S. Kraft, E. Hanuschek, R. Beckhaus, D. Haase and W. Saak, *Chem.-Eur. J.* **2005**, *11*, 969.

[257] R. S. Mulliken, *J. Chem. Phys.* **1955**, *23*, 1833.

[258] W. Kabsch, *J. Appl. Crystallogr.* **1988**, *21*, 916.

[259] *CAD4 Express Software*, Enraf-Nonius, Delft, The Netherlands, **1994**.

[260] L. J. Farrugia, *J. Appl. Crystallogr.* **1999**, *32*, 837.

[261] K. Harms and S. Wocadlo, *XCAD4, CAD4 Data Reduction*, University of Marburg, **1995**.

[262] A. C. T. North, D. C. Phillips and F. S. Mathews, *Acta. Crystallogr. A* **1968**, *24*, 351.

[263] G. M. Sheldrick, *Acta Crystallogr. A* **2008**, *A64*, 112.

[264] L. J. Barbour, *J. Supramol. Chem.* **2003**, *1*, 189.

[265] *Gaussian 03, Revision E.01*, M. J. Frisch, G. W. Trucks, H. B. Schlegel, G. E. Scuseria, M. A. Robb, J. R. Cheeseman, J. A. Montgomery, Jr., T. Vreven, K. N. Kudin, J. C. Burant, J. M. Millam, S. S. Iyengar, J. Tomasi, V. Barone, B. Mennucci, M. Cossi, G. Scalmani, N. Rega, G. A. Petersson, H. Nakatsuji, M. Hada, M. Ehara, K. Toyota, R. Fukuda, J. Hasegawa, M. Ishida, T. Nakajima, Y. Honda, O. Kitao, H. Nakai, M. Klene, X. Li, J. E. Knox, H. P. Hratchian, J. B. Cross, V. Bakken, C. Adamo, J. Jaramillo, R. Gomperts, R. E. Stratmann, O. Yazyev, A. J. Austin, R. Cammi, C. Pomelli, J. W. Ochterski, P. Y. Ayala, K. Morokuma, G. A. Voth, P. Salvador, J. J. Dannenberg, V. G. Zakrzewski, S. Dapprich, A. D. Daniels, M. C. Strain, O. Farkas, D. K. Malick, A. D. Rabuck, K. Raghavachari, J. B. Foresman, J. V. Ortiz, Q. Cui, A. G. Baboul, S. Clifford, J. Cioslowski, B. B. Stefanov, G. Liu, A. Liashenko, P. Piskorz, I. Komaromi, R. L. Martin, D. J. Fox, T. Keith, M. A. Al-Laham, C. Y. Peng, A. Nanayakkara, M. Challacombe, P. M. W. Gill, B. Johnson, W. Chen, M. W. Wong, C. Gonzalez, and J. A. Pople, Gaussian, Inc., Wallingford CT, **2004**.

[266] *Gaussian 09, Revision A.02*, M. J. Frisch, G. W. Trucks, H. B. Schlegel, G. E. Scuseria, M. A. Robb, J. R. Cheeseman, G. Scalmani, V. Barone, B. Mennucci, G. A. Petersson, H. Nakatsuji, M. Caricato, X. Li, H. P. Hratchian, A. F. Izmaylov, J. Bloino, G. Zheng, J. L. Sonnenberg, M. Hada, M. Ehara, K. Toyota, R. Fukuda, J. Hasegawa, M. Ishida, T. Nakajima, Y. Honda, O. Kitao, H. Nakai, T. Vreven, J. A. Montgomery, Jr., J. E. Peralta, F. Ogliaro, M. Bearpark, J. J. Heyd, E. Brothers, K. N. Kudin, V. N. Staroverov, R. Kobayashi, J. Normand, K. Raghavachari, A. Rendell, J. C. Burant, S. S. Iyengar, J. Tomasi, M. Cossi, N. Rega, J. M. Millam, M. Klene, J. E. Knox, J. B. Cross, V. Bakken, C. Adamo, J. Jaramillo, R. Gomperts, R. E. Stratmann, O. Yazyev, A. J. Austin, R. Cammi, C. Pomelli, J. W. Ochterski, R. L. Martin, K. Morokuma,

V. G. Zakrzewski, G. A. Voth, P. Salvador, J. J. Dannenberg, S. Dapprich, A. D. Daniels, Ö. Farkas, J. B. Foresman, J. V. Ortiz, J. Cioslowski, and D. J. Fox, Gaussian, Inc., Wallingford CT, **2009**.

Appendix A

General Experimental

All large scale (in excess of 50 mg) manipulations were performed under a high purity argon atmosphere using standard Schlenk techniques. Small scale manipulations and sample storage was undertaken under an atmosphere of dry nitrogen in a glove box. Solvents (THF, PhMe, Et_2O, pet. ether) were dried by passage through an Innovative Technologies Solvent Purification system and, where appropriate, stored over a sodium mirror. Benzene was dried over sodium, fractionally distilled and freeze-degassed prior to use. For the preparation of organic intermediates and ligands, solvents including methanol, ethanol, dichloromethane, toluene, pet. ether and diethyl ether were used as received. NMR solvents were dried over sodium using benzophenone indicator and trap-to-trap distilled prior to use. Volatile liquid reagents were purchased from commercial sources and dried over 4 Å sieves and then trap-to-trap distilled prior to use. Volatile solid reagents were purchased from commercial sources and sublimed prior to use. Non-volatile solid reagents were purchased from commercial sources and used as received after prolonged heating under vacuum.

NMR spectra were recorded in $CDCl_3$ or appropriately dried C_6D_6, D_8-THF or D_8-PhMe, as noted, using a Varian Mercury Plus 300 NMR operating at 299.91 MHz (^1H) and 75.42 MHz (^{13}C). The ^1H NMR spectra were referenced to the residual solvent resonances of $CDCl_3$ (7.26 ppm), C_6D_6 (7.16 ppm), D_8-THF (1.73 or 3.75 ppm) and D_8-PhMe (2.09 ppm). ^{13}C NMR spectra were referenced to the ^{13}C resonances of $CDCl_3$ (77.2 ppm) or C_6D_6 (128.4 ppm).

Elemental analysis and GC-MS were undertaken at the Central Science Laboratory, University of Tasmania. Elemental analysis was conducted by Dr. Thomas Rodemann using a ThermoFinnigan Flash EA 1112 Elemental Analyser. GC-MS was conducted by A/Prof. Noel Davies using a Varian 1200 triple quadropole benchtop GC-MS.

With few exceptions, the structures reported herein are reported for X-ray diffraction data that were collected at the Australian Synchrotron using the MX1 and MX2 (formerly PX1 and PX2) beamlines at -173 °C for crystals mounted on Hampton Scientific cryoloops. Data was collected on a single axis goniometer with 360 ° rotation at maximum resolution using the fixed detector. The Blu-Ice software package[144] was employed to control the diffractometer and the data were reduced using XDS.[258]

The remaining few structures reported herein and explicitly noted in the text were obtained *via* X-ray diffraction data collected at the University of Tasmania and were obtained with an Enraf Nonius TurboCAD4 the Mo Kα radiation (λ = 0.71073 Å) at -80 °C on crystals mounted on glass fibres within a preset 2θ limit of 50 ° using conventional scans. Data were reduced using the CAD4 Express,[259] WinGX,[260] XCAD4[261] and PsiScans[262] programmes.

With the exception of complex (**10**), all structures reported herein were solved and refined by the author. Structures were solved by direct methods with SHELXS-97[263] and refined using full-matrix least-squares routines against F^2 with SHELXL-97,[263] visualised using X-SEED.[264] Unless specifically noted, all non-hydrogen atoms were refined anisotropically and all hydrogens were placed in calculated positions. Calculated hydrogens were refined using a riding model with fixed C−H distances of 0.95 (sp^2-CH), 0.99 (sp^3-CH, CH_2), 0.98 Å (CH_3). The thermal parameters of all calculated hydrogen atoms were estimated as $U_{iso}(H) = 1.2U_{eq}(C)$, except for CH_3 where $U_{iso}(H) = 1.5U_{eq}(C)$.

Details for the handling of special cases, such as disorder, are provided electronically in Appendix C *via* .CIF file in the format '*compound number*.CIF'. The .CIFs are sorted into discrete folders by Chapter.

Theoretical calculations were performed using Gaussian03[265] and Gaussian09[266] on the National Computational Infrastructure (NCI) supercomputer cluster Vayu, in Canberra, ACT, Australia. Computational output files are provided electronically in Appendix D *via* .OUT file in the format '*compound number*'.OUT or '*compound name'*.OUT, as appropriate. The .OUTs are sorted into discrete folders by Chapter.

Appendix B

Definition of the Molecular Environment

Figure 8-1 shows the typical coordination of a substituted pyridine ligand within the samarium macrocycle species. Clearly, the steric bulk of the ancillary ligand must lie within the binding groove; bulk across the cavity (at the level of coordination) will prohibit any encounter.

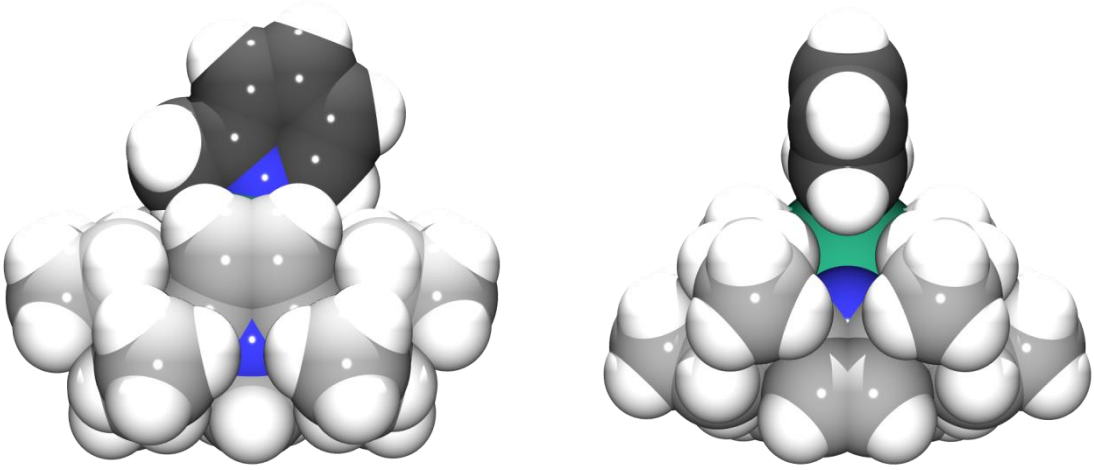

Figure 8-1: Space-filling representations of [($Et_8N_4Me_2$)Sm(2-methylpyridine)],(**15**), looking at the face of the pyridine ring, left, and looking down the binding groove, right.
Dark grey carbon atoms denote $C_{pyridine}$ while light grey denote $C_{macrocycle}$.

To meaningfully discuss and compare the coordination (and the effect on the macrocyclic geometry of that coordination) of this series of complexes, it is necessary to first define several relationships within the molecule. The foundations of this definition are the three least-squares plane made by a) the four *meso*-carbon atoms of the macrocycle, b) the two nitrogens of the pyrrolide rings and the samarium, and c) the two nitrogens of the *N*-methylpyrrole rings and the samarium. These three planes are orthogonal to each other and thus define three spatial axes.

Cursory visual inspection of the coordination environment reveals that it is usual for any 2,6- asymmetrically substituted coordinating pyridine to be subject to some angle of tilt within the binding groove, Figure 8-2. The relationship between the difference in the distance to the N_{Me}-Sm-N_{Me} plane for C_4 and N, a_x and b_x respectively, and the directly measurable distance between C_4 and N, d, give, by use of the sine trigonometric identity for a right-angled triangle, the angle of tilt. Similarly, the difference in height above the *meso* plane of C_4 and N, a_y and b_y respectively, may be used with the cosine trigonometric identity for a right-angled triangle to find the angle of tilt.

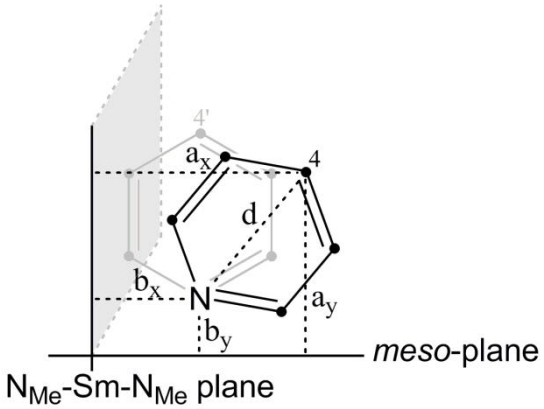

Figure 8-2: Finding the tilt angle of the pyridine ring relative to the *meso*-plane, viewing the N_{Py}-Sm-N_{Py} plane lying on the page and with the N_{Me}-Sm-N_{Me} plane projected into the page for clarity.

For a right-angled triangle the expression $(a_x - b_x)^2 + (a_y - b_y)^2 = d^2$ holds true. It was found that this relationship does not hold true in most cases under investigation; the triangle is not a right triangle and thus quantification of the tilt angle cannot be achieved *via* this method.

Further consideration revealed that the distance between N and C_4 in the N_{Py}-Sm-N_{Py} plane, a_y - b_y, cannot be measured relative to the *meso*-plane since the pyridine ring does not lie in the N_{Py}-Sm-N_{Py} plane. The pyridine ring, relative to the *meso*-plane, is potentially subject to not only a tilt, but an angle of incidence and/or a twist, Figure 8-3. Furthermore, N is often displaced from both N_{Py}-Sm-N_{Py} and N_{Me}-Sm-N_{Me} planes. Thus

the right-angled triangle trigonometric identities, which apply for coplanar points, are not initially applicable and values, particularly for the vertical (orthogonal to the *meso*-plane) distance, are not immediately forthcoming. For all of these reasons, direct measurement of the angle between Sm, N and C_4 is meaningless.

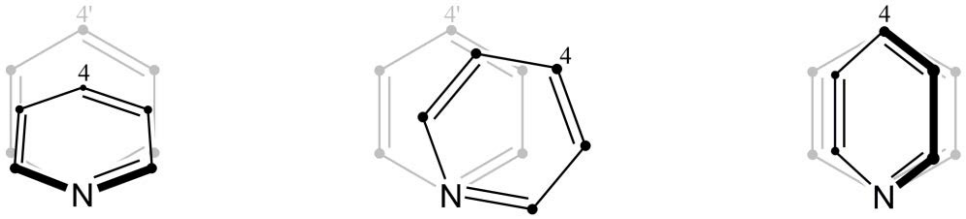

Figure 8-3: Rotation of the pyridine ring about the nitrogen atom in each dimension relative to the initial ring containing N′ and C4′.

The distance between N and C_4 on the N_{Me}-Sm-N_{Me} plane, c (Figure 8-4), can be measured by applying the sine relationship for a right triangle to the angle of incidence of the pyridine ring to the *meso*-plane (x), since the distance between N and C_4, d (Figure 8-2), is known. It should be noted that when the pyridine ring lies in the N_{Py}-Sm-N_{Py} plane, $c = a_x - b_x$.

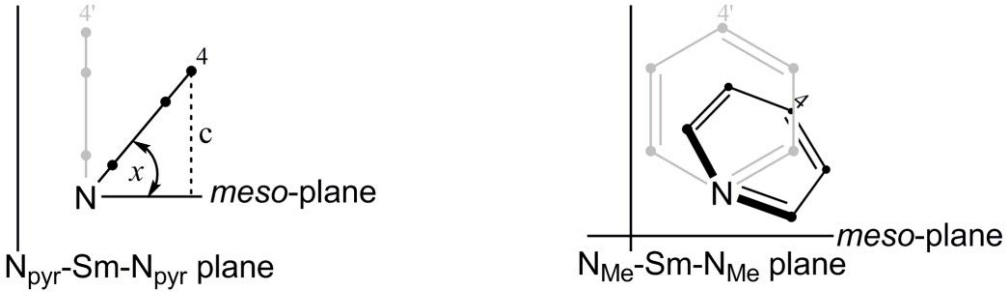

Figure 8-4: Orthogonal views of a pyridine ring with significant angles of incidence and tilt.

With length c found, the distance from N to C_4 in the N_{Me}-Sm-N_{Me} plane is known. The distance from the N_{Me}-Sm-N_{Me} plane is known (a_x - b_x, Figure 8-2) and the distance from N to C4, d, is known. Thus the tilt angle can be calculated using the general cosine rule for a non-right triangle, Equation 8-1:

$$\cos(tilt) = \frac{c^2 + d^2 - (a_x - b_x)^2}{2cd}$$ **Equation 8-1**

Quantification of the twist angle (Figure 8-3) is obtained by finding the angle between the plane of the pyridine ring and the N_{Me}-Sm-N_{Me} plane. The angle of twist is the difference from orthogonal; any significant twist within the binding groove is sterically prohibited, thus the angle of twist is always small for this system.

The angle of incidence (Figure 8-3) is obtained by simply measuring the angle between the plane of the pyridine ligand and the N_{Py}-Sm-N_{Py} plane, and begins at zero for „vertical' attack down on the metal and increases in value as the attack angle departs from vertical.

The tilt angle (Figure 8-3) defies measurement *via* a simple relationship between ligand and macrocycle planes (thus requiring the calculation outlined, *vide supra*) as no plane can be appropriately defined relative to the *meso*-plane for planar ligands; simplistically, it is „side-on' and no third point is available to define the desired plane.

Having thus defined the rotation of a plane about the axis of all three spatial dimensions relative to the macrocycle, quantification of the molecular environment of the series of planar, pyridine based complexes formed with samarium *trans-N,N'*-dimethyl-*meso*-octaethylporphyrinogen is described Chapter 4.

8.1 Satisfactory Approximation

In all cases reported in this thesis, the use of the sine function for a right-angled triangle provided the same value for the tilt angle as the more rigorous method described above to within 0.3 °, and would thus be appropriate as an approximation, Equation 8-2 (where a_x and b_x are the distance to the N_{Me}-Sm-N_{Me} plane for C_4 and N, respectively, and d is the distance between C_4 and N). The cosine and tangent operators showed significant variation using the right-triangle relationship, with variation in values for the tilt angle of up to 9.5 ° from the non-right triangle calculated angle (the variation was most marked in the cosine relationship). The Sm−N−C through-bond angle, which is a combination of tilt, displacement and angle of incidence, was shown to vary from the calculated tilt angle by up to 26 ° for bis(adducts) and up to 12 ° for mono(adducts), and is clearly not a meaningful relationship.

$$\sin tilt = \frac{a_x - b_x}{d} \qquad \text{Equation 8-2}$$